FACULTY OF ENGINEERING
AND ARCHITECTURE

Fractional Order Models Enabling Control Strategies Based on Material Properties

Isabela Roxana Birs

Doctoral dissertation submitted to obtain the academic degree of
Doctor of Engineering

Supervisors
Prof. Clara-Mihaela Ionescu, PhD - Dana Copot, PhD

Department of Electromechanical, Systems and Metal Engineering
Faculty of Engineering and Architecture, Ghent University

May 2022

GHENT
UNIVERSITY

FACULTY OF ENGINEERING AND ARCHITECTURE

Fractional Order Models Enabling Control Strategies Based on Material Properties

Isabela Roxana Birs

Doctoral dissertation submitted to obtain the academic degree of
Doctor of Engineering

Supervisors
Prof. Clara-Mihaela Ionescu, PhD - Dana Copot, PhD

Department of Electromechanical, Systems and Metal Engineering
Faculty of Engineering and Architecture, Ghent University

May 2022

GHENT UNIVERSITY

ISBN 978-94-6355-591-3
NUR 950, 954
Wettelijk depot: D/2022/10.500/32

Members of the Examination Board

Chair

Prof. Patrick De Baets, PhD, Ghent University

Other members entitled to vote

Annelies Coene, PhD, Ghent University
Prof. Frederik De Belie, PhD, Ghent University
Christoph Portier, PhD, Ghent University
Prof. Antonio Visioli, PhD, Università degli Studi di Brescia, Italy

Supervisors

Prof. Clara-Mihaela Ionescu, PhD, Ghent University
Dana Copot, PhD, Ghent University

Acknowledgements

This project would not have been possible without the support of my two promoters. I would like to thank Prof. Clara Ionescu for her outstanding mentorship, guidance and unconditional support. Apart from research, she also taught me how to always think outside the box and that many doors can be opened by hard work, perseverance and determination. Many thanks to Dr. Dana Copot for her patience, invaluable feedback and the continuous assistance she has provided during the last 4 years, always pushing me to work harder.

Thanks to the Research Foundation Flanders for awarding me a strategic basic research fellowship, providing me with the financial means to complete this project. Special thanks to Maria and Mihaela for making my time in Gent memorable, offering advice and encouragement with a perfect blend of insight and humor.

And finally, I would like to thank my parents, friends and Prof. Cristina Muresan who endured this long process with me, always offering unconditional love and support.

Isabela Roxana Bîrs
Ghent, May, 2022.

Contents

List of Figures

List of Tables

Samenvatting

Een specifieke klasse vloeistoffen wordt beschreven door niet-lineaire vergelijkingen die buiten de context vallen van de Newtoniaanse vloeistofmechanica, die nogal wat (lokale) lineaire parametereigenschappen veronderstelt:

- homogeniteit,
- causaliteit,
- herhaalbaarheid,
- constante parameters in tijd en ruimte,
- lineaire dynamica, enz.

Modelleren en regelen van een niet-Newtoniaanse vloeistof dynamische omgeving heeft een vrij groot aantal interdisciplinaire toepassingen. Nauwkeurige karakterisering van de eigenschappen van dit type vloeistofdynamica is van fundamenteel belang op gebieden zoals:

- voorspellingen van klimaatverandering,
- analyse van bloedeigenschappen,
- dynamica van grondwater transportsystemen,
- positionering van deeltjes in elektromagnetisch aangedreven vloeistoffen (productie van vloeibaar staal),
- nano-sensor geleiding voor structurele veranderingen in arteriële bloedwanden,
- navigatie van onbemande onderwatertuigen in water- en ijsmengsels voor verschillende opmetingen (petroleumlekken, vervuilingsgraad, in kaart brengen van de oceaanbodem, enz.).

De meeste eigenschappen van niet-Newtoniaanse vloeistoffen overlappen met die van visco-elastische materialen, zoals polymeren, longweefsel,

gel-achtige substanties, rubber, enz. Specifieke eigenschappen zoals geheugen, kruip en schuifspanning volgen Newton's klassieke wet van dynamische viscositeit niet. Ze kunnen gekarakteriseerd worden door combinaties van machtswetten met exponentiële functies. Dit zijn niet-rationele uitdrukkingen van gecombineerde niet-lineaire effecten in materiaalkruip en -rek en ze staan voor een veralgemening van differentiaalvergelijkingen van gehele orde naar differentiaalvergelijkingen van fractionele orde.

Veralgemeende-orde vergelijkingen zijn krachtige wiskundige hulpmiddelen die uit fractionele calculus voortkomen en met succes geïntroduceerd werden in technische en interdisciplinaire toepassingsgebieden. Tot nu toe blijft het gebruik van fractionele calculus tools voor het modelleren en regelen van niet-Newtoniaanse omgevingen zeer beperkt en de meeste theoretische ontwikkelingen bouwen verder op de bekende, volwassen, klassieke Newtoniaanse theorie.

In deze verhandeling worden de huidige beperkingen die opduiken bij het modelleren en regelen van niet-Newtoniaanse vloeistofdynamica onderzocht teneinde originele oplossingen te vinden om de overvloed aan toepassingen die hierin worden beschreven aan te pakken. Het proefschrift richt zich op het uitbreiden van de modellering van niet-Newtoniaanse vloeistofdynamica voorbij de stand van het huidig onderzoek, met veelbelovende resultaten die geboekt worden door het gebruik van fractionele wiskunde. Veralgemeende contextbewuste concepten op basis van fractionele calculus theorie worden gebruikt voor industrieel geschikte oplossingen in het kader van Industrie 4.0-paradigma's.

Naast nieuwe niet-Newtoniaanse modelontwikkeling en experimentele studies omtrent de invloed van variërende parameters op verschillende fractionele-orde modellen, bevat het proefschrift ook relevante casestudies en waarnemingen.

Het proefschrift krijgt een strategische en industriële connotatie, belichaamd door meerdere casestudies geïnspireerd door concepten rond gerichte medicijnafgifte:

- positioneren van een duikboot in een niet-Newtoniaanse, op bloed lijkende vloeistof,
- modelleren en regelen van het vloeibaar staal debiet in de continugieterij van ArcelorMittal te Gent en
- ConSigma fabricage van pillen in farmaceutische processen.

Verder bestaat het fysieke resultaat van het proefschrift uit het ontwerp en de bouw van een contextbewuste, zeer veelzijdige experimentele proefopstelling, die een goedkope, laagdrempelige en leerzame oplossing biedt voor de problematiek van modellering, identificatie en regeling van objecten in niet-Newtoniaanse vloeistoffen. De opstelling is bedoeld als een toegankelijk hulpmiddel die een systematische analyse van het dynamisch

gedrag van zwevende objecten in niet-Newtoniaanse vloeistoffen mogelijk maakt. Dankzij het pragmatisch en schaalbaar ontwerp kan deze opstelling op een eenvoudige manier herbouwd worden teneinde een veelvoud aan toepassingen die verband houden met niet-Newtoniaanse vloeistofstroming te analyseren.

Het proefschrift is opgebouwd uit 9 hoofdstukken, gericht op diverse aspecten van de niet-Newtoniaanse vloeistofstroming.

Hoofdstuk 1 situeert het hoofdonderwerp van het proefschrift in de algemene onderzoekscontext, met betrekking tot de stand van het onderzoek. De belangrijkste doelstellingen, persoonlijke bijdragen en innovatieve resultaten zijn opgenomen om de lezer kennis te laten maken met de huidige uitdagingen en beperkingen van niet-Newtoniaans gericht onderzoek en met de voorgestelde originele oplossingen.

Het volgende hoofdstuk 2, presenteert de relevante wiskundige achtergrond van fractionele calculus. De voordelen van dit krachtig hulpmiddel worden toegelicht voor zowel modellering als regeling. Er wordt aangetoond dat fractionele-orde modellen complexe dynamica omvatten binnen een transfertfunctie, met een verminderd aantal parameters maar met een grotere veelzijdigheid om complexe fenomenen vast te leggen. Dit rechtvaardigt de onderzoekshypothese dat niet-Newtoniaanse vloeistoffen van nature via hun specifieke eigenschappen het gebruik van fractionele-calculus tools vereisen. Verder wordt ook fractionele-orde regeling geanalyseerd en de toegevoegde waarde ten opzichte van klassieke gehele-orde regelaars wordt aangetoond door middel van performantie, stabiliteit en intrinsieke robuustheid. De meest populaire afstellingsprocedures worden kort gepresenteerd als startpunt voor de regelstrategieën die verder in dit proefschrift worden gebruikt.

Niet-Newtoniaanse vloeistofstroming wordt kort geïntroduceerd in Hoofdstuk 3. Verschillen tussen Newtoniaanse en niet-Newtoniaanse dynamica worden geïllustreerd, waarbij de bevindingen van Hoofdstuk 2 worden gelinkt aan de complexe dynamica aanwezig in dit soort vloeistoffen. Een beknopte classificatie die relevant is voor het huidige proefschrift wordt gepresenteerd, gebaseerd op tijdsafhankelijke en -onafhankelijke criteria. Algemene Navier-Stokes vergelijkingen worden voorgesteld, die veelvuldig worden gebruikt bij het modelleren van niet-Newtoniaanse gerelateerde verschijnselen. Van het eerder genoemde model wordt een fractionele-orde veralgemening uitgevoerd met behulp van snelheidsprofielen in de pijpleiding, waarbij ook rekening wordt gehouden met opvoerhoogteverlies door wrijving. Het resultaat is een theoretisch kader voor het modelleren van snelheidsprofielen en zwevende (infinitesimale) objecten in een niet-Newtoniaanse vloeistofomgeving, met behulp van fractionele constitutieve vergelijkingen voor snelheidsprofielen en stroming. Deze theoretische analyse wordt uitgevoerd onder veronderstelling van stabiele en pulserende stromingsomstandigheden, met onsamendrukbare eigenschappen.

Hoofdstuk 4 presenteert contextbewuste regelparadigma's om de voordelen van gebeurtenis-gebaseerde regelmethodes - zoals resource optimalisatie en bandbreedte toewijzing - te combineren met de superieure prestaties van fractionele-orde regeling. Theoretische en implementatie aspecten worden gepresenteerd die leiden tot een veralgemening van gebeurtenisgebaseerde regeling naar het fractionele-calculus gebied. Verschillende numerieke voorbeelden valideren de voorgestelde methodologie en bieden een nuttig hulpmiddel, vooral voor industriële toepassingen waar gebeurtenisgebaseerde regeling het meest nodig is. Deze strategie zal verder gebruikt worden voor energiezuinige en contextbewuste implementaties met betrekking tot niet-Newtoniaanse vloeistoffen.

Het effect van wisselende eigenschappen in niet-Newtoniaanse vloeistoffen wordt in Hoofdstuk 5 vanuit een experimentele benadering aangepakt. Impedantiespectroscopie wordt gebruikt in een laboratoriumopstelling die in staat is om te experimenteren met de eigenschappen van verschillende niet-Newtoniaanse vloeistoffen: glucose, honing, handzeep, shampoo, avocado-/maïs-/olijfolie, zachte/standaard wasmiddelen. Een fractionele-orde impedantiemodel om vloeistofmechanische eigenschappen vast te leggen wordt voorgesteld en dan verder gevalideerd via de experimentele waarnemingen.

Hoofdstuk 6 richt zich vanuit experimenteel oogpunt op objecten die in niet-Newtoniaanse vloeistoffen zijn ondergedompeld. Deze studie houdt verband met toepassingen zoals gerichte medicijnafgifte. De proefopstelling is ontworpen en gebouwd om niet-Newtoniaanse vloeistofstroming te illustreren. Een miniatuur duikboot wordt beschouwd als het ondergedompelde object. Dit hoofdstuk richt zich op het modelleren van de bewegingsdynamica van deze onderwater robot, uitgaande van reeds bekende Newtoniaanse interacties tussen de duikboot en de vloeistof. Voor het resulterende niet-Newtoniaans fractionele-orde procesmodel wordt een fractionele-orde regelstrategie gebruikt om de positie van het onderwater object in de visco-elastische omgeving te beïnvloeden. De voorgestelde modellering- en regelmethodologieën worden geconsolideerd met experimentele gegevens die worden gebruikt om de betrouwbaarheid van de gepresenteerde concepten te valideren. De robuustheid van de regelstrategie wordt experimenteel gevalideerd in zowel Newtoniaanse als niet-Newtoniaanse omgevingen. Verder wordt contextbewustzijn geëxploreerd met behulp van de paradigma's die geïntroduceerd werden in Hoofdstuk 4.

Vloeibaar staal wordt gemodelleerd als een niet-Newtoniaanse vloeistof in Hoofdstuk 7 op basis van geregistreerde procesgegevens binnen ArcellorMittal Gent. Alle bestaande studies modelleren de stroming van gesmolten metaal in de gietvorm van een continugieterij met behulp van gehele-orde differentiatie; dit beperkt het vermogen van de verkregen modellen om de visco-elastische fysische verschijnselen nauwkeurig te omschrijven. Een nauwkeuriger model voor de vloeistofsnelheid wordt verkregen door middel van fractionele calculus op basis van procesgegevens

en van bevindingen uit Hoofdstukken 3 en 5.

Het resulterende fractionele-orde model wordt vergeleken met een vorig gehele-orde model teneinde de verbeteringen te evalueren die door de generalisatie worden bekomen. Bovendien wordt een gebeurtenis-gebaseerde fractionele-orde PI-regelaar afgesteld via specificaties in het frequentiedomein en uitgetest onder verschillende werkomstandigheden. De implementatie is gebaseerd op Hoofdstuk 4, met het oog op het verbeteren van oppervlaktedefecten in de geproduceerde staalplaten. Realistische procesomstandigheden zoals verstopping en sensorruis worden gebruikt om de verkregen modellen en regelstrategie te valideren.

Hoofdstuk 8 volgt in de farmaceutische industrie de paradigmaverschuiving van batch naar continue productie bij de fabricage van pillen. Sommige subprocessen in de productie van pillen brengen veranderingen teweeg in poeder- en vloeistofmengsels, granulatie, dichtheid, waardoor de stromingsomstandigheden van de grondstof veranderen en niet-Newtoniaanse karakteristieken opduiken tijdens het productieproces. Met behulp van impedantiepectroscopie (zoals eerder vermeld in Hoofdstuk 5) in een continue detectie- en monitoringcontext, is het mogelijk om online identificatie uit te voeren van gegeneraliseerde (fractionele) orde parametrische modellen waarbij de coëfficiënten gecorreleerd zijn met veranderingen in materiaaleigenschappen. De modelparameters zijn dan deel van een zelfafstellende regelversterking die wordt gebruikt in verhoudingsregeling als onderdeel van de lokale procesregellus. De hier voorgestelde oplossing is eenvoudig te implementeren en vormt een belangrijke toegevoegde waarde in de huidige stand van zaken op gebied van farmaceutische productietechnologieën.

Ten slotte, Hoofdstuk 9 sluit het proefschrift af. Onderzoeksrichtingen, vooruitzichten en algemene bevindingen worden kort weergegeven.

Summary

A particular class of fluids are those governed by nonlinear equations outside the context of Newtonian fluid mechanics theory, which assumes a manifold of (local) linear parameter properties: homogeneity, causality, repeatability, constant variables in time and space, linear dynamics, etc. Modeling and control of non-Newtonian fluid dynamic environment has quite a plethora of cross-disciplinary applications. Accurate characterization of properties in this type of fluid dynamics has a wide relevance in fields such as:

- climate change predictions,
- blood properties analysis,
- dynamics of ground water transportation systems,
- positioning particles in electro-magnetic actuated fluids (liquid steel manufacturing),
- nano-sensor guidance for structural changes in blood arterial walls,
- unmanned underwater vehicles navigation in water and ice mixtures for various surveys (petrol leaks, pollution levels, ocean floor mapping, etc.).

Most properties of non-Newtonian fluids overlap with that of viscoelastic materials, such as polymers, lung tissue, gel-like substances, rubber, etc. Specific properties as memory, creep and shear stress do not follow classical Newton's law of dynamic viscosity and has been proven to be well characterized by combinations of power-law with exponential functions. These are non-rational expressions of combined nonlinear effects in material creep and strain, and they represent a generalization from integer order differential equations to fractional order differential equations.

Generalized order equations are powerful mathematical tools emerging from fractional calculus and successfully introduced in engineering and cross-disciplinary application fields. Hitherto, the use of fractional calculus tools for modeling and control of non-Newtonian environments has been very scarce, while most of the theoretical state of art relies on the well-known, mature, classical Newtonian theory.

Consequently, this dissertation aims at overcoming the current limitations encountered in modeling and control of non-Newtonian fluid dynamics, by searching for original solutions to resolve the plethora of applications described herein. The thesis focuses on extending the modeling of non-Newtonian fluid dynamics beyond the state of art, with promising results obtained through the usage of fractional calculus. Generalized context-aware concepts based on fractional calculus theory are used for an industrially suitable solutions with respect to Industry 4.0 paradigms.

Apart from novel non-Newtonian model development and experimental studies on the influence of varying parameters on different fractional order models, the thesis also includes relevant case studies for stepping beyond current state of art.

The thesis is given an industrial connotation, epitomized through multiple case studies inspired by targeting drug delivery concepts, i.e., positioning of a submersible in a non-Newtonian, blood-resembling fluid, modeling and controlling the liquid steel flow inside the continuous caster from ArcelorMittal Ghent and ConSigma tablet manufacturing in pharmaceutical processes.

Furthermore, the physical outcome of the dissertation is the design and execution of a context-aware, highly versatile experimental benchmark, offering a low-cost, approachable, and instructive solution to the problematic of modeling, identification, and control of objects in non-Newtonian fluids. This is meant to be an accessible tool that enables systematic analysis of dynamic behavior of suspended objects in non-Newtonian fluids. The benchmark can be easily recreated for a manifold of applications related to non-Newtonian fluid flow.

The thesis is structured into 9 chapters, focusing on various aspects of non-Newtonian fluid flow.

Chapter 1 places the thesis's main topic into the general research context, with respect to the state of art. Main objectives, personal contributions and innovative results are included to introduce the reader to current challenges and limitations of non-Newtonian focused research and proposed solutions.

The next chapter, Chapter 2, presents the relevant mathematical background associated with fractional calculus. The benefits of this powerful tool are highlighted for both modeling and control. It is shown how fractional order models encompass complex dynamics within a transfer function that has a reduced number of parameters, but an increased versatility to capture complex phenomena. This justifies the research hypothesis that non-Newtonian fluids require naturally via their specific properties the use of fractional calculus tools. Furthermore, fractional order control is also analyzed, proving its superiority over classical, integer order controllers, through performance, stability and intrinsic robustness. The most popular tuning approaches are briefly presented as starting point for the control strategies employed throughout the thesis.

Non-Newtonian fluid flow is briefly introduced in Chapter 3. Differences between Newtonian and non-Newtonian dynamics are illustrated, connecting the findings of Chapter 2 with complex dynamics present in this type of fluids. A brief classification relevant for the current thesis is presented, based on time dependent and independent criteria. General Navier-Stokes equations are provided, widely used in modeling non-Newtonian associated phenomena. From the previously mentioned model, a fractional order generalization is performed using velocity profiles in the pipeline, while also considering frictional head loss. The result is a framework for modeling velocity profiles and suspended (infinitesimal) objects in non-Newtonian fluid environment, using fractional constitutive equations for velocity profiles and flow. The theoretical analysis is performed under assumptions of steady and pulsatile flow conditions, with incompressible properties.

Chapter 4 presents context-aware control paradigms, to combine benefits of event-based control such as resource optimization and bandwidth allocation with the superior performance of fractional order control. Theoretical and implementation aspects are presented to provide a generalization of event-based control into the fractional calculus field. Different numerical examples validate the proposed methodology, providing a useful tool, especially for industrial applications where the event-based control is most needed. This strategy will be used further for energy efficient, and context aware implementations related to non-Newtonian fluids.

The effect of varying properties in non-Newtonian fluids is tackled in Chapter 5 from an experimental approach. Impedance spectroscopy is used in a laboratory setup able to experiment on the properties of various non-Newtonian fluids: glucose, honey, hand soap, shampoo, avocado/corn/olive oils, soft/standard detergents. A fractional order impedance model is proposed to capture fluid mechanical properties which is further validated on the experimentally acquired data.

Chapter 6 focuses on objects submerged in non-Newtonian fluids from an experimental perspective. This case study is connected to targeted drug delivery applications. The experimental benchmark is designed and built to demonstrate non-Newtonian fluid flow. A transiting submersible is considered the submerged object. This chapter focuses on modeling the motion dynamics of the submersible, starting from already known Newtonian interactions between the submersible and the fluid. For the obtained non-Newtonian fractional order process model, a fractional order control approach is employed to sway the submerged object's position inside the viscoelastic environment. The presented modeling and control methodologies are solidified by real-life experimental data used to validate the veracity of the presented concepts. The robustness of the control strategy is experimentally validated in both Newtonian and in non- Newtonian environments. Furthermore, context awareness is explored using the paradigms introduced in Chapter 4.

Liquid steel is modeled as a non-Newtonian fluid in Chapter 7 based on real-life plant data from ArcellorMittal Ghent. All existing studies model the flow of molten metal inside the mould of a continuous caster using integer order differentiation, limiting the ability of obtained models to accurately encapsulate the viscoelastic physical phenomena. A more accurate model is obtained for the fluid's velocity through fractional calculus based on real data and the findings of Chapters 3 and 5. The resulting fractional order model is compared to a previous integer order model to evaluate the improvements offered by the generalization. Furthermore, an event-based fractional order PI controller is tuned based on frequency domain specifications and tested under different operating conditions. The implementation is based on Chapter 4, with the main goal of improving surface defects of the produced steel slabs. Realistic process conditions such as clogging and noisy sensor data are used to validate the obtained models and control strategy.

Chapter 8 follows the paradigm shift in the pharmaceutical industry from batch to continuous production in tablet manufacturing. Some of the sub-processes involved in tablet manufacturing perform changes in powder and liquid mixtures, granulation, density, therefore changing flow conditions of the raw material, exhibiting non-Newtonian traits along the production process. Using impedance spectroscopy (as in the case study from Chapter 5) in a continuous sensing and monitoring context, it is possible to perform online identification of generalized (fractional) order parametric models where the coefficients are correlated to changes in material properties. The model parameters are then part of a self-tuning control gain used in ratio control as part of the local process control loop. The solution proposed here is easy to implement and poses a significant added value to the current state of art in pharmaceutical manufacturing technologies.

Finally, Chapter 9 concludes the thesis. Research directions, perspectives and general findings are briefly presented.

List of Acronyms

Notation	Description
CC	Continuous Casting
CFE	Continued Fraction Expansion
CRONE	Commande Robuste d'Ordre Non Entier
CPSO	Craziness based Particle Swarm Optimization
DE	Differential Evolution
EMA	Electromagnetic Actuator
FOMPC	Fractional Order Model Predictive Control
FOC	Fractional Order Control
FOPID	Fractional Order Proportional-Integral-Derivative
FOPDT	First Order Plus Dead Time
FOIM	Fractional Order Impedance Models
FOPI	Fractional Order Proportional-Integral
FOTF	Fractional Order Transfer Function
GA	Genetic Algorithm
GL	Grünwald-Letnikov
IAE	Integral Absolute Error
ITAE	Integral of Time Multiply Absolute Error
ISE	Integral Square Error
IOC	Integer Order Control
ISE	Integral Square Error
ISU	Integral of the Squared Control Signal
ITSE	Integral of Time Multiply Squared Error
ISCI	Integral Squared Control Input
LTI	Linear Time Invariant
ML	Mittag-Leffler
MSE	Mean Square Error
NMSE	Normalized Mean Square Error
PID	Proportional-Integral-Derivative
PD	Proportional-Derivative
PI	Proportional-Integral
PSO	Particle Swarm Optimization
PWM	Pulse-Width Modulation
RL	Riemann-Liouville
RAMI	Reference Architectural Model Industrie

SOTF	Second Order Transfer Function

List of Symbols

Symbol	Description
α	fractional order of differ-integration
β	fractional order of differ-integration
β_r	empirical parameter based on the ellipsoidal shape of the robot
γ	shear strain (Pa)
$\gamma\prime$	linear diffusion velocity coefficient (m/s)
$\dot{\gamma}$	shear strain rate ($1/s$)
$\Gamma(\cdot)$	Euler's gamma function
δ	Womersley parameter
η	fluid viscosity ($Pa * s$)
η'	dynamic viscosity (kg/ms)
η_B	plastic viscosity ($Pa * s$)
τ	shear stress (N)
τ_0^B	Bingham yield stress (N)
μ	dynamic viscosity (kg/ms)
ρ	density (kg/m^3)
ρ_c	density of hard material (kg/m^3)
ρ_s	density of soft material (kg/m^3)
ω	frequency (rad/s)
ω_{gc}	gain crossover frequency (rad/s)
ϕ_m	phase margin ($^\circ$)
ν	velocity matrix on the three axes
$\mathscr{L}\cdot$	Laplace transform
$\mathbb{N}$	set of natural numbers
$\mathbb{R}$	set of real numbers
A	area (m^2)
A_f	frontal area (m^2)
A_P	amplitude of pressure wave (Pa)
${}_aD_t^\alpha$	fractional derivative of order α with lower limit a
${}_aD_t^{-\alpha}$	fractional integration of order α with lower limit a
${}^\alpha I_a^b(\cdot)$	fractional-order operator
$E_{\alpha,\beta}(\cdot)$	Mittag-Leffler function
$E^{(k)}_{1,1+\alpha k}(\cdot)$	k^{th} derivative of Mittag-Leffler function
$c_m^{(\alpha)}$	binomial coefficient

C	linear concentration of diffusion species (mol/m)
C_d	drag coefficient
C_t	thrust coefficient
C_A	hydrodynamic centripetal and Coriolis force (N)
C_{RB}	rigid centripetal and Coriolis force (N)
d	diameter (m)
D	diffusion coefficient in porous media (m^2/s)
D_l	linear damping
D_n	inertia of the rigid body with added mass (matrix representation)
$e(\cdot)$	error signal
E	elastic modulus
$E(s)$	Laplace transform of the error signal
F	shear force (N)
$F(s)$	Laplace transform
h_{act}	elapsed time since the previous event (s)
h_{max}	maximum time between two consecutive events (s)
j	imaginary number, $j^2 = -1$
$J(\cdot)$	cost function
J_1	first degree Bessel function
k_p	proportional gain
k_i	integral gain
k_d	derivative gain
K_C	flow consistency index $(Pa \cdot s^n)$
K	fractional diffusion coefficient (m^2/s^α)
$K(\cdot)$	power-law kernel
l	length (m)
L	memory length (samples)
L_e	electrical inductance (H)
m'	memory term related to initial conditions of fractional order equations
m	mass (kg)
$M(\cdot)$	molar mass (g/mol)
M_A	added mass (kg)
M_P	modulus
M_{RB}	inertia of the rigid body $(kg\ m^2)$
n	index
$p(r, z, t)$	pressure in polar coordinates for radial direction Pa
$\frac{dp}{dz}$	pressure gradient (Pa/m)
r	radial coordinate (m)
r_z	velocity on the Z axis (m/s)
R	radius (m)
R_e	resistance (Ω)
s	complex variable used in Laplace transform
$S(\cdot)$	sensitivity function (dB)
t	time (s)

T	time constant (s)
T_d	derivative time constant (s)
T_f	filter time constant (s)
T_i	integration time constant (s)
T_p	time period (s)
T_s	sampling time (s)
T_K	temperature (K)
$T(\cdot)$	complementary sensitivity function (dB)
$Th(\cdot)$	thrust force (N)
u	flow velocity (m/s)
$u(t)$	control signal at time t
$u(r, z, t)$	velocity in polar coordinates in the radial direction (m/s)
$u_{fd}(k)$	fractional order derivative signal value at sample k
$u_{fi}(k)$	fractional order integral signal value at sample k
$u_{fp}(k)$	fractional order proportional control signal value at sample k
$u_d(k)$	derivative signal value at sample k
$u_i(k)$	integral signal value at sample k
$u_p(k)$	proportional control signal value at sample k
u_x	velocity on the X axis (m/s)
$U(\cdot)$	Laplace transform of the control signal
v	volumetric flow of species diffusion in (m^3/s)
v_y	velocity on the Y axis (m/s)
V	volume (m^3)
V_e	electrical voltage (V)
V_l	flow velocity (m/s)
w	angular velocity (rad/s)
$w(r, z, t)$	velocity in polar coordinates in the axial direction (m/s)
$X_{\dot{u}}$	surge mass coefficient
$X_{\lvert u\rvert u}$	surge drag coefficient
$Y_{sp}(\cdot)$	process setpoint
$Y(\cdot)$	process output
z	discrete-time Laplace operator
Z_f	impedance of the faradaic process (Ω)
Z_w	Warburg impedance (Ω)
$\lvert\cdot\rvert$	magnitude
$\lvert\cdot\rvert_{dB}$	magnitude (dB)
$\angle\cdot$	phase $(^\circ)$

1

Introduction

1.1 Problem Formulation

A particular class of fluids are those governed by nonlinear equations outside the context of Newtonian fluid mechanics theory, which assumes a manifold of (local) linear parameter properties (homogeneity, causality, repeatability, constant variables in time and space, linear dynamics, etc) [1, 2]. Modeling and control of non-Newtonian fluid dynamic environment has quite a plethora of cross-disciplinary applications. Accurate characterization of properties in this type of fluid dynamics has a wide relevance in fields such as:

- prediction of glacier movement (mixture of ice and water - non-Newtonian fluid) [3]
- prediction of blood properties as a result of medication and or arterial disease progress (blood - non-Newtonian fluid) [4]
- evolution and dynamics of ground (muddy) water transportation systems (muddy water - non-Newtonian fluid) [5]

Among vast applications of (model based) control are worth mentioning:

- positioning particles in electro-magnetic actuated fluids such as in liquid steel manufacturing in the continuous casting process [4]
- guiding nano-sensors for detection of structural changes in blood arterial walls [6, 7]
- unmanned underwater vehicles navigation in water and ice mixtures to perform surveys such as mapping the ocean's floor, detecting high levels of pollution, petrol leaks, vessel obstructions or tracking marine currents and fauna migrations [8].

Most properties of non-Newtonian fluids overlap with that of viscoelastic materials, such as polymers, lung tissue, gel-like substances, rubber, etc [9]. Specific properties as memory, creep and shear stress do not follow classical Newton's law of dynamic viscosity and has been manifold proven to be well characterized by combinations of power-law with exponential functions [7, 10]. These are non-rational expressions of combined nonlinear effects in material creep and strain and they represent a generalization from integer order differential equations to fractional order differential equations. Their local solution is the Mittag-Leffler function [11, 12, 13]. Such generalized order equations are mathematical tools emerging from fractional calculus and successfully introduced in engineering, medical, and interdisciplinary application fields [6, 7, 14]. Hitherto, the use of fractional calculus tools for modeling and control of non-Newtonian environments has been very scarce, while majority of theoretical state of art relies on the well known, mature, classical Newtonian approach.

Existing state of the art related to accurate non-Newtonian modeling based on the highly suitable fractional calculus paradigm is scarcely available. In [15] it is proposed a complex model to describe time-dependent flow in non-Newtonian fluids by means of a fractional order differ-integral equation for muddy clay. This is a generalization of classic Newtonian fluid flow theory following the fractionalisation rationale. The idea has been extended in [16] for Maxwell elements in mechanical models of viscoelasticity. Further on, these mechanical models are then the basis for electrical model analogous [17]. The physical basis for this non-uniform velocity gradient can be the non-uniformity of fluid particles (e.g. mixtures of solid and liquid particles), molecular interaction, biological and chemical effects.

Similarly, previous in-house work at UGent-DySC Research Group on generalizing the time constants for accommodating anomalous diffusion in compartmental models for drug concentration gradients in blood and tissue has indicated that each gradient can be expressed in terms of its kernel and integral form of mass transfer [18]. This thesis is a natural continuation on using fractional calculus emerging tools to model physical systems in order to investigate the development of a fractional derivative constitutive equation for the velocity gradient in non-Newtonian fluid.

A manifold of applications in specialized literature deal with design, material properties, manufacturing and functioning of nanorobot objects for motion in non-Newtonian fluids. An exponential success was received in nanomedicine and other application fields [19]. Analysis of existing state of the art provides a set of **theoretical problems** open for being resolved:

- Lack of established know-how on motion of suspended objects in non-Newtonian fluids;
- Lack of know-how on the closed loop control of velocity, position or

other functionality of suspended objects in Non-Newtonian environments;

- Powerful emerging tools from fractional calculus are not yet acknowledged by the community and studies are limited and scarce;
- Optimal natural solutions are replaced by linear approximations of high order and high numerical complexity.

Similarly, a set of **practical problems** are also identified as:

- A general lack of (affordable) lab scale setups mimicking the main properties of non-Newtonian fluids;
- Missing efficient numerical procedures/functions for computer implementation tailored to the industrial/practical use.
- Lack of systematic analysis tools;

Consequently, this dissertation aims at overcoming the limitations encountered in modeling and control of non-Newtonian fluid dynamics, by searching for original solutions to resolve the plethora of applications described herein. This thesis focuses on extending the modeling of non-Newtonian fluid dynamics beyond the state of art, with promising results obtained through the usage of fractional calculus. A context-aware, highly versatile experimental benchmark is designed and built, offering a low-cost, approachable and instructive solution to the problematic of modeling, identification and control of objects in non-Newtonian fluids. The resulting benchmark is used as a tool to enable a systematic analysis of dynamic behaviour of suspended objects in non-Newtonian fluids. It provides a manifold of possibilities associated to validation of the obtained models, development and real-life testing of control strategies related to position, velocity while also embedding functionalities such as non-Newtonian environmental assessment and decision making algorithms. All of these are embedded in a small-scale, highly customizable submersible which is capable of transiting both Newtonian and non-Newtonian environments, offering also experimental environmental data for comparing models and testing robustness of control loops. Furthermore, the thesis also tackles industrial approaches to non-Newtonian fluids related to liquid steel manufacturing and pharmaceutical tablet production using wet/dry granulation. The findings suggest that non-Newtonian fractional order models enable suitable representation of the physical phenomena and suitable control strategies.

1.2 Main Objectives

The research hypothesis is that non-Newtonian fluids require naturally via their specific properties (i.e. viscoelasticity), the use of fractional calculus tools i.e. distributed parameter, fractional order, differential equations which lead to lumped fractional order impedance models. Such generalized order models can better describe experimental data than classical rational transfer function models, while being minimal in the number of parameters, yet allowing a more accurate representation of complex physical phenomena.

The ultimate goal is to fully understand and capture the effects of non-Newtonian fluids on transiting objects, enabling suitable control strategies. In addition, the aim is to overcome current limitations associated to non-Newtonian modeling and control through innovative mathematical formulations in terms of fractional calculus and suitable advanced control strategies.

The main objective of the dissertation unites theoretical contributions in the field of non-Newtonian fluid dynamics, the mathematics branch of fractional calculus with its manifold of applications and control engineering through modelling, identification and control tools.

A set of intermediary subgoals can be enumerated:

1. Develop a fundamental theoretical framework for non-Newtonian fluid environment based on system properties: explore the suitability of fractional calculus and develop an analytical model based on known non-Newtonian fluid dynamics (i.e. Navier-Stokes general equations) and lumped compartmental fractional order impedance models.

2. Design, build and implement an operational benchmark setup for testing non-Newtonian fluid properties and dynamics. The developed setup should be highly versatile and easily built using affordable and on the shelf components in order to enable its translation to academic and research purposes enabling a better understanding of non-Newtonian fluid dynamics.

3. Validate the developed framework through experimental tests using the benchmark and fluids with different properties.

4. Develop a suitable control strategy for position or motion control of a submerged object in non-Newtonian fluids. Test and validate the control strategy on the experimental benchmark.

5. Develop and implement a decision making algorithm for better non-Newtonian environmental assessment with respect to context-awareness. The purpose of this step is to easily implement the

findings of this research to various applications that require non-Newtonian properties monitoring. Provide a scalable solution for various applications related to cyber-physical systems.

Additionally, the project has exploratory objectives related to industrial use cases:

6 In collaboration with ArcelorMittal Gent (AMG), validate the proposed framework on the continuous casting plant through modeling and control of non-Newtonian molten steel flow. The main objective of this step, apart from further validation of the developed framework, is to improve surface defects of steel slabs - economic context.

7 A feasibility study on using impedance spectroscopy sensing to monitor material properties

8 Employ lumped fractional order parametric models for online estimation of material properties. This will enable a self-tuning function for ratio control of material flows in manufacturing processes.

All the previously mentioned goals are realized through original solutions, well beyond the current state of the art. As can be observed, the focus of the objectives have both a theoretical and a practical component. The industrial objectives (no. 6,7,8) earns the thesis a place in the real world, showing that the chosen theme is relevant for the current socio-economic context, providing incentives for further analysis and applications thereof.

1.3 Innovative Results

This project's innovative results with respect to state of art are listed as following:

- A general overview related to fractional calculus, focusing on its suitability to model complex physical phenomena. The relevance of fractional order models in non-Newtonian fluid interactions is explored from time and frequency domain perspectives. In addition, a state of the art focusing on works from the last decade justifies the usage fractional calculus for viscoelastic phenomena. Control strategies of these complex models are also analyzed, emphasizing on the necessity of fractional order controllers for increased performance, robustness and stability.

- An analysis of non-Newtonian fluid flow based on material theory with varying properties, resulting in a generalized fractional order mathematical framework to characterize the time-space variability of fluid flow dynamics properties. The starting point of the conceptual mathematical model consists in Navier-Stokes models, on which Fractional Order Impedance Models (FOIM) are developed to capture and link the model parameter structure to the existence of specific properties in non-Newtonian fluids. An experimental protocol is designed and applied to a series of time independent and time dependent fluid classes. Variations of FOIMs are presented and validated on the dataset. The original contribution of this work is the motivational background information and systematic analysis of the FOIM structure versus the fluid properties. A set of recommendations are given for the future use of FOIMs in capturing material properties.

- Development of FOIMs to capture non-Newtonian material models on different fluids: honey, glucose, shampoo, oils, etc. based on real-life impedance spectroscopy. This is an experimental laboratory validation of the fractional order framework developed for non-Newtonian interactions.

- Design, construction and implementation of a laboratory setup to mimic non-Newtonian fluid flow under pulsatile flow conditions. The rationale is to mimic dynamic flow with non-Newtonian properties and control the velocity of suspended objects. The experimental benchmark is highly versatile, easy to use for both education and research purposes and can be easily built using low-cost, widely available components. It consists of two parts: the circulatory system and a transiting submersible. Non-Newtonian fluid is recirculated through two tubes with different diameters and contraction/expansion possibilities. The robot is submerged in the fluid

and can be used to asses fluid properties (with added sensors) and also to analyze the effect of the non-Newtonion fluid on the position/velocity of the submersible.

- Modeling fluid object interaction based on non-Newtonian FOIMs and experimental data from the benchmark during free and controlled motion of the object. Validation of the obtained models on the experimental platform.

- Development of a fractional order control strategy for the object's position and velocity through the non-Newtonian fluid. Robustness is a key design specification for varying properties of the fluid. Experimental validation of the control strategy for both position and velocity using the laboratory setup. Analysis of the obtained performance for steady state errors, settling time, robustness and stability of the closed loop system.

- Integration of context-awareness paradigms and operation protocols to transform the experimental setup in a highly versatile platform. Implementation and validation of decision making algorithms on the submerged robot for environmental assessment, extending the possible applicability of the platform in a manifold of domains (i.e. surveillance tasks in non-Newtonian fluids such as climate changes in ice/water mixtures, targeted drug delivery with experimental glucose detection, etc.). A novel concept of fractional order event-based control with respect to environmental changes is also developed, tested and validated on the platform.

- Modeling of non-Newtonian fluid flow in the continous casting process at ArcelorMittal Gent, Belgium based on the previously defined FOIM models and experimental plant data. A connection between the applied current to the elctromagnetic stirrer (EMA device) and the molten steel's velocity is realized through fractional calculus. The complex model is validated on multiple datasets to confirm the veracity of the concepts and the obtained model. The obtained model is compared to a previously determined integer order flow model that does not take into account the non-Newtonian nature of liquid steel. Experimental results suggest that fractional calculus is more suitable for the task in favor of integer order models because it better captures the real-life dynamics of the fluid.

- A fractional order control strategy is employed to control the molten steel's velocity inside the mold. The obtained controller is validated through simulations and compared to a previously determined integer order PI controller. It is shown that fractional order control developed for fractional order models that accurately capture material

properties outperforms other approaches, less focused on capturing physical compositions and interactions.

- Use of FOIM models in the pharmaceutical industry in tablet manufacturing. Changes between powder, liquid mixtures, granulation and density exhibit non-Newtonian fluid properties among the production process. FOIM models are employed to encapsulate changes in material properties, further enabling a ratio control strategy to improve the manufacturing process.

1.4 Thesis Outline

The structure of this thesis is organized as follows.

Chapter 2 introduces the state of art on fractional calculus with a focus on modeling and control. General definitions and theoretical aspects are presented from both time and frequency domains. The effects of fractional order integration and differentiation are analyzed, concluding that the increased flexibility provided by any arbitrary order of differ-integral operations is highly suitable to capture complex physical phenomena. Furthermore, fractional order control strategies through the generalization of the widely popular integer order Proportional Integral Derivative (PID) controller are analyzed, showing that this type of advanced control leads to improved closed loop system performance. A recent literature overview focusing on the last decade related to fractional calculus in modeling physical phenomena and controller tuning strategies is also provided in this chapter.

Chapter 3 introduces the reader with the dynamics of non-Newtonian fluid flows together with classifications and examples. Navier-Stokes relations are employed followed by fractional constitutive equations for velocity profiles and flow. Theoretical analysis is performed under assumptions of steady and pulsatile flow conditions, with incompressible properties. The fractional derivative model for velocity and friction drag effect upon a suspended object are determined.

Furthermore, laboratory experiments are performed for different classes of non-Newtonian fluids: pseoduplastic/shear-thinning fluids, visco-plastic fluids, dilatant/shear-thickening fluids. Impedance measurements are performed for varying properties such as glucose, honey, hand soap, shampoo, engine oil and food oils: avocado, corn and olive oils. Fractional Order Impedance Models are identified using various algorithms (Genetic Algorithms, Particle Swarm Optimization and Nonlinear Least Squares Algorithms) to characterize non-Newtonian varying properties.

Chapter 4 presents context-aware control paradigms, to combine benefits of event-based control such as resource optimization and bandwidth allocation with the superior performance of fractional order control. Theoretical and implementation aspects are presented to provide a generalization of event-based control into the fractional calculus field. Different numerical examples validate the proposed methodology, providing a useful tool, especially for industrial applications where the event-based control is most needed. This strategy will be used further for energy efficient, and context aware implementations related to non-Newtonian fluids.

Chapter 5 studies the effects of varying properties in non-Newtonian fluids from an experimental approach. Impedance spectroscopy is used in a laboratory setup able to experiment on the properties of various non-Newtonian fluids: glucose, honey, hand soap, shampoo, av-

ocado/corn/olive oils, soft/standard detergents. A fractional order impedance model is proposed to capture fluid mechanical properties which is further validated on the experimentally acquired data.

Chapter 6 focuses on objects submerged in non-Newtonian fluids. An experimental benchmark is designed and built to demonstrate non-Newtonian fluid flow. A transiting submersible is considered the submerged object. The chapter focuses on modeling the motion dynamics of the submersible. The mathematical model is developed starting from already known Newtonian interactions between the submersible and the fluid. The obtained model is therefore altered through optimization techniques to describe non-Newtonian interactions on the motion of the vehicle by using real-life data regarding non-Newtonian influences on submerged thrusting. For the obtained non-Newtonian fractional order process model, a fractional order control approach is employed to sway the submerged object's position inside the viscoelastic environment. The presented modeling and control methodologies are solidified by real-life experimental data used to validate the veracity of the presented concepts. The robustness of the control strategy is experimentally validated on both Newtonian and non-Newtonian environments.

Context awareness paradigms are encapsulated in this chapter through autonomous decisions performed by the submersible. An event-based control law is implemented to offer various advantages such as energy efficiency, while environmental measurements trigger the robot to perform context-relevant decisions. The platform provides high versatility and the results presented throughout the study can be adapted to a manifold of multidisciplinary fields.

Chapter 7 gives a concrete real-life applicability of the developments of this dissertation through a case study performed at ArcellorMital Gent (AMGent), Belgium, the second largest company in the world for steelmaking. Rheology studies performed on flow behavior and viscosity analysis proves that liquid steel exhibits shear thinning and time independent, non-thixotropic flow for all shear rate regimes. Hence, molten steel is a non-Newtonian fluid. The first part of the chapter presents the continuous caster at AMGent and justifies the need of accurate modeling and control of the molten steel's dynamics through product defects. The flow of liquid steel in the mould of the continuous caster is modeled using real-life plant data. The obtained fractional order models are successfully validated on different datasets and compared to existing integer order models. The developed fractional order model also takes into account non-Newtonian characteristics of the steel, whereas the integer order model does not consider the fluid type when modeling the flow. The chapter proves that taking into account fluid properties leads to a more accurate model which further enables proper fractional order control strategies. A fractional order PI controller is tuned to control the velocity of the steel in the continuous caster which is validated on the fractional order model. Re-

alistic process disturbance and operating conditions are considered when performing the validation and assessment of the results. The chapter is concluded with an event-based control strategy that uses process intrinsic events to further reduce product faults.

Chapter 8 follows the paradigm shift in the pharmaceutical industry from batch to continuous production in tablet manufacturing. Some of the sub-processes involved in tablet manufacturing perform changes in powder and liquid mixtures, granulation, density, therefore changing flow conditions of the raw material, exhibiting non-Newtonian traits along the production process. Using impedance spectroscopy (as in the case study from Chapter 5) in a continuous sensing and monitoring context, it is possible to perform online identification of generalized (fractional) order parametric models where the coefficients are correlated to changes in material properties. The model parameters are then part of a self-tuning control gain used in ratio control as part of the local process control loop. The solution proposed here is easy to implement and poses a significant added value to the current state of art in pharmaceutical manufacturing technologies.

Finally, *Chapter 9* concludes the dissertation with general findings and proposes some future research directions.

1.5 Publication Output from Research Performed in Relation to this Manuscript

Journal articles

A1

- **I. Birs**, C. Muresan, D. Copot, C. Ionescu. "Model Identification and Control of Electromagnetic Actuation in Continuous Casting Process with Improved Quality", in *Journal of Automatica Sinica* - **accepted**

- M. Ghita, **I. Birs**, D. Copot, I. Nascu, C. Ionescu. "Impedance Spectroscopy Sensing Material Properties for Self-Tuning Ratio Control in Pharmaceutical Industry", in *Applied Sciences*, vol. 12, no. 1, pp. 509, DOI: 10.3390/app12010509, 2022.

- **I. Birs**, C. Muresan, O. Prodan, S. Folea, C. Ionescu. "An Experimental Approach towards Motion Modeling and Control of a Vehicle Transiting a Non-Newtonian Environment," in *Fractal and Fractional*, vol. 5, no. 3, pp. 104, DOI: 10.3390/fractalfract5030104, 2021.

- C. I. Muresan, **I. Birs**, E. H. Dulf, D. Copot and L. Miclea. "A review of recent advances in fractional-order sensing and filtering techniques", in *Sensors*, vol. 21, no. 17, 2021.
- **I. Birs**, I. Nascu, C. Ionescu, C. Muresan. "Event-based fractional order PID control", in *Journal of Advanced Research*, vol. 25, pp.191-203, DOI: 10.1016/j.jare.2020.06.024, 2020.
- C. Ionescu, **I. Birs**, D. Copot, C. Muresan, R. Caponetto. "Mathematical modelling with experimental validation of viscoelastic properties in non-Newtonian fluids", in *Philosophical Transactions of The Royals Society A*, pp. 20190284, doi:10.1098/rsta.2019.0284, 2020.
- **I. Birs**, S. Folea, O. Prodan, E. Dulf, C. Muresan. "An experimental tuning approach of fractional order controllers in the frequency domain", in *Applied Sciences*, vol. 10, no. 9, pp. 2379 , 2020.
- R. Cajo, M. Ghita, D. Copot, **I. Birs**, C. Muresan, C. Ionescu. "Context Aware Control Systems: An Engineering Applications Perspective," in *IEEE Access*, vol. 8, pp. 215550-215569, 2020.
- **I.Birs**, D. Copot, C. Muresan, I. Nascu, C. Ionescu. "Identification For Control Of Suspended Objects In Non-Newtonian Fluids", in *Fractional Calculus and Applied Analysis*, vol. 22, no.5, pp. 1378-1394 , DOI: 10.1515/fca-2019-0072, 2019.
- C. Muresan, **I. Birs**, C. Ionescu, R. De Keyser. "Tuning of fractional order proportional integral/proportional derivative controllers based on existence conditions", in *Proceedings of the Institution of Mechanical Engineers, Part I: Journal of Systems and Control Engineering*, vol. 223, no. 4, pp. 384-391, 2019.
- C. Muresan, **I. Birs**, S. Folea, C. Ionescu. "Fractional order based velocity control system for a nanorobot in non- Newtonian fluids", in *Bulletin Of The Polish Academy Of Sciences- Technical Sciences*, vol. 66, no. 6, pp. 991-997, DOI: 10.24425/bpas.2018.125946, 2018.

Book Chapters

B2

- **I. Birs**, C. Muresan. "A non-Newtonian impedance measurement experimental framework: modeling and control inside blood-like environments - fractional-order modeling and control of a targeted drug delivery prototype with impedance measurement capabilities," in *Automated drug delivery in anesthesia*, D. Copot, Ed. Academic Press, pp. 51-90, 2020.

Conference papers

P1

- **I. Birs**, C. Ionescu, I. Nascu, C. Muresan, "A comparison between FOIMC and FOPI controllers for a submerged robot", in *2021 25th IEEE International Conference on System Theory, Control and Computing (ICSTCC)*, Iasi, Romania, pp. 166-171, 2021.

- **I. Birs**, C. Muresan, and C. Ionescu, "An event based implementation of a fractional order controller on a non-Newtonian transiting robot," in *2020 European Control Conference (ECC 2020)*, St. Petersburg, Russia, pp. 1436-1441, 2020.

- **I. Birs**, C. Muresan, I. Nascu, and C. Ionescu, "An energy-efficient context aware solution for environmental assessment," in *IFAC PAPERSONLINE*, Beijing, China, vol. 53, no. 5, pp. 756-761, 2020.

- **I. Birs**, M. Ghita, M. Ghita, D. Copot, C. Muresan, and C. Ionescu, "An interdisciplinary, low-cost methodological framework for analysing dynamical material properties for control-related applications," in *IFAC PAPERSONLINE*, Philadelphia, USA, vol. 52, no. 9, pp. 159-164, 2019. - **2^{nd} place, Young Author Award**.

- **I. Birs**, D. Copot, M. Ghita, C. Muresan, and C. Ionescu, "Fractional-order modeling of impedance measurements in a blood-resembling experimental setup," in *2019 IEEE International Conference on Systems, Man and Cybernetics (SMC)*, Bari, ITALY, pp. 898-903, 2019.

- **I. Birs**, D. Copot, C. Pilato, M. Ghita, R. Caponetto, C. Muresan, C. Ionescu, "Experiment design and estimation methodology of varying properties for non-Newtonian fluids," in *2019 IEEE International Conference on Systems, Man and Cybernetics (SMC)*, Bari, Italy, pp. 324-329, 2019.

- **I. Birs**, D. Copot, C. Muresan, R. De Keyser, and C.Ionescu, "Robust fractional order PI control for cardiac output stabilisation," in *IFAC PAPERSONLINE*, Florianopolis, Brazil, vol. 52, no. 1, pp. 994-999, 2019.

- M. Ghita, J. Juchem, **I. Birs**, R. Cajo, D. Copot, C. Ionescu. "Electrical circuits to mimic respiratory diseases: an interdisciplinary bachelor project", in *2019 IEEE 7th International Conference on Control, Mechatronics and Automation (ICCMA 2019)*, Delft, Netherlands, pp. 483-487, 2019.

- **I. Birs**, C. Muresan, S. Folea, O. Prodan, and C. Ionescu, "Fractional order modeling and control of a carrier prototype for targeted drug delivery," in ICCBB 2018: Procedings of the 2018 2nd International Conference on Computational Biology and Bioinformatics, Bari, Italy, pp. 1-5, 2018.

Papers using concepts from this thesis, but not directly related to the scope

- C. Muresan, **I. Birs**, R. De Keyser. "An Alternative Design Approach for Fractional Order Internal Model Controllers for Time Delay Systems", in *Journal of Advanced Research*, vol. 31, pp. 177-189, DOI: 10.1016/j.jare.2021.01.004, 2021.

- **I. Birs**, E. Dulf, I. Nascu, C. Muresan. "Comparison of various fractional order controllers on a poorly damped system", in *Perspectives in Dynamical Systems III: Control and Stability*, Springer Proceedings in Mathematics & Statistics, Springer, 2021.

- **I. Birs**, C Muresan, M Ghita, M Ghita, D Copot, M. Neckebroek, C. Ionescu, "Development and validation of preliminary fractional order impedance models for experimental pain assessment", in *2021 International Conference on Electrical, Computer, Communications and Mechatronics Engineering (ICECCME)*, Mauritius, pp. 1-6, 2021.

- **I. Birs**, C. Muresan, I. Nascu, R. De Keyser, "Experimental comparison between discrete time and event-based PID controllers on a nonlinear process", in *2021 International Conference on Electrical, Computer, Communications and Mechatronics Engineering (ICECCME)*, Mauritius, pp. 1-6, 2021.

- C. Muresan, **I. Birs**, E.H. Dulf. "Event- Based Implementation of Fractional Order IMC Controllers for Simple FOPDT Processes", in *Mathematics*, vol. 8, no. 8, pp. 1378, DOI: 10.3390/math8081378, 2020.

- **I. Birs**, C. Muresan, I. Nascu, C. Ionescu. "A Survey of Recent Advances in Fractional Order Control for Time Delay Systems", in *IEEE Access*, vol. 7, no. 1, pp. 30951-30965, DOI: 10.1109/ACCESS.2019.2902567, 2019.

- E. Hegedus, **I. Birs** and C. Muresan, "Fractional order control of the combined anaesthesia-hemodynamic system: a preliminary study," in *IFAC PAPERSONLINE*, Ghent, Belgium, vol. 54, no. 15, pp. 19-24, 2021.

- D. Copot, C. Muresan, **I. Birs**, L. Kovacs, "Robust Hemodynamic Control Under General Anesthesia Conditions", in *IFAC-PapersOnLine*, vol. 53, no. 2, pp. 16179-16184, 2020.

2

Fractional Calculus Concepts

2.1 Introduction

This chapter lays down some of the basic notions from fractional calculus which are necessary for the reader to understand the background for the solutions proposed in this thesis. The notions introduced are limited to those concepts and definitions further employed in the remainder of the book.

The differential operators $\frac{d}{dx}$, $\frac{d^2}{dx^2}$, etc. are widely studied and used as classical tools. While being commonly used by many, some few wonder whether the order of the differentiator must always be an integer number. The first person to raise questions regarding the integer order of the differentiator was Leibniz in a letter to L'Hopital written in 1695. The response of L'Hopital was that non-integer order differentiators "will lead to a paradox, from which one day, useful consequences will be drawn". 320 years later, the question raised by Leibniz received its answer through fractional calculus, a generalization of ordinary differentiation and integration to non-integer order [20].

The accurate term for "fractional order" is actually "non–integer order" since the order of the differentiation can also be irrational, but all the specialized literature refers to the concept as "fractional". There is still an open battlefield when it comes to terminology, as the concept is fairly a new comer in the engineering field.

Among the years, many well-known scientists contributed to the mathematical development of non-integer order differentiation: Euler and Lagrange (theoretical contributions in the 18^{th} century); Riemann, Liouville and Holmgren (systematic studies at the beginning of the 19^{th} century), Liouville (function expansion in series of exponentials and definition of n order derivative by operating term-by-term); Riemann (definite integral

applicable to power series with non-integer exponents); Grünwald and Krug (unified the results of Liouville and Riemann); Abel (first application of fractional calculus, 1823); Heaviside (symbolic methods for solving linear differential equations of constant coefficients); Weil and Hardy (differ-integral operator properties); Riesz (multivariable functions), etc. A comprehensive description of all these definitions can be found in the textbook [21].

In the last decades, the number of applications for fractional order calculus has grown exponentially, mainly in the fields of control engineering, signal processing and system theory. The main advances were made by: Bode (Bode's ideal loop transfer function); Manabe (frequency and transient response of the non–integer integral and its application in control), Oustaloup (demonstrated the superiority of CRONE – Commande Robuste d'Ordre Non Entier) and Podlubny (the $\mathrm{PI}^{\lambda}\mathrm{D}^{\mu}$ controller) [20].

The number of applications with solutions based on fractional calculus tools has seen a rapid growth over the last decade, thanks also to increasing number of specialised scientific events. Fractional calculus can be easily defined as a generalization of classical integer-order calculus with the particular feature that the order of the differ–integral operator is fractional. Its versatility in modeling and control theory has received a lot of attention recently, although it is still a concept insufficiently understood. This limits the wide acceptance of fractional calculus in industrial use, especially for PID control applications, despite its close relation to commonly used PID-type of control. Fractional calculus has been regarded as a much better way to cover the dynamics of certain type of phenomena, such as anomalous diffusions [22], viscoelasticity [7], epidemic spreading [23], etc. At the same time, fractional calculus tools used to design and tune parameters in various types of controllers has indicated a large versatility and performance robustness [24,25]. For an overview, some recent review papers on the use of fractional calculus in control engineering are [23,26,27,28].

2.2 Mathematical Background

The fractional operator is denoted by ${}_aD_t^{\alpha}f(t)$, with $t, a \in \mathbb{R}$, where $(t > a)$ are the upper and lower limits of the *differintegral*, representing a generalization of integral and derivative operations to any arbitrary order, $\alpha \in \mathbb{R}$.

The most widely used definitions of ${}_aD_t^{\alpha}f(t)$ have been introduced by Riemann–Liouville (RL), Grünwald–Letnikov (GL) and Caputo (C) [29].

Fractional-order control strategies are mainly developed based on the Riemann–Liouville definition given as

$$ {}_a^{RL}D_t^{\alpha}f(t) = \frac{1}{\Gamma(m'-\alpha)}\frac{d^{m'}}{dt^{m'}}\int_a^t \frac{f(\tau)}{(t-\tau)^{\alpha-m'+1}}d\tau, \tag{2.1} $$

where $m' - 1 \leq \alpha < m'$, with m' being the smallest integer greater than α and $\Gamma(m' - \alpha)$ is the Euler gamma function [30]. The upper and lower bounds, t and a, need to be established in the case of the RL definition.

Another popular representation of the fractional differ-integral operation is the Caputo fractional derivative, introduced in 1967 by Michele Caputo [31]. The advantage of this definition is that the fractional-order initial conditions do not have to be defined as in the RL case. Discussions on the issue of initial conditions are ongoing in the applied mathematics and physics community, but are out of the scope of this work.

$$ {}_a^C D_t^\alpha f(t) = \frac{1}{\Gamma(m' - \alpha)} \int_a^t \frac{f^{(m')}(\tau)}{(t - \tau)^{\alpha - m' + 1}} d\tau, \tag{2.2} $$

with $m' - 1 < \alpha < m'$ and $\alpha > 0$.

Grünwald-Letnikov (GL) defines ${}_a D_t^\alpha f(t)$ as:

$$ {}_a^{GL} D_t^\alpha f(t) = \lim_{h \to 0^+} h^{-\alpha} \sum_{m'=0}^{\left[\frac{t-a}{h}\right]} (-1)^{m'} \binom{\alpha}{m'} f(t - m'h), \tag{2.3} $$

where $\alpha \in \mathbb{R}$ and $\alpha > 0$.

A numeric approximation of the GL definition from Equation (2.3) has been proposed by [32] as:

$$ \begin{aligned} {}_a^{GL} D_t^\alpha f(t) &\approx T_s^{-\alpha} \sum_{m'=0}^{M(t)} (-1)^{m'} \binom{\alpha}{m'} f(t - m'T_s) \\ &\approx T_s^{-\alpha} \sum_{m'=0}^{M(t)} c_{m'}^{(\alpha)} \binom{\alpha}{m'} f(t - m'T_s), \end{aligned} \tag{2.4} $$

where T_s denotes the sampling time and L is a memory length chosen to satisfy:

$$ \begin{aligned} L &\geq \frac{1}{\delta_0^2 \Gamma(\alpha)} \\ \delta_0 &= \frac{|{}_a^{GL} D_t^\alpha f(t) - {}_{t-L}^{GL} D_t^\alpha f(t)|}{P} \\ P &= \max_{[0,\infty]} |f(t)| \end{aligned} . \tag{2.5} $$

$M(t)$ is the minimum between t/h and L/h, while $c_{m'}^{(\alpha)}$ are binomial coefficients defined as:

$$ c_{m'}^{(\alpha)} = \left(1 - \frac{1 + \alpha}{m'}\right) c_{m'-1}^{(\alpha)} \tag{2.6} $$

with $c_0^{(\alpha)} = 1$.

Another important piece in fractional calculus theory is the Mittag-Leffler (ML) function

$$E_\alpha(t) = \sum_{m'=0}^{\infty} \frac{t^{m'}}{\Gamma(\alpha m' + 1)} \tag{2.7}$$

that connects the pure exponential and power-law behavior, characterizing both integer and fractional-order phenomena [33], resulting in:

$$\mathscr{L}\{E_\alpha(\pm a t^\alpha)\} = \frac{s^{\alpha-1}}{s^\alpha \mp a}. \tag{2.8}$$

A major advantage associated with the RL definition is that $f(t)$ does not have to be continuous at the origin, nor differentiable. Another advantage of RL is that there is no singularity at the origin for all functions, such as ML. Modeling physical phenomena with the RL definition is a tedious process since the RL derivative of a constant is different than zero. Furthermore, a constant $f(t)$ at the origin leads to a singularity in its fractional derivative, reducing its field of applications [34].

The main advantage brought by the Caputo derivative is that it allows the specification of initial and boundary conditions in a traditional manner and the derivative of a constant is also zero. This is the reason why Caputo is considered the most appropriate definition for modeling real-world problems [35]. However, the Caputo derivative requires the computation of the derivative of $f(t)$ to compute its fractional-order derivative. There is also the limitation that Caputo defines the differ-integral only for differentiable functions, and arguably, functions that do not have a first-order derivative could have fractional derivatives of all orders [36].

2.3 Suitability for Modeling Complex Phenomena

Several definitions of the fractional operator have been proposed, as seen in the previous subsection. All of them generalize the standard differential–integral operator in two main groups: (a) they become the standard differential–integral operator of any order when n is an integer; (b) the Laplace transform of the operator D_t^α is s^α (provided zero initial conditions), and hence the frequency characteristic of this operator is $(j\omega)^\alpha$. The latter proves the versatility of the fractional operator in the frequency domain.

A fundamental D_t^α operator, a generalization of integral and differential operators (*differ-integration* operator), is introduced as follows:

$$D_t^\alpha = \left\{ \begin{array}{cc} \frac{d^\alpha}{dt^\alpha}, & \alpha > 0 \\ 1, & \alpha = 0 \\ \int_0^t (d\tau)^\alpha, & \alpha < 0 \end{array} \right\}, \tag{2.9}$$

where α is the fractional order and $d\tau$ is the derivative function. Since the entire work will focus on the frequency-domain approach for fractional order derivatives and integrals, we shall not introduce the complex mathematics for time domain analysis. Instead, focus will be given to Laplace and Fourier domains. The Laplace transform for integral and derivative order α are, respectively:

$$\mathscr{L}\left\{D_t^{-\alpha} f(t)\right\} = s^{-\alpha} F(s), \tag{2.10}$$

$$\mathscr{L}\left\{D_t^{\alpha} f(t)\right\} = s^{\alpha} F(s), \tag{2.11}$$

where $F(s) = L\{f(t)\}$ and s is the Laplace complex variable. The Fourier transform can be obtained by replacing s by $j\omega$ in the Laplace transform and the equivalent frequency-domain expressions are:

$$\frac{1}{(j\omega)^{\alpha}} = \frac{1}{\omega^{\alpha}} \left(\cos\frac{\pi}{2} + j\sin\frac{\pi}{2}\right)^{-\alpha} = \frac{1}{\omega^{\alpha}} \left(\cos\frac{\alpha\pi}{2} - j\sin\frac{\alpha\pi}{2}\right). \tag{2.12}$$

$$(j\omega)^{\alpha} = \omega^{\alpha} \left(\cos\frac{\pi}{2} + j\sin\frac{\pi}{2}\right)^{\alpha} = \omega^{\alpha} \left(\cos\frac{\alpha\pi}{2} + j\sin\frac{\alpha\pi}{2}\right) \tag{2.13}$$

From the frequency domain perspective, the magnitude of the fractional order operator $(j\omega)^{\alpha}$ is:

$$|s^{\alpha}|_{dB} = 20\log_{10}\omega^{\alpha}, \tag{2.14}$$

while the phase is given by:

$$\angle s^{\alpha} = \operatorname{atan}\frac{\sin\frac{\alpha\pi}{2}}{\cos\frac{\alpha\pi}{2}} = \frac{\alpha\pi}{2}. \tag{2.15}$$

Drawing the magnitude in the Bode diagram gives a straight line for the plot of s^{α} with a fixed slope of $20\alpha dB/dec$, whereas the phase plot depicts a constant phase value for the entire frequency range $\omega \in (0, \infty)$. The slope variation as well as the fixed phase values are shown in Fig. 2.1 for any $\alpha \in (0, 2]$. Note that for the integer order differentiation corresponding to $\alpha = 1$ and $\alpha = 2$ the slope is $20dB/dec$ and $40dB/dec$, respectively. For the same values of α, the phase is a constant value equal to 90° and 180°, respectively.

Another fractional order transfer function relevant for the present study is:

$$G_1(s) = \frac{k}{Ts^{\beta} + 1}, \tag{2.16}$$

where $k \in \mathbb{R}$ is the gain and $T > 0$ is the time constant. The fractional order is again denoted by $\beta \in (0, 2]$. Fig. 2.2 shows the response of $G_1(s)$ for $k = 1$, $T = 1$ and different values of β.

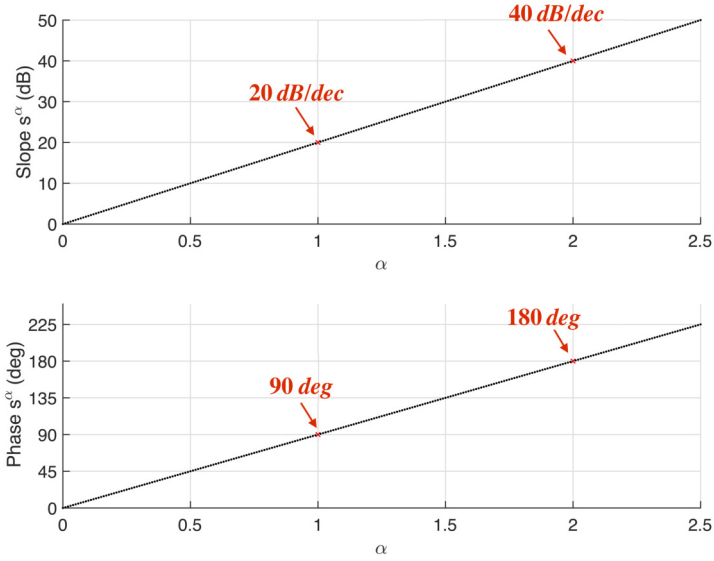

Figure 2.1: Correlation between the slope of the magnitude plot and phase of s^α for different values of α in s^α

The piecewise linear asymptotic approximation of the magnitude Bode diagram for the transfer function from (2.16) is given by [37] as:

$$|G_1(s)|_{dB} = \begin{cases} 20\log_{10}|k|, \omega < \left(\frac{1}{T}\right)^{1/\beta} \\ 20\log_{10}|k| - 20\beta\log_{10}\omega, \omega \geq \left(\frac{1}{T}\right)^{1/\beta} \end{cases}. \tag{2.17}$$

From (2.17), it can be observed that the slope of the asymptotic magnitude plot of (2.16) is $0dB/dec$ for low frequencies and $-20\beta dB/dec$ for high frequencies. Hence, the magnitude slope variation shown in Fig. 2.1 is also valid for $G_1(s)$ at high frequencies.

The phase of the frequency response of (2.16) is given by

$$\angle G_1(s) = -\arctan\frac{T\omega^\beta \sin\left(\frac{\beta\pi}{2}\right)}{T\omega^\beta \cos\left(\frac{\beta\pi}{2}\right) + 1}. \tag{2.18}$$

The phase representation is an arctangent having the value 0 at low frequencies and converging to $\frac{-\beta\pi}{2}$ for high frequencies.

Another important aspect in the graphical representation of the frequency response of $G_1(s)$ is the corner frequency. In a piecewise linear asymptotic representation of the magnitude response, the corner frequency is considered the point where the slope changes. In the phase

representation, it is considered that this is the frequency at which the arctangent's inflection point is present. For an integer order transfer function of (2.16), $\beta = 1$, the corner frequency is approximated to $\omega_c = \frac{1}{T}$. Fig. 2.3 shows the approximated corner frequencies of $G_1(s)$, for $k = 1$, $T \in (0, 1]$ and different fractional orders β.

Another example to be considered is based on the classical second order transfer function, whose denominator orders are scaled by a non-rational factor denoted by α

$$G_2(s) = \frac{1}{s^{2\alpha} + s^{\alpha} + 1}. \tag{2.19}$$

The response of (2.19) at a unit step signal is simulated in Fig. 2.4 for $\alpha \in [0.25, 0.5, 0.75, 1, 1.25]$. It can be observed that the overshoot increases with the value of α. However, for small values of $\alpha \in [0\ 1]$ the settling time decreases if α increases. The Bode diagrams for the same fractional scaling factors are shown in Fig. 2.5. It can be observed that the magnitude peak is more prominent and the magnitude slope at high frequencies increases with greater values of α. From the phase plot, one can see the high frequency asymptote also increasing with α.

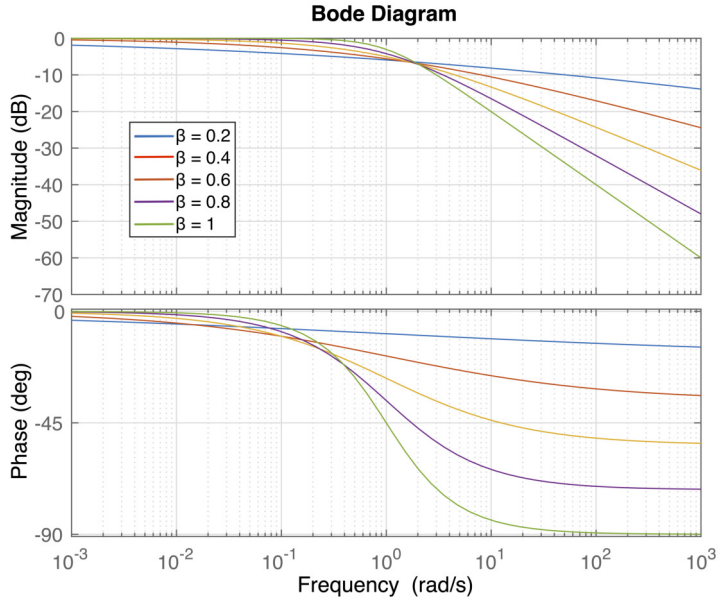

Figure 2.2: Bode diagram of $G_1(s)$ from (2.16) for $k = 1$, $T = 1$ and different values of β

It has been proven that integer order calculus cannot accurately describe complex diffusion processes due to the limitations brought by the constant order, while a generalized order of differentiation is a natural solution to determine diffusion patterns [38, 39].

Fractional order models are extensively used to incorporate physical properties that overlap the ability of accurate physical representation of the surrounding world using classical, integer-order, differentiation [40]. The viscoelastic nature of non-Newtonian fluids makes fractional calculus the ideal candidate to accurately represent the real life dynamics of such an environment [41]. Specific properties of non-Newtonian fluids such as memory properties and nonlinear dynamic viscosity make fractional differentiation a powerful tool to model non-Newtonian dynamics [42]. Some approaches use power-law and exponential functions [43]. Other interpretations are based on Mitag-Leffler functions [10, 11, 12]. The well known Hagen-Poseuille equation in the field of fluid dynamics is generalized using fractional order differentiation in [44] for accurate modeling of viscoelastic flow. Navier-Stokes models are also employed by [45] to capture specific non-Newtonian context properties.

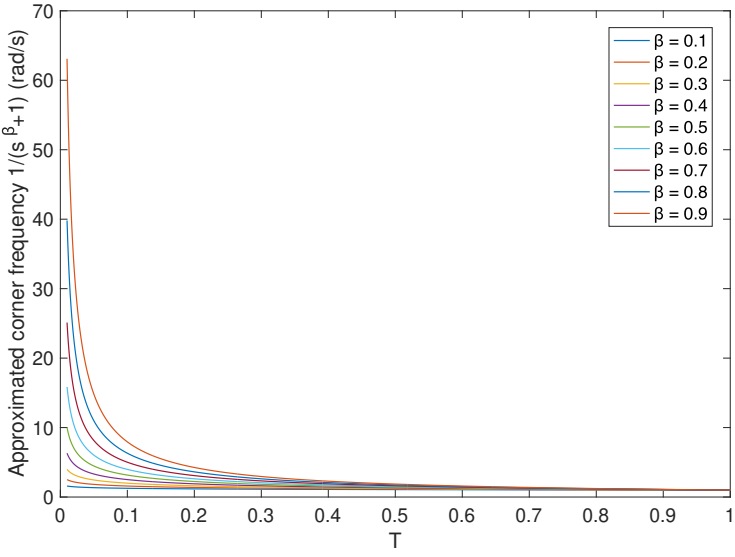

Figure 2.3: Approximated corner frequency of $G_1(s)$ from equation (2.16) for $k = 1$ and different values of β

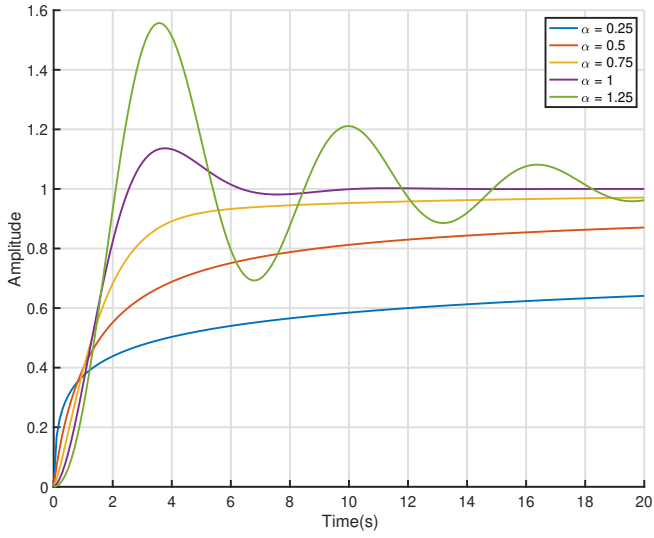

Figure 2.4: Step response of $G_2(s)$ from (2.19) for different values of α

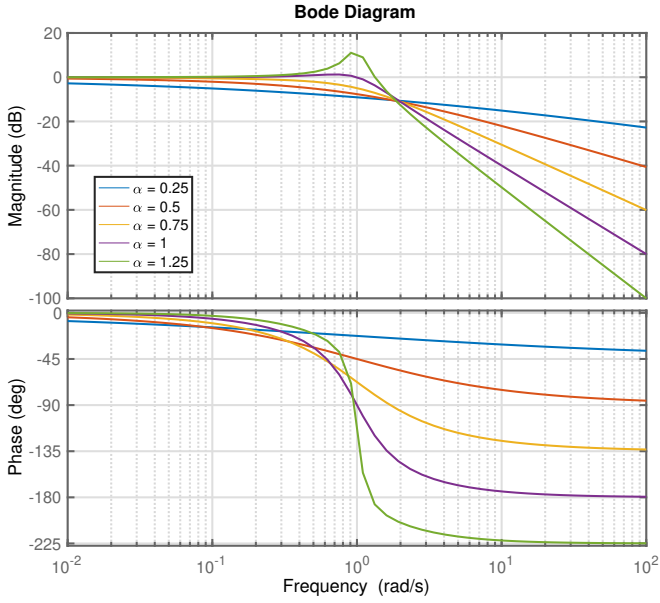

Figure 2.5: Bode diagram of $G_2(s)$ from (2.19) for different values of α

2.4 Fractional Order PID Control

The connotations of equations (2.9) in control engineering consists in extending the integer order PID (Proportional-Integral-Derivative) controller to its fractional order generalization. The classical textbook PID transfer function is

$$C_{PID}(s) = k_p \left(1 + \frac{1}{T_i s} + T_d s\right), \tag{2.20}$$

where k_p is the proportional gain, T_i is the integral time and T_d stands for the derivative time. The transfer function of the fractional order PID controller (FOPID) is given by

$$C_{FOPID}(s) = k_p \left(1 + \frac{k_i}{s^\lambda} + k_d s^\mu\right), \tag{2.21}$$

where k_p is, again, the proportional gain, k_i and k_d are integral and derivative gains, respectively. λ is the fractional order of integration and μ the fractional order of differentiation. For particular cases of $\lambda = 1$ and $\mu = 1$, the controller (2.21) is equivalent to the classical textbook definition (2.20).

In order to define and exemplify fractional order controller we shall use Fig. 2.6 which shows a classical negative feedback control loop. $R(s)$ is the input signal, while $Y(s)$ is the output. The process to be controlled is shown as $G(s)$. The considered controller is a fractional order Ks^μ, which encapsulates both integral and derivative actions, depending on μ. For $\mu = 0$, the controller is proportional. If $\mu = -1$, the action is a pure integral, while $\mu = 1$ gives a classical derivative effect. Fractional calculus appears for cases when μ is generalized to any arbitrary order, usually $\mu \in [-2, 2]$ for the controller to have physical relevance, as shown by [46]. For negative values the controller is a fractional order PI (FOPI), while for positive values of μ, the controller is a fractional order PD (FOPD).

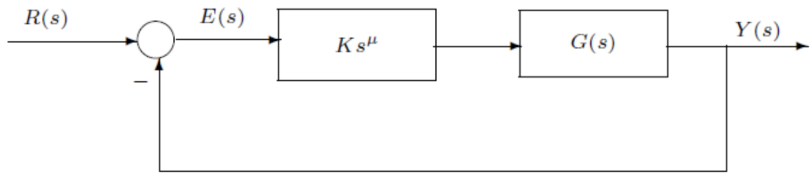

Figure 2.6: Closed loop negative feedback system with fractional order control actions

In order to illustrate the fractional order integral control effects, the

error signal is analyzed:

$$e(t) = \sum_{k=0}^{N} (-1)^k u_0(t - kT_p), \quad k = 0, 1, 2, ... \tag{2.22}$$

where $u_0(t)$ is the unit step signal. The Laplace transform of the error signal results as:

$$E(s) = \sum_{k=0}^{N} (-1)^k \frac{e^{-kT_p s}}{s}. \tag{2.23}$$

The control signal is denoted as:

$$u(t) = \mathscr{L}^{-1} U(s) = \mathscr{L}^{-1} \left\{ K \sum_{k=0}^{N} (-1)^k \frac{e^{-kT_p s}}{s} \right\}, \tag{2.24}$$

resulting in

$$u(t) = K \sum_{k=0}^{N} \frac{(-1)^k}{\Gamma(1-\mu)} (t - kT_p)^{-\mu} u_0(t - kT_p). \tag{2.25}$$

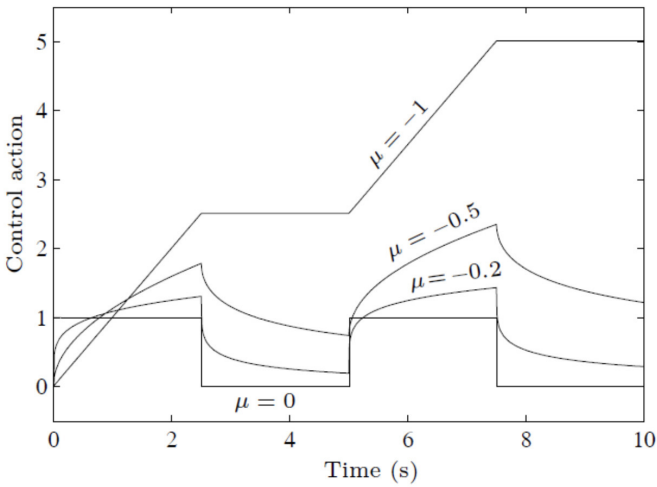

Figure 2.7: Fractional order integral action [20]

Fig. 2.7 depicts the control signal $u(t)$ for varying $\mu = 0, -0.2, -0.5, 1$, $T = 30$ and $N = 4$. As observed in the plot, the error signal varies between proportional actions (for $\mu = 0$ - rectangular signal) and a pure integrative effect ($\mu = -1$ - straight line). For intermediary values of μ, the control signal increases for a constant error, resulting a null steady

state error. Furthermore, the control value decreases when the error is 0, showing increased stability.

The frequency domain magnitude equation is:

$$20\log_{10}|s^{\mu}G(s)|_{s=j\omega} = 20\log_{10}|G(j\omega)| + 20\mu\log_{10}\omega, \tag{2.26}$$

whereas the phase is given as:

$$\angle s^{\mu}G(s)|_{s=j\omega} = \angle G(s) + \mu\frac{\pi}{2}. \tag{2.27}$$

For $\mu \in [0,1]$, the magnitude plot has a variable slope between 0 and -20 dB/dec, whereas the phase is a constant value between $0°$ and $-90°$. The slope values are a mirror image of Fig. 2.1 from Subsection 2.3, with respect to the ω axis.

Differentiating the error signal leads to an increased system stability, but amplifies high frequency noise. Performance improvements related to settling time and overshoot can be observed in the transient regime. In the complex plane, a derivative control action adds a zero at the origin, moving the root locus toward the left half plane. In the frequency domain, an integer order differentiator adds a constant phase at $90°$ and a magnitude plot with fixed slope of $+20$ dB/dec.

In order to illustrate the fractional order derivative effect, let us consider a trapezoidal error signal:

$$e(t) = tu_0(t) - t(t-T_p)u_0(t-T_p) - t(t-2T_p)u_0(t-2T_p) + t(t-3T_p)u_0(t-3T_p). \tag{2.28}$$

The Laplace transform of (2.28) is:

$$E(s) = \frac{1}{s^2} - \frac{e^{-T_p s}}{s^2} - \frac{e^{-2T_p s}}{s^2} + \frac{e^{-3T_p s}}{s^2}, \tag{2.29}$$

resulting in the time domain control signal $u(t)$ as:

$$\begin{aligned} u(t) &= \mathscr{L}^{-1}\left\{K\left(\frac{1}{s^2} - \frac{e^{-T_p s}}{s^2} - \frac{e^{-2T_p s}}{s^2} + \frac{e^{-3T_p s}}{s^2}\right)\right\} \\ &= \frac{K}{\Gamma(2-\mu)}[t^{1-\mu}u_0(t) - (t-T_p)^{1-\mu}u_0(t-T_p) \\ &\quad - (t-2T_p)^{1-\mu}u_0(t-2T_p) + (t-T_p)^{1-\mu}u_0(t-3T_p)]. \end{aligned} \tag{2.30}$$

The magnitude and phase equations are similar with the fractional order integral action from equations (2.26) and (2.27). The derivative action influence on the Bode plot has been already plotted in Fig. 2.1 from subsection 2.3.

Additionally, Bode plots of fractional order PID controllers with different orders of differ-integration are compared to the frequency response

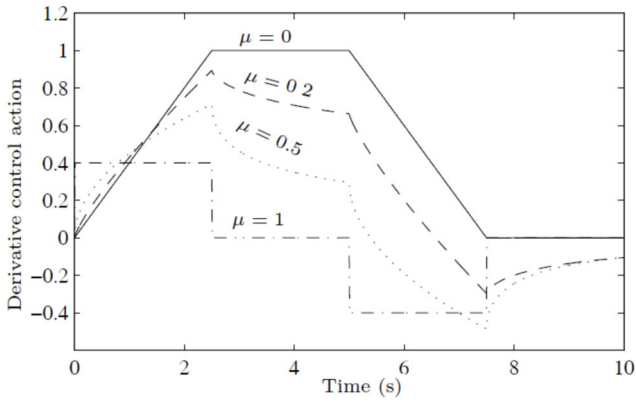

Figure 2.8: Fractional order derivative action [20]

of the classical PID controller in Fig. 2.9. Here, time constants and proportional gains are considered equal to 1 for numerical simplicity. The Bode plots show that fractional order controllers remove the limitations of the integer order PID controller, offering increased versatility in tuning an increased number of design parameters.

2.5 Fractional Order Tuning Methodologies

Fractional order control actions such as proportional, integral and derivative, add more flexibility to the set of performance specifications the closed loop system is able to fulfil. This is mainly due to the extra tuning parameters of the fractional order PID (FOPID), namely the fractional order of integration and the fractional order of differentiation. Even though the FOPID represents the most common fractional order control algorithm, other types of fractional order controllers have been designed. Review papers focusing on the use of fractional calculus in control engineering have been published recently in [47, 48, 49, 50] and provide an insight into different algorithms of fractional order control.

Classical tuning algorithms are used in the design of fractional order controllers, such as the Ziegler-Nichols rules [51], Hermite-Biehler and Pontryagin theorems [52, 53], linear programming formulation [54], AMIGO and F-MIGO optimization [20]. Alternative tuning methods based on optimizing a certain performance index were developed [55, 56].

However, the most popular method for tuning the fractional order PID controller is based on determining the controller parameters by solving a system of nonlinear equations expressing specifications related to phase margin, gain crossover frequency, sensitivity functions and robustness to

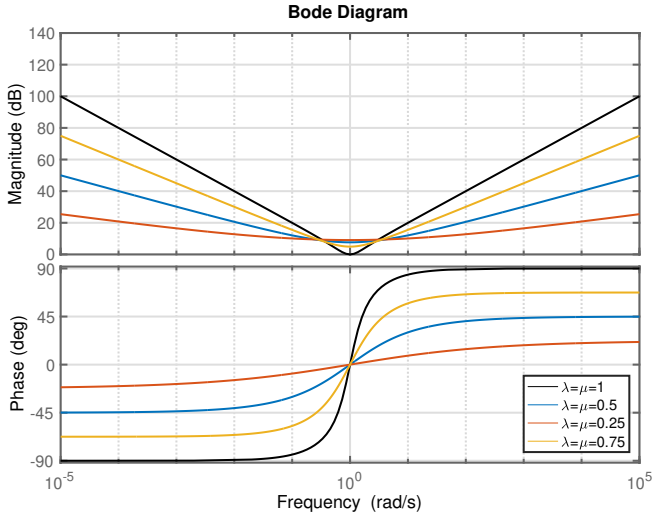

Figure 2.9: Bode plots of integer and fractional order controllers with $k_p = k_i = k_d = T_i = T_d = 1$ for variable values of differ-integer orders

gain changes in a limited frequency interval. The particularities of the system to be controlled dictates the requirements the controller needs to fulfil, determining the choice of tuning specifications. Several works such as [20, 26, 57, 58, 59] approach the tuning of the fractional order PID controller through frequency domain specifications, which is a highly relevant method for any process with time delay, regardless of the time delay values with respect to time constants.

The constraints related to the imposed phase margin, denoted by ϕ_m, and gain crossover frequency ω_{cg} influence the damping ratio of the closed loop system, the settling time, as well as the overall robustness. The mathematical representations of the phase margin and gain crossover frequency are given by the following equations:

$$\angle(C(j\omega_{cg})G(j\omega_{cg})) = -\pi + \phi_m \tag{2.31}$$

and

$$|C(j\omega_{cg})G(j\omega_{cg})| = 1. \tag{2.32}$$

The robustness to gain variations requires a flat phase for the open loop. Also known in literature as the time response iso-damping property, this specification ensures a constant overshoot within a certain frequency range. The range of gain variations for which the system exhibits robustness is limited by the frequency characteristics of the controlled plant and the obtained controller parameters. A flat phase translates in specialised

terminology into a constant phase, with the derivative always zero, creating the mathematical interpretation of the robustness characteristic:

$$\frac{d(\angle(C(j\omega_{cg})G(j\omega_{cg})))}{d\omega}|_{\omega=\omega_{cg}}. \tag{2.33}$$

Robustness can also be expressed by means of sensitivity and complementary sensitivity functions since the closed loop system can fail to perform robustly when exposed to other process uncertainties than gain variations. The sensitivity function $S(j\omega)$ is closely related to good performance regarding disturbance rejection for a desired frequency range and can be expressed by means of:

$$\begin{array}{l} |S(j\omega) = \frac{1}{C(j\omega_{cg})G(j\omega_{cg})}|_{dB} \leq A\,[dB] \\ \forall\omega \leq \omega_s[rad] \Rightarrow |S(j\omega)|_{dB} \leq A\,[dB] \end{array}, \tag{2.34}$$

where A is the desired value for the sensitivity function frequencies [60,61].

An uncertain plant can exhibit high-frequency noise. Specifications related to the complementary sensitivity function denoted by $T(j\omega)$ can result in the rejection of this high frequency noise:

$$\begin{array}{l} |T(j\omega) = \frac{C(j\omega_{cg})G(j\omega_{cg})}{1+C(j\omega_{cg})G(j\omega_{cg})}|_{dB} \leq B\,[dB] \\ \forall\omega \leq \omega_s[rad] \Rightarrow |T(j\omega)|_{dB} \leq B\,[dB] \end{array}, \tag{2.35}$$

with B being the desired high frequency noise attenuation around the frequencies surrounding the gain crossover frequency [60, 61].

Tuning of the FOPID in (2.21) implies usually solving a system of nonlinear equations composed of all or part of the design constraints in (2.31 - 2.35). The resulting controller ensures a robust closed loop system in terms of gain uncertainties, with the ability of rejecting high frequency noise and disturbances, while fulfilling time domain specifications, such as overshoot and settling time. The method can be applied to processes with or without time delay.

For particular cases of the FOPID controller, such as fractional PI or PD controllers, any three (of the five) design specifications can be chosen to be solved as a system of nonlinear equations. The gain crossover frequency and phase margin specifications coupled with the differential equation for robustness to gain variations are the most common three specifications chosen to compute fractional order controllers of type PI or PD. Such an example is provided by [62] to tune a fractional order PD for a first order plus dead time (FOPDT) process model. The work presented in [20] uses a nonlinear system formed of these commonly used specifications to tune a fractional order PI for a second order plus time delay plant. A fractional order PI controller is tuned in [63] by solving the system of nonlinear equations composed by the gain crossover frequency, phase margin and robustness constraints in order to control the level of

a spherical tank. Their comparison in numerical simulations indicates that fractional order control outperforms classical integer order control in terms of closed loop performance.

Controller tuning through optimization by minimizing a frequency domain performance criterion with a constraint on the maximum sensitivity function is proposed in [64]. The optimized criterion measures the ability of the closed loop system to reject low frequency input disturbances.

Solving the nonlinear system composed of the five frequency domain equations for different cases of non-integer order plants with time delay (NOPDT) is studied in [65]. Different process models are identified for the same plant around different working points and several FOPID controllers are successfully tuned and tested, all of them fulfilling all imposed specifications.

Some of the most common methods of solving the system of nonlinear equations is using different optimization routines [20].

Another feasible approach is the graphical system solving procedure such as the one detailed in [66] in order to stabilize FOPDT process with a fractional order PID controller. The controller presented is computed by stabilizing the upper bound of the derivative gain and computing the other parameters with respect to this using a graphical approach. The obtained set of stabilizing controllers provide good stability margin when compared to the conventional PID controller.

A thorough analysis regarding frequency domain stabilization of FOPDT systems is performed in [67] where both fractional and integer order PID controllers are tuned to simultaneously fulfil the three frequency domain design specifications previously presented: robustness, gain crossover frequency and phase margin. The paper presents a set of guidelines regarding the choice of feasible specifications for plant stabilization purposes. The achievable frequency domain boundaries are presented graphically and all possible combinations of controller parameters are verified inside the feasible regions. In addition, [67] highlights by means of numerical simulations the better performance of the fractional order controllers over the classical PIDs in terms of overall closed loop performance.

Variations of using the previously described frequency domain specifications can be found by combining the frequency constraints with other tuning techniques. Such an example is presented in [68] where the authors tune a PI controller based on Bode's ideal transfer function for the open loop system. Iterative optimization routines are used to minimize a quadratic cost function based on the sum of squares of the control signal input and the sum of the integral squared error between the closed loop system with the PI controller and the time response desired process response. The optimization features two additional constraints regarding the sensitivity and the complementary sensitivity equations from (2.34) and (2.35). The proposed method is highly versatile, being validated on both integer and fractional order models as well as processes with con-

siderable time delays. A set of tuning rules to determine both integer and fractional order controllers for first order plus time delay plants are highlighted in [55]. The procedure minimizes the integral absolute error (IAE):

$$IAE = \int_0^\infty |e(t)|dt = \int_o^\infty |r(t) - y(t)dt \tag{2.36}$$

with a constraint applied to the maximum sensitivity function from (2.34). Set-point tracking and achieved performance IAE indexes, as well as disturbance rejection are considered to asses the proposed method. The conclusion of this study, based solely on simulated data, states that the fractional order derivative action improves the overall system performance, while the fractional order integral does not bring significant improvements when compared to integer order PID controllers tuned in the same manner.

In [56], both fractional and integer order PID controllers are computed using genetic algorithms that minimize a given cost function for a third order plus time delay system. Performance criteria such as IAE from equation (2.36), ISE:

$$ISE = \int_0^T e^2(t)dt \tag{2.37}$$

and ITAE :

$$ITAE = \int_0^T t|e(t)|dt \tag{2.38}$$

are minimized in order to obtain the controllers. The genetic algorithm searches for a solution starting from a random population and the parameters of the controller are computed. Simulations prove the superiority of fractional order control compared to integer order PID.

Minimization of the ISE performance combined with frequency domain specifications has been achieved in [69]. Differential Evolution (DE) algorithms are used to tune parallel 2-Degrees of Freedom PID for load frequency control of interconnected power systems in [70]. The design of the controllers is also viewed as an optimization problem where the DE searches for the optimal solution by minimizing the Integral of Time multiplied by ITSE and ISE. ITAE is also used to further increase the performance as well as time domain specifications such as settling time and overshoot, weighted by coefficients. The technique is compared to the Craziness based Particle Swarm Optimization (CPSO) and the proposed method proves its superiority. System uncertainties are introduced by varying the process parameters, testing and validating the robustness of the optimized controller.

2.6 Summary

This chapter presents the problems with respect to fractional calculus applied to modelling and control. Popular definitions of the fractional order operator are provided with an emphasis on the most popular ones for identification and control. The proof that fractional differ-integer operators are powerful tools in encapsulating complex real life phenomena has been provided through analyzing various fractional order elements, as seen through the Laplace domain.

Furthermore, the classical, integer order PID controller is generalized in the fractional order field with the addition of two extra parameters representing the fractional orders of differentiation and integration, respectively. A state of art focusing on the last decade related to popular tuning methodologies for FOPID controllers is present. The study claims that the most widespread tuning strategy is based on imposing frequency domain specifications related to gain crossover frequency, phase margin, robustness, sensitivity and complementary sensitivity functions are presented. However, minimization of different cost functions such as ISE, ITAE performance indexes is also widely popular.

There are also many other tuning approaches available throughout the literature, but only studies relevant for the present dissertation have been included. The FOPID tuning methodologies discussed will be used in the next chapters to tune different fractional order PI and PD controllers related to non-Newtonian case studies. Some definitions presented in this chapter are used herein this book.

The review presented in this chapter has been published in:

- **I. Birs**, C. Muresan, I. Nascu, C. Ionescu. "A Survey of Recent Advances in Fractional Order Control for Time Delay Systems", in *IEEE Access*, vol. 7, no. 1, pp. 30951-30965, DOI: 10.1109/ACCESS.2019.2902567, 2019.

- **I. Birs**, S. Folea, O. Prodan, E. Dulf, C. Muresan. "An experimental tuning approach of fractional order controllers in the frequency domain", in *Applied Sciences*, vol. 10, no. 9, pp. 2379 , 2020.

- C. Muresan, **I. Birs**, E. H. Dulf, D. Copot and L. Miclea. "A review of recent advances in fractional-order sensing and filtering techniques", in *Sensors*, vol. 21, no. 17, 2021.

3

Some Properties of Non-Newtonian Fluids

3.1 Introduction

The purpose of this chapter is to present those properties of non-Newtonian (NN) fluids and soft materials on which several assumptions are made throughout this thesis [1, 9]. This information also provides the necessary motivation to characterize such material properties using fractional calculus introduced in Chapter 2.

The chapter also introduces a non-Newtonian fluid classification separating fluids into time dependent and time independent properties. Pseudoplastic, visco-plastic and dilatant are subcategories of time independent fluids, whereas tixothrophic and rhepectic fluids are characterized from both shear rate and shear time perspectives. Some general notions are introduced to better understand the dynamics of different types of non-Newtonian behavior, to enable the proper development of fractional order models.

Fractional order systems have been recently applied in modeling non-Newtonian fluid dynamics. In [71] the authors propose a fraction seepage model of a non-Newtonian fluid. The non-local characteristic of the fluid has been modeled in the case of a porous media. In the paper, the authors make a first hand attempt to relate the fractional order of the model with the fractal dimension of media tortuosity. A further application can be found in [72], where the authors describe, via fractional derivative models, the flow of non-Newtonian fluid driven by spatially nonlocal velocity in steady pipe flow conditions. A more specific fractional system, i.e. the extension of the Fractional-order Maxwell model, has been applied in [73] to incorporate a relaxation process with non-Newtonian viscosity behavior. As a general conclusion of these studies, the main added value in using such models stands in their capability to describe the non-local and

memory effects. Furthermore, the exponents of the integro-differential equations can be used as optimization parameters in data driven identification.

3.2 Newtonian vs. Non-Newtonian Fluids

Consider the infinitesimal volume fluid element made by the overlapping of infinitesimal thickness layers. If a very thin layer of Newtonian fluid is contained within two plates, as in Fig. 3.1, it is possible to observe the linearity of the fluid's velocity profile as a direct consequence of a shearing force F applied to the moving plate [9]. In this linear context, the external force is balanced by an internal frictional force in the fluid arising from its viscosity. In other words, the fluid is subjected to a uniform strain rate $\dot{\gamma}$: the governing equation that relates the shear stress τ_{yx} pressure-like, and the shear rate $\dot{\gamma}_{yx}$, or strain rate, is

$$\tau_{yx} = -\eta \, \dot{\gamma}_{yx} \tag{3.1}$$

also known as the *Newton's law of fluids*. The subscript yx is used to underline the direction of the stress and strain in the fluid. The negative sign on the right-hand side of this relation suggests that the shear stress is a resisting force. Looking at equation (3.1) it can be noticed the similarity with Hook's law for a solid, except it refers to the shear rate $\dot{\gamma}_{yx}$. Moreover, the relation is linear and the constant coefficient η is called viscosity of the fluid. This value is well known for a great variety of Newtonian fluids, and it varies with temperature and pressure of the fluids, hence it has time varying properties. All gases, as well as most common liquids like water, oils, hydrocarbon and also metals, in liquid form, are examples of Newtonian fluids.

By contrast, a fluid is called non-Newtonian when it does not obey Newton's law. This means that the relation between shear stress and shear rate is no longer linear, i.e. the viscosity varies in time, dependent on conditions such as:

- flow conditions, *e.g.* flow geometry,
- shear stress applied to the fluid,
- shear rate developed within the fluid,
- time of shearing stress applied,
- kinematic history of the sample, etc.

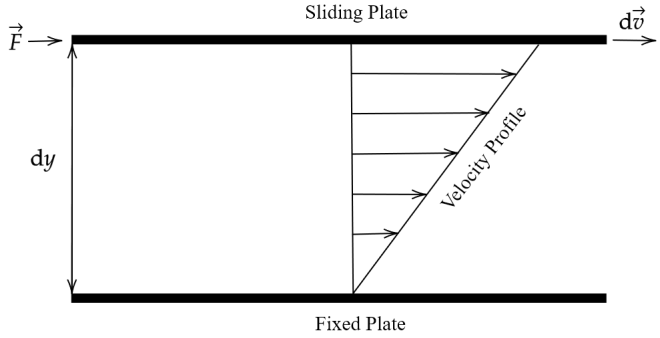

Figure 3.1: Schematic representation of unidirectional shearing flow.

3.3 Non-Newtonian Fluids Classification

A classification of non-Newtonian fluids can be made based on variations in viscosity, as given in Fig. 3.2. This is however just informative, as real materials often display a combination of two or more properties. Nevertheless, in most cases, it is possible to identify the dominating non-Newtonian feature and to use it as the basis for subsequent process engineering calculations. We will elaborate on most important used in this thesis, hereafter.

3.3.1 Time Independent Properties

Fluids whose flow properties are independent of the duration of shearing may be described as:

$$\tau_{yx} = f(\dot{\gamma}_{yx}) \qquad \text{or vice-versa} \qquad \dot{\gamma}_{yx} = f^{-1}(\tau_{yx}) \tag{3.2}$$

which implies that the shear rate depends on the local value of the shear stress. Depending on the functions of (3.2), these fluids may be further subdivided into three different types:

1. Shear-thinning or pseudoplastic,
2. Viscoplastics, including Bingham plastics,
3. Shear-thickening or dilatant.

3.3.1.1 Pseudoplastic or Shear-thinning Fluids

A great part of commonly known fluids belong to this family: nail polish, whipped cream, ketchup, molasses, syrups, paper pulp in water, latex

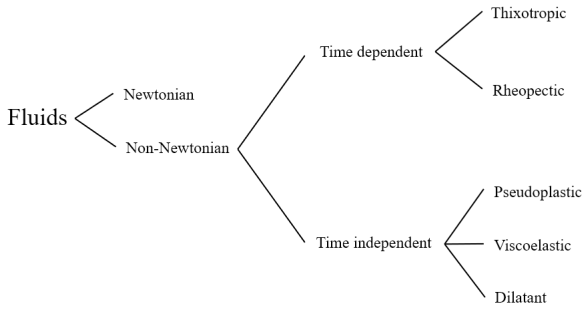

Figure 3.2: Classification tree of non-Newtonian fluids.

paint, ice, some silicone oils, sand in water and some silicone coatings. This kind of fluids have an apparent viscosity which decreases with the increment of the shear rate. Most of pseudoplastic fluids are piecewise linear and the following limit variables can be introduced:

$$\lim_{\dot{\gamma}_{yx}\to 0} \frac{\tau_{yx}}{\dot{\gamma}_{yx}} = \eta_0 \qquad \text{Zero shear viscosity} \tag{3.3a}$$

$$\lim_{\dot{\gamma}_{yx}\to \infty} \frac{\tau_{yx}}{\dot{\gamma}_{yx}} = \eta_\infty \qquad \text{Infinite shear viscosity} \tag{3.3b}$$

In Fig. 3.3, it can be observed that the central region of the curve is piecewise linear. Taking into account that the plot is in logarithmic scale, this behaviour can be well modelled as a power law relation:

$$\tau_{yx} = K_C(\dot{\gamma}_{yx})^n, \tag{3.4}$$

where K_C is the flow consistency index ($Pa\ s^n$), with n the flow behavior index (dimensionless). By using equation (3.1) in (3.4) and resolving with respect to the viscosity one obtains

$$\eta = K_C(|\dot{\gamma}_{yx}|)^{n-1} \tag{3.5}$$

which is also known as *Ostwald-De Waele model* for pseudoplastic fluid [74]. The two model parameters n and m are called respectively the power-law index and the fluid consistency coefficient. For a Newtonian fluid $n = 1$, while for a pseudoplastic substance $n < 1$. The lower the value of the power-law index, the greater is the degree of shear-thinning. Admittedly, equation (3.5) provides the simplest description of shear-thinning behaviour, but it also has a number of limitations. Another model is based on the assumption that the shear-thinning behavior is caused by the formation and breakdown of "structural linkages or units", also observed in

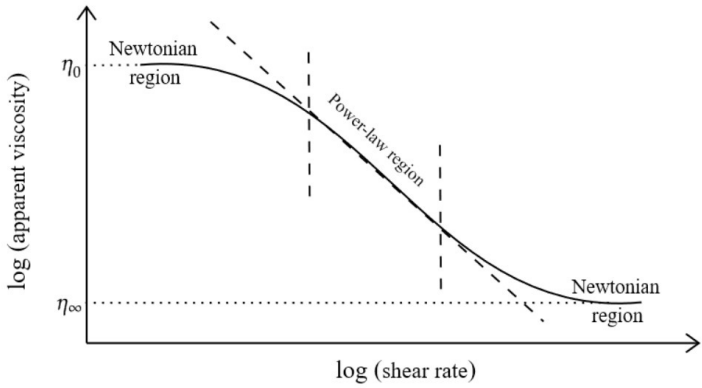

Figure 3.3: Qualitative representation of the apparent viscosity behaviour for a shear-thinning fluid.

polymers and lung tissue [75]. For one-dimensional steady shearing we have:

$$\frac{\eta - \eta_\infty}{\eta_0 - \eta_\infty} = \frac{1}{1 + (\lambda \dot{\gamma}_{yx})^{2/3}} \tag{3.6}$$

where η_0 and η_∞, respectively, are the zero and infinite shear viscosities while λ is a constant with units of time. This formula was successfully used to fit the shear stress-shear rate data for a wide variety of pseudoplastic systems. This model is also a first hand example as to how the theory of fractional order systems is able to reproduce this behaviour, rather than using higher orders in classical models of integer order approximation.

3.3.1.2 Visco-plastic Fluids

This class of materials is characterized by the existence of a threshold value in the minimal yield stress τ_0 that must be exceeded before deformation (or equivalently, flow) occurs. It implies that the substance at rest consists of a three-dimensional structure of sufficient strength to resist any external stress less than τ_0. For stress levels greater than τ_0, the structure loosens, and the material behaves as a viscous fluid. A fluid with a linear flow curve for $|\tau_{yx}| > \tau_0$ is called a Bingham plastic fluid and is characterized by a constant value of plastic viscosity [13].

Among the many mathematical equations to model this kind of flow behaviour, the simplest and perhaps the most widely used can be written as:

$$\begin{aligned} \tau_{yx} &= \tau_0^B + \eta\, \dot{\gamma}_{yx} \qquad \text{if } \tau_{yx} > \tau_0^B \\ \dot{\gamma}_{yx} &= 0 \qquad\qquad\qquad \text{if } \tau_{yx} \leq \tau_0^B \end{aligned} \tag{3.7}$$

where τ_0^{B} is the Bingham yield stress and η_{B} is the plastic viscosity. Another model for visco-plastic fluids is known as the *Herschel-Bulkley* model [76], written for a simple shear flow as:

$$\begin{aligned} \tau_{\mathrm{yx}} &= \tau_0^{\mathrm{H}} + m\,(\dot{\gamma}_{\mathrm{yx}})^n \qquad \text{if } \tau_{\mathrm{yx}} > \tau_0^{\mathrm{H}} \\ \dot{\gamma}_{\mathrm{yx}} &= 0 \qquad\qquad\qquad\quad \text{if } \tau_{\mathrm{yx}} \leq \tau_0^{\mathrm{H}} \end{aligned} \tag{3.8}$$

This formula can be seen as a generalization of the simple Bingham model (3.7), in which the linear shear rate dependence has been replaced by a power-law behaviour. This model is broadly used to model blood viscosity [13] and muddy clay modelling applications [15].

3.3.1.3 Dilatant or Shear-thickening Fluids

In these (dilatant) materials, their apparent viscosity increases with increasing shear rates. Most commonly, this behaviour is encountered in concentrated suspensions of solids, and can be qualitatively explained as follows. When a suspension is at rest, the gap between one particle and another is minimum and the liquid present is just sufficient to fill the void spaces. At low shear rates, the liquid lubricates the motion of one particle over another, and the resulting stresses are consequently low. By contrast, at high shear rates, the dense packing of solids breaks down and the material expands or dilates slightly causing an increase in the gap. The amount of liquid available is no longer sufficient to lubricate the solid motion of one particle over another and the resulting solid-solid friction causes the stresses to increase rapidly, which, in turn, causes an increase in the apparent viscosity.

Experimental data suggests that the apparent viscosity-shear rate curves often result in a linear behaviour on log-log coordinates over a limited shear rate range of interest [72]. This observation directly suggests that the power-law model (3.5) may be used with $n > 1$ in this case.

The entire behaviour of typical shear-thickening fluids, as given in Fig. 3.4 gives evidence of three distinct zones. Two of them, for very low and very high shear rate respectively, are regions in which the fluid shows shear-thinning characteristics, i.e. the viscosity decreases with increasing shear rates. However, for mid-range shear rate the liquid behaves like shear-thickening, resulting in increasing viscosity with shear rate. This region is linear in the log-log plot, as mentioned earlier. In other words, depending on the context conditions, the behaviour of the material or fluid changes. The model has been revised taking into account the three

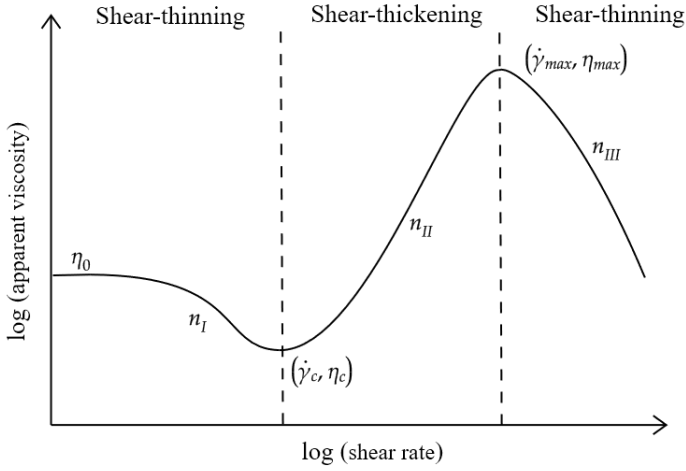

Figure 3.4: Qualitative viscosity curve for a shear-thickening fluid.

different regions [77, 78]:

$$\eta = \begin{cases} \eta_{\mathrm{c}} + \dfrac{\eta_0 - \eta_{\mathrm{c}}}{1 + \left[K_{\mathrm{I}} \frac{\dot{\gamma}^2}{\dot{\gamma} - \dot{\gamma}_{\mathrm{c}}}\right]^{n_{\mathrm{I}}}} & \text{for } \dot{\gamma} \leq \dot{\gamma}_{\mathrm{c}} \\ \eta_{\max} + \dfrac{\eta_{\mathrm{c}} - \eta_{\max}}{1 + \left[K_{\mathrm{II}} \frac{\dot{\gamma} - \dot{\gamma}_{\mathrm{c}}}{\dot{\gamma} - \dot{\gamma}_{\max}} \dot{\gamma}\right]^{n_{\mathrm{II}}}} & \text{for } \dot{\gamma}_{\mathrm{c}} < \dot{\gamma} \leq \dot{\gamma}_{\max} \\ \dfrac{\eta_{\max}}{1 + [K_{\mathrm{III}}(\dot{\gamma} - \dot{\gamma}_{\max})]^{n_{\mathrm{III}}}} & \text{for } \dot{\gamma} > \dot{\gamma}_{\max} \end{cases} \tag{3.9}$$

It must be noticed that the three branches of equation (3.9) have a functional form based on that of the Cross model: the similarity can be found if equation (3.6) is rearranged by solving it with respect to η. Hence, the parameters appearing in equation (3.9) have the same dimensions and interpretation: $K_{\mathrm{I}}, K_{\mathrm{II}}, K_{\mathrm{III}}$, possess a time component and are responsible for the transitions between the plateaus and the power-law, while the dimensionless exponents n_i are related to the slopes of the power-law regimes. It is worth recalling here that various power-law regimes can be directly linked to various values of fractional order models.

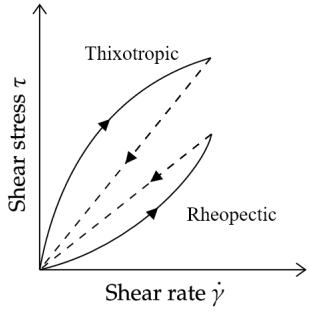

Figure 3.5: Qualitative shear stress-shear rate behaviour for thixotropic and rheopectic materials.

3.3.2 Time Dependent Properties

For many industrial materials, as well as some common food materials, the viscosity depends on both shear rate and shear time. The most common textbook example is honey: when it is sheared at a constant rate of shear, following a period of rest, its apparent viscosity gradually decreases as its internal "structure" breaks down progressively. As the number of " structural linkages "available for breaking down decreases, also the rate of variation drops towards zero. On the other hand, the rate at which the linkages can reform increases, and eventually a state of dynamic equilibrium is reached: the rates of build-up and breakdown linkages are equal. This type of fluid behaviour may be further divided into two categories: thixotropic and rheopectic or anti-thixotropic.

3.3.2.1 Thixotropic Fluids

A material is said to exhibit thixotropy if its apparent viscosity (or shear stress) decreases with time when sheared at a constant rate of shear. If the flow curve is measured in a single experiment in which the shear rate is steadily increased at a constant rate from zero to a maximum value, and then decreased at the same rate to zero again, a hysteresis loop, as shown schematically in Fig. 3.5, is obtained. The height, the shape, and the enclosed area of the loop, depend on the kinematic parameters such as duration and rate of shearing, past deformation history of the material sample, etc.

In practice, thixotropic substances show very similar properties to the shear-thinning fluids. Common examples are yogurt, peanut butter, honey, aqueous iron oxide gels, gelatin gels, carbon black suspension

in molten tire rubber, some drilling muds, many paints, many colloidal suspensions.

3.3.2.2 Rheopectic Fluids

The relatively few systems for which the apparent viscosity increases with the duration of shearing display rheopexy, i.e. negative thixotropy. Hysteresis effects are observed in the flow curve in Fig. 3.5, but in this case it is inverted as compared to that for a thixotropic material. By analogy with thixotropy, rheopexy is associated with a gradual build-up of "structure" as the fluid is sheared, without any guarantee that an equilibrium will ever be reached. Thus, in a rheopectic material, the structure builds up by shear and it breaks down when the material is at rest. Hence, it can be associated with the shear-thickening, or dilatant fluids. Some examples of rheopectic fluids are: synovial fluid, printer ink, gypsum paste.

To conclude, we have observed that the material properties can change as a function of various dynamic conditions, requiring several individual model structures. Power-law, exponential and combinations thereof are commonly shown to be dynamics which naturally require generalized models such as fractional order models. Previous know-how and specialised literatures offers numerous examples of such solutions in various applications. The remainder of this thesis will deal with fractional order impedance models represented in Laplace domain for frequency domain identification, as it directly results from the material characterization.

3.4 General Navier-Stokes Equations

In this section, Navier-Stokes equations are briefly introduced, correlated to non-Newtonian fluid flow from [79,80,81,82,83]. The purpose is to provide a minimal theoretical framework for supporting rationale on which the fractional order system is designed and used. Prior know-how is employed from modelling flow in biological systems [75].

Any pulsatile flow can be analyzed in terms of periodical functions, such as the pressure gradient:

$$-\frac{\partial p}{\partial z} = M_P \cos(\omega t - \Phi_P), \tag{3.10}$$

where z is the axial coordinate, $\omega = 2\pi f$ is the angular frequency (rad/s), with f the frequency (Hz), M_P the modulus and Φ_P is the phase angle of the pressure gradient.

Conform linear system theory, it follows that also the pressure and the velocity components will be periodic, with the same angular frequency ω. The purpose is to determine the velocity in radial direction $u(r, z, t)$ with r the radial coordinate, the velocity in the axial direction $w(r, z, t)$, the pressure $p(r, z, t)$.

One may use the Womersley parameter defined as the dimensionless parameter:

$$\delta = R\sqrt{\frac{\omega\rho}{\eta'}}, \tag{3.11}$$

with R the absolute radius of the cylinder (pipeline). If the simplest form of axi-symmetrical flow in a cylindrical pipeline is considered, the simplified Navier Stokes equations can be written as

$$\frac{\partial}{\partial\theta} = \frac{\partial^2}{\partial\theta^2} = 0 \tag{3.12}$$

at contour velocity $v = 0$. Further on, no external forces F_r, F_z are considered. For infinitesimal segments, the total pressure drop variations can be neglected and locally can be divided by density ρ and introduce the dimensionless parameter $y = r/R, 0 \leq y \leq 1$ in the relation

$$\frac{d}{dy} = \frac{d}{dr}\frac{dr}{dy} = R\frac{d}{dr}, \tag{3.13}$$

$$\frac{d}{dr} = \frac{1}{R}\frac{d}{dy}. \tag{3.14}$$

A set of simplifying assumptions can be introduced at this point:

i) the radial velocity component is small, as well as the ratio u/R and the term in the radial direction;

ii) the terms $\frac{\partial^2}{\partial z^2}$ in the axial direction are negligible.

It follows that:

$$\frac{\partial u}{\partial t} = -\frac{1}{\rho R}\frac{\partial p}{\partial y} + \frac{\eta'}{\rho}\left[\frac{1}{yR^2}\frac{\partial u}{\partial y} + \frac{1}{R^2}\frac{\partial^2 u}{\partial y^2} - \frac{u}{R^2y^2}\right] \tag{3.15}$$

$$\frac{\partial w}{\partial t} = -\frac{1}{\rho}\frac{\partial p}{\partial z} + \frac{\eta'}{\rho}\left[\frac{1}{yR^2}\frac{\partial w}{\partial y} + \frac{1}{R^2}\frac{\partial^2 w}{\partial y^2}\right] \tag{3.16}$$

$$\frac{u}{Ry} + \frac{1}{R}\frac{\partial u}{\partial y} + \frac{\partial w}{\partial z} = 0. \tag{3.17}$$

Since the pressure gradient is periodic, also the pressure $p(y, z, t)$ and the other velocity components $u(y, z, t), w(y, z, t)$ are periodic and can be defines as:

$$\begin{aligned} p(y, z, t) &= A_P(y)e^{j\omega(t-z/\tilde{c})} \\ u(y, z, t) &= A_U(y)e^{j\omega(t-z/\tilde{c})} \\ w(y, z, t) &= A_W(y)e^{j\omega(t-z/\tilde{c})} \end{aligned}, \tag{3.18}$$

where $\tilde{c}$ denotes the complex velocity of wave propagation and $j = \sqrt{-1}$. Using these definitions, it follows the system of equations:

$$u = \frac{j\omega R}{\eta' \tilde{c}} \{C_1 \frac{2}{\delta j^{3/2}} J_1(\delta j^{3/2} y) + \frac{A_P}{\rho \tilde{c}} y\} e^{j\omega(t - \frac{z}{\tilde{c}})} \tag{3.19}$$

$$w = \{C_1 J_0(\delta j^{3/2} y) + \frac{A_P}{\rho \tilde{c}}\} e^{j\omega(t - \frac{z}{\tilde{c}})} \tag{3.20}$$

$$p(t) = A_P e^{j\omega(t - \frac{z}{\tilde{c}})} \tag{3.21}$$

with $C_1 = -\frac{A_P}{\rho \tilde{c}} \frac{1}{J_0(\delta j^{3/2})}$, A_P the amplitude of the pressure wave, J_0 the Bessel function of the first kind and zero degree, J_1 the Bessel function of the first kind and first degree, and in which:

$$-\frac{dp}{dz} = \frac{j\omega}{\tilde{c}} A_P e^{j\omega(t - \frac{z}{\tilde{c}})} = M_P e^{j(\omega t - \Phi_P)} \tag{3.22}$$

such that

$$A_P e^{j\omega(t - \frac{z}{\tilde{c}})} = \frac{\tilde{c}}{\omega} M_P e^{j(\omega t - \Phi_P - \pi/2)}. \tag{3.23}$$

For non-Newtonian fluid flows inside pipelines, the effective elastic modulus and wall density, respectively, may be considered in function of the pipeline rugged structure:

$$\begin{aligned} E &= \kappa E_c + (1 - \kappa) E_s \\ \rho_{wall} &= \kappa \rho_c + (1 - \kappa) \rho_s \end{aligned}, \tag{3.24}$$

taking into account at each section of the setup the fraction amount κ of corresponding hard material (index c) and soft material (index s). This can be then used to model interaction between fluid and transporting materials. Wall density refers to the density of the material from which the pipeline is built. Elastic properties and wall density of the material influence the elasticity of the pipeline. When the non-Newtonian fluid flows through the pipes, these can expand or contract, influencing the interaction between the fluid and transporting material.

3.5 Fractional Flow Dynamics in Non-Newtonian Fluids

Classical constitutive relationship for shear stress in terms of the velocity gradient can be expressed as [84]:

$$\tau = \eta' \frac{du}{dy}, \tag{3.25}$$

with τ the viscous shear stress, η' (kg/m s) the dynamic viscosity, u the flow velocity (m/s) and y (-) the radial direction in normalized form, i.e.

$y = r/R$ with R (m) the radius of the transporting pipeline and r (m) the radial coordinate. This relation no longer holds for non-Newtonian fluids such as blood, detergent, gel, plasma, etc.

Previous work on fractionalising compartmental models for drug concentration gradients in blood and tissue has indicated that each gradient can be expressed in terms of its kernel and integral form of mass transfer [18, 85]. Consider the pipeline with our fluid divided in compartments of equal infinitesimal distance. The gradient is given by:

$$u(1) - u(0) = k \int_0^1 M(\tau) d\tau, \tag{3.26}$$

where the parameter M denotes mass or molar amounts of material in the respective compartment, and k (1/s) are rate constants. Each of the mass transfer integral includes a kernel, i.e.

$$u(1) - u(0) = k \int_0^1 K \cdot \tilde{M}(\tau) d\tau. \tag{3.27}$$

In the classic theory case, the kernel is simply equal to one. By choosing the kernel in an appropriate form of power-law, one can then use Riemann-Liouville fractional integrals or others. This power-law kernel has been formerly introduced in earlier studies of non-Newtonian materials and fluids [16, 17, 86]. For instance, using the kernel

$$K(t, \tau) = \frac{(t - \tau)^{\alpha - 1}}{\Gamma(\alpha)} \tag{3.28}$$

with $0 < \alpha < 1$, we have for $\alpha = 1$ the classical case since $K = 1$. Recall the Riemann-Liouville fractional integral (2.1)

$${}_0D_t^{-\alpha} M(t) = \int_0^1 \frac{(t - \tau)^{\alpha - 1}}{\Gamma(\alpha)} \tilde{M}(\tau) d\tau, \tag{3.29}$$

where D stands for an integral when the order is negative and for a derivative when the order is positive. Finally, equation (3.27) can be written as

$$u(1) - u(0) = k {}_0D_t^{-\alpha} M(t). \tag{3.30}$$

The zero initial values are commonly employed in compartmental models. Alternatively, for non-zero initial conditions one can use the Caputo derivative, in the form

$${}_0D_t^{1-\alpha} M(t) = {}_0^C D_t^{1-\alpha} M(t) + \frac{M(0) t^{\alpha - 1}}{\Gamma(\alpha)}, \tag{3.31}$$

where the superscript C on the left denotes a Caputo fractional derivative. Note the units of the rate constant are no longer $time^{-1}$ but $time^{-\alpha}$,

suggesting time related memory effects are intrinsically captured by such representations.

In [15] a model has been proposed to describe time-dependent flow in non-Newtonian fluids:

$$\tau(t) = \tau_0 + a \cdot \lambda_\beta \frac{d^{\beta-1}\dot{\epsilon}}{dt^{\beta-1}}, \tag{3.32}$$

where $0 \leq \beta \leq 1$, a and λ are material constants, and ϵ (m) denotes strain. This is a generalization of equation (3.25) following the generalized order rationale. This has been used (in various forms) to model Maxwell elements in mechanical models of viscoelasticity [86]. Further on, such mechanical models can be used to express electrical model analogy in various real life applications, but mostly successful employed in modelling properties of biological tissues [10, 17].

To address the non-locality problem of properties in non-Newtonian fluids, one may use equation (3.32), for $0 < \alpha = \beta - 1 < 2$. The physical basis for this non-uniform velocity gradient can be the non-uniformity of fluid particles (e.g. mixtures of solid and liquid particles), molecular interaction, biological and chemical effects. Using the fractional derivative definition from [15]:

$$\frac{d^\alpha u(y)}{dy^\alpha} = \frac{1}{\Gamma(n-\alpha)} \int_0^y \frac{u^{(n)}(\tau)}{(y-\tau)^{\alpha-n+1}} d\tau, \tag{3.33}$$

with $n-1 < \alpha \leq n$, and n the smallest integer greater than the order α, the relationship between velocity gradient and viscous shear stress is given by:

$$\tau = \left\{ \begin{array}{c} \tau_0 + \eta' I^{1-\alpha} \frac{du}{dy}, 0 < \alpha < 1 \\ \tau_0 + \eta' \frac{du}{dy}, \alpha = 1 \\ \tau_0 + \eta' I^{2-\alpha} \frac{d}{dy} \frac{du}{dy}, 1 < \alpha < 2 \end{array} \right\}, \tag{3.34}$$

where $I^{1-\alpha}$ and $I^{2-\alpha}$ represent the fractional integral:

$$I^\gamma f(y) = \frac{1}{\Gamma(\gamma)} \int_0^y (y-\tau)^{\gamma-1} f(\tau) d\tau, \gamma > 0. \tag{3.35}$$

3.5.1 Velocity Profile in Pipeline

In the context exemplified here, the following assumptions are made:

- the non-Newtonian fluid is incompressible, and
- the flow is laminar.

Consider a suspended object as in Fig. 3.6. The force balance relation in the flow direction is given by

$$A(p_1 - p_2 + \rho g l \sin(\phi)) - \tau \cdot 2\pi r l = 0 \tag{3.36}$$

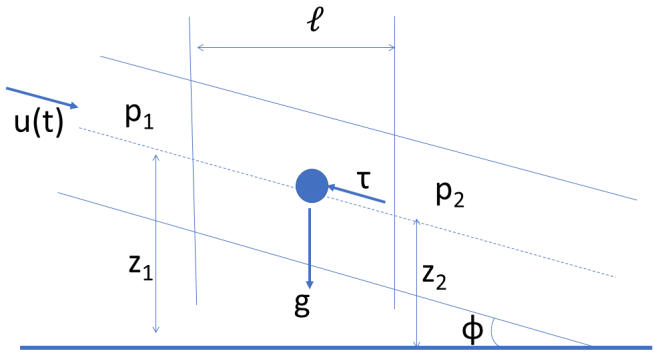

Figure 3.6: Schematic representation of a suspended object in pipeline.

with A (m^2) cross section, r (m) radial direction, ρ (kg/m^3) the density of the non-Newtonian fluid, and ℓ (m) is the length considered and R (m) the absolute radius of the cylinder. Given that $\sin(\phi) = \frac{z_1 - z_2}{l}$, thus the hydraulic gradient is given by:

$$J = \frac{(z_1 + p_1/\rho g) - (z_2 + p_2/\rho g)}{l} = \frac{2\tau}{\rho g r}. \tag{3.37}$$

Employing the velocity gradient constitutive equation from previous section we impose

$$\eta' \frac{d^\alpha u}{dr^\alpha} = -\rho g r J/2 \tag{3.38}$$

and obtain

$$u(r) - u(r=0) = -\frac{\rho g J r^{1+\alpha}}{2\eta' \Gamma(\alpha+2)}. \tag{3.39}$$

Imposing the no slip condition, where $u(r = R) = 0$, hence:

$$u(r) = \frac{\rho g J r^{1+\alpha}}{2\eta' \Gamma(\alpha+2)}. \tag{3.40}$$

The velocity profile is written as

$$u(r) = \frac{\rho g J}{2\eta' \Gamma(\alpha+2)} (R^{1+\alpha} - r^{1+\alpha}) \tag{3.41}$$

which reduces to the Newtonian velocity profile for $\alpha = 1$.

The maximum velocity is then calculated as

$$u_{max} = \frac{\rho g J R^{1+\alpha}}{2\eta' \Gamma(\alpha+2)} \tag{3.42}$$

and the mean velocity is

$$\bar{u} = \frac{\rho g J}{2\eta' \Gamma(\alpha+2)}(1 - \frac{2}{3+\alpha})R^{1+\alpha}. \tag{3.43}$$

When the ration of these velocities is 0.5, then we have Newtonian fluid - this is again the case for $\alpha = 1$. It follows that the velocity gradient may be non-uniform in non-Newtonian fluids.

3.5.2 Frictional Head Loss

For objects moving forward in a non-Newtonian fluid, there is a frictional head loss of velocity, which can be calculated from the mean velocity relation:

$$F = \frac{2\frac{\eta'}{\rho}\Gamma(\alpha+2)}{g} \frac{3+\alpha}{1+\alpha} \frac{l\bar{u}}{R^{1+\alpha}} \tag{3.44}$$

with $\frac{\eta'}{\rho}$ the kinematic viscosity. For a circular pipeline, this can be expressed in terms of the diameter of the cylinder $D = 2R$:

$$F = \frac{64}{\frac{2^{3-\alpha}}{(3+\alpha)\Gamma(1+\alpha)} \frac{\bar{u}D^{\alpha}}{\frac{\eta'}{\rho}}} \frac{l}{D} \frac{\bar{u}^2}{2g}. \tag{3.45}$$

Again this reduces to the classical frictional head loss for Newtonian fluid when $\alpha = 1$.

3.6 Summary

This chapter proposes a framework for modelling velocity profiles and suspended (infinitesimal) objects in non-Newtonian fluid environment. Navier-Stokes relations from classical fluid flow theory are employed, followed by fractional constitutive equations for velocity profiles and flow. The theoretical analysis is performed under assumptions of steady and pulsatile flow conditions, with incompressible properties. The fractional derivative model for velocity and friction drag effect upon a suspended object are determined.

The results presented in this chapter have been published in:

- **I.Birs**, D. Copot, C. Muresan, I. Nascu, C. Ionescu. "Identification For Control Of Suspended Objects In Non-Newtonian Fluids", in *Fractional Calculus and Applied Analysis*, vol. 22, no.5, pp. 1378-1394 , DOI: 10.1515/fca-2019-0072, 2019.

4

Fractional Order Control with Event Based Dynamics

4.1 Introduction

In its industry relevant impact report, the IEEE Control System Society provided useful information as to those tools from systems and control engineering mostly employed by industry [87]. Not surprising, the top three most used solutions in industry are: PID controllers, system identification and model predictive control. With a gripping 90% of regulatory loops, PID control is the obvious first line candidate for emerging concepts such as fractional calculus. It follows a notable success of the generalization of the popular Proportional Integral Derivative (PID) controller, as described in Chapter 2. The resulting strategy outperforms its integer order version. The closed loop systems featuring fractional order control (in general, but prevalently PID type) have an improved time domain performance, stability, robustness and flexibility from the frequency response perspective [20, 21, 88]. Its diverse benefits contribute to the enhancement of multiple control possibilities such as the fractional order Internal Model Control (IMC) strategy, fractional order filter integration to available integer-order structures, fractional order Linear Quadratic Regulator (LQR), [89, 90, 91] etc.

The present chapter focuses on introducing fractional calculus in a control branch that has not been previously explored from this perspective: the event-based control strategy. Event-based control is a relatively novel concept that triggers the computation of a new control signal through events, in comparison to classical controller implementations that trigger time based changes in the control signal [92, 93]. The strategy is mostly beneficial for processes that have limited resources such as CPU mem-

ory, bandwidth allocation and require a reduced energy demand [94, 95]. All of these features show the necessity of the event-based strategy in today's industrial settings [96, 97]. Furthermore, cloud control systems are becoming more popular, the industry being the main beneficiary of such an approach that externalizes automatic control, providing a versatile solution that could be easily debugged and adapted [98, 99]. It can be speculated that event-based control combined with cloud based implementations is a powerful tool for the future of industrial control in the Industry 4.0 paradigm. The benefits provided by fractional order control into the event-based strategy are introduced, offering multiple possibilities to exploit these advantages to benefit the current industrial need.

The original contribution of the current work to the fractional calculus field is the engineering applicability of this numerical tool into the event-based control strategies. In this chapter, the theoretical background for event-based fractional order controllers is proposed and several implementation options are explored. The method is validated for the general fractional order PID controllers using varied numerical examples. Furthermore, the proposed approach is compared with classical, non-event based, discrete-time approaches showing the efficiency of the methodology as well as the benefits regarding the control effort.

4.2 Main Industrial Benefits

The fourth industrial revolution, known as Industry 4.0, integrates the latest scientific advances of the 21^{st} century into the architecture of traditional manufacturing plants [96]. State of the art smart manufacturing systems and technologies take the industrial setting a step further into the future. Human intervention is minimized by add-on automation technologies featuring state machines, self-monitoring and abilities to perform machine to machine communication. The emerging Internet of Things (IOT) protocol is the principal constituent in the smart manufacturing trend, creating connected networks of distributed systems [100].

The new industrial cloud architectures are equipped with a wide range of sensors and actuators creating a widespread network that gathers and shares data. Decisions are (semi-)autonomously taken by interpreting the available information [101], sometimes through semantic reasoning. However, an overflow of unnecessary, unusable or corrupted data leads to an overburden of the bandwidth and wireless network sharing. Introducing the context awareness modules into the smart manufacturing process enables the interpretation and filtering of the gathered information as well as performing decisions regarding its relevance [102]. The main idea is to process data in the lower levels of the system and forwarding the contextual information to the upper layers of the architecture - known as RAMI4.0 (Refererence Architectural Model Industry). There are four main layers

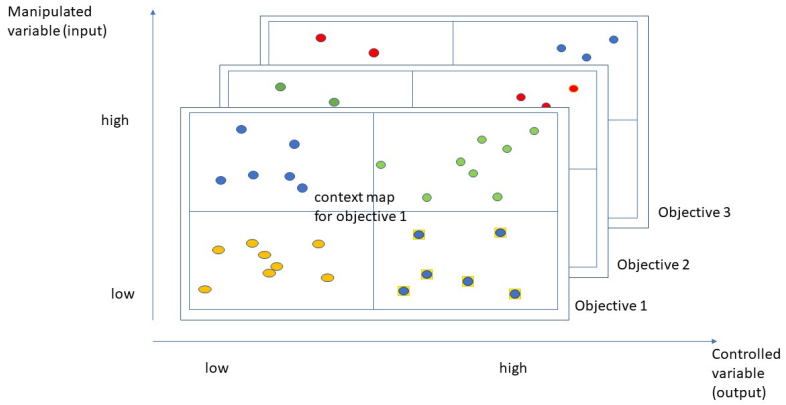

Figure 4.1: Conceptual representation of layer-based context awareness management using context maps

of the context management, as presented in Fig. 4.1. Furthermore, the layers of the RAMI architecture together with the communication and administration shells are shown in Fig. 4.2. The connection takes place over the Industry 4.0 communication protocol, where the administration shell performs the digital part and the physical "things" perform the real part.

In the conceptual Fig. 4.1, at determined or triggered time instances, each objective of the system is analyzed and a context map is created based on regression data. The context map determines various sets of input and output pairs that are particularly useful in reaching the objective (with green), pairs that are layabout for reaching the goal (with orange) or the pairs that hinder the main objective (with red). The next step involves an analysis of the process with respect to the previously defined sets and identifying events. These events will ultimately lead to a new context, with different solution pairs than the previous, which in turn can trigger the computation of a new set of control parameters in order to reach the main objective.

From the control engineering point of view, the natural solution of such context awareness paradigm lies in the event-based control methodology. The system's context is mapped based on some predefined conditions for reaching a certain objective, specific to the controlled process.

Even if traditional sampled data control, known as Riemann sampling, is the standard tool for implementing computer control, there are severe difficulties when dealing with systems having multiple sampling rates or systems with distributed computing [104]. With multi-rate sampling, the

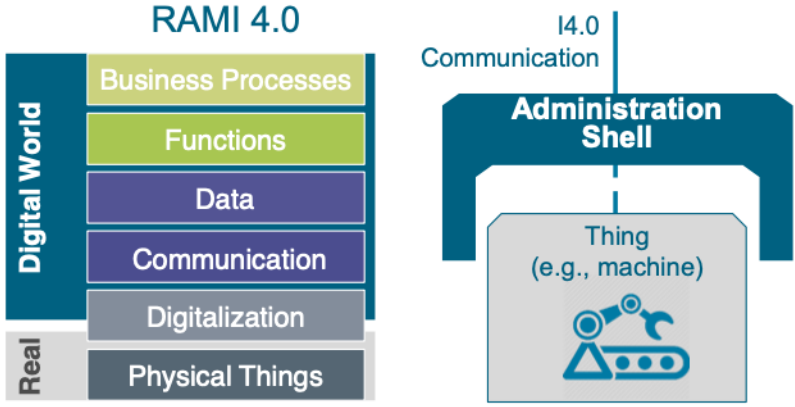

Figure 4.2: RAMI4.0 layered architecture and element integration via the administration shell [103], https://www.flandersmake.be/en/news/industry-40-report

complexity of the system depends critically on the ratio of the sampling rates. For distributed systems, the theory requires that the clocks are synchronized. However, in networked distributed systems, current research revolves around solving problems such as sampling jitter, lost samples and delays on computer controlled systems [105]. Event based sampling, also known as Lebesgue sampling, is a context aware alternative to periodic sampling [106]. Signals are then sampled only when significant events occurs, such as when a measured signal exceeds a limit or when an encoder signal changes. Event based control has many conceptual advantages. Control is not executed unless it is required, control by exception. For a camera based sensor it could be natural to read off the signal when sufficient exposure is obtained. Event based control is also useful in situations when control actions are expensive, for example when controlling manufacturing complexes, and when when it is expensive to acquire information like in computer networks [97, 107].

As with any novel concept, very little theory is available. All sampled systems, periodic as well as event based, share a common property that the feedback is intermittent and that control is open loop between the samples. After an event, the control signal is generated in an open loop manner and applied to the process. In traditional sampled-data theory the control signal is simply kept constant between the sampling instants, a scheme that is commonly called a zero order hold (ZOH). In event based systems, the generation of the open loop signal is an important issue and the properties of the closed loop system depends critically on how the signal is generated [107]. There has not been much development of theory

for systems with event based control, compared to the widely available strategies developed for periodic sampled control [108, 109].

Mathematical analysis related to the efficiency of the Lebesgue sampling algorithms has been realized by [107]. The study compares the performance of Riemann sampling to event based sampling and shows that the latter gives a better performance, even if the variable sampling theory is still in its infancy.

Successful industrial event based applications have been reported during recent years in works such as [92, 110, 111] spanning on a manifold of industrial processes from the simple tank level control [112] to microalgae cultures in industrial reactors [113, 114].

Event-based or event-driven control is a strategy based on variable sampling of the control action. The concept is best explained in contrast to the classical, non-event based, discrete-time implementation. The latter implies the realization of the discrete-time controller using a control signal computed every T_s seconds, without exceptions. For step references, the control signal varies while the system is in the transient regime, afterwards the control variable is constant for most processes. The only exception to this is the presence of unwanted disturbances, when the control action tries to bring the system back to the steady-state regime. Hence, the control variable changes during the transient regime until the process variable reaches the desired reference or when rejecting disturbances, while for the other time slots it is constant. However, discrete-time control implementations compute a new value for the control signal every T_s seconds. From a computational point of view, the approach is inefficient and that the control effort can be reduced to the periods of time when the process variable is outside the steady-state boundaries. The efficiency problem is solved in an elegant manner by the introduction of event-based control approaches that allow the computation of a new control signal with variable sampling, removing the burden on the controlling board/circuitry for unnecessary computations. This is of particular interest in autonomous systems, which have limited energy resources (battery).

Event-based control introduces multiple benefits such as CPU resource optimization by limiting the number of times the control signal is computed. This allows the sharing of the CPU with other processes in distributed architectures and also improves energy efficiency in a control scheme [92, 115].

Another trend in industrial control [98] is industrial cloud computing. The concept externalizes the process computer to a cloud-based implementation. For complex control necessities, the control signal can be computed into the cloud by a powerful computer, shared with other processes. This approach reduces the cost and removes the necessity of powerful process computers. Event-based strategies are useful in this scenario through the reduced bandwidth allocation [98, 116].

4.3 Event-Based Control Principles

A schematic of the event-based implementation concept is presented in Fig. 4.3.

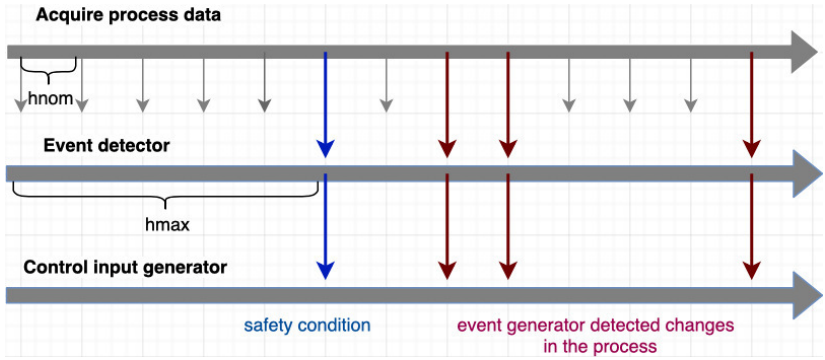

Figure 4.3: Basic operating principles of event based control implementation

The process data is acquired with the sampling time h_{nom}, which is a constant value, chosen in a similar fashion as the sampling period in classical discrete-time implementations. The data is transferred into the *event detector*, which as the task to determine whether or not to trigger an event. The event detector can be customized with any rule that optimizes the control process [117, 118].

One of the most popular event triggering rule is focused on the error variation between a predefined interval $[-\Delta_e \ \Delta_e]$:

$$|e(t) - e(t - h_{act})| \geq \Delta_e, \tag{4.1}$$

where h_{act} is the elapsed time since the triggering of the previous event, $e(t - h_{act})$ is the error at the previous event triggering moment and $e(t)$ is the error at the current moment. Note that the error signal at the present moment t is computed using $e(t) = Y(t) - Y_{sp}(t)$, where $Y(t)$ is the current process variable and $Y_{sp}(t)$ is the setpoint value.

Another popular event detection condition is the maximum allowed time between two consecutive events, known throughout literature as the safety condition. The maximum time is denoted by h_{max}, while the elapsed time since the previous event is h_{act} [119]. The safety condition can be expressed as:

$$h_{act} \geq h_{max}. \tag{4.2}$$

The triggering of an event employs the *control input generator* to compute a new value for the control signal. The control input generator encapsulates the chosen method to solve the control task. Since the action of the event-based implementation is triggered with a variable sampling

h_{act}, the controller should be a discrete-time representation and the sampling time parameter for the discretization must be a variable parameter in the event-based implementation.

As such, the challenge one needs to overcome is the variable sampling while extending the event-based control strategy to the fractional order control domain.

4.4 Event-Based Integer Order Control

Let us first consider a standard case of event-based control. A brief example of the discrete-time model of the controller inside the control input generator is given for the integer order PID controller. The transfer function is provided in equation (2.17) for the particular case of $\lambda = \mu = 1$. The PID control signal in the Laplace domain can be computed using:

$$U(s) = k_p(Y_{sp}(s) - Y(s)) + \frac{k_p k_i}{s}(Y_{sp}(s) - Y(s)) + k_p k_d s(Y_{sp}(s) - Y(s)). \tag{4.3}$$

Denoting $e(t) = Y_{sp}(t) - Y(t)$ and splitting the control law into three individual signals : proportional $u_p(s)$, integral $u_i(s)$ and derivative $u_d(s)$ gives:

$$\begin{aligned} u_p(s) &= k_p e(s), \\ u_i(s) &= \frac{k_i}{s} e(s), \\ u_d(s) &= k_p k_d \ s \ e(s). \end{aligned} \tag{4.4}$$

The discrete-time PID control law can be computed as the sum of the three individual signals into their discrete-time approximation. Using the Tustin method from equation (4.6) where $\alpha = 1$ and replacing $s = \frac{2}{h_{act}} \frac{1-z^{-1}}{1+z^{-1}}$ in the individual components from equation (4.4) gives:

$$\begin{aligned} u_p(k) &= k_p e(k), \\ u_i(k) &= h_{act} \frac{k_i}{2} \left(e(k) + e(k-1)\right) + u_i(k-1), \\ u_d(k) &= \frac{1}{h_{act}} 2k_d \left(e(k) - e(k-1)\right) - u_d(k-1). \end{aligned} \tag{4.5}$$

where $u_i(k-1)$ is the previously computed integral component and $u_d(k-1)$ is the previous derivative component. Notice that in this context, a *previous computation* refers to the moment of the last recorded event. Note also that the discrete sampling time T_s has been replaced by h_{act} which is the variable sampling time.

Hence, the set of variables in equation (4.5) gives the control values of the PID controller with variable sampling time. In a similar rationale, other controllers such as the integer order IMC can be discretized and

implemented inside the control input generator, as long as the sampling time is kept as a time varying variable. In addition, the discretization method is not limited to Tustin, any viable discrete-time mapper can be used.

4.5 Event-Based Fractional Order Control

4.5.1 Direct Discrete-Time Mappers

Analog implementation possibilities of this type of control are scarcely available, most of them based on *fractance* circuits [120]. Continuous controller implementation requires electronic components that are mostly suitable for integer order transfer functions. Some works such as [121, 122, 123, 124] tackle analog fractional devices using electronic systems. However, these devices are difficult to tune and also provide some physical restrictions.

An broadly used method to implement a fractional order controller is to approximate it using finite-dimensional integer-order transfer functions. The aim of this approach is to capture the effects of fractional order operators through integer order transfer functions, both in the continuous and discrete-time domains. The aim on this section is to discuss the discrete-time representation of the fractional operator. A manifold of discrete-time approximations have been studied among the years. These can be classified into indirect and direct discrete-time mappers [125, 126, 127].

Indirect discrete-time fractional order approximations are those methods that describe the dynamics of a fractional operator through high-order integer transfer functions in the Laplace domain [20,128,129]. This is a solution based on the mathematical development that distributed parameter system representations lead to the appearance of fractional orders in the lumped parameterization models [130]. The fractional dynamics are captured through the usage of high order transfer functions, that are further discretized using already available integer order discrete-time mappers. A wide variety of approximation methods are available, providing reliability through certain aspects, such as Continued Fraction Approximations, Oustaloup Filter Approximation, Modified Oustaloup Filter, etc. Recalling here the concepts introduced in Chapter 2, the Laplace representation of the fractional-order operator s^{α} is a straight line in both magnitude and phase plots. A finite order filter that fits the infinitely straight line is impossible. However, it is possible to approximate it over a limited interval of frequency range (ω_b, ω_h) [131, 132].

By contrast, *direct* discrete-time mappers use a single step approximation to map the fractional differ-integral operation straight to the discrete-time domain [133]. Recent studies introduce several approaches

such as frequency fitting of the discrete-time model to the response of the fractional order term [132, 134]. The recursion based formulas proposed in [135] provide two direct discrete-time mappers relevant for the present study. They are based on the Tustin formula as the generating function with a sampling time T_s:

$$s^\alpha \approx \left(\frac{2}{T_s}\frac{1-z^{-1}}{1+z^{-1}}\right)^\alpha. \tag{4.6}$$

The first mapper is based on the Muir recursion scheme [136]. For a positive order of differ-integration, $\alpha > 0$, the formula is first introduced in [135]:

$$s^\alpha = \left(\frac{2}{T_s}\right)^\alpha \left(\frac{1-z^{-1}}{1+z^{-1}}\right)^\alpha = \left(\frac{2}{T_s}\right)^\alpha \lim_{n\to\infty} \frac{A_n(z^{-1},\alpha)}{A_n(z^{-1},-\alpha)}, \tag{4.7}$$

where $A_n(z^{-1},\alpha)$ is a polynomial computed with:

$$\begin{aligned} &A_0(z^{-1},\alpha) = 1, \\ &A_n(z^{-1},\alpha) = A_{n-1}(z^{-1},\alpha) - c^n z^n A_n(z^{-1},\alpha) \end{aligned} \tag{4.8}$$

and $c_n = \frac{\alpha}{n}$ for odd values of n, or $c_n = 0$ for even values of $n \in \mathbb{N}$. Equation (4.8) computes the fifth order polynomial $A_5(z^{-1},\alpha)$ through:

$$\begin{aligned} A_5(z^{-1},\alpha) = &-\frac{1}{5}\alpha z^{-5} + \frac{1}{5}\alpha^2 z^{-4} - \left(\frac{1}{3}\alpha + \frac{1}{15}\alpha^3\right) z^3 + \\ &+ \frac{2}{5}\alpha^2 z^{-2} - \alpha z^{-1} + 1. \end{aligned} \tag{4.9}$$

The second direct mapper of interest throughout this study is the Continued Fraction Expansion (CFE) of the Tustin formula proposed in [135]:

$$s^\alpha = \left(\frac{2}{T_s}\right)^\alpha CFE\left\{\left(\frac{1-z^{-1}}{1+z^{-1}}\right)^\alpha\right\}_{p,q} = \left(\frac{2}{T_s}\right)^\alpha \frac{P_p(z^{-1})}{Q_q(z^{-1})}, \tag{4.10}$$

where *CFE* denotes the function generated by applying the Continued Fraction Expansion, p and q are the orders of approximation, while $P_p(z^{-1})$ and $Q_q(z^{-1})$ are polynomials in the z^{-1} variable. For $p = q = 5$, the fifth order polynomials needed by the CFE approximation are computed as:

$$\begin{aligned} P_5(z^{-1}) = &(-\alpha^5 + 20\alpha^3 - 64\alpha)z^{-5} + (-195\alpha^2 + 15\alpha^4 + 225)z^{-4} + \\ &+ (-105\alpha^3 + 735\alpha)z^{-3} + (420\alpha^2 - 1050)z^{-2} - 945\alpha z^{-1} + 945, \\ Q_5(z^{-1}) = &(\alpha^5 - 20\alpha^3 + 64\alpha)z^{-5} + (-195\alpha^2 + 15\alpha^4 + 225)z^{-4} + \\ &+ (105\alpha^3 - 735\alpha)z^{-3} + (420\alpha^2 - 1050)z^{-2} + 945\alpha z^{-1} + 945. \end{aligned} \tag{4.11}$$

The fifth order discrete time approximations from equations (4.7) and (4.10) based on the integer order Tustin formula should be sufficient for most applications. These approximations will be used further to directly map the fractional order s^{α} into the discrete-time domain with the purpose of creating the event-based fractional order control theory.

The reason for choosing these direct mappers is the ability to isolate T_s from the fixed polynomials generated by the discrete-time mappers, which allows the event-based FOPID implementation with a variable sampling time. CFE can be applied to any generating function (Euler, Al-Alaoui, Tustin, Simpson, etc.) to approximate FOPID controllers if T_s can be isolated. However, discretization by Muir recursion has been developed only for usage with the Tustin generating function. The numerical examples presented in this implement both Muir and CFE direct mappers. The Tustin formula is also selected for CFE in order to accurately compare the performance obtained by the two mappers. Good results can also be obtained through different CFE generating functions, the methodology and implementation strategy remains stays the same, but the polynomials from equation (4.10) will differ.

4.5.2 Implementation Methodology

The theoretical contribution of the present study is the generalization of the available event-based control strategy into the fractional order field. The challenge lies in the isolation of the sampling time and introducing its variability in the fractional order discrete-time approximation. Hitherto, no specialized literature reports are available to explore the possibility of implementing fractional order controllers in the control input generator.

The proposed development of the discrete fractional order control actions is based on fractional order direct discrete-time mappers. Both the Muir recursive and CFE discrete-time approximations from equations (4.7) and (4.10) will be used hereafter, with the end goal to claim that any direct mapper whose sampling time can be isolated from the rest of the function can be successfully used in fractional order event-based implementations.

The event-based implementation of the fractional order PID controller from (2.17) with $\lambda, \mu \in (0, 1)$ will be exemplified further. Given the versatility of the proposed approach, any fractional order controller can be discretized and implemented in the fractional order control signal generator.

Similarly to the classical integer order PID control action from equation (4.5), the fractional order control law can also be written as a sum of the three individual components as $U_f(s) = u_{fp}(s) + u_{fi}(s) + u_{fd}(s)$, with $u_{fp}(s)$, $u_{fi}(s)$ and $u_{fd}(s)$ being the proportional, integer and derivative

fractional order control signals. Hence, generalizing equation (4.4) gives:

$$\begin{aligned} u_{fp}(s) &= k_p e(s), \\ u_{fi}(s) &= \frac{k_p \cdot k_i}{s^\lambda} e(s), \\ u_{fd}(s) &= k_p \cdot k_d \; s^\mu \; e(s). \end{aligned} \tag{4.12}$$

Both aforementioned direct discrete-time approximations approximate the fractional order term s^α to a transfer function of the form:

$$s^\alpha \approx \left(\frac{2}{T_s}\right)^\alpha \frac{a_n z^{-n} + a_{n-1} z^{-n+1} + ... + a_0}{b_n z^{-n} + b_{n-1} z^{-n+1} + ... + b_0} = \left(\frac{2}{T_s}\right)^\alpha \frac{N_n(z^{-1})}{D_n(z^{-1})}. \tag{4.13}$$

Mapping of s^α employs the polynomials:

- $N_n(z^{-1}) = A_n(z^{-1}, \alpha)$ and $D_n(z^{-1}) = A_n(z^{-1}, -\alpha)$, for the Muir recursion method, and
- $N_n(z^{-1}) = P_n(\alpha)$ and $D_n(z^{-1}) = Q_n(\alpha)$, for the CFE method.

Notice that in 4.13 the sampling time has been isolated from the rest of the model and from this point it is possible to be treated as a variable in the event-based implementation. The polynomials $N_n(z^{-1})$ and $D_n(z^{-1})$ need to be computed only once, as they remain unchanged for every iteration through the control signal generator.

Furthermore, the fractional order terms will be treated separately and approximated to the discrete-time domain using the generalized formula from (4.13). The fractional order proportional component is identical to the integer-order PID proportional term since it does not introduce any fractional order operation:

$$u_{fp}(k) = k_p e(k). \tag{4.14}$$

The fractional order integral term can be rewritten $\frac{1}{s^\lambda} = \frac{s^{1-\lambda}}{s}$ such that the direct discretization of s^α respects the $\alpha > 0$ condition. It follows that the discrete-time transfer function of the fractional order integral component can be computed using the Tustin formula for the $\frac{1}{s}$ term and a direct n^{th} discrete-time formula for the $s^{1-\lambda}$ term, where $1 - \lambda > 0$, $\lambda \in (0, 1)$:

$$\frac{1}{s^\lambda} = \frac{1}{s} s^{1-\lambda} = \frac{T_s}{2} \frac{1 + z^{-1}}{1 - z^{-1}} \left(\frac{2}{T_s}\right)^{1-\lambda} \frac{N_n(z^{-1})}{D_n(z^{-1})}. \tag{4.15}$$

After expanding equation (4.15), the recurrence formula of the fractional

order integral component is obtained:

$$\begin{aligned} u_{fi}(k) &= \left(\frac{2}{h_{act}}\right)^{-\lambda} \frac{k_p k_i}{d_0}\mathcal{E}_{fi_n}(k) - \frac{1}{d_0}\mathcal{U}_{fi_n}(k), \\ \mathcal{E}_{fi_n}(k) &= n_0 e(k) + (n_0+n_1)e(k-1) + (n_1+n_2)e(k-2) + \\ &\quad + ... + (n_{n-1}+n_n)e(k-n) + n_n e(k-(n+1)), \\ \mathcal{U}_{fi_n}(k) &= (d_1-d_0)u_{fi}(k-1) + (d_2-d_1)u_{fi}(k-2) + \\ &\quad + ... + (d_n-d_{n-1})u_{fi}(k-n) - d_n u_{fi}(k-(n+1)), \end{aligned} \tag{4.16}$$

where $e(k-n)$ denotes the previous n^{th} error signal and $u_{fi_n}(k-n)$ denotes the previous n^{th} fractional order integral control action.

The fractional order derivative component is obtained by directly replacing s^μ, $\mu \in (0,1)$ with any direct discrete-time mapper:

$$\begin{aligned} u_{fd}(k) &= \left(\frac{2}{h_{act}}\right)^{\mu} \frac{k_p T_d}{d_0}\mathcal{E}_{fd_n}(k) - \frac{1}{d_0}\mathcal{U}_{fd_n}(k), \\ \mathcal{E}_{fd_n}(k) &= n_0 e(k) + n_1 e(k-1) + ... + n_n e(k-n), \\ \mathcal{U}_{fd_n}(k) &= d_1 u_{fd}(k-1) + d_2 u_{fd}(k-2) + ... + d_n u_{fd}(k-n), \end{aligned} \tag{4.17}$$

where $e(k-n)$ denotes the previous n^{th} error value and $u_{fd}(k-n)$ is the previous n^{th} fractional order derivative control value.

The fractional order PID exemplified in this section stands as a basis to any fractional order event based implementation. For example, for a fractional order IMC implementation, a similar approach can be employed.

Another important aspect in this proposed approach is that it allows the actual tuning of the fractional order controller to be a completely independent process from the event-based implementation. In other words, any fractional order controller can be tuned using any available method. The present algorithm completes the fractional order controller's implementation by offering a direct discretization possibility and a fractional order event based implementation. The controller should be tuned accordingly, by imposing any performance specification as for a non-event based implementation [137, 138, 139].

4.5.3 General Guidelines

In an event-based control implementation, some parameter selection is required, apart from determining the direct discrete-time transfer function of the fractional order operators. The parameters need to be customized as a function of process properties, and are: the nominal sampling time h_{nom}, the maximum allowed time between two consecutive events h_{max} and the error variation threshold Δ_e. The other parameters of the event-based implementation are purely implementation variables, independent of the process. For a correct and efficient execution, it is crucial that the

parameters are used correctly inside the event detector and the control input generator. Table 1 provides an overview of the parameters as well as some brief descriptions.

The nominal sampling time choice h_{nom} is identical to the sampling time in any discrete-time implementation, based on Shannon's theorem.

The maximum allowed time between events is denoted through h_{max}, which is a multiple of h_{nom}. This is effective in implementing the safety condition. Choosing $h_{nom} = h_{max}$ in an event-based implementation leads to a pure discrete-time effect, thus eliminating all the benefits brought by the event-based approach. Hence, h_{max} should always be greater than h_{nom}. In fact, the greater the value, the better the control signal computation is optimized, especially in the steady state regime. However, special attention should be given when choosing a value for this parameter such that the safety condition is not completely eliminated. As a starting point, one could select a h_{max} based on the dominant time constants of the process. Trial and error is also a viable option, but alternatively, optimization schemes could be used if a objective function is defined.

The previous error value is denoted by e_s in the available event-based literature [119]. Note that this error cannot include any weighting factor, unlike the error values used to compute the fractional order proportional and derivative gains, respectively. The e_s variable stores the error value at the previous detected event. This value is updated for every iteration of the control input generator. The value of e_s is used inside the event detector to check if an event should be triggered due to the error variation. The condition is usually written as $(e(k) - e_s) \in [-\Delta_e, \Delta_e]$. The $[-\Delta_e, \Delta_e]$ interval is composed by a predefined maximum error threshold. As a guideline, Δ_e should be chosen as a small percentage, usually between 1-5% to the desired setpoint value.

The parameter h_{act} is a variable that stores the actual time elapsed since the previous event. The value should be updated every h_{nom} seconds whether an event is triggered or not. The formula that increments h_{act} can be written as $h_{act} = h_{act} + h_{nom}$, making h_{act} another multiple of h_{nom}. Note that h_{act} should be reset to 0 at the triggering of an event. The purpose of h_{act} is to determine if the safety condition is met.

An overview of the event detector and control signal generator is given in the algorithms hereafter.

Table 4.1: Event-based implementation parameters

Parameter	Type	Description
h_{nom}	custom	nominal sampling time
h_{max}	custom	safety condition trigger time
Δ_e	custom	maximum error variation
h_{act}	variable	time since the previous event
e_s	variable	previous error value

Algorithm 1: The fractional order control input generator

Result: The control signal u

Data: $ni_0, ni_1, ..., ni_n, di_0, di_1, ..., di_n, nd_0, nd_1, ..., nd_n, dd_0, dd_1, ..., di_n$

$e = Y_{sp} - Y$

`/* compute the fractional order proportional component */`

$u_{fp} = kp * e$

`/* compute the fractional order integral component */`

$a = k_p * k_i * pow(2/hact, -\lambda)$

$u_{fi} = 1/d_0 * (a * (ni_0 * e + (ni_0 + ni_1) * ei_1 + ... + (ni_{n-1} + ni_n) * ei_n + ni_n * ei_{n+1}) - ((di_1 - di_0) * ui_1 + (di_2 - di_1) * ui_2 + ... + (di_n - di_{n-1}) * ui_n - di_n * ui_{n+1}))$

$ei_{n+1} = ei_n; ei_n = ei_{n-1}; ...ei_1 = e$

$ui_{n+1} = ui_n; ui_n = ui_{n-1}; ...ui_1 = u_{fi}$

`/* compute the fractional order derivative component */`

$b = kp * kd * pow(2/hact, \mu)$

$u_{fd} = 1/dd_0 * (b * (nd_0 * e + nd_1 * ed_1 + ... + nd_n * ed_n) - (dd_1 * ud_1 + dd2 * ud_2 + ...dd_n * ud_n))$

$ed_n = ed_{n-1}; ...ed_1 = e$

$ud_n = ud_{n-1}; ...ud_1 = u_{fd}$

`/* compute the entire fractional order control signal */`

$u = u_{fp} + u_{fi} + u_{fd}$

Algorithm 2: The event detector

Result: The control signal u
Data: k_p, k_i, k_d, λ, μ, h_{nom}, h_{act}, Δ_e, Y_{sp}
$h_{act} = 0$
$e_s = Y_{sp}$

while *simulation ongoing* **do**
    read process value Y
    e = Y_{sp} - Y

    if *(*$|e - e_s| > \Delta_e$ *or* $h_{act} \geq h_{max}$*)* **then**
        u = `control_input_generator`(Y_{sp}, Y) $h_{act} = 0$
        $e_s = e$

4.5.4 Numerical Validation

In this section, the proposed event-based fractional order strategy is validated using numerical simulations targeting a wide range of processes from the simple FOPDT to a complex fractional order transfer function. The strategy is validated using fractional order PID controller case study. The case studies are intended to show the fractional order control versatility of the proposed methodology as well as to analyze its efficacy for a class of relevant process types from real life applications.

All controllers employed in the numerical examples hereafter have been previously tuned using different fractional order methodologies such as frequency domain specifications or experimental procedures. As mentioned before, the tuning method is independent from the event-based part of the execution. Hence, the tuning procedure of each controller is irrelevant in proving the efficacy of the event based fractional order implementation and it will not be detailed here.

Both the Muir and CFE discrete-time approximations are tested with identical event-based implementation parameters in order to show the validity of any direct mapper for the present strategy and to asses the best suited discrete-time mapper for every example.

Three implementation scenarios are performed and analyzed for every numerical example. The first test case analyzes the performance of the closed loop system obtained with the fractional order controller for a pure discrete-time implementation with the Muir recurrence-based direct discrete-time mapper from equation (4.7) and the CFE direct discrete-time mapper from (4.10). The test scenario validates the discrete-time fractional order controller on the selected process. The second and third test cases validate the proposed event-based fractional order control strategy, focusing on comparing the pure discrete-time realization of the fractional order controller to its event-based implementation.

4.5.4.1 First Order Plus Dead Time

For the first order plus dead time (FOPDT) model defined by the transfer function model:

$$H(s) = \frac{1}{4s+1}e^{-s} \tag{4.18}$$

a fractional order PI controller is computed by imposing a set of frequency domain specifications targeting the gain crossover frequency $w_{gc} = 0.2rad/s$, the phase margin $\phi_m = 44^\circ$ and a certain degree of robustness to gain variations. The resulted controller that meets these frequency domain constraints is given by the fractional order transfer function model:

$$C(s) = 0.0021\left(1 + \frac{162.6923}{s^{0.833}}\right). \tag{4.19}$$

The Muir and CFE 5^{th} order discrete-time mappers from equations (4.9) and (4.11) are used to compute the discrete-time approximation of the fractional order PI controller. The same sampling time $T_s = 0.001$ seconds is used for both discretizations. The pure discrete-time implementation of the closed loop with every discrete-time controller is presented in Fig. 4.4a. Notice that the Muir and CFE approximations lead to a similar closed-loop system response.

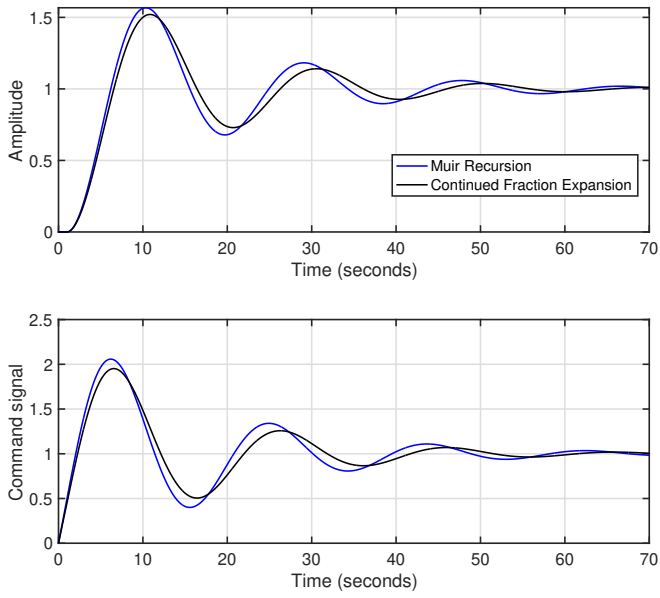

(a) Discrete-time controller validation on the FOPDT process for a unit step reference

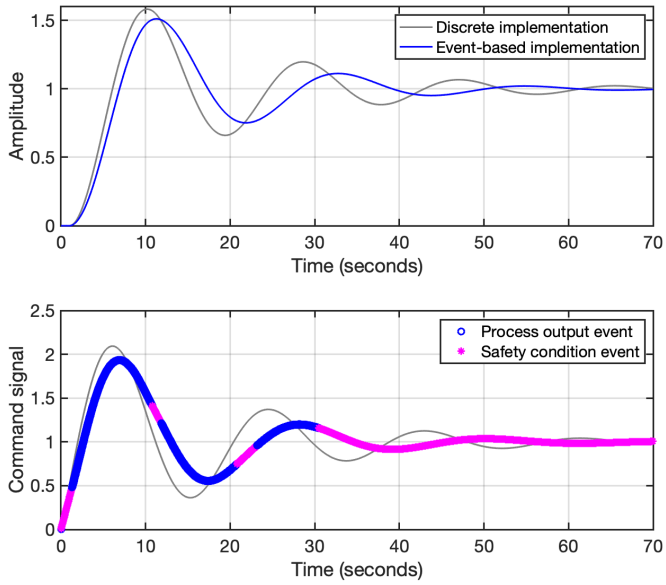

(b) Event-based fractional order PI implementation based on the Muir recursion

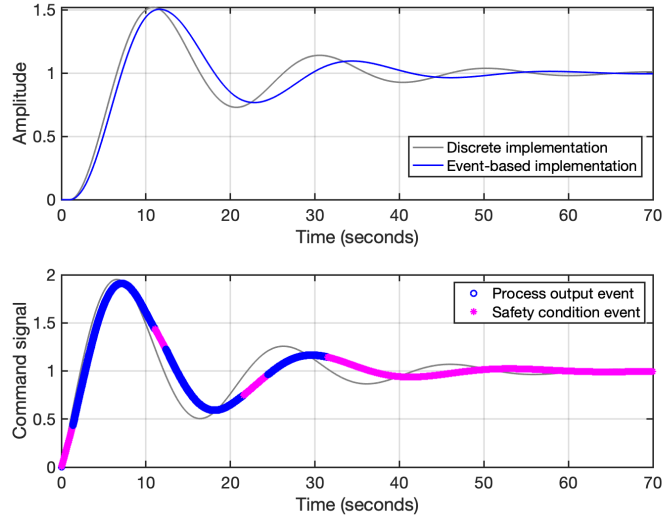

(c) Event-based fractional order PI implementation based on the CFE recursion

Figure 4.4: A fractional order PI controller applied to a FOPDT process

The event-based fractional order PI implementation based on the Muir scheme is shown in Fig. 4.4b, while the CFE approximation is given in Fig. 4.4c, respectively. The nominal sampling time is chosen such as $h_{nom} = T_s = 0.001$ seconds and the safety condition time as $h_{max} = 0.02$ seconds, i.e. manifold 20 times larger than h_{nom}, while the error threshold is set as $\Delta_e = 0.0005$. The other parameters are identical for both the Muir and CFE implementations. The simulation results clearly show the cause of the control signal computations. It can be seen that in the transient response, the error triggered control prevails, whereas the safety condition is employed mostly in the steady-state regime. Hence, both event-based fractional order implementations can be successfully used on the FOPDT process.

However, one can still make a comparison in terms of computational effort among these methods. During the 70 seconds duration of the simulation tests, the Muir based controller triggers a new computation of the control signal 5824 times, the CFE controller 6508 times. In a classical, discrete-time implementation, a new control values is computed at every sampling time. For the present example, a classical controller would compute the control signal 70000 times in 70 seconds. The computational improvement brought by the event based approach is clear.

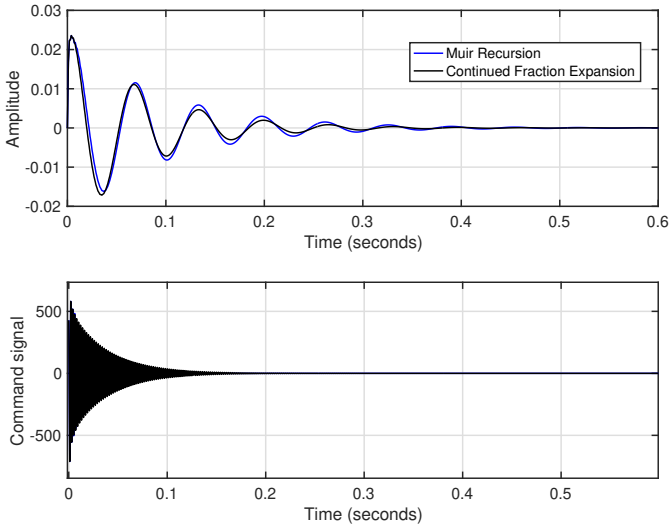

(a) Impulse response of the closed-loop SOTF system with the discrete-time controller implementation

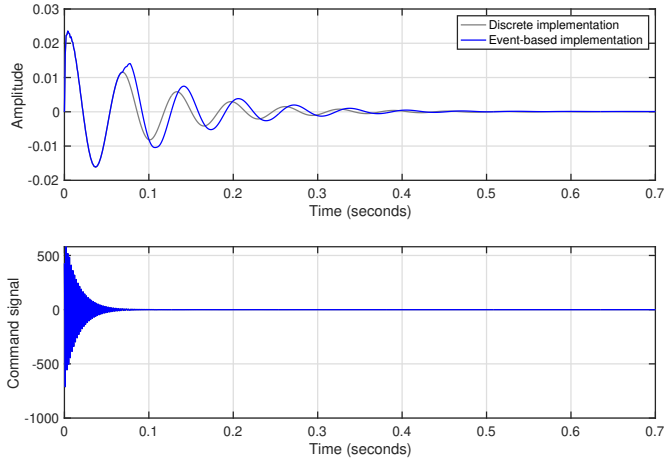

(b) Event-based fractional order PID implementation based on the Muir recursion

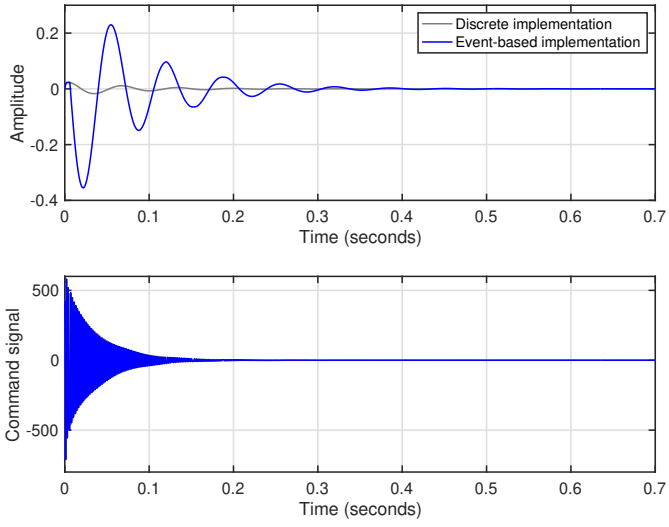

(c) Event-based fractional order PID implementation based on the CFE recursion

Figure 4.5: A fractional order PID controller applied to a SOTF process

4.5.4.2 Second Order Transfer Function

The second order transfer function (SOTF) chosen as the second numerical example:

$$H(s) = \frac{78.35}{s^2 + 1.221s + 822} \tag{4.20}$$

represents the oscillatory dynamics of a real life flexible beam [140]. For the SOTF process a fractional order PID controller is tuned in [140] using an experimental optimization procedure. The obtained controller is defined by the transfer function model:

$$C(s) = 0.0288 \left(1 + \frac{3.4722}{s^{0.1039}} + 28.743 s^{0.822}\right). \tag{4.21}$$

Fig. 4.5a illustrates the impulse response of the SOTF process with the classical discrete-time implementation of the fractional order PID controller with $T_s = 0.001$ seconds. Again, the dynamics of the output variable are similar for both approaches.

Fig 4.5b shows the event-based fractional order PID controller discretized using the Muir recursion formula. The output of the closed loop system with the event-based controller is similar to the non-event-based Muir controller. The implementation parameters are chosen as follows: $h_{nom} = T_s = 0.001$ seconds, $h_{max} = 0.005$ seconds and $\Delta_e = 10^{-4}$. The error threshold is chosen based on the amplitude of the closed-loop system response from Fig. 4.5a. The CFE event-based implementation is depicted in Fig. 4.5c. The process stabilizes with the same settling time as the Muir scenario.

From the control effort perspective, the Muir mapper computes the control signal value 368 times, the CFE controller 494 times, while the classical discrete-time controller command is evaluated 700 times for the total simulation time of 0.7 seconds in which the tests were performed. It can be stated that for this numerical example, the Muir based controller is the better choice both from the performance and the control optimization criteria.

4.5.4.3 Second Order Plus Time Delay

In this case, consider the model:

$$H(s) = \frac{22.24}{s^2 + 0.6934s + 5.244} e^{-0.8s}. \tag{4.22}$$

The same tuning methodology as for the FOPDT numerical example is employed which tunes a robust fractional order PI controller that offers an open-loop system with a gain crossover frequency $\omega_{gc} = 0.4 rad/s$ and a phase margin $\phi_m = 75°$:

$$C(s) = 0.0422 \left(1 + \frac{492.2867}{s^{0.9288}}\right). \tag{4.23}$$

Additional details regarding the real-life process and the control strategy can be found in [62].

Fig. 4.6a provides the closed-loop system response with the discrete-time Muir mapper and the CFE direct approximation using the sampling time $T_s = 0.005$ seconds. It can be observed that the dynamics of the closed-loop system are similar for the classical implementation of the controllers.

The implementation settings of the event-based fractional order controller are $h_{nom} = T_s = 0.005$ seconds, $h_{max} = 0.2$ seconds and $\Delta_e = 0.01$ representing the 1% interval of the unit step reference value.

The closed-loop response of the event-based fractional order PI controller approximated using the 5^{th} order Muir recursion from equation (4.9) is depicted in Fig. 4.6b. In the command signal plot one may observe the different types of events triggered to compute the control value. The error threshold events are more prominent during the transient response, while the safety condition triggers the control value computation mostly in the steady-state regime. The results indicate that the event-based implementation obtains similar closed-loop system performance as the classical implementation.

Furthermore, Fig. 4.6c shows the closed loop response of the event-based controller with the CFE approximation. The system reaches its steady-state value with the same sampling time as in the Muir approximation from Fig. 4.6b. However, the amplitude is increased by 50% from 1 to approximately 1.5. Since the dynamics of the system with the event-based controller differ from the classical approximation, an in-depth investigation is realized. In Fig. 4.7 the obtained results are given to analyze the effects of the event-based parameters on the system's response.

More restrictive parameters are imposed in order to verify if the event-based strategy is able to obtain a similar result as the one obtained with the Muir recursion. The implementation from Fig. 4.6c uses a h_{max} value which is 20 times greater than the nominal sampling time.

The parameter h_{max} is varied to be 10 times and 5 times greater than $h_{nom} = 0.005$ seconds and the results are given in Fig. 4.7. By lowering h_{max}, the events are triggered faster if the same error threshold is kept. h_{max} is chosen as a multiple of h_{nom}. Choosing $h_{max} = h_{nom}$ gives a pure discrete-time implementation since an event is triggered by the safety condition at every sampling time. Hence, h_{max} should be at least two times larger than h_{nom} for the safety condition to have a real effect. The upper bound of the interval can be chosen with respect to the process' response. For fast processes, the maximum allowed time between two consecutive events should be lower than for slow response processes.

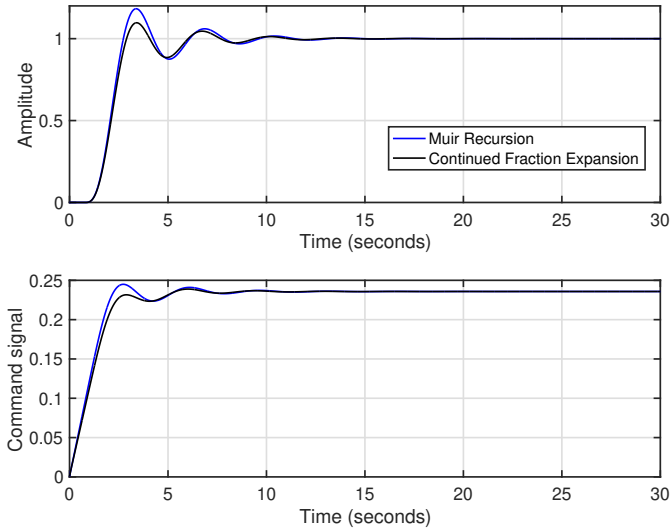

(a) Discrete-time controller validation on the SOPTD process for a unit step reference

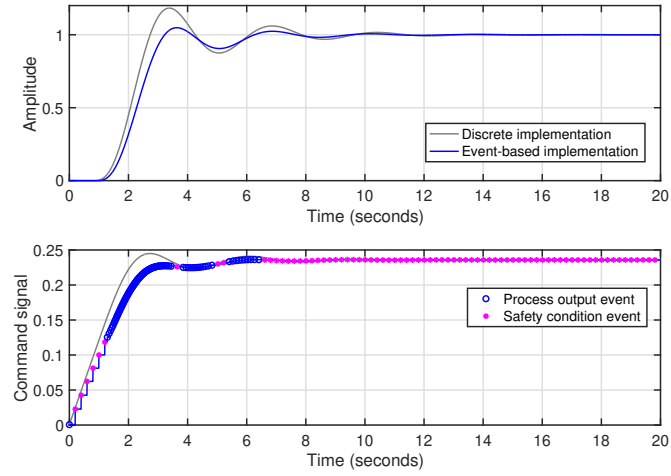

(b) Event-based fractional order PI implementation based on the Muir recursion

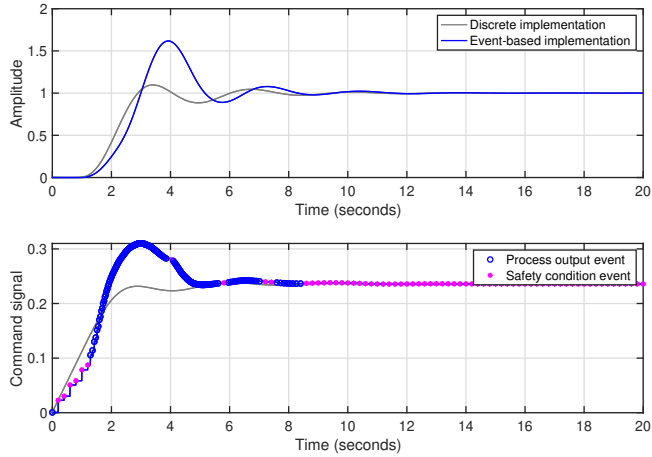

(c) Event-based fractional order PI implementation based on the CFE recursion

Figure 4.6: A fractional order PI controller applied to a SOPTD process

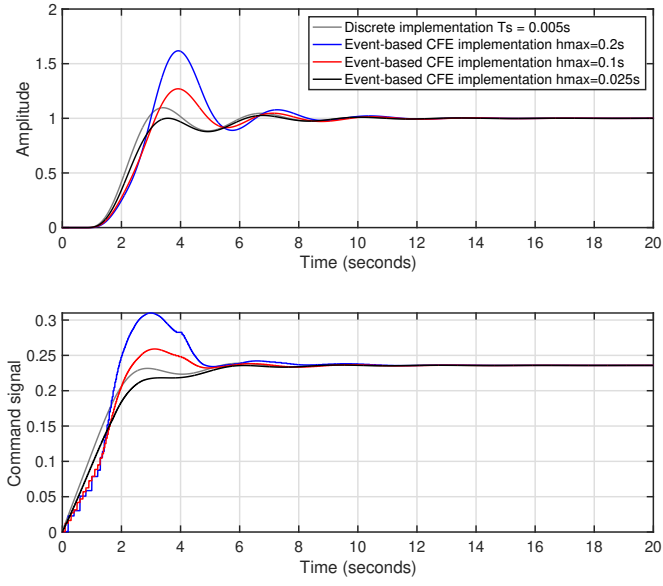

Figure 4.7: Closed-loop system performance analysis for varying parameters of the event-based CFE implementation

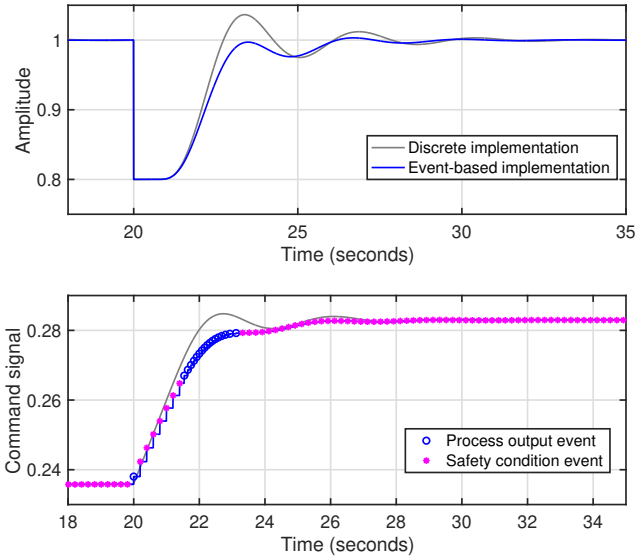

Figure 4.8: Closed-loop system performance analysis for disturbance rejection of the event-based Muir implementation

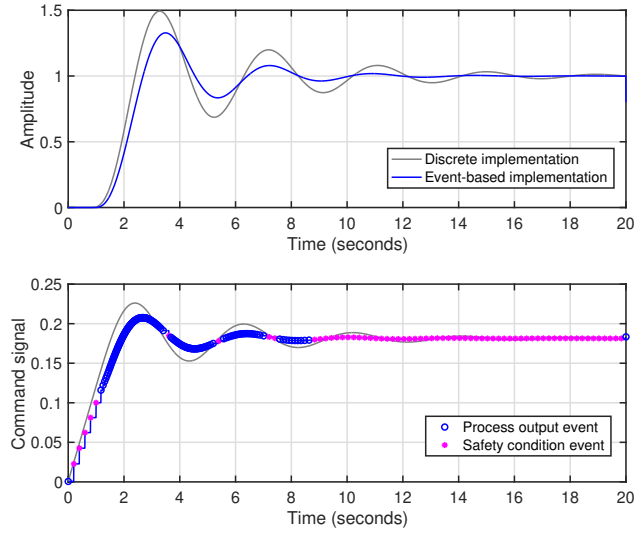

Figure 4.9: Closed-loop system performance analysis for robustness of the event-based Muir implementation

The influence of h_{max} is investigated for the SOPDT process because identical CFE and Muir implementations give different responses. The settling time of the closed loop system response with the pure CFE discrete-time implementation is 8 seconds. For the first case (blue line), h_{max} is 0.2s (20 times greater than hnom), representing 2.5% from the process' settling time. Lowering h_{max} to 1.25% (red line) or 0.31% (black line) from the process settling time gives better results.

It can be concluded that lowering the h_{max} value leads to a better closed loop system response. For the current study case, it can be stated that the Muir approach outperforms the CFE implementation, for the same fractional order event-based parameters.

Currently, there are no specific guidelines available for event-based controllers. In [141], the authors state that one of the most relevant absences in the literature may be that of specific tuning rules. Some authors provide guidelines based on intensive simulations or obtain the controller parameters from tuning rules designed for continuous or discrete standard PID controllers. However, the guidelines are only provided for particular, non-generic architectures. Moreover, event-based PID controllers possess more parameters than their time-triggered counterparts (one or two thresholds, minimum and maximum inter-event times. As a rule of thumb based on the observations on the examples presented in the thesis, h_{max} should not be greater than 10 times the value of h_{nom} for the CFE approximation to yield good results. The Muir approach is more permissive, good results can be obtained with h_{max} up to 20-30 times larger than h_{nom}. When selecting event-based implementation parameters such as h_{max}, several values can be investigated. The ultimate choice is made by the engineer as a trade-off between desired performance and resource optimization.

The validation of the control strategy developed in [62] for the SOPDT experimental platform involves the experimental endorsement of the fractional order PI controller for reference tracking, disturbance rejection and robustness. To further validate the proposed Muir event-based control strategy for the real-life test scenarios, disturbance rejection and robustness assessment are also investigated.

Fig. 4.8 presents the closed loop response of the experimental platform equipped with the event-based fractional order PI controller. An amplitude of 0.2 disturbance, representing 20% from the steady state value, is introduced at moment $t = 20$ seconds. The event-based implementation parameters $h_{nom} = T_s = 0.005$ seconds, $h_{max} = 0.2$ seconds and $\Delta_e = 0.01$ are the same as the ones used in Fig. 4.6. It is observed that the output converges to the desired set point value, while rejecting the disturbance. The event detector generates mostly process output events during the transient regime, which is to be expected from the event based implementation.

Fig. 4.9 targets the validation of the event based fractional order controller in a robustness test scenario. The fractional order controller from

equation (4.23) has been tuned in [62] with respect to the isodamping condition, ensuring a certain degree of robustness of the closed loop system to gain variations. Hence, the gain of the SOPDT process from equation (4.22) is altered by 30% and the response of the closed loop system to a unit step reference is analyzed. The test is identical to the one used to generate Fig. 4.6b, featuring the same event based implementation parameters. Comparing the nominal and the altered process responses, it can be easily observed that the settling time is increased by 40%, (i.e. from 6 to 10 seconds), and the overshoot from about 10% to 40%. However, the event-based fractional order PI controller is very robust, considering the large gain variation.

4.5.4.4 Fractional Order Transfer Function

The last case study is focused on proving the applicability of the proposed event-based strategy to complex fractional order (FOTF) models. The transfer function

$$H(s) = \frac{0.1}{s(0.005682s^{1.7263} + 0.11031s^{0.8682} + 1)} \tag{4.24}$$

describes the braking effect of a non-Newtonian fluid, such as blood, on a transiting submersible.

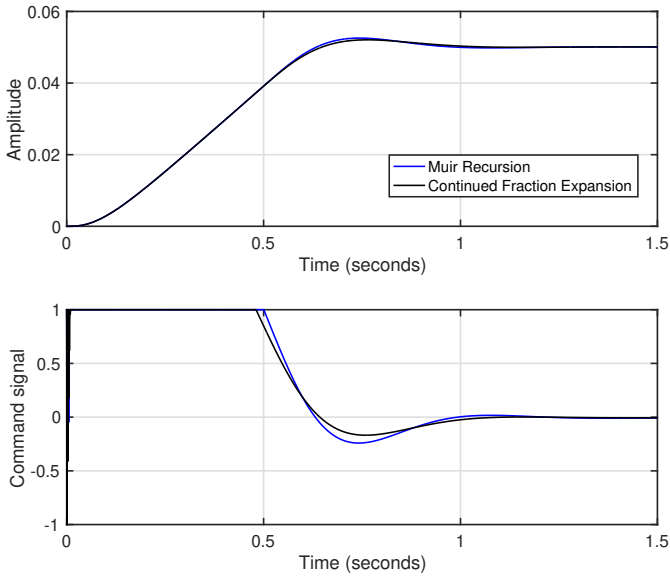

(a) Discrete-time controller validation on the FOTF process for a unit step reference

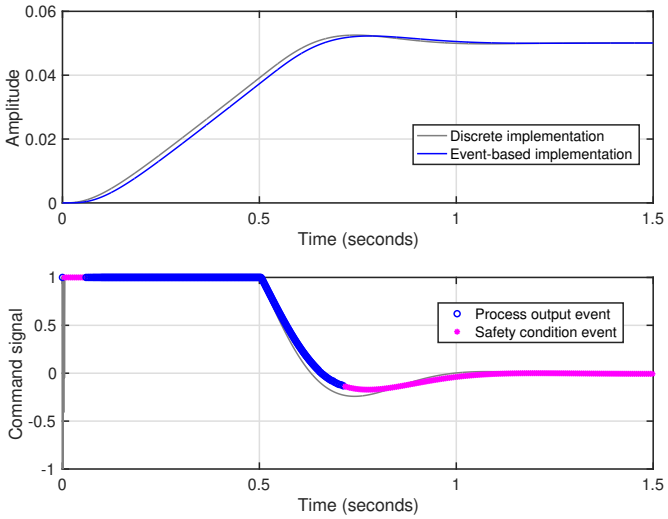

(b) Event-based fractional order PD implementation based on the Muir recursion

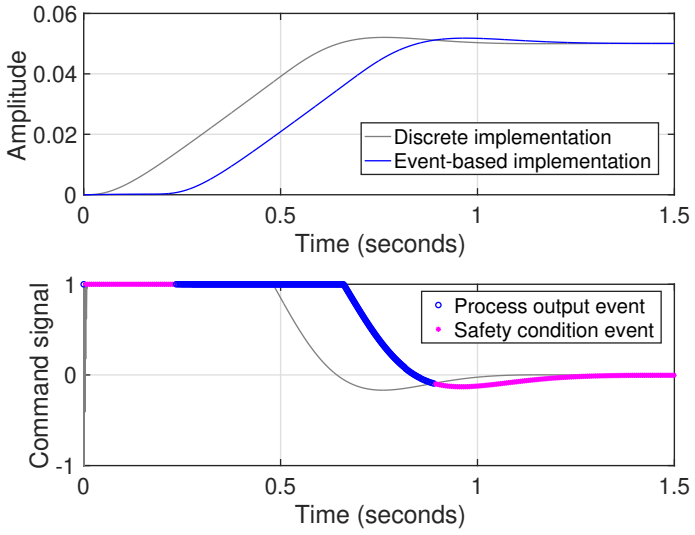

(c) Event-based fractional order PD implementation based on the CFE recursion

Figure 4.10: A fractional order PD controller applied to a FOTF process

The main applicability of the study from [142], where the model and control have been developed, is in targeted drug delivery biomedical applications. One of the main request of the physical submersible is energy efficiency. This particular example is highly relevant to the proposed event-based fractional order methodology in order to show that the method can be useful to reduce computational effort in complex applications where energy efficiency is paramount. The control of the submersible's position is done using the fractional order PD controller

$$C(s) = 65.0028\left(1 + 0.0305s^{0.6524}\right). \tag{4.25}$$

Fig 4.10a shows the response of the system with the classical discrete-time implementations using 5^{th} order Muir compared to the CFE direct mapper with $T_s = 0.001s$. In order to be true to the real process, the control signal that represents a PWM duty ratio is saturated between $[0, 1]$. Hence, the event-based fractional order control strategy is tested on another real life situation where the control signal range is limited. It can be seen that the dynamics of the closed-loop system are similar for the three discrete-time implementations.

The implementation parameters for the event-based Muir and CFE controllers are $h_{nom} = T_s = 0.001s$, $h_{max} = T_s = 0.005s$ - 5 times greater than h_{nom} and $\Delta_e = 0.01$ representing 1% of the desired reference value.

The closed-loop system responses using the event-based fractional order controllers with the Muir and CFE mappers are shown in Fig. 4.10b and Fig. 4.10c, respectively. Both controllers obtain similar responses as their non-event-based implementation. However, it can be clearly observed that the Muir realization of the discrete-time fractional order PD controller is the better choice.

From the control effort perspective, the Muir approximation computed the command value 380 times, whereas the CFE approach computed it 473 times. Both implementations reduce the 1500 number of computations realized with the non-event-based controller, bringing an improvement of more than 70% to the control effort.

4.6 Summary

This chapter provided the original contribution to the generalization of event-based control to the field of fractional calculus, combining the benefits brought by the two approaches into an industrial-suitable control strategy. Although in recent years, control applications based on fractional order differ-integral operators have gained popularity due to their proven superior performance when compared to classical, integer order, control strategies, the current industrial setting is not yet prepared to fully adapt to these newcomer solutions. It is often believed that complex

fractional order control implementations require hefty computational resources; needing highly-efficient methods of implementation to adhere to minimum control efforts. The solution to this particular problem lies in combining benefits of event-based control such as resource optimization and bandwidth allocation with the superior performance of fractional order control. Theoretical and implementation aspects are developed in order to provide a generalization of event-based control into the fractional calculus field. Different numerical examples validate the proposed methodology, providing a useful tool, especially for industrial applications where the event-based control is most needed. Several event-based fractional order implementation possibilities are explored, the final result being an event-based fractional order control methodology.

The work presented in this chapter has been published in:

- **I. Birs**, I. Nascu, C. Ionescu, C. Muresan. "Event-based fractional order PID control", in *Journal of Advanced Research*, vol. 25, pp. 191-203, DOI: 10.1016/j.jare.2020.06.024, 2020.
- **I. Birs**, C. Muresan, and C. Ionescu, "An event based implementation of a fractional order controller on a non-Newtonian transiting robot," in *2020 European Control Conference (ECC 2020)*, St. Petersburg, Russia, pp. 1436-1441, 2020.

5

Case Study - Varying Properties of Non-Newtonian Fluids

5.1 Introduction

The great potential of fractional order impedance models (FOIMs) for capturing natural properties of materials in a variety of disciplines has been long recognized and established experimentally [143, 144, 145]. Applications in medicine and biology are most prevalent as these dynamical systems feature core properties such as multi-scale dynamics, diffusion, viscoelasticity and relaxation [146, 147, 148]. The same properties are often used to model dynamics in the areas of geology, manufacturing, food industry and chemical products. The list of their applicability is vast and summarized in several excellent surveys, e.g. [7]. The prevalence of these properties is much increased in non-Newtonian fluids and soft materials. As such, one can identify classes of non-Newtonian fluids in each of the above mentioned application areas.

A common approach in modelling and simulating non-Newtonian behavior is based on the numerical calculus via Computational Fluid Dynamics (CFD). In this case dedicated software as Ansys Fluent, Open Foam, SIMSCALE, SimFlow, to mention just a few, are used. In this case effective applications can be found different areas. In [149] where Newtonian and non-Newtonian blood viscosity models have been considered in simulating the flow in atherosclerotic coronary arteries; as well as in [150] where the authors, in order to realize a continuous way of measuring and monitoring drilling fluid properties, they simulate a non-Newtonian fluid that is best described by a Yield-Power Law (YPL) rheological model. Numerical methods and time complex time domain models using power law models and fractional derivatives have been proposed in [151], providing

excellent simulation analysis tools. The memory property of such fluids was also captured with variations of the fractional order in time [151]. Such in-depth theoretical analysis is a solid basis and motivation for using the FOIMs.

The term fractional order impedance model (FOIM) has been coined some decades ago in an application of modelling respiratory tissue properties such as tissue compliance as a function of anatomical and structural changes in respiratory disorders [75, 147]. It has since then been used in many applications, such as tissue modelling, drug diffusion and blood viscosity characterizations [152]. The high versatility of FOIMs stands in their combination of general-order integrators and differentiators. The fractional orders are usually limited between physical values capturing properties defined by classical (Newtonian) theory of fluids or materials.

The representation of FOIM in frequency domain greatly simplifies their applicability to experimental data. The collection of data is time based, but suitably transformed into equivalent complex or polar coordinates. Dynamic response methods are applied to obtain the material reaction to an input signal suitably designed. Although there are time-based models defined for capturing material properties, these require a high computational complexity and a careful choice of time-based definitions [153].

A great advantage of FOIMs expressed in Laplace and their equivalent frequency domain forms, is their capability to capture in a compact form complex nonlinear properties and have these identified in a real-time context. This will be further shown in designing a closed loop control of suspended objects in blood-like varying context of viscoelastic fluid properties in Chapter 6.

Beyond the specific application, this chapter proposes to use a mathematical framework of FOIMs to capture and link the model parameter structure to the existence of specific properties in non-Newtonian fluids previously presented in Chapter 3. The novelty of this approach consists in the justification of using FOIMs, as well as the systematic analysis of the FOIM structure versus fluid properties. Novel is also the experimental protocol designed and applied to a series of fluid classes (oil, sugar, detergent and liquid soap). An additional original element of this research consists in the presentation and validation of several variations of FOIMs on the dataset. Finally, a set of recommendations concerning the future use of FOIMs in capturing material properties have been formulated.

5.2 Fractional Order Impedance Model

A commonly used FOIM for (biological) material characterization is the model given by

$$Z(s) = R + L(s)^{\alpha} + \frac{1}{Cs^{\beta}} \tag{5.1}$$

as a function of the Laplace variable s, containing a scaling factor R and two fractional order terms which denote low and high frequency dependency whose gains L and C are constants denoting gain in the slope of the constant phase intervals related to the fractional order values. This is a compact model, consisting of the minimal term to characterize variations in frequency response of combined increasing and decreasing monotonic values. This model has been shown to be the natural solution of materials with mechanical properties modelled by combinations of Maxwell, Kelvin and Voigt elements [10, 17]. This implies that the model structure and parameters may be suitable for detecting various degrees of viscoelasticity.

Looking at the model in equation (8.18) and considering the fact that the parameter α has always a negative value, then it is possible to rearrange the model as:

$$Z(s) = \frac{Rs^{\alpha+\beta} + Ls^{\beta} + Ds^{\alpha}}{s^{\alpha+\beta}}, \qquad -2 < \alpha, \beta < 2 \tag{5.2}$$

with $D = 1/C$. Therefore it is possible to notice that for some materials the appropriate model may have a pole in the origin and two other fractional order derivative. However through an electrical comparison, this impedance could correspond to a circuit which has one resistor and two fractional order capacitors, also known as constant phase elements. Such model is broadly used for dielectric materials and neural network transmission pathway [154, 155].

The complete FOIM will take the form of (8.18) in frequency domain as:

$$Z(j\omega) = R + L(j\omega)^{\alpha} + \frac{D}{(j\omega)^{\beta}}, \qquad -2 < \alpha, \beta < 2 \tag{5.3}$$

which is a five parameters model. When optimization is involved, it may be useful to verify the equivalent real and imaginary parts of this model:

$$\mathcal{R}\{Z(j\omega)\} = R + L\omega^{\alpha}\cos\left(\frac{\alpha\pi}{2}\right) + \frac{D}{\omega^{\beta}}\cos\left(\frac{\beta\pi}{2}\right) \tag{5.4a}$$

$$\mathcal{I}\{Z(j\omega)\} = -\left[L\omega^{\alpha}\sin\left(\frac{\alpha\pi}{2}\right) + \frac{D}{\omega^{\beta}}\sin\left(\frac{\beta\pi}{2}\right)\right] \tag{5.4b}$$

where one can see the real part is no longer constant with frequency as in the classical integer order formulation, but it varies as a function of frequency.

The full model is used to characterize the impedance data, assuming the variations in the parameter values will depend on the degree of viscoelasticity in the test sample.

5.3 Identification Methodologies

5.3.1 Nonlinear Least Squares Algorithm

The available nonlinear least squares minimization algorithm from Matlab has been used to fit the FOIM to the test sample data. The initial values are randomly selected at the beginning of the optimization from the intervals of feasible region.

The function `lsqnonlin` was used the following options:

- 1000 different calls;
- 500 maximum number of iteration per call;
- $1 \cdot 10^{-9}$ as goal for the cost function minimum;
- 10 recurrent iterations to further optimize the solution.

5.3.2 Genetic Algorithm

The genetic algorithm (GA) is a biologically inspired optimization algorithm [156]. It is a stochastic global search method that tries to mimic the process of natural biological evolution. This algorithm operates on a population of potential solutions applying the principle of survival of the fittest, ideally to produce increasingly better approximations towards an optimal solution. At each generation, a new set of approximations is created by the process of selecting individuals according to their level of fitness in the problem domain and breeding them together using operators borrowed from natural genetics. This process leads to the evolution of populations of individuals that are better suited to their environment than the individuals that they were created from, just as in a natural adaptation mechanism.

Fig. 5.1 illustrates the flowchart of the GA, emphasizing the main execution steps. At the very beginning, the domain for each parameter to be found must be set properly. It is straightforward to understand that the larger the domain the more difficulties that the optimization process can have, especially if the problem is strongly nonlinear. Each of this range is then "discretized" through a binary conversion, according to the specified number of bits. The binary elements of each range are called *chromosomes*. The binary number is called *genotype* while the relative decimal, real number, represents the *phenotype*. Then, the first population is created by random selecting chromosomes and the size depends on the number of individuals, that is another option to be set properly. The key role of the optimization process is played by the *objective function*: it can be seen as the cost function to be minimized is the one which actually represents the minimization problem to solve. Each chromosome is therefore converted to get the phenotype and it is evaluated through

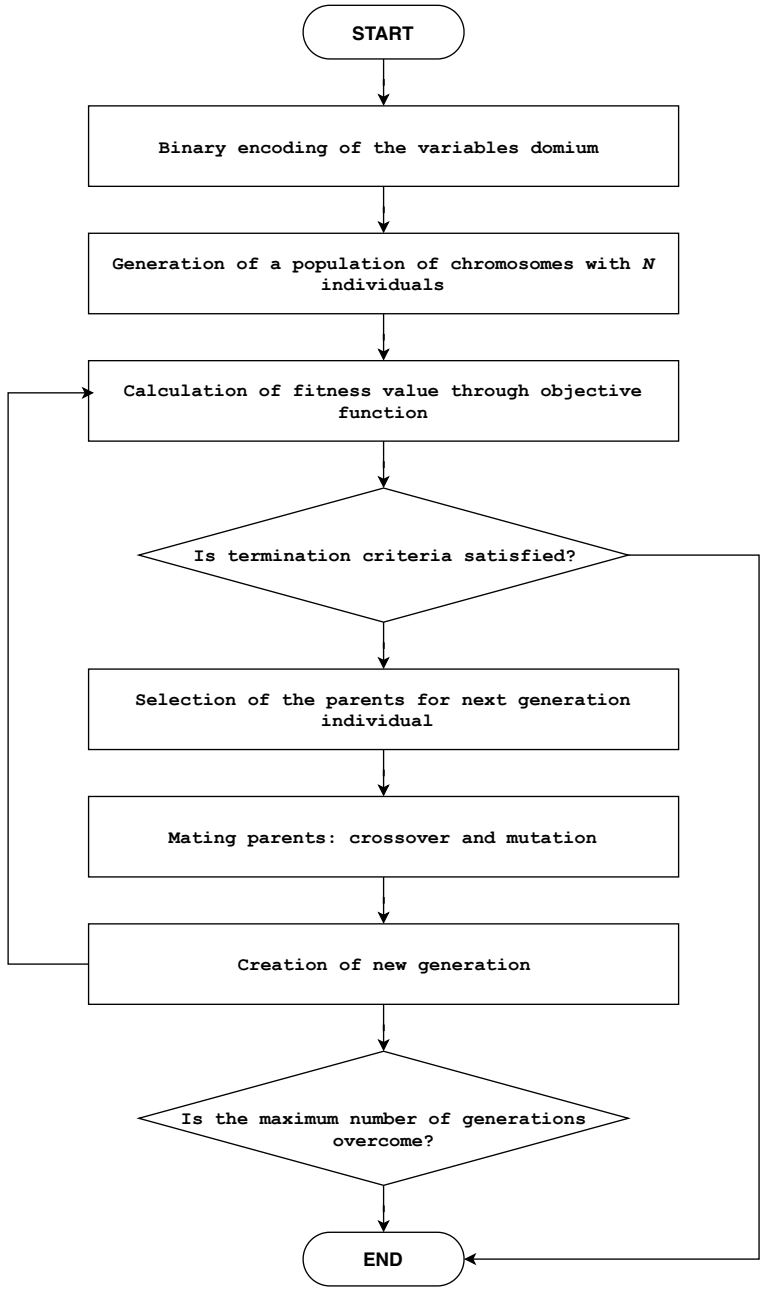

Figure 5.1: Flowchart of typical implementation of the Genetic Algorithm.

the objective function; the value of the function for the given set of parameters is called *fitness value*. This allows to evaluate the goodness of the chromosome by determining its probability to be selected. In this version of the algorithm the *roulette wheel* selection method is used: it means that the chromosomes selected to become the parents of the next generation individuals are chosen with a probability proportional to their fitness value. Notice that the objective function has to be minimized such that the better the chromosome, the lower the objective function value: i.e. the fitness value is usually its inverse.

After the selection, the chromosomes mate in pairs and the resulting one will have part of the genotype from both parents: this kind of process is called *crossover*. It represents the biological ability to evolve through generations inheriting mainly the good genes. Another process that can occur is called *mutation* and consists in the random change of parts in the genotype. This can be seen as a perturbation given to the solution, useful to escape from local minimums and converge towards the global minimum, if one exists. Each pair generates two children and the probability that crossover and mutation occurs are P_c and P_m established in the program, with $P_m \ll P_c$. Once the new population is generated, the process restarts and continues until the stopping criteria is met, usually set by a lower bound for the objective function and a maximum number of generations. An additional strategy states that the size of the offspring should not remain the same, and yet another design parameter is introduced called *generation gap*, representing the ratio between the new population and the old one. In this case the GA is said to follow an elitist strategy.

The `ga` function parameters are:

- 10 independent calls of the algorithm;
- 1000 individuals per generation;
- 300 maximum number of generations;
- 90% of generation gap;
- 5 parameter to optimize, *i.e.* number of chromosomes;
- 10 bit to discretize the domain;
- limited range; and
- $1 \cdot 10^{-9}$ as limit value for the cost function minimum.

5.3.3 Particle Swarm Optimization

The particle swarm optimization (PSO) concept was introduced in 1995, by simulating social behaviour of observed in animals or insects, e.g., bird flocking, fish schooling, afterwards the algorithm was simplified and it was

observed to be performing optimization [157]. PSO is an evolutionary computation technique that optimizes a problem by iteratively trying to improve a candidate solution with regard to a given measure of quality.

It is inspired by the behaviours of swarms based on their movement and intelligence, which are seeking the most fertile feeding location. A swarm is a seemingly badly planned and disordered collection of moving individuals that tend to gather closely while each individual moves with random changes in direction. It uses a collection of particles that are part of a swarm moving around in the search space for finding the best solution to an optimization problem. The concept consists of changing the velocity (or accelerating) of each particle toward its p_{best} and the g_{best} position at each time step

Each particle adjusts its own trajectory in an n-dimensional space, according to its own trajectory experience and the experience of other particles in the swarm. Each particle keeps track of the best position in the problem space, which it has reached so far. This value is called p_{best}. Another best value called g_{best} is achieved so far by any particle associated with the best value found among all the particles.

In the PSO algorithm, with flowchart given in Fig. 5.2, each particle moves around in the n-dimensional space with a velocity (or accelerating) that is updated by p_{best} and the g_{best} position of the particle at each time step. The current position and the velocity of each particle are modified by the distance between its current position and p_{best}, and the distance between its current position and g_{best} as given in the following. At each step n, by using the individual best position p_{best} and global best position g_{best}, a new velocity for the i^{th} particle can be modelled according to the following equation:

$$\begin{aligned} V_i(n) = \chi[V_i(n-1) + \varphi_1 r_1(p_{best_i} - P_i(n-1)) + \\ + \varphi_2 r_2(g_{\text{best}} - P_i(n-1))], \end{aligned} \tag{5.5}$$

where each particle represents a potential solution and it has a position represented by the position vector P_i, with r_1 and r_2 random numbers between 0 and 1; φ_1 and φ_2 positive constant learning rates and χ is called the constriction factor defined as:

$$\chi = \frac{2}{\left|2 - \varphi - \sqrt{\varphi^2 - 4\varphi}\right|}, \quad \varphi = \varphi_1 + \varphi_2, \quad \varphi > 4 \tag{5.6}$$

Based on the updated velocity, each particle changes its position as following:

$$P_i(n) = P_i(n-1) + V_i(n) \tag{5.7}$$

The position is confined within the range of $[p_{\min}, p_{\max}]$. Changing position enables the i^{th} particle to search around its local best position, p_{best}, and global best position, g_{best}.

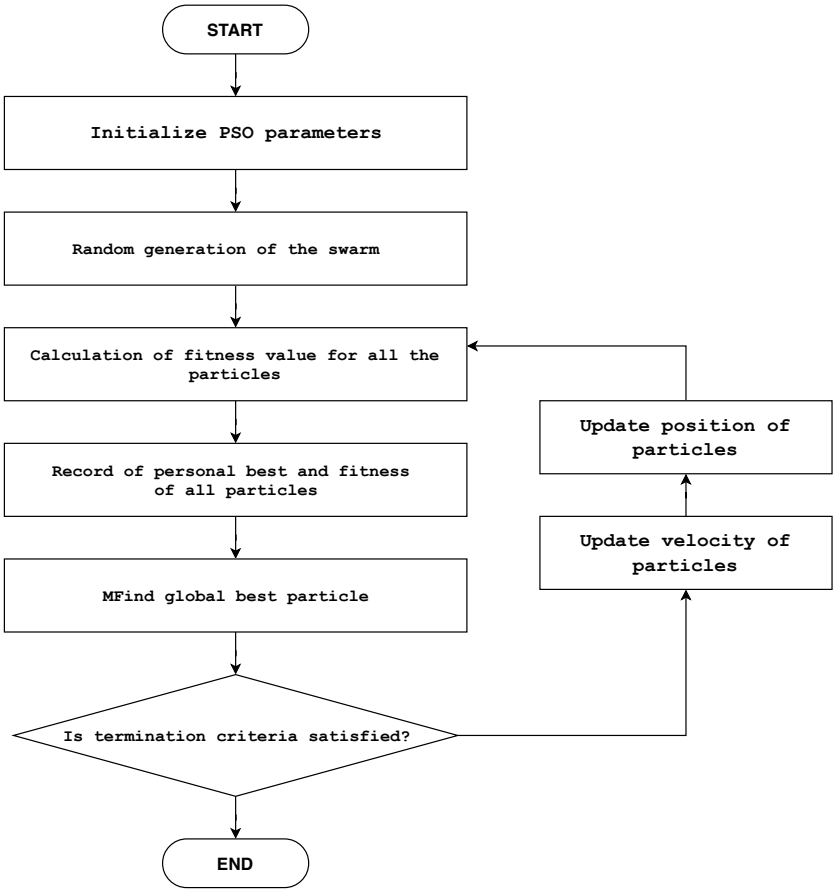

Figure 5.2: Flowchart of typical implementation of PSO algorithm.

Particle swarm optimization is an extremely simple algorithm that seems to be effective for optimizing a wide range of cost functions. The adjustment toward p_{best} and g_{best} by the optimizer is conceptually similar to the crossover operation utilized by genetic algorithms.

The PSO algorithm used in various optimization problems has certain advantages:

- it does not involve selection operation or mutation calculation, i.e. the search can be carried out by repeatedly varying particle's speed;
- particles fly only to good areas, as learning from group's experiences;
- it is based on artificial intelligence enabling broad application areas;
- it has a low computational cost.

Some of the disadvantages of the method may be listed as:

- complexity increases exponential with the dimension of the optimization space;
- it is vulnerable to partial optimism, which leads to a sub-optimal regulation of its search speed and direction;
- with the lack of dimensionality this method cannot be used for problems of non-coordinate system, such as the solution to the energy field and the moving rules of the particles in the energy field.

To conclude, due to the flexibility and versatility of this algorithm, it can be used to overcome complex non-linear optimization tasks like non-convex problems, being a good compromise between computational time and accuracy.

Matlab's Optimization Toolbox has been used for the `particleswarm` function with the following options:

- 10 independent calls of the algorithm;
- 1000 particles in the swarm;
- 500 maximum number of generations;
- 50 maximum stall iterations, to explore neighbourhood of a solution;
- 5 parameter to optimize;
- limited range; and
- $1 \cdot 10^{-9}$ as limit value for the cost function minimum.

Table 5.1: Upper and lower bounds for class NN1 (honey and glucose) and class NN2 (hand soap and shampoo) test samples.

Class		R	L	D	α	β
$NN1$	Min	0	-10^{10}	10^8	-2	0
	Max	10^2	-10^8	10^{10}	0	2
$NN2$	Min	0	-10^5	10^3	-2	0
	Max	10^2	-10^3	10^5	0	2

5.3.4 Optimization in Feasible Region

Irrespective of the optimization algorithm applied to nonlinear cost functions, there is no guarantee for convergence to the global minimum. The cost function defined for GA, PSO and nonlinear least square algorithm has been defined by using the so called *normalized mean square error*, provided by built-in Matlab function `calNMSE`. Its mathematical form is:

$$NMSE = \frac{\|Z_m(j\omega) - Z_e(j\omega)\|^2}{\|Z_m\|^2} \tag{5.8}$$

where Z_m is the measured impedance and Z_e the estimated impedance. The optimization algorithms use vector format and for this reason is useful to make another normalization by dividing the *NMSE* of equation (5.8) for the length of the impedance vector itself. This definition allows to choose the cost function J as follows:

$$J = w_r \cdot NMSE_R + w_i \cdot NMSE_I \tag{5.9}$$

which is the weighted sum of the normalized mean square error for the real and the imaginary part of the impedance. The weight values $w_r = 1$ and $w_i = 2$ could be chosen differently. However, the problem is highly nonlinear in the five parameters and the aim is to find the proper domain with nested loops, trying to optimize the cost function per decade of frequency. Monte Carlo analysis provided the empirical values for the upper and lower bounds in test sample groups.

5.4 Laboratory Setup

The device depicted in Fig. 5.3 performs Electrochemical Impedance Spectroscopy in fluid samples. The method behind is the classical transfer function analyzer algorithm. The reference signal is applied by means of a *potentiostat* and then through the *frequency response analyzer* the actual measurement of the impedance can be performed. The *Modulab*

XM is a highly versatile electrochemical test system that measures the characteristics of a wide range of materials including organic/inorganic, specialized corrosion, electroplating and energy cells. Reference grade system components (potentiostat / galvanostat, frequency response analyser and optional high voltage amplifier) are combined in a single unit, avoiding the need for stacking and wiring separate units. The device communicates via an Ethernet link to an external PC, running XM-STUDIO ECS software for control and monitoring purposes. The testing signal covers a range of frequencies from μHz to MHz.

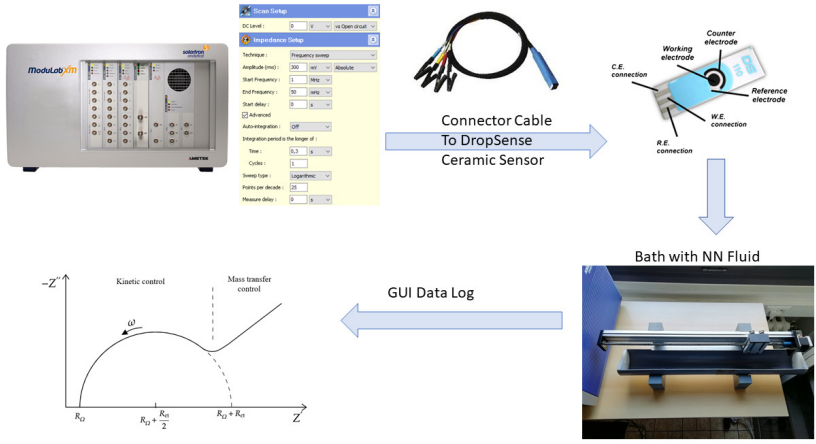

Figure 5.3: ModuLab XM measurement device with afferent instrumentation for experimental testing of various NN fluid impedance characteristics. The GUI data is a polar plot, with real and imaginary parts as a function of excited frequencies.

The software XM-STUDIO ECS provides the data logging in a graphical form as a polar plot, and in an Excel file as numerical values for further processing. The measurement options are listed below:

- DC level: 0mV
- RMS Amplitude: 300mV
- Starting frequency: 1MHz
- Ending frequency: 5Hz
- Integration period time: 0.3s
- Integration period cycles: 1

- Sweep type: logarithmic
- Points per decade: 25

5.5 Results

There are three identification methods applied to the experimental data in complex form. The comparison in terms of fitting performance did not deliver statistical meaningful differences. However, the CPU time evaluated for the total time of identification (including iterations) was:

- genetic algorithms at 0.72 ± 0.26 seconds;
- particle swarm optimization at 0.19 ± 0.13 seconds and
- nonlinear least squares at 0.13 ± 0.05 seconds.

The identification was performed on a Dell OptiPlex 7060 desktop Intel Core I7 8th Gen, Win10 and Matlab R2017a version. Depending on the application, these times can be put into the context of continuous evaluation of context properties, in this case estimating the time-varying model parameters which may change over time. Given the ease of implementation and computational burden, the nonlinear least squares algorithms seems to be the most practical.

The model from equation (8.18) has been used to fit the experimental data. The results of the identification algorithms for class NN1 fluids are given in Fig. 5.4 and Fig. 5.5, respectively. It can be observed the data is very well fitted by the model over many frequency decades. NN1 and NN2 have been classified and exemplified in chapter 3.

The results of the identification algorithms for class NN2 fluids are given in Fig. 5.6 and Fig. 5.7, respectively. Also in this case, the data is very well fitted by the model over many frequency decades.

No significant difference between the optimization algorithms was observed within the obtained results. This is an indication that the same (global) minimum was reached by all three algorithms. The model values are summarized in Table 5.2.

For reasons of ease of implementation, nonlinear least squares optimization method was used to fit the data presented hereafter. Another set of shear-thickening and shear-thinning NN fluids was tested to see whether the model parameter values was sensitive to variations in temperature, i.e. car engine oil. The results are given in Table 5.3. A non-monotonic evolution of the parameter values can be observed, which is expected from the shear-variations from Fig. 3.3.

Table 5.2: Identified model parameter values and normalized error.

		R	L	D	α	β	$NMSE$
Glucose	GA	0	$-5.35 \cdot 10^9$	$3.91 \cdot 10^9$	-0.96	0.91	$4.32 \cdot 10^{-5}$
	PSO	0	$-7.19 \cdot 10^9$	$5.84 \cdot 10^9$	-0.95	0.92	$4.46 \cdot 10^{-5}$
	LSQ	0	$-7.19 \cdot 10^9$	$5.84 \cdot 10^9$	-0.95	0.92	$4.28 \cdot 10^{-5}$
Honey	GA	0	$-2.04 \cdot 10^9$	$3.61 \cdot 10^8$	-1.10	0.82	$4.53 \cdot 10^{-5}$
	PSO	0	$-3.26 \cdot 10^9$	$2.09 \cdot 10^9$	-0.97	0.90	$4.03 \cdot 10^{-5}$
	LSQ	0	$-5.05 \cdot 10^9$	$5.05 \cdot 10^9$	-0.84	0.84	$1.24 \cdot 10^{-4}$
Hand soap	GA	33.2	$-1.67 \cdot 10^4$	$1.48 \cdot 10^5$	-0.89	0.89	$2.22 \cdot 10^{-5}$
	PSO	32.5	$-1.01 \cdot 10^4$	$1.37 \cdot 10^5$	-0.89	0.89	$2.16 \cdot 10^{-5}$
	LSQ	32.8	$-1.30 \cdot 10^4$	$2.66 \cdot 10^5$	-0.89	0.89	$2.22 \cdot 10^{-5}$
Shampoo	GA	18.5	$-1.00 \cdot 10^4$	$3.92 \cdot 10^4$	-2.00	0.84	$6.46 \cdot 10^{-5}$
	PSO	18.0	$-1.00 \cdot 10^4$	$3.47 \cdot 10^4$	-2.00	0.82	$5.67 \cdot 10^{-5}$
	LSQ	18.3	$-1.03 \cdot 10^4$	$5.25 \cdot 10^4$	-0.85	0.85	$6.67 \cdot 10^{-5}$

Table 5.3: Identified model parameter values in car engine oil as a function of temperature.

Temperature	$R \cdot 10^3$	$L \cdot 10^9$	$D \cdot 10^9$	α	β
22^oC	1.602	-2.124	7.099	-1.340	1.070
27^oC	1.073	-3.041	6.584	-1.005	1.004
46^oC	1.792	-1.955	7.008	-1.320	1.066
63^oC	1.347	-2.152	8.099	-1.304	1.084

5.6 Discussions

The FOIM discussed in this chapter was successfully employed in a prior study to fit the impedance of water-glucose solutions [18]. In this study, the parameters have quite small values, in the order of the unity for constants, while α and β are in the order of 10^{-3} and 10^{-4}, respectively. This is an indication that the solutions have properties closer to Newtonian fluids. It is also within the physical abilities of the available laboratory setup conditions for testing.

The FOIM and a simplified variant was used to identify honey and glucose properties in [26]. The simplified FOIM was in the form $R + \frac{D}{s^\beta}$ as the values of the α parameter were always negative. This observation is similar to the findings in this chapter as reported in Table 5.2. Our findings are in the same line as those in [158], where a FOIM variant was linked also to materials with viscoelastic properties.

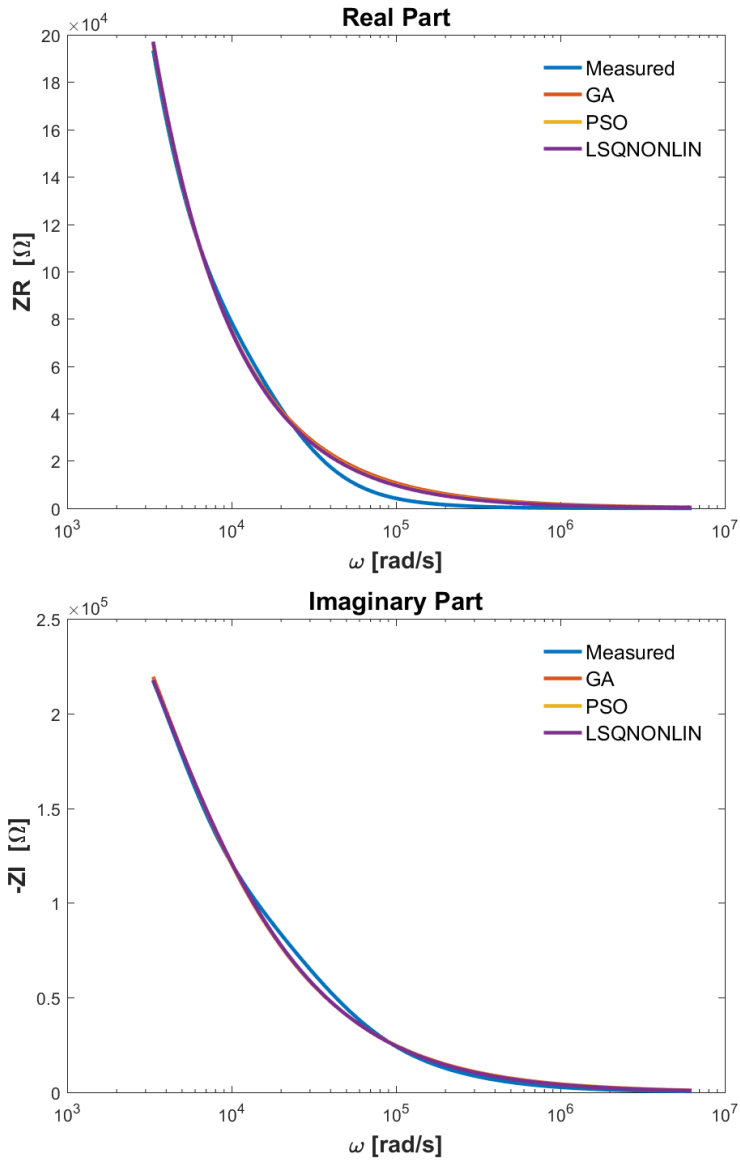

Figure 5.4: Glucose: comparison between optimization algorithms.

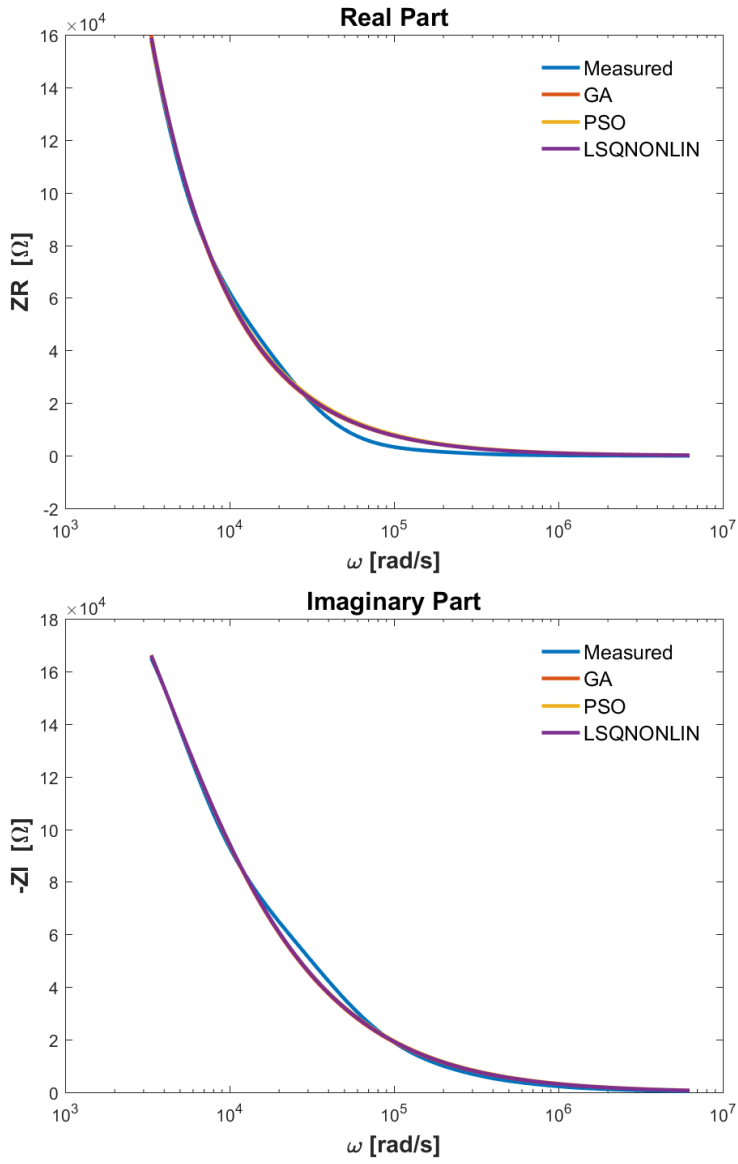

Figure 5.5: Honey: comparison between optimization algorithms.

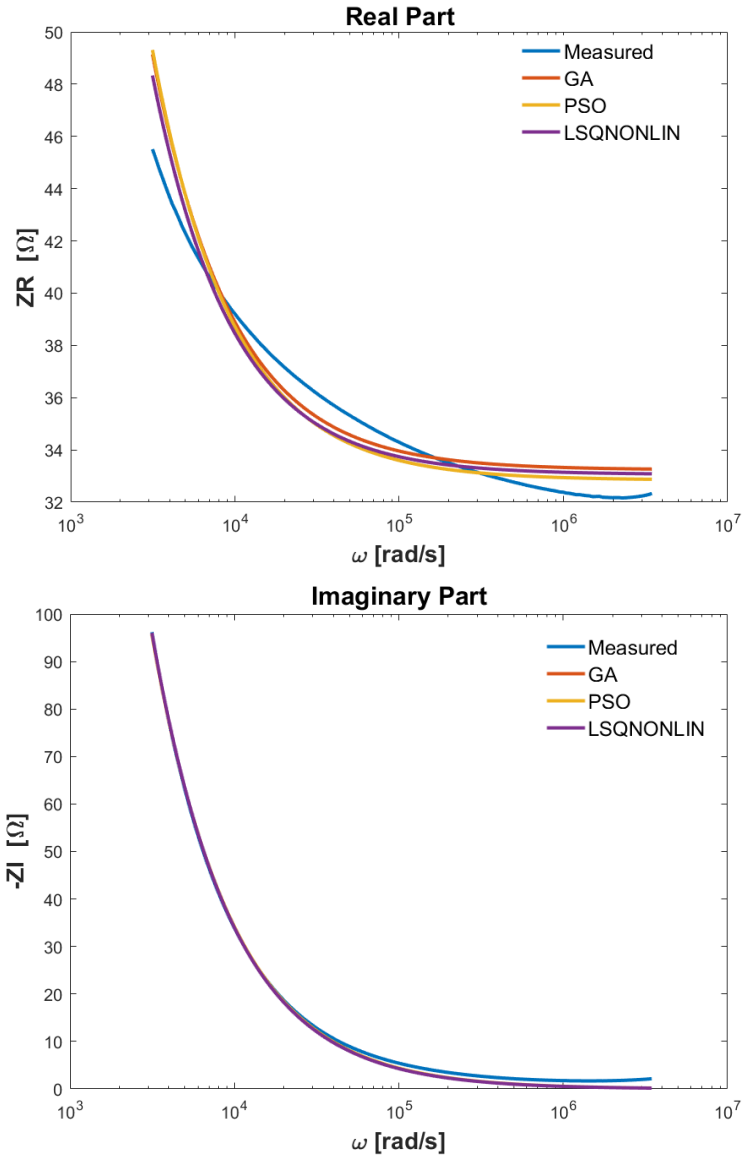

Figure 5.6: Hand Soap: comparison between optimization algorithms.

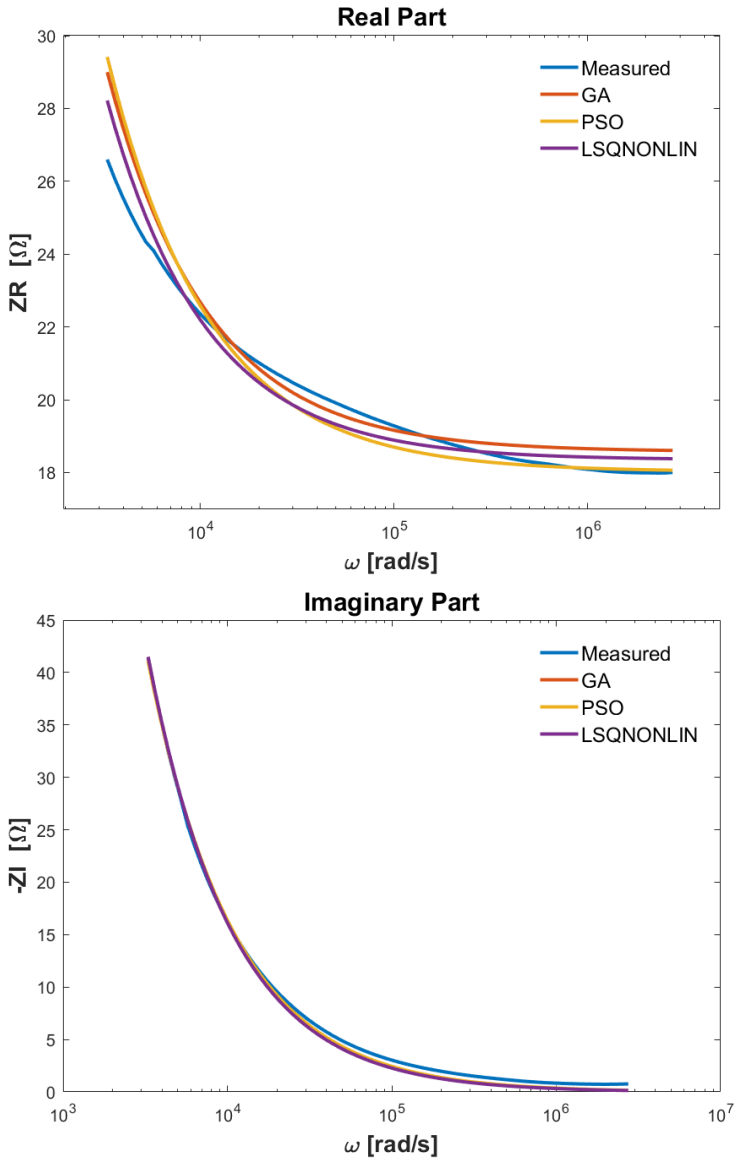

Figure 5.7: Shampoo: comparison between optimization algorithms.

For all sample tests, it seems that parameters R and D are most correlated to changes in viscosity. This is not at all surprising, as in [13], it was physically shown that a ladder network of RC-cells leads to appearance of fractional order terms in this form in the limit impedance value, and that its value depends directly on the compliance represented by these cells. The application on lung tissue property modelling and identification from real data validated this theory. Moreover, despite the small sample test analysis and rather limited test conditions, the model parameters varied as a function of material even in small values, which indicate a good sensitivity of the model to inherent changes in material properties.

In this study, it was not yet found the specific property of a non-Newtonian fluid to demand fractional derivative order Ls^{α}. It can be concluded that other types of fluids with properties exhibiting increasing high frequency dependence will require this term, i.e. rubber like materials, high resistance polymers, plasma etc.

The relevance of this work is substantial in its fundamental nature as identification for control in NN fluid dynamic environment has quite a large number of cross-disciplinary applications.

A limitation of this study is that the proposed model, despite its versatility, was not perfectly able to fit the data on large range of frequencies. Some NN fluids, such as engine oils depend on temperature in a non-monotonic progression, and some frequency intervals are better fit than others. Such non-local elastic properties are visible in materials under mechanical and momentum stress [159]. This observation may suggest that other models could be used in those particular frequency intervals. Although several variants of FOIM exist, the choice of the frequency interval and model structure depends heavily on the end-objective of the identification exercise and application use.

A set of NN fluids whose consistency is significantly different was tested to see whether the model parameter values was sufficiently able to distinguish among them. There are three test samples of food oils with results given in Table 5.4. The results indicate that the scaling factor R is proportional to the increase in consistency.

Table 5.4: Identified model parameter values in various food oils.

Oil type	$R \cdot 10^3$	$L \cdot 10^9$	$D \cdot 10^9$	α	β
avocado	1.103	−5.146	7.271	−1.095	1.037
corn	4.543	3.422	2.934	−1.583	0.995
olive	6.691	−5.230	3.003	−1.576	0.997

Another set of NN fluids was tested, whose consistency was varying. The identified results for household fluids are given in Table 5.4. Again,

the results suggest the scaling factor R is proportional to the increase in consistency, a property of shear-thinning NN fluids.

Table 5.5: Identified model parameter values in household fluids.

Type	$R \cdot 10^3$	$L \cdot 10^5$	$D \cdot 10^4$	α	β
soft detergent	2.671	−0.510	0.521	−0.818	0.827
handsoap	2.322	−0.507	0.516	−0.601	0.637
shampoo	3.514	−0.564	0.504	−0.628	0.651
standard detergent	4.415	−0.508	0.500	−0.755	0.787

An interesting set of NN fluid was that of thixotropic fluids, which resembles biological tissue. This was achieved by standard gelatin -water proportions, as given in increasing density in Table 5.6. As expected from our prior expertise in [7, 13, 18, 75], the parameter D and β were most correlated to the change in viscoelastic properties of the sample. The compliance property, determined by this parameter as explained in [147], is consistently identified to decrease as the sample becomes more stiff.

Table 5.6: Identified model parameter values in mimicked biotissue consistency.

Type	$R \cdot 10^3$	$L \cdot 10^9$	$D \cdot 10^9$	α	β
gelatin1	3.415	−0.510	0.604	−0.131	0.380
gelatin2	3.221	−0.486	0.501	−0.142	0.493
gelatin3	2.915	−0.681	0.320	−0.158	0.560
gelatin4	2.704	−0.690	0.310	−0.163	0.602

5.7 Summary

This chapter formulates a mathematical framework for the use of fractional order impedance models to capture fluid mechanics properties in frequency domain experimental data sets. The use of fractional order models as natural solutions to capture fluid dynamics are motivated by the non-Newtonian fluid classification presented in Chapter 3. Four classes of fluids are tested, featuring different NN properties: oil, sugar, detergent and liquid soap.

Furthermore, three nonlinear identification methods are used to fit the model: nonlinear least squares, genetic algorithms and particle swarm

optimization. The model identification results obtained from experimental data sets suggest the proposed model is useful to characterize various degree of viscoelasticity in non-Newtonian fluids. The advantage of the proposed model is that it is lumped, while capturing the fluid properties and can be identified in real-time for further use in prediction or control applications.

The main result of this study is a minimal parameter versatile fractional order impedance model to identify viscosity-related properties in non-Newtonian fluids. The experimental test samples and identified model parameters suggest the model is adequate to determine variations in fluid properties from several applications.

The results presented in this chapter have been published in:

- **I. Birs**, C. Muresan, M. Ghita, M. Ghita, D. Copot, M. Neckebroek, C. Ionescu, "Development and validation of preliminary fractional order impedance models for experimental pain assessment", in *2021 International Conference on Electrical, Computer, Communications and Mechatronics Engineering (ICECCME)*, Mauritius, pp. 1–6, 2021.

- C. Ionescu, **I. Birs**, D. Copot, C. Muresan, R. Caponetto. "Mathematical modelling with experimental validation of viscoelastic properties in non-Newtonian fluids", in *Philosophical Transactions of The Royals Society A*, pp. 20190284, doi:10.1098/rsta.2019.0284, 2020.

- **I. Birs**, D. Copot, C. Pilato, M. Ghita, R. Caponetto, C. Muresan, C. Ionescu, "Experiment design and estimation methodology of varying properties for non-Newtonian fluids," in *2019 IEEE International Conference on Systems, Man and Cybernetics (SMC)*, Bari, Italy, pp. 324-329, 2019.

6

Case Study - Suspended Objects in Non-Newtonian Fluids

6.1 Introduction

A manifold of applications in specialized literature deal with design, material, manufacturing and functioning of nanorobot objects for motion in non-Newtonian fluids. With that respect, precise, high-performance design and material properties have been investigated over the last decade with exponential success in nanomedicine and other application fields [19]. Our work differentiates to the extent of offering a low-cost, approachable and rather instructive benchmark solution for analysing various problems arising from modeling, identification and control of objects in non-Newtonian fluids.

In this context, this chapter contains details upon the design, the manufacture and implementation of such a benchmark system, allowing experiments to verify and finally to sustain the theoretical claims from Chapter 3. The fractional velocity gradient in developed plug flow conditions, as well as the dynamic response have been well captured in a non-Newtonian environment, i.e. liquid detergent/soap. With regard to academic tools for teaching control, reports on such effective low-cost solutions have not been found in the control engineering literature, hence the work has an original added value to the learning aspects of the control community.

In this chapter, the focus is on the development and experimental validation of a fractional order model that captures the interaction between a submerged object and its non-Newtonian environment. To begin with, an integer order model is formulated for objects transiting through Newtonian fluids, based on classical concepts and readily available in-

formation regarding underwater propulsion on submarines in maritime environments. The initial integer order navigation model is a simplified model, capturing only essential aspects of Newtonian fluid submersion. Next, this initial model is calibrated on experimental data acquired from a custom built platform that mimics non-Newtonian conditions, leading to a generalized fractional order model. The obtained fractional order model for non-Newtonian submersion is using fractional calculus tools previously introduced in Chapter 2. The purpose of the fractional order representation is to encompass complex motion dynamics within a transfer function that has a reduced number of parameters but a relatively increased versatility to capture complex phenomena. In conclusion, the initial model is a rough approximation and serves as the starting point in the search for a more accurate fractional order model, which ultimately will capture high order dynamic characteristics and various physical aspects that have been neglected throughout the development of the initial, classical, integer order navigation model.

The novelty of this chapter is in the modeling and control of non-Newtonian interactions from an experimental perspective. Modeling non-Newtonian system dynamics has been realized based on Navier–Stokes equations in Chapter 3. Here the aim is to validate the complex fractional order differential equations for system identification from experimental data sets. The modeling step is based on generalizing the already available Newtonian interaction models towards non-Newtonian motion models, and ultimately identifying their parameters from experimental data acquired from the proposed customized setup platform. The obtained model is successfully validated in the non-Newtonian setting, allowing the next step, i.e. to design a fractional order motion controller. The control strategy is also validated experimentally, proving once again the suitability of fractional calculus for both modeling and control purposes. Finally, the versatility of the experimental platform through environmental changes allows a robustness analysis of the controller in various types of liquids, both Newtonian and non-Newtonian, representing yet another novel aspect of this study.

6.2 Experimental Benchmark Setup

6.2.1 General Aspects and Purpose

Mixed fluids such as ice-water, muddy water, sludge, petrol-water, liquid detergents, etc., can be tested upon their fluid properties in a suitably (i.e. customized) built-in experimental setup to verify the added value and relevance of manifold modeling and control techniques in their intrinsic non-Newtonian conditions for operation. The proposed solution here is a versatile setup which encapsulates the dynamics of a moving object,

suspended within a non-Newtonian fluid, along with data measurements and control actions for the object's motion dynamics.

The challenges encountered by a substance carrier device inside a non-Newtonian environment are here recreated inside this custom built platform to a scaled laboratory setup. Initial design featured properties mimicking baseline changes in circulatory system (artey, vein, pump). It consists of two main parts: the circulatory system with non-Newtonian characteristics, and the carrier device capable of transiting and analysing dynamic impedance information from the non-Newtonian environment.

As such, the circulatory system fused with the carrier prototype create a generic experimental platform for non-Newtonian fluid flow analysis. The two parts are designed and built as two independent pieces of the puzzle. The only connection that has to be taken into consideration is the dimension of the submersible which should fit inside the mimicked circulatory system, i.e. a scalable solution.

The framework is used for calibrating and validating a generalized model for motion of the submersed robot in non-Newtonian conditions and for testing different control strategies for its relative position and velocity.

The working principles of the ensemble is elegantly simple and straightforward, designed with the idea in mind to be easily reproducible for academic/other purposes. The circulatory system unit is an airtight environment equipped with a pump moving non-Newtonian fluid through tubes of different diameters. The prototype robot is a sealed carrier device able to adequately sense in real time the impedance of the fluid in which it is submerged. The robot navigates through the fluid with a constant velocity and sends acquired impedance data to an external server. When a change in impedance levels is detected, the robot remains hovering in order to acquire more data from that particular location.

6.2.2 Lumped Circulatory System

The mimicked lumped circulatory system is designed such that it encapsulates these main characteristics:

- non-Newtonian blood flow dynamics;
- tubes that have a certain amount of elasticity and are able to slightly expand and contract with the fluid's flow;
- submersion of the object in tubes of different diameters to create a pressure drop.

The pipes have been chosen as elastic tubes with metal insertions built from polyurethane. There is a transition by physically joining two tubes of different diameters. This creates a drop/increase in pressure and respectively flow variations inside the environment. The non-Newtonian fluid

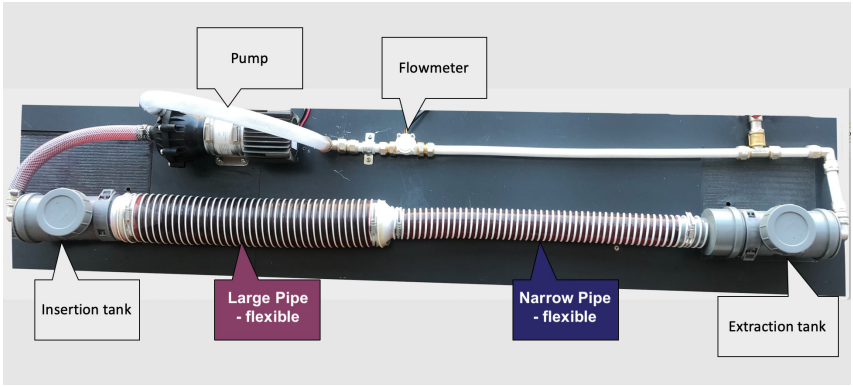

Figure 6.1: Snapshot of the experimental framework - the lumped circulatory system

flow is obtained by inserting any non-Newtonian fluid. Density and flow profile may vary in order to better asses the properties from an experimental perspective. In order to move the fluid through the pipes following a given flow pattern, a volumetric/peristaltic pump and a flow meter device are added to the setup. The *brain* of the circulatory system setup is a microcontroller that measures the flow inside the pipes and gives the pump the necessary command signal in order to generate a certain flow value.

The resulting experimental solution to mimic the lumped circulatory system is shown in Fig. 6.1. The immersion and extraction tanks without the screwed cover are given in Fig. 6.2 and Fig. 6.3.

The insertion and extraction areas are two small buffer tanks that feature a screwing lid used to seal the fluid inside the framework. The main purpose of these buffer points are to insert and to extract the prototype robot device. The role of the insertion and extractions points can not be interchanged due to the fact that the trajectory of the carrier prototype will always be from the larger tube towards the smaller one. This is caused by the shape of the part that joins the two tubes, allowing a smooth crossing from the larger tube inside the smaller one - similarly when blood is transiting from artery to veins. Another role for the two buffer tanks are to seal the circuit and eliminate deposits of air from the small and larger tubes, respectively. For each test, the prototype robot must be manually removed from the extraction tank and inserted back into the system while ensuring airtight conditions. Non-Newtonian fluid is added if necessary to fill the entire system as needed.

The insertion and extraction buffer tanks are connected by two tubes of different diameter: the large one represents an artery, while the other represents the vein. The transition connective area between the tubes is

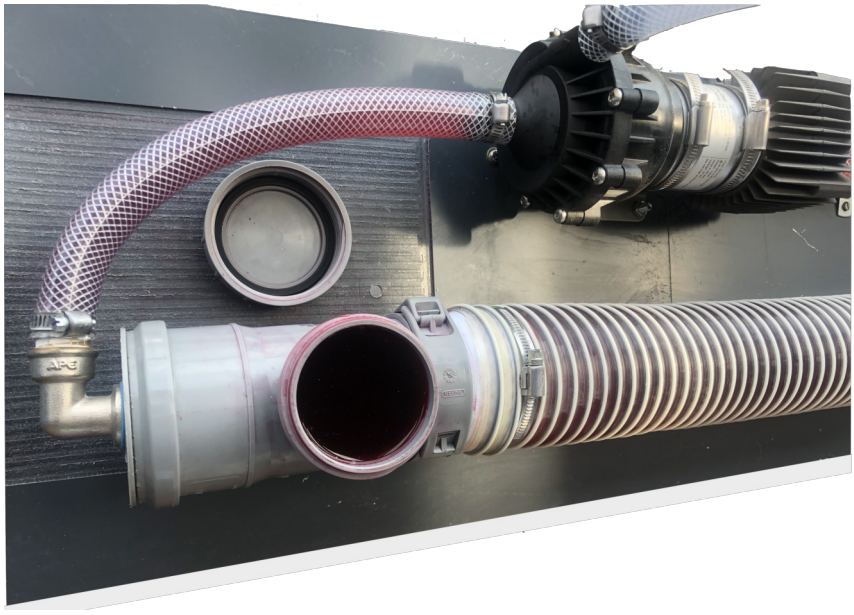

Figure 6.2: Snapshot of the immersion point in the lumped circulatory system

Figure 6.3: Snapshot of the extraction point in the lumped circulatory system

Figure 6.4: Snapshot of the transition area between the two flexible tubes of different diameter

displayed in Fig. 6.4.

The tubes are slightly flexible and the amount of flexibility is constant along the length of the tubes due to equally spaced metal insertions that act as a resistance for expansion and contraction of the tubes. The white lines sectioning the pipes are steel insertions, with density of the rings $\rho = 1140$ kg/m^3 and an elastic modulus $E = 22781$ Pa.

The material chosen for the pipes is polyurethane. The reasons for choosing this material are high tear resistance and high tensile properties. In addition, polyether compounds are used in submerged sea applications and maintains its properties in harsh environments for many years. Hence, several non-Newtonian fluids can be used without the risk of altering the environment (e.g. highly concentrated liquid detergent). The density of the polyurethane material is $\rho = 1060$ kg/m^3. It's elastic modulus is equal to $E = 272.5$ Pa, while the wall thickness is $h = 0.0009$ m. The density and elastic properties are valid for both tubes. However, the small tube has a diameter of $d = 0.051$ m, while the larger tube has a diameter of $d = 0.08$ m.

The red-coloured fluid flowing inside the pipes has non-Newtonian characteristics. The viscosity of the fluid in steady state conditions (when there are no external forces acting upon it) is $\mu = 0.085 * 10^{-5}$ ks/ms and a density equal to $\rho = 1.03 * 10^{-3}$ kg/m^3. The pulsing frequency of the pulsatile blood flow is chosen as the one of the human blood flow with a value $\omega = 2 * \pi * 7/6$ rad/s.

Since the aim is to have a continuous flow of fluid, a microcontroller and a flow meter are necessary. The microcontroller regulates the variable flow pump, CM10P7-1-24, that acts as the system's "heart". The chosen "brain" is the NI myRIO real-time microcontroller. The graphical programming language LabVIEW is used to implement the code. In order to close the flow control loop, a simple PI controller is tuned that uses the signal from a SNS-FLOW201 flow meter as feedback information. A working diagram between the described parts with the purpose of non-Newtonian flow control is presented in Fig. 6.5.

An important limitation of the present study refers to the mechanical

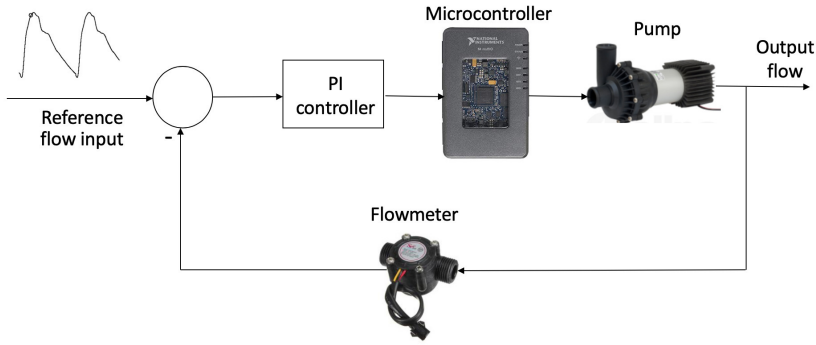

Figure 6.5: Non-Newtonian fluid flow control diagram through the mimicked lumped circulatory system

properties of the tubes selected. Their elasticity is certainly below the biological value of arteries, such that more interactive dynamic interplay between walls and transiting object is not emulated, and some of their viscoelastic properties are not fully captured. It should be noted that fractional order impedance models have been previously reported to be good candidates for modeling creep and tension, related to viscoelastic properties of arteries in sheep [160, 161]. Effects of distension and elongation of the tubes during pulsatile flow conditions are not enabled here and also do not make the objective of our investigation. Hence, the properties of the proposed benchmark, as of this moment, are situated somewhere in-between biomedical and technical applications of non-Newtonian fluid mechanics.

6.2.3 Autonomous Submerged Vehicle

One of the most important aspects to account for when designing and building the submersible prototype is the reduced dimensions such that it fits inside both tubes and is able to slide effortlessly (because it is battery operated) through them. Another important aspect when choosing the parts to incorporate inside it is the desired functionality of the robot.

To ensure proper operation and maximum efficacy in completing the task of impedance measurement while transiting the environment, the robot must incorporate the following characteristics enumerated hereafter.

- The robot should have the ability to operate on batteries for a long period of time. Also, all the chosen electronics should be energy efficient and of reduced size.

- All the embedded electronics should be completely sealed from fluid

leaks inside the robot. In addition, the battery should be replaced when needed by opening the robot, hence the need to reseal the carcass without damage.

- Remote robot programming should be considered in order to correct possible errors, change operating modes and add new control features.

- Accurate estimations of the 3D position inside the circulatory system based solely on data read by embedded sensors should be performed. The robot can not use information from the outside environment in order to compute its position (e.g. external satellites for triangulation). For this functionality, a positioning sensor should be chosen and custom algorithms should be developed.

- Problem detection and problem solving capabilities should be added to the robot. Changes of the surrounding non-Newtonian environment should be detected such as impedance changes or fluid velocity/pressure changes.

- Decision making algorithms such as stopping/hoovering at areas when unusual impedance levels are detected and release a substance to stabilize the impedance measurements.

- Velocity control algorithms are needed for efficient stopping of the submersible.

- Ability to navigate to a certain position specified by a user within a mapped environment or a detectable point of interest is also necessary for impedance measurements at certain locations.

Taking into consideration all of the above mentioned aspects, the electronic devices have been selected in order to fulfil all these expectations in a cost-effective, energy-efficient and size reducing manner.

From the mechanical point of view, an exterior hull has been designed that is 5 0mm long, 30 mm wide and has an ellipsoidal shape inspired from real submarines. The aqua-dynamic shape also features 4 prominent additions disposed across its length. The additional lines are 1 mm thick and their main role is to prevent the submersible from rotating when supposed to thrust forces. The symmetrical hull has been 3D printed using a combined material of polyamide and resin. The advantage of 3D printing is that the entire housing of the submersible is made from a single piece, minimizing the possibility of fluid entering inside the device through crevices. However, printing the entire submersible at once is not a viable option because electronics and balancing units need to be inserted inside, hence the hull should provide easy access inside the device. The only viable solution was to divide the submersible into two identical sections

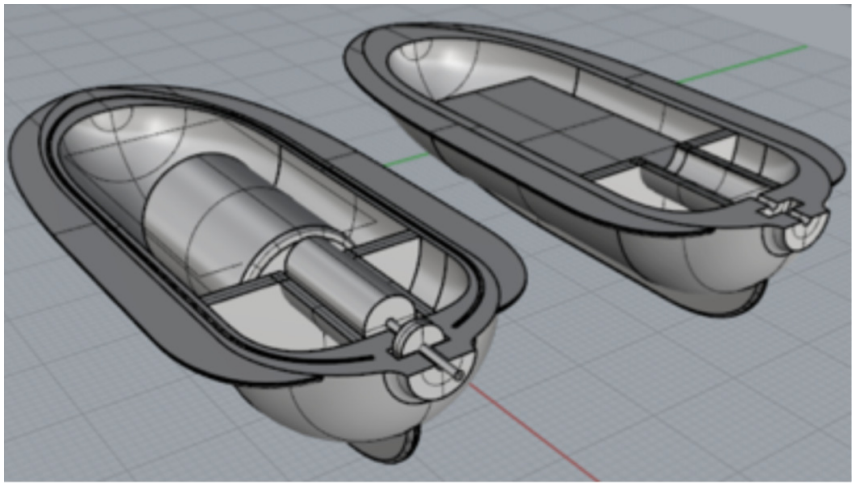

Figure 6.6: Illustration of the 3D design of the submersible

as shown in Fig. 6.6. The carcass is 0.003 m thick and the inner volume is empty, with the exception of a solid part at the rear used to fasten a motor, propeller and a sealing gasket. When fusing these two parts, the space between the two identical pieces is sealed with headlamp gasket and the two parts are screwed together using two screws in the rear and one in front inserted in previously printed spots.

Propulsion is what thrusts the submersible through the non-Newtonian fluid. Strategies for optimum propulsion analysis are evaluated for multiple domains and a wide variety of options are available [162, 163, 164, 165, 166]. The basic principles of vehicle propulsion are simple regardless of their environment: in the case of an aeroplane, the generated thrust needs to overcome air friction; for a ship, the generated force must overcome air and water friction in order to move the vessel; while for a submarine, the generated thrust has to be greater than the fluid's braking effect. For non-Newtonian fluids, the braking effect is larger than for Newtonian fluids. Hence, an efficient propeller is needed. Propeller generated propulsion is influenced by a number of factors: the number of propeller blades, the size of each blade, the geometrical arc created by a blade and the swirling direction of the blades [164]. Propellers are chosen based on the direction of the thrust force. For example, a propeller configured for forward motion will have the described behavior when thrusting the submersible forward, but its efficiency will dramatically drop if the propeller rotates in the opposite direction, aiming for a backward motion for the device [167]. Usually, submersibles have multiple propellers from which can be distinguished a large, principal propeller that thrusts the submersible forward and a secondary, smaller propellers used to manoeuvre the submarine.

Figure 6.7: View inside the open submersible, hull, motor and propeller.

The size and placement of the propeller is established based on shape of the controlled submarine [168, 169].

The shape of the designed submersible is perfectly symmetrical and aqua-dynamic in order to facilitate forward movement through the non-Newtonian environment. The hull's reduced dimension suggests as optimal solution to use a three-blade propeller equal in diameter to the wideness of the robot. The robot's movement is only longitudinal through the two tubes, hence eliminating the need of secondary propellers. Notice that the similar diameters of the tubes and the robot make it impossible for the robot to turn inside the two tubes. In other words, motions are limited to forward or backward movements along the X axis. Consequently, the propeller is placed in the rear, central to the symmetry line of the robot, guaranteeing the maximum yield of the thrusting force versus its relative velocity. The chosen thrusting unit is a 40 mm, 3-blade propeller, built by Graupner.

A 3V DC motor is responsible for rotating the propeller. The motor connects to the thrusting unit through a shaft which presents a water tightening gasket. The reduced-size motor has a diameter of 6 mm and a length of 16 mm. The maximum angular velocity is 1650 rpm and the transmission ratio is 25:1. The motor driver is the DRV8833 circuit.

The submersible's hull, motor, gasket and the 3-blade propeller are presented in Fig. 6.7. The screwing holes are visible in the front and in the rear. As observed, the DC motor fits inside the provided volume.

Acceleration is measured using the BNO055 9-DOF magnetometer built by Bosch. The circuit features an accelerometer, magnetometer and gyroscope. An accurate position is obtained by fusing the sensor data and filtering the signals inside the board: acceleration, linear acceleration,

magnetic field measurements. The board has an integrated magnetometer that offers a variety of options for data readings. Another advantage is the low energy consumption and small size that fits well inside the printed hull.

Positioning of the submersible is obtained by double integrating the acceleration signals. The well known problem of error accumulation towards infinity during data integration is caused by the noisy signal read from the accelerometer sensor. The BNO055 already has a pre-implemented filtering algorithm for the measurements and it also features the ability to extract gravitational acceleration, providing only linear acceleration data if proper settings are used. The linear acceleration is integrated over short periods of time and then the signals are reset to zero, thus avoiding the effect of a slow accumulating error over large periods of time. Data regarding positioning has been validated experimentally proving the algorithm accurate and reliable over time [170].

The ceramic sensor used for impedance measurements is the DS550 from Dropsens.Its functionality regarding possible measurements of substance/species concentration will be detailed in Section 6.5.

As aforementioned, the *brain* of the entire submersible is the ESP8266 microcontroller. This particular device has been chosen due to its integrated WiFi module. The microcontroller can be programmed through the Arduino IDE that has an easy to understand syntax similar to C language. All the data measurements and computations are performed inside the ESP8266 module. This communicates with the BNO055 via the I2C protocol, registers acceleration data, performs the integration and obtains the position. The ESP communicates also with an external server via the TCP/IP protocol where it sends the positioning data at predefined sampling time intervals.

The entire unit is fed by a 3 V CR2 type lithium-ion battery. A TPS61090 voltage booster circuit ensures a stabilized operating tension of 3.3 V. Several batteries are available on the market with different shapes and sizes which fit inside the submersible's hull.

The actual version of the robot has been designed based on components that are largely available on the market. The design is also cost-effective for possible mass production for educational purposes. However, the size of the submersible can be dramatically reduced by using embedded electronic circuits that are custom built for this particular purpose. A diagram showing the selected electrical components as well as the robot's functionality is given in Fig. 6.8.

A snapshot of the device ready for air tightening is shown in Fig. 6.9, while the sealed submersible with all the embedded electronics and mechanical parts is displayed in Fig. 6.10.

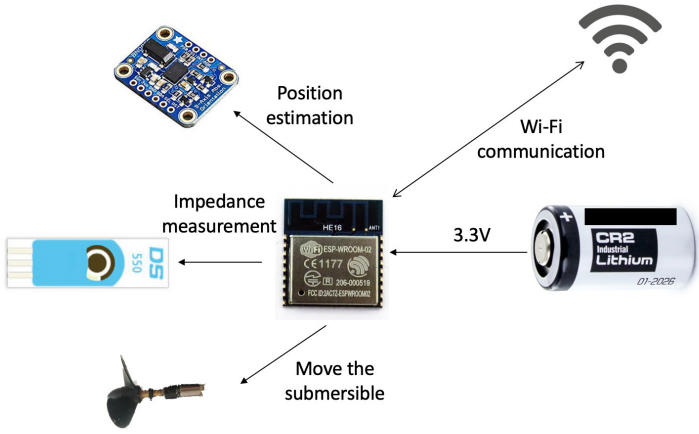

Figure 6.8: Functionality diagram of the submersible

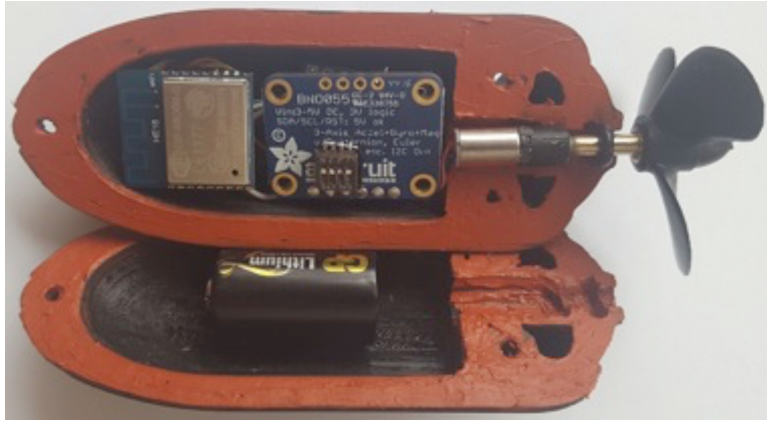

Figure 6.9: Snapshot of the open hull of the submersible

Figure 6.10: Snapshot of the sealed submersible

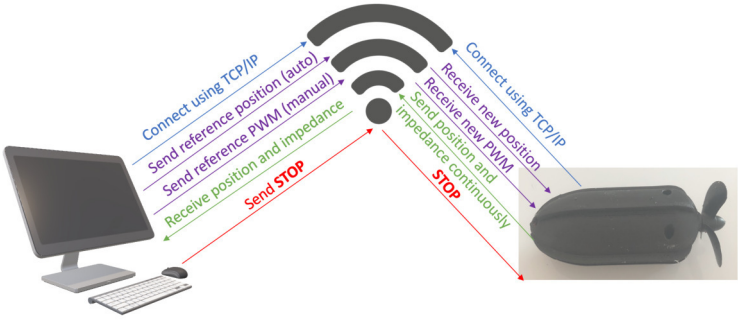

Figure 6.11: Robot and server communication diagram

6.2.4 Software Development

One of the main features of the platform is the ability to communicate via WiFi. This means that data can be sent in real-time and logged into a server for further in-depth analysis. The software part of this benchmark project is divided into server side and robot side. The connection among them is realized using the TCP/IP (Transmission Control Protocol, Internet Protocol) protocol over WiFi. A diagram of the shared functionality between the robot and the server is presented in Fig. 6.11.

6.2.4.1 Server Functionality and Implementation

The server runs a script written in MatLAB that connects to a router using TCP/IP. The protocol is secure and guarantees that the messages are sent without errors from one device to another. TCP/IP fragments the bytes flux and sends them to the TCP/IP stack which ensures proper routing of the packages from source to destination. The bidirectional com-

munication is done by sending or receiving packets of bytes that incorporate string values. Connection issues such as communication drop and reconnecting attempts are addressed inside the TCP/IP protocol. The communication is possible if both devices are connected to the same WiFi network. A pseudocode illustrating the server's implementation logic is given in Algorithm 3.

The main task of the server is to continuously receive data regarding the current position and substance concentration values as recorded by the robot. Data logs are created for every test. The sampling time is 0.1 seconds, meaning that 3600 data values are saved every minute. The servers logs the data allowing further processing and analysis.

The server is also able to dictate the operating mode of the robot: manual or automatic. The user inputs into MatLAB's command window desired operating values and the information is sent to the robot.

In the manual scenario, the server can send a PWM value (with a duty ratio between 0 and 1) to be applied to the motor acting the propeller. The velocity of the submersible depends on the applied PWM but also on the environment's characteristics such as the pressure and flow inside the two tubes. In the manual mode, the user has no control on the velocity of the submersible, but acts on the propeller's rotation. This scenario is useful for modeling a mathematical relation between the applied PWM and the robot's velocity/position.

For automatic operation, the operator can introduce a reference position to which the robot should navigate. For this case, the server can control only the position at which the robot stops, without being able to control the velocity or the PWM applied to the motor. Positioning control algorithms are implemented locally on the submersible's microcontroller. Closing the control loop over WiFi is not a reliable method to implement discrete control actions because of variable time delays in the communication protocols. Dedicated algorithms that tackle variable time delay processes or over the WiFi control can be easily implemented by extending the current implementation for the server.

The server offers the ability to send a STOP command that overrides all the operating modes. Upon receiving the STOP command, the robot halts its movement regardless of the enabled operating mode. This feature has been designed for stopping the submersible in emergency situations.

6.2.4.2 Deploying the Submersible

By comparison, programming the submersible is a more complex task than programming of the server. Several modules that interprets data from the sensors as well as the communication part need to be programmed. The code is written using the Arduino IDE.

The first step is to configure the BNO055 magnetometer to measure linear acceleration with a 2G accuracy. The BNO055 Arduino library is

Algorithm 3: An insight into the server's implementation

```
Data: User inputs commands into the MatLAB command window
Result: Server sends instructions to the robot based on the user's input
perform initialization;
establish connection via TCP/IP;
while communication ongoing do
    read position and concentration data;
    log data received from the robot;
    read user input;
    if STOP then
        send STOP message to robot;
    else
        if user sets manual mode then
            send desired pwm to robot;
        if user sets auto mode then
            send position to robot;
    while messages not received successfully and max retries not reached do
        retry sending;
```

used for acquiring data from the sensor. In order to set the 2G accuracy, the library is extended to include this functionality. Then, the linear acceleration data should be interpreted as velocity and positioning data. Kinematic equations of motion express a connection between acceleration, velocity and positioning:

$$a = \frac{v_f - v_i}{t_f - t_i} \tag{6.1}$$

$$v = \frac{d_f - d_i}{t_f - t_i} \tag{6.2}$$

where v_f and v_i are the final and initial velocities, d_f and d_i are the final and initial displacements with t_f and t_i the final and initial times. For the formula to be effective, $t_f - t_i - > 0$. However, since the code is written for a microcontroller, the time difference becomes the sampling time of the signal acquisition, chosen as 0.1 seconds. In order to compute the velocity and position of the submersible, the following formulas are implemented in the Arduino IDE:

$$v_f = a(t_f - t_i) * v_i \tag{6.3}$$

$$d_f = v_f(t_f - t_i) * d_i. \tag{6.4}$$

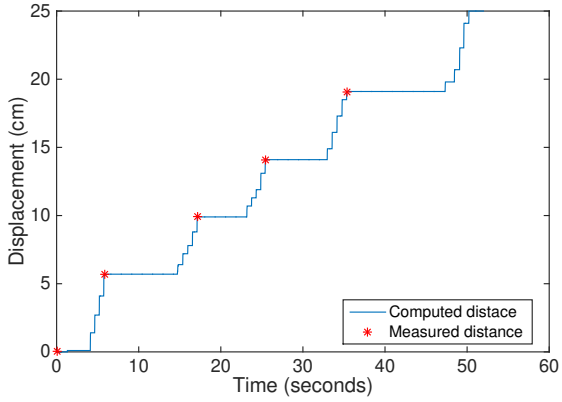

Figure 6.12: Experimental validation of the displacement algorithm based on BNO055 acceleration data

Experimental tests depicted in Fig. 6.12 validate the displacement logic used to compute the robot's position. Additional measurements have been performed using a video camera and image recognition to register the position of the vehicle. The camera is placed above the circulatory system with a clear fluid (i.e. detergent) to accurately see the transiting vehicle. The footage is used at the end of the experiment to validate the positioning/velocity measurement algorithms. It can be seen that the chosen algorithm registers the positioning in an accurate manner.

The substance concentration is measured with the DS550 sensor which is directly connected to the ESP microcontroller. The sensor sends this data via one of the available analogue ports. There is no special setup required for the concentration sensor and reading the data is realized with the same sampling time as computing the position.

The following operating modes are implemented on the submersible:

- **manual**: receive a constant PWM value from the server and feed it to the propeller;
- **auto**: send a reference velocity or position, the robot will navigate using a local control law for velocity/positioning;
- **explore**: a fusion between the *auto* mode and environmental assessment with the ability to halt the robot for a period of time in areas where changes are detected;
- **emergency**: overrides all other operating modes, halts the robot and interrupts all communication with the server.

The robot communicates with the server via WiFi. After the connection is successfully established via the TCP/IP protocol, the robot

sends its position, environmental measurements and PWM values to the server every 0.1 seconds. In addition, the robot listens/awaits for new instructions from the server. The server sets the operating mode of the submersible into one of the previously mentioned: "manual", "auto", "explore" or "emergency".

The manual mode is used to send only a PWM value to the robot, i.e.: "manual: 25". This will be further fed to the propeller until a new command arrives. Manual mode is used for velocity/positioning identification data and for the extraction of the submersible from the setup.

The auto mode is given by the message "auto:" followed by a desired position or velocity in meters or meters/second, respectively. Such commands look like "auto: position: 0.8" or "auto: velocity: 0.1". The auto mode works only if discrete-time control laws are implemented on the microcontroller. The logic automatically chooses between the position or velocity controller with respect to the received input.

Explore mode is the most complex scenario implemented and will be discussed in detail with regard to context awareness in Section 6.5.

The last operating mode is an emergency stop that overrides any other command and halts the robot with the command "STOP". It is designed for emergency situations, hence all communication is lost and the submersible is shut down. The mode is not intended to be used for stopping the propeller, this is performed with the manual mode with 0 PWM duty ratio. After the emergency is activated, the robot cannot be restarted by the server and has to be removed from the tubes for manual restart.

Apart from the previously described scenarios, the robot also covers communication problems such as interruptions or communication loss. If the communication is lost, 5 re-connection attempts are performed before enabling the sleep mode. When the robot is sleeping, it still searches for connection attempts from the server every 10 seconds in an energy efficient manner. The robot is automatically turned on when the server re-connects to it and waits for new commands before re-starting its movement.

A brief view onto the robot's software implementation flowchart is presented in Algorithm 4.

Algorithm 4: An insight into the robot's software implementation

```
Data: Server sends command to the submersible
Result: The robot sends positioning and concentration data to
        the server and operates according to the server's input
set 2G accuracy of BNO55;
while server communication successfull do
    read acceleration;
    compute velocity;
    compute position;
    read concentration;
    listen to new messages;
    change operating mode if necessary;
    if emergency then
        halt robot;
        shut down microcontroller;
        break;
    if manual then
        robot receives new pwm command;
        robot received new position;
    else if auto mode then
        register new position;
        compute pwm using control law;
    else if explore mode then
        robot stops;
    set pwm of the motor;
    send position, concentration and pwm values;
if communication lost then
    try to reconnect 5 times
stop;
go into sleep mode until new communication is established;
```

6.2.5 Benchmark Versatility For Research and Education

The platform proves to be an important ally into demonstrating concepts such as submerged motion dynamics, non-Newtonian dynamics and properties, programming a client-server architecture, implement control strategies in real life situations, experiment with various fluid dynamics, mimicking context changing operability tasks, etc.

There is also the possibility of replacing the non-Newtonian fluid with a Newtonian one (water) and experiment with both environments in order to compare their interaction with submerged objects. Analyzing the submersible's motion inside the two environments provides an insight into the braking effect of the viscoelastic characteristic of the non-Newtonian fluid. Also, several experiments can be made using non-Newtonian fluids with different viscosity.

Another challenge is exploring the pressure change occurring at the joining point of the two pipes. The robot's trajectory goes through the larger pipe which features a lower pressure and lower velocity of the fluid flow into the smaller tube with higher pressure of the fluid. Pressure also depends upon the viscosity and non-Newtonian features of the fluid. Non-Newtonian behavior may also be studied by increasing the flow from the pump and analyzing it's effect of the submersible's dynamics (e.g. buoyancy).

The platform is also useful into programming submerged objects as well as programming a client-server architecture and setting up the communication between them. Communication related issues as well as effects of decision making actions such as choosing the right protocol can be easily illustrated using the built setup.

The submarine can be programmed into multiple ways to study submerged dynamics. A relationship between the propeller's angular velocity, generated thrust, fluid viscosity and submersible velocity can be experimentally established with respect to non-Newtonian braking effect. Also, operating modes of the submersible can be explored for system identification purposes.

Detection of variations in the substance concentration (or density) measurement values relates to determining areas of relative high impedance values. Targeted drug delivery may be introduced as an educational concept by creating decision taking algorithms and developing custom treatment controllers in order to release substance where it is most needed. Other controllers targeting velocity or positioning may also be experimentally tested inside the fluid, familiarizing the user with actual real-life implementation of different control strategies.

The components needed to recreate the benchmark are given in Tables 6.1 and 6.2.

Table 6.1: Circulatory system hardware components

Component	Description
Tee elbow with PVC door	Used as immersion and submersion points, 2 pieces
Small tube	Polyurethane with metal insertions $R = 51/1000$ (m), $h = 0.9/1000$ (m), $\kappa = 0.1$.
Large tube	Polyurethane with metal insertions $R = 80/1000$ (m), $h = 0.9/1000$ (m), $\kappa = 0.9$
Funnel	Narrow diameter $d_n = 0.102$ (m), Wide diameter $d_w = 0.16$ (m)
Tube	Tube to recirculate the fluid, any diameter
Plumbing elbow	Connection purpose, 2 pieces
CM10P7-1-24	Variable flow pump
EM-174A	Pump driver
SNS-FLOW201	Flowmeter
NI myRIO	Real-time microcontroller
Power Supply	24 (V) supply
Non-Newtonian fluid	Approx. 10 (l) e.g. water and starch mixtures, conditioning shampoo, liquid detergent

Table 6.2: Submersible hardware components

Component	Description
Submersible case	The custom hull, 2 halves, 3D printed
CRC232	Battery powering the submersible
TPS61090	Power booster circuit that ensures the nominal voltage of [+2.7, 3.0]V
ESP232 WROOM-02	WiFi module and microcontroller
Bosch BNO055	Inertial Measurement Unit - Accelerometer, Gyroscope and Magnetometer
Graupner 3 blade propeller	Propeller for miniature ship design used to thrust the submersible
DC motor	10 mm x 6 mm DC motor
DRV8833	Motor driver
Screws	Self locking screws, 3 pieces
Glue	Gasket sealant, 1 tube

6.2.6 Submersible Miniaturization Opportunities

The purpose of this study is to provide a framework to analyze the interaction between the moving object and the non-Newtonian fluid. The concepts are proven at a large scale, and the current dimension of the submersible is far from reaching targeted drug delivery sizing. Non-Newtonian fluid dynamics analysis is an emerging topic, one of the novelties of this study being the accessible experimental setup which is affordable and reproducible.

The current submersible sizing is justified by the desire to build the setup by entirely using widely available components at a reasonable price. In addition, the microcontroller has been chosen to be easily programmed using the Arduino IDE, a popular programming language based on C language compiler, a lighter alternative to embedded C programming kit that is studied mostly by students with electrical oriented degrees. The motivation behind this choice is the ease of reproduction for both research and educational purposes.

The main factors that influence the increased size of the submersible are the battery, the propeller, and the impedance sensor. The 40 mm propeller has been chosen such that the submersible is able to navigate counter currents, in fact not needed for the current purpose of the setup. The DC motor has a reduction box in order to be able to spin the large propeller, which can be eliminated when the propeller size is reduced. Another aspect that adds to the overall sizing is the 3D printed hull featuring sturdy walls with a thickness of approximately 4 mm. The increased wall thickness ensures that the two halves of the case can be dismounted and re-glued without damage, for easy access to the components during the development and testing phase of the submersible. Since the submersible has reached its final version both from design and programming perspectives, the hull's thickness can be drastically reduced.

For instance, reducing the size of the submersible to 15 mm in length and 8 mm in width can be realized by replacing the current ESP8266 microcontroller with a dedicated printed circuit board (PCB), changing the CR123A battery with a smaller sized 3.3 V alternative, eliminating the motor's reduction box, and reducing the propeller's diameter from 40 mm to 8 mm. The battery will always be a critical element inside the robot because it can produce damage through heating. An alternative to the battery is the usage of a supercapacitor [171]. Wi-Fi can be replaced by Bluetooth low energy (BLE) protocol for energy efficiency, and the 3D printed hull will be realized through Teflon injection [172] or milling. The advantage of this approach is that the design of the submersible is similar to the current solution. However, the drawback is that the cost for a prototype is increased, as well as the need to custom made PCBs, instead of simply buying the components.

Further dimension reduction can be performed in the 1-2 mm scale. In

this scenario, the entire propulsion system must be completely redesigned. The motor and the propeller should be replaced with piezoelectric materials (the most popular being Lead Zirconate Titanate) or any other material that produces vibration through deformation. The submersible's motion concept is based on propellant-less thrusting of the object using vibration [173, 174]. Apart from complete redesign of the propeller, the battery is also replaced by an environment-based energy harvesting circuit of reduced size. Multiple options are available based on temperature, vibration, chemicals, etc., such as those detailed in [175]. Furthermore, the impedance sensor is replaced by printed electro-mechanical cells of nanometer dimensions [176]. In this scenario, the submersible's dimension fits the targeted drug delivery paradigm. However, producing a single prototype is difficult with costs spanning over kEUR, making the platform inaccessible for educational purposes.

The generic non-Newtonian properties discussed in our study hold irrespective of the setup scalability. We speculate that particular material features may be detected at some scale than other (i.e. micro-, meso- and macro-scale specific properties). However, the modelling, identification and control methodologies presented hereafter will be valid irrespective of the setup scale.

6.3 Motion Dynamics Modeling for Submerged Objects in a Non-Newtonian Environment

A two-step procedure is proposed to obtain an accurate model for the interaction between the submersible and the non-Newtonian environment. The first step is to develop a generalized navigation model inspired from ship propulsion. Ship propulsion models are available throughout literature and can serve as a basis to start calibrating the non-Newtonian floating object framework from Chapter 3. The fractional order dynamics are determined using the ship propulsion model as a startup point to search for a fractional equivalent to better describe the dynamics of the submersible. For determining the final fractional order model, a minimization procedure is employed that searches for the minimum error between the simulated model and the experimentally obtained positioning data.

The modeling procedure implies the adaptation of available submerged ship propulsion models that are extended to non-Newtonian dynamics based in the fractional order framework introduced in Chapter 3.

6.3.1 General Navigation Model for Submerged Objects in Newtonian Fluids

Firstly, the submarine dynamics are divided into smaller parts that influence each other. A schematic is depicted in Fig. 6.13.

The modeling goal is to obtain: i) a model that connects the motor voltage to the angular velocity of the propeller, ii) a model that connects the angular velocity of the propeller to the generated thrust and iii) a model that connects the thrust to the velocity.

A connection between the motor voltage and the propeller's angular velocity is determined experimentally by applying a 2.4 V step input on the motor and measuring the resulting velocity. An identification procedure is employed resulting in a model with first order dynamics:

$$H_{motor} = \frac{700}{0.022s + 1}. \tag{6.5}$$

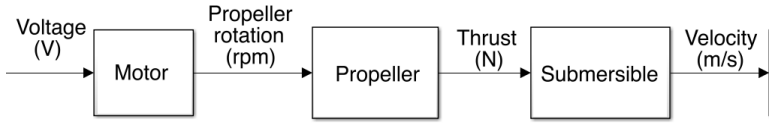

Figure 6.13: Schematic of the submersible's individual parts considered for modeling purpose.

The propeller's rotation is then connected to the generated thrust. The particularities of the propeller such as the number of blades, radius R (m), rotor blade area A (m^2) and a thrust coefficient C_t are known to strongly influence the output [164].

$$Th = C_t \cdot \rho \cdot A \cdot (w \cdot R)^2 \tag{6.6}$$

where Th is the thrust (N), ρ is the fluid's density (kg/m^3), R the radius (m) and w represents the propeller's speed (rad/s). The area is given by:

$$A = \pi \cdot d^2/4 \tag{6.7}$$

where d is the diameter (m).

The characteristics of the propeller as well as the chosen fluid/material density are known. In order to obtain a physical model for Newtonian submersion which is closer to the parameters of the experimental setup, the density value of liquid soap is considered. The Graupner 3-blade propeller thrust coefficient has been determined experimentally by [177].

Linearizing (6.6) around a working propeller speed of 1 m/s, gives the relation between the propeller's rotation and the thrust generated by it:

$$H_{thrust} = \frac{\Delta Th(s)}{\Delta W(s)} = C_t \cdot \rho \cdot A \cdot R^2 \cdot w_0 \tag{6.8}$$

where ω_0 is the initial angular velocity.

Next, we search for the relation between the propeller generated thrust and the velocity of the submersible. The interaction of a single-propeller submarine which is operating in Newtonian environments (such as water) is given by the following nonlinear equation:

$$(M_{RB} + M_A)\dot{\nu} + (C_{RB} + C_A)\nu + (D_l + D_n)\nu = \tau. \tag{6.9}$$

where M_{RB} is the inertia of the rigid body, M_A is the added mass, C_{RB} is the rigid centripetal force and the Coriolis force, C_A is the hydrodynamic centripetal and Coriolis force, D_l is the linear damping and D_n is the matrix representation of the inertia of the rigid body with added mass.

The velocity of the submarine can be written as a matrix ν composed by single axis velocities u_x for X axis, v_y for the Y axis and r_z for the Z.

$$\nu = [u_x \ v_y \ r_z]^T \tag{6.10}$$

For the purpose of this study, we simplify the model by ignoring the Y and Z axis effects. Hence, only the motion along the longitudinal X axis is considered. In this case, the velocity matrix reduces to:

$$\nu = [u_x \ 0 \ 0]^T. \tag{6.11}$$

The linear velocity equation around a working operating point u_{x0} can be written as:

$$\nu = \nu_0 + \Delta\nu = [u_{x0} + \Delta u_x \ 0 \ 0]^T. \tag{6.12}$$

Considering a submarine of mass m moving with a linear velocity gives the generated thrust equation:

$$\Delta Th = [-2u_{x0}X_{|u|u} - X_u \ 0 \ 0]\Delta\nu + [m - X_{\dot{u}} \ 0 \ 0]\Delta\dot{\nu}. \tag{6.13}$$

from where the connection between propeller's thrust and the longitudinal velocity can be written as:

$$H(s) = \frac{\Delta U(s)}{\Delta Th(s)} = \frac{1}{(m - X_{\dot{u}})s - 2u_0X_{|u|u} - X_u} \tag{6.14}$$

The longitudinal acceleration on the X axis adds a surged mass coefficient denoted by $X_{\dot{u}}$:

$$X_{\dot{u}} = \frac{-4\beta_r\rho\pi}{3}(\frac{d}{2})^2. \tag{6.15}$$

where ρ (kg/m^3) is the density of the fluid in which the submarine operates, β_r is an empirical parameter based on the ellipsoidal shape of the robot and $d(m)$ is the diameter of the hull. X_u is the force component given by:

$$X_u = -\rho V_l A_f C_d \tag{6.16}$$

where $A_f(m^2)$ is the frontal area of the submarine, $V_l(m/s)$ gives the vectorial magnitude of the liquid's flow velocity and C_d is a drag coefficient which is experimentally determined by the manufacturer of the propeller. The surge drag coefficient $X_{|u|u}$ is:

$$X_{|u|u} = \frac{1}{2}\rho C_d A_f. \tag{6.17}$$

The angular velocity generated by the propeller is strongly dependent on the angular velocity of the motor acting upon the propeller which in turn is a function of the applied voltage. The relationship between the motor voltage and w can be modelled by a first order transfer function:

$$H_{motor}(s) = \frac{k_m}{T_m s + 1} \tag{6.18}$$

where k_m is the gain of the process and T_m is the time constant.

An analytic model for the velocity of a submerged object into a Newtonian environment that connects the motor voltage to the velocity of the submersible within the liquid is expressed as

$$H_{IO}(s) = \frac{k_m C_t \rho A R^2}{(T_m s + 1)[(m - X_{\dot{u}})s - 2u_{x0}X_{|u|u} - X_u]}. \tag{6.19}$$

Table 6.3 illustrates all the numerical parameters needed to determine the model between the velocity and the thrust.

Table 6.3: Submersible and propeller parameters.

Parameter	Value
C_d	0.6
ρ	1060 kg/m^3
A_f	0.031 m^2
d	0.04 m
V	0.1 m/s
β_r	0.2473 [-]
u_0	1 m/s
m	0.1 kg

Combining the three obtained models gives the general navigation model for a submerged object in a Newtonian fluid but with the density of liquid detergent.

$$H_{process} = \frac{232}{s^2 + 60.13 + 667.1} \tag{6.20}$$

Although not entirely physically correct, this model is a good approximation of initial guess.

6.3.2 Fractional Order Modeling of Objects Transiting Non-Newtonian Fluids

A general fractional order model that is similar to the previously determined analytic model from (6.20) can be written as

$$H_{FO-Velocity}(s) = \frac{k_p}{b_1 s^{\alpha} + b_2 s^{\beta} + b_3} \tag{6.21}$$

with k_p being the proportional gain, b_1, b_2, b_3 are coefficients of the Laplace operator s, α and β denoting fractional orders of differentiation.

The fractional order modeling procedure consists in calibrating the Newtonian model onto the acquired experimental data. A minimization procedure is employed that searches the parameters of (6.21) such that the response of the simulated fractional order model fits the acquired experimental data. A cost function used in the minimization procedure is defined as:

$$J = \min \int_0^{\infty} |x_m(t) - x(t)| dx \tag{6.22}$$

where $x_m(t)$ is the experimental measurement at time t and $x(t)$ is the simulated response of the candidate fractional order model.

The results obtained by the minimization procedure depend on the starting point that is chosen to perform the search (i.e. initial search values). In order to obtain a realistic result, with physical meaning, the obtained analytic model is used as a startup point. Hence, the search starts from $k_p = 232$, $b_1 = 1$, $b_2 = 60.13$, $b_3 = 667.1$, $\alpha = 2$ and $\beta = 1$. The search interval of the fractional orders of differentiation is limited to $\alpha \in [1, 2]$ and $\beta \in [0, 1]$ to reduce computation time and obtain a model of reduced order.

The optimization procedure has been implemented in MatLAB using the Optimization Toolbox with the 'active-set' algorithm setting. The obtained fractional order model for the positioning of the submersible inside a non-Newtonian environment is obtained as:

$$H_{FO-Position} = \frac{0.1}{s(0.005682 s^{1.7263} + 0.11031 s^{0.8682} + 1)} \tag{6.23}$$

for the position and

$$H_{FO-Velocity} = \frac{0.1}{0.005682 s^{1.7263} + 0.11031 s^{0.8682} + 1}. \tag{6.24}$$

for the velocity. It is worth emphasizing the values of the fractional orders of differentiation: $\alpha = 1.7263$ and $\beta = 0.8682$, i.e. values inside the imposed intervals.

Fig. 6.14 shows the validation of the fractional order model on position experimental data, while Fig. 6.15 shows the validation on experimental velocity data. The test is based on applying a 0.3 PWM duty ratio to the motor.

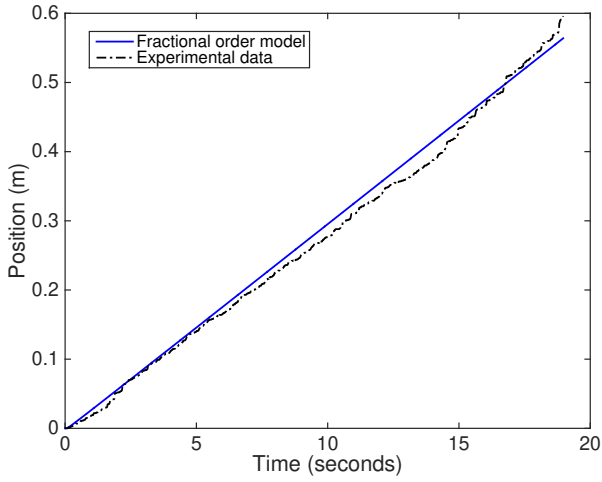

Figure 6.14: Experimental validation of the obtained fractional-order model for the robot's position in the non-Newtonian fluid

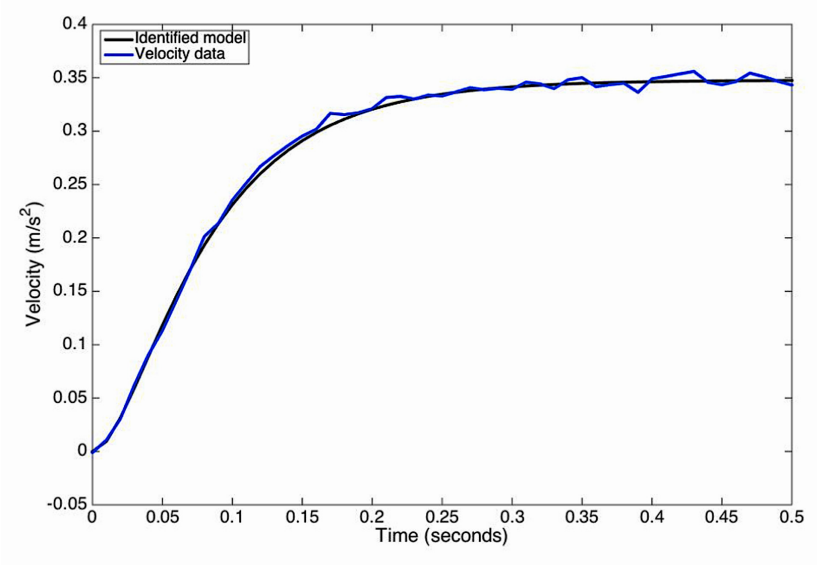

Figure 6.15: Experimental validation of the obtained fractional-order model for the robot's velocity in the non-Newtonian fluid

6.4 Control of an Object Transiting a Non-Newtonian Fluid

Viscoelasticity is a phenomenon better described by fractional order models than by the classical, integer order motion dynamics as has been previously explained in Chapter 3. Naturally, fractional order control strategies are more suitable for this type of processes, as summarized in Chapter 2. However, control strategies for this type of environments should also include the fractional order characteristics, otherwise the extended dynamics will be limited by integer order control actions.

The reasons stated above motivate the development of a fractional order controller for the positioning of the submersible, such that substance concentration values can be easily acquired and corresponding action can be taken. For this purpose, we propose to design a fractional order Proportional Derivative (FO-PD) controller.

The transfer function of a FO-PD controller is given by:

$$H_{FO-PD} = k_p(1 + k_d s^{\mu}) \tag{6.25}$$

where k_p represents the proportional gain, k_d the derivative gain and μ gives the fractional order of differentiation. For an integer order controller, $\mu = 1$, while for the generalized case of a fractional one the values are limited to the $\mu \in (0, 1)$ interval. The process of controller tuning involves determining the three parameters characterizing the controller.

The most popular fractional order tuning methodology is chosen, consisting of solving a system of frequency domain nonlinear equations related to the gain crossover frequency, phase margin and robustness characteristics.

$$|H_{FO-PD}(j\omega_{cg})H_{FO-Position}(j\omega_{cg})| = 1. \tag{6.26}$$

The phase margin equation imposes a value ϕ_m for the open loop system at the gain crossover frequency ω_{cg}. The phase equation is expressed as

$$\angle H_{FO-PD}(j\omega_{cg}) + \angle H_{FO-Position}(j\omega_{cg}) = -\pi + \varphi_m. \tag{6.27}$$

The phase margin and gain crossover frequency specifications ensure a stable closed loop system as well as a reduced settling time for the controlled process' response.

The last frequency specification is related to the closed loop robustness to gain uncertainties. In a real-life context of operation of the cardiovascular system, robustness is essential because of the particularities of every treated individual and various actions (rest, exercise). The developed controller must perform similarly even if the process parameters vary in

time. In frequency domain, robustness implies to have a constant phase around the gain crossover frequency. This further implies that if the gain crossover frequency slightly changes, the value of the phase remains the same and the controller's performance is consistent. A constant phase graphically translates into a straight line. In order to mathematically express the required straight line, we impose a zero derivative of the phase around the gain crossover frequency:

$$\frac{d(\angle H_{FO-PD}(j\omega)H_{FO-Position}(j\omega))}{d\omega} = 0|_{\omega=\omega_{cg}} \tag{6.28}$$

The three parameters needed for the fractional order PD controller are obtained by solving the system of nonlinear equations formed by (6.26, 6.27) and (6.28). The gain crossover frequency and the phase margin are imposed with respect to [46] such that the resulting controller has physical meaning. Imposing the gain crossover frequency as $\omega_{cg} = 0.02$ rad/s and the phase margin $\phi_m = 72\,\text{deg}$ gives the following fractional order PD controller

$$H_{FO-PD} = 65.0028(1 + 0.0305s^{0.6524}) \tag{6.29}$$

which is guaranteed to be robust by the third frequency domain specification.

The frequency Bode diagram obtained with the computed fractional order PD controller is shown in Fig. 6.16. As observed, all imposed frequency domain constraints are met.

The usability of the FO-PD as a positioning controller requires imposing a null steady state error. However, the transfer function is obtained by adding an additional integrator to the velocity transfer function which already ensures a zero steady state error, meaning that the robot will stop at the imposed reference position.

For physical implementation, the controller from (6.29) has been mapped to the discrete-time domain using the method provided by [132]. The discretization method represents a direct mapper between the fractional order transfer function and its discrete time representation. The resulting discrete time model has order 5, validated by comparing the frequency responses of the initial continuous time model to its discrete time representation. The control law has been implemented as a recurrence relation inside the submersible using the ESP8266 microcontroller. The discrete sampling frequency is 100 Hz, the same as that used for the real-life measurements. Several experiments have been performed by sending a desired position to the submersible over WiFi and analyzing the closed loop position profile. The experimental test from Fig. 6.17 has been performed by sending a reference position of 0.1 m. At moment $t = 20$ seconds, a bias disturbance of -0.05 m is given in software in order to validate the disturbance rejection capabilities. As observed, the submersible successfully reached the desired position, and the disturbance is rejected without the presence of overshoot.

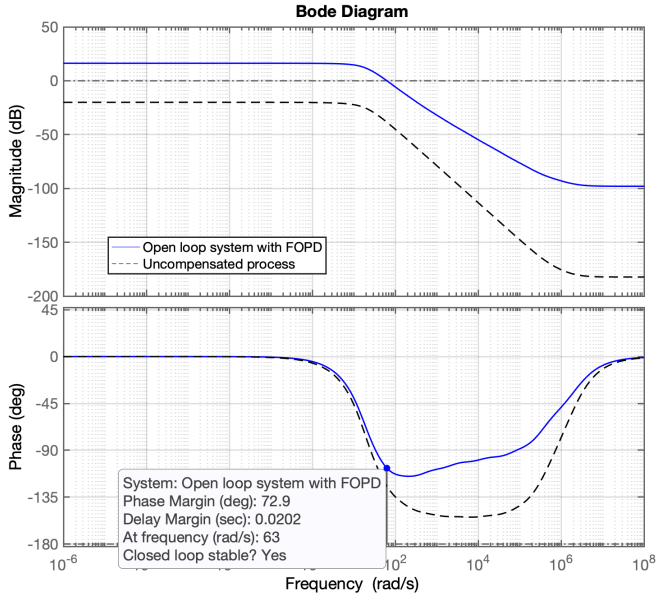

Figure 6.16: Bode diagram of the open loop system with the fractional order PD controller

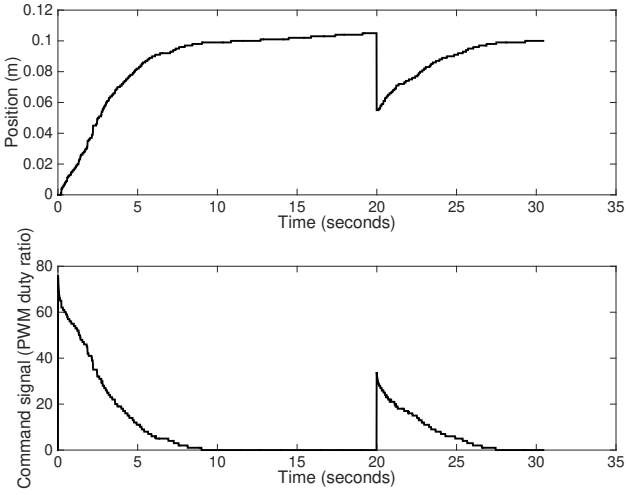

Figure 6.17: Fractional order FO-PD controller experimental validation in the non-Newtonian environment.

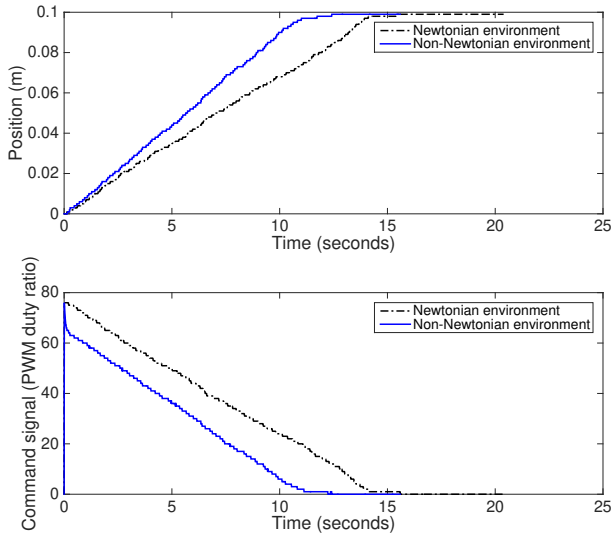

Figure 6.18: Fractional order FO-PD controller experimental robustness validation in Newtonian and non-Newtonian operating conditions.

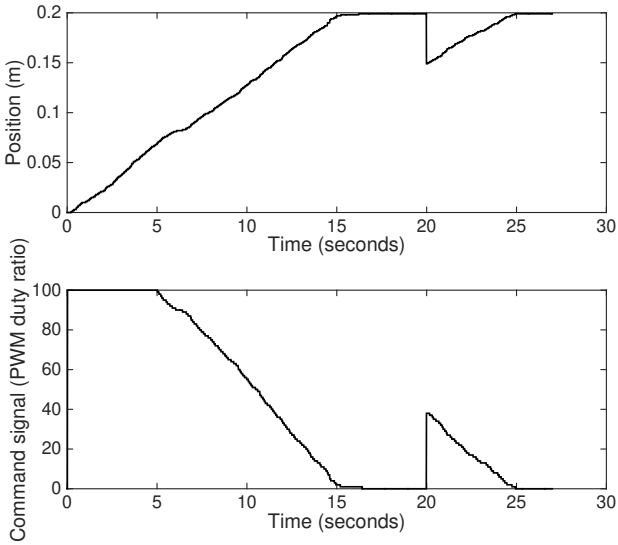

Figure 6.19: Fractional order FO-PD controller experimental validation in a Newtonian environment.

Experimental robustness tests have been performed by replacing the non-Newtonian liquid inside the cardiovascular setup with tap water. The same desired input is given to the submersible in the two operating environments, Newtonian and non-Newtonian, and the position profile for both cases is presented in Fig. 6.18. It can be observed that the settling time for the Non-Newtonian case is 5 s faster than the tap water experiment. However, the controller proves to be robust to high environmental variations, such as the nature of the fluid, proving robustness to more than just the process's proportional gain changes.

Disturbance rejection capabilities are also analysed in the Newtonian framework in Fig. 6.19. A software disturbance is also introduced at moment $t = 20$ seconds, which is also successfully rejected.

The experimental tests provided in this section demonstrate that the chosen fractional order model calibrated based on analytically derived equations is accurate enough to describe the dynamics of a small scale submersible in non-Newtonian fluids.

The control strategy is designed for non-Newtonian operating conditions. Since the controllers have been tuned using the isodamping frequency domain specification, they are robust to model uncertainties. Hence, the controllers also operate in other environments, as has been shown by the experimental data. The only limitations connected to the control strategy arise from the physical limitations of the submerged vehicle itself.

In terms of closed loop performance, the experimental results clearly prove the efficiency and robustness of the proposed fractional order controller for accurate positioning of the submersible in non-Newtonian fluids.

6.5 Context-Awareness in Non-Newtonian Fluids

The submersible is context-aware from two point of views: control law computation based on context (regression data) and environmental recordings of its varying surroundings.

6.5.1 Event Based Control - a Solution to Energy Efficiency

Event based control is the natural solution to context awareness paradigms of control laws. Discrete-time systems are usually sampled in a periodic manner, known as Riemann sampling. In traditional approaches, after a period of time T_s has elapsed, the control law computes a new value for the manipulated variable, regardless if it is necessary or not. For example, in a steady state regime, the control signal is usually constant and a new

value is computed every T_s seconds that is identical to the previous control value. This means that the effort performed to compute the new control variable overburdens the core of the system and it also drains the battery levels [178].

A solution to this problem lies in discrete-time control laws implemented with aperiodic sampling, known as Lebesgue sampling. Event-based control strategies are based on Lebesgue sampling, every control computation being triggered by a context. A context manager defines events that should trigger new computations of the control signal, known as event detectors. The laws are customized for the need of every process and usually involve the error value being inside a predefined interval and a safety condition, ensuring that at least one control value is computed in an apriori defined maximum time period. The objective of the event-based control strategy is to reach the objective defined as the reference of the process [92].

The event-based solution is particularly useful for the submersible case study in order to avoid the computation of the control law taking most of the CPU allocation, the control signal being computed locally on the submersible. Traditional, non-event-based control algorithms should run asynchronously to all other tasks such as data acquisition, position computation and server communication. However, the event-based implementation removes this constraint through the usage of variable sampling techniques. Another benefit is the improvement of energy efficiency. Experimental tests suggest that using a context aware control strategy such as event-based control, the battery life is improved up to 4 times. Control values computations are reduced by 90%. Making battery studies, it was observed that the battery is mostly drained by ongoing closed loop control and server communication. Reducing the number of times the control value is computed/applied to the propeller improves battery life.

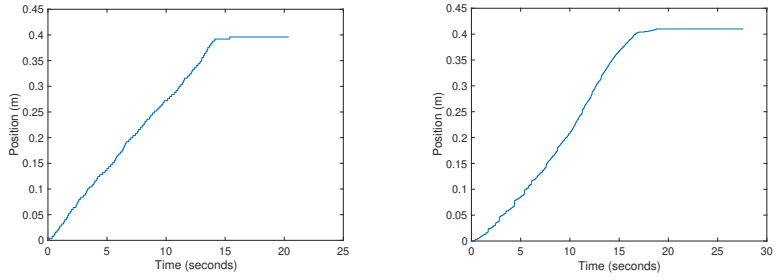

(a) **(b)**

Figure 6.20: Submersible going to a desired position in a) Non-Newtonian fluid and b) Newtonian fluid using fractional order control with event-based dynamics

The fractional order controller from (6.29) is implemented on the experimental robot using the event-based strategy from Chapter 4 and the results are presented in Fig. 6.20 for Newtonian and non-Newtonian fluids, respectively. The experiments involve the robot operating in *auto mode* and receiving the 0.4 m reference position from the server. The null (0) position is considered the position of the submersible at the moment the new reference value is received. As observed from the two figures, the robot successfully reaches the desired position in both environments.

6.5.2 Environmental Awareness

The second context aware aspect of the cyber-physical system is the environmental assessment realized in the *explore* operating mode. An additional module is used to measure fluid impedance that enables detection of changes in environment properties. The *explore mode* implies data acquisition regarding the surroundings with a constant velocity (the control law is implemented using the previously described algorithm) and if a change is detected, the robot halts at the respective area in order to register more (detailed) data. The decision whether or not the robot should halt for a few seconds is realized internally, by the ESP8266 core unit, as explained in the software functionality section of this chapter.

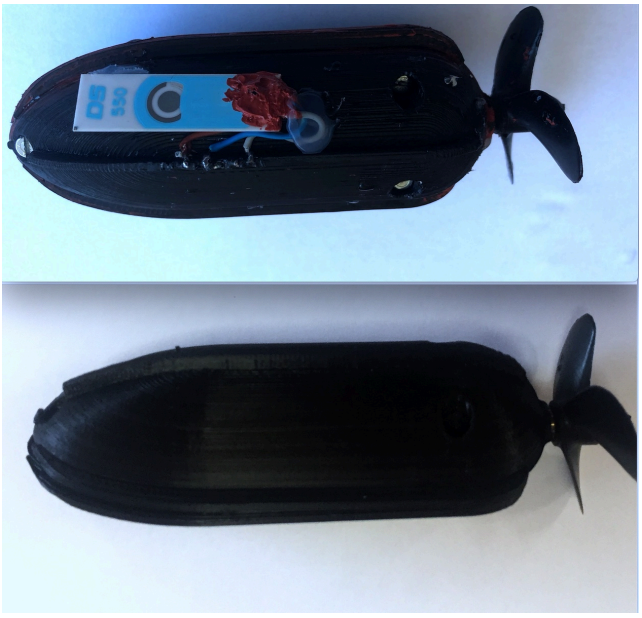

Figure 6.21: Impedance sensor Dropsens 550 attached to the hull of the submersible and connected to the internal microcontroller

As a case study, a Dropsens 550 impedance ceramic sensor has been attached to the robot, as depicted in Fig. 6.21. The sensor may be replaced with any hardware that fits the purpose of the submersed investigation, as long as it does not significantly alter the physical/motion properties of the submersible. Experimental data with nominal concentration values from the non-Newtonian fluid is illustrated as an example in Fig. 6.22.

In the test scenario depicted in Fig. 6.23, the robot navigates a non-Newtonian environment with a constant environmental impedance between 0 and approximately 18 seconds. It can be observed that the environmental values remain unchanged until time 18 seconds, but afterwards there is a gradual change in the recorded voltage values. The context manager implemented inside the robot decided that the robot should continue its movement in order to further inspect the surroundings. The gradual changes were physically created by mixing non-Newtonian fluid with glucose and pouring the mixture in the extraction reservoir.

The second test case is shown in Fig. 6.24. In this test, it can be seen an abrupt change of the environmental variable at time 18 seconds. For this case, the context manager decided to halt the robot for 5 seconds at the area, in order to gather more data. This can be seen in the position data being constant in the $[18 : 23]$ seconds interval. Afterwards, the robot continues its movement through the fluid. This scenario was created by injecting glucose through the pipe, while the robot was already moving towards that position.

The plots from both Figs. 6.23 and 6.24 illustrate data that was logged by the server. In the *explore mode*, the robot autonomously decides its actions based on the environmental context of the fluid in which it is submersed.

6.6 Summary

The present work tackles the modeling of the motion dynamics of an object submerged in a non-Newtonian environment. The mathematical model is developed starting from already known Newtonian interaction model between the submersible and the fluid. The final model is obtained by optimization techniques to describe non-Newtonian interactions on the motion of the vehicle by using real-life data regarding non-Newtonian influences on submerged thrusting. For the obtained non-Newtonian fractional order process model, a fractional order control approach is employed to regulate the submerged object's position inside the environment. The presented modeling and control methodologies are endorsed by real-life experimental data used to validate the veracity of the presented concepts. The robustness of the control strategy is experimentally validated for both Newtonian and non-Newtonian environments.

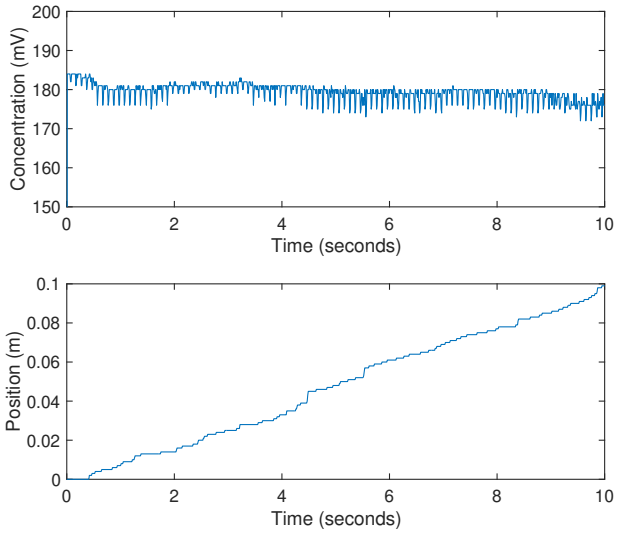

Figure 6.22: Environmental assessment experimental data with the Dropsens 550 sensor under normal operating conditions

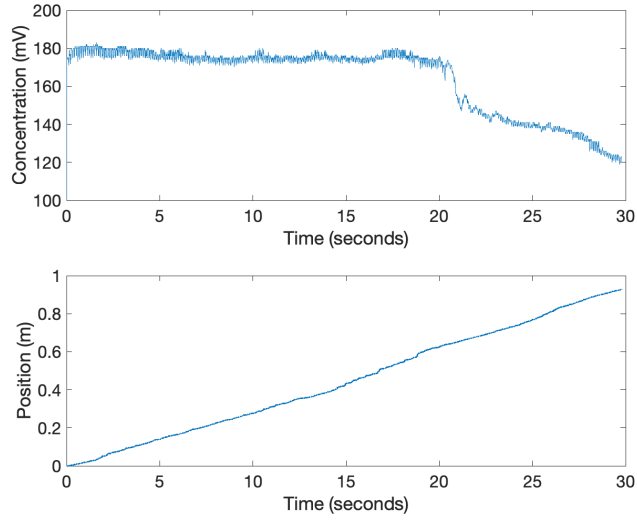

Figure 6.23: Environmental assessment of gradually changing context - glucose mixed with the fluid

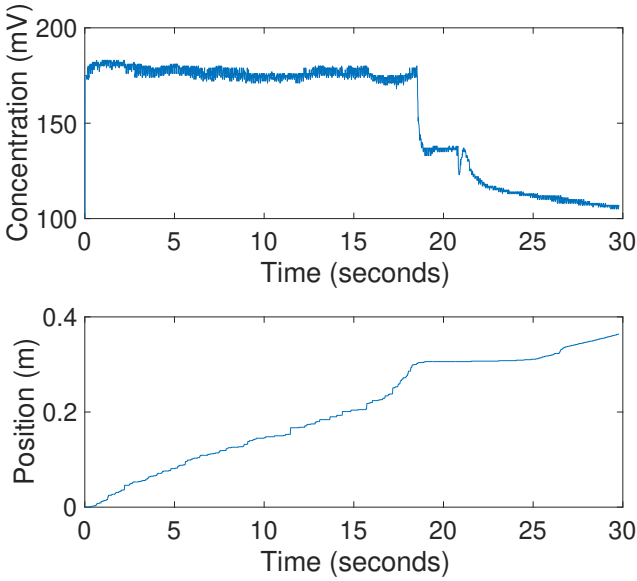

Figure 6.24: Environmental assessment of brusque changing context - glucose injected in a target area

The study also presents an operation framework to facilitate a context aware cyber-physical system used for submerged environmental assessment. The submersible can operate in both Newtonian and non-Newtonian fluids and can be easily adapted to any monitoring task, although the versatility of its tasks are limited by its own CPU performance constraints. The present study shows experimental tests that prove the efficacy of an energy efficient control law as well as the ability of the system to detect and analyse its operation context.

Environmental assessment based on context aware information can be useful in a wide variety of multidisciplinary processes such as below ice cap exploration (the mixture of water and ice being a non-Newtonian fluid), muddy water monitoring (in waste water treatment plants/basins), transportation (pipelines), biomedical applications such as targeted drug delivery, lung inflammatory response monitoring (fluid in lungs), anesthesia (in vivo or by-pass blood concentration monitoring), etc. or in manufacturing processes that involve both Newtonian and non-Newtonian characteristics such as steel manufacturing, pharmaceuticals (material properties of granulation processes), etc. The examples on these last two manufacturing processes make the scope of subsequent chapters in this book.

The results presented in this chapter have been published in:

- M. Ghita, **I. Birs**, D. Copot, I. Nascu, C. Ionescu. "Impedance

Spectroscopy Sensing Material Properties for Self-Tuning Ratio Control in Pharmaceutical Industry", in *Applied Sciences*, vol. 12, no. 1, pp. 509, DOI: 10.3390/app12010509, 2022.

- **I. Birs**, C. Muresan, O. Prodan, S. Folea, C. Ionescu. "An Experimental Approach towards Motion Modeling and Control of a Vehicle Transiting a Non-Newtonian Environment," in *Fractal and Fractional*, vol. 5, no. 3, pp. 104, DOI: 10.3390/fractalfract5030104, 2021.

- **I Birs**, C. Ionescu, I. Nascu, C. Muresan, "A comparison between FOIMC and FOPI controllers for a submerged robot", in *2021 25th IEEE International Conference on System Theory, Control and Computing (ICSTCC)*, Iasi, Romania, pp. 166-171, 2021.

- R. Cajo, M. Ghita, D. Copot, **I. Birs**, C. Muresan, C. Ionescu. "Context Aware Control Systems: An Engineering Applications Perspective," in *IEEE Access*, vol. 8, pp. 215550-215569, 2020.

- **I. Birs**, C. Muresan, and C. Ionescu, "An event based implementation of a fractional order controller on a non-Newtonian transiting robot," in *2020 European Control Conference (ECC 2020)*, St. Petersburg, Russia, pp. 1436-1441, 2020.

- **I. Birs**, C. Muresan, I. Nascu, and C. Ionescu, "An energy-efficient context aware solution for environmental assessment," in *IFAC PAPERSONLINE*, Beijing, China, vol. 53, no. 5, pp. 756-761, 2020.

- **I. Birs**, M. Ghita, M. Ghita, D. Copot, C. Muresan, and C. Ionescu, "An interdisciplinary, low-cost methodological framework for analysing dynamical material properties for control-related applications," in *IFAC PAPERSONLINE*, Philadelphia, USA, vol. 52, no. 9, pp. 159-164, 2019. - **2^{nd} place, Young Author Award**.

- **I. Birs**, D. Copot, M. Ghita, C. Muresan, and C. Ionescu, "Fractional-order modeling of impedance measurements in a blood-resembling experimental setup," in *2019 IEEE International Conference on Systems, Man and Cybernetics (SMC)*, Bari, ITALY, pp. 898-903, 2019.

- **I. Birs**, C. Muresan, S. Folea, O. Prodan, and C. Ionescu, "Fractional order modeling and control of a carrier prototype for targeted drug delivery," in *ICCBB 2018: Procedings of the 2018 2nd International Conference on Computational Biology and Bioinformatics*, Bari, Italy, pp. 1-5, 2018.

- C. Muresan, **I. Birs**, S. Folea, C. Ionescu. "Fractional order based velocity control system for a nanorobot in non- Newtonian fluids", in *Bulletin Of The Polish Academy Of Sciences- Technical Sciences*, vol. 66, no. 6, pp. 991-997, DOI: 10.24425/bpas.2018.125946, 2018.

7

Industrial Case Study - Modeling and Control of Non-Newtonian Fluid Flow through EMA Actuators

7.1 Introduction

Continuous Casting (CC) or strand casting is a procedure where molten metal is transformed into slabs through solidification, which will be consequently rolled in finishing mills. Most of the world's steel is produced using this technological process [179]. The procedure was firstly introduced in the 1950s as an alternative to ingots obtained through mold pouring. Advances in continuous casting led to an improved yield, final product quality, increased productivity and reduction of costs. [180].

Rheological studies performed on liquid steel show non-Newtonian fluid flow characteristics. Flow behavior and viscosity analysis proves that liquid steel exhibits shear thinning and time independent, non-thixotropic flow for all shear rate regimes. The physical explanation is that short range atomic orders lead to non-Newtonian characteristics [181]. Continuous casting of liquid steel encapsulates a wide variety of interacting complex physical phenomena such as: heat transfers, various states of turbulent and laminar flows, clogging, steel solidification, electromagnetic effects, entrapment of air particles, thermical and mechanical distortion, non-linear stress, segregation and various micro-structural formations [182].

Currently, all existing literature focusing on modeling CC processes use classical differentiation and integration operations of fixed orders

[182, 183, 184, 185, 186, 187]. However, recent advances in non-Newtonian fluid flow show that fractional calculus is more suitable in modeling this complex phenomena. Fractional order Navier-Stokes equations, Mittag-Leffler functions, space fractional constitutive equation models and Maxwell elements in mechanical models of viscosity have been previously used to model non-Newtonian characteristics in [73, 142, 188, 189, 190].

Fractional calculus is a powerful branch of mathematics that introduces differ-integral operations of any arbitrary rational, non-integer, order [36, 191], as shown in Chapter 2. Hence, classical differentiation and integration is generalized, allowing a more accurate mathematical description of complex physical phenomena [143]. Several advances prove the veracity of fractional calculus, especially in the field of viscoelasticity [41, 192], as proven in Chapter 3. Furthermore, fractional differintegrals generalize the Proportional Integral Derivative (PID) controller to a more powerful, multi-degree of freedom controller that is able to satisfy a wider set of design specifications, with increased stability, better performance and inherent robustness.

The present study provides an original and novel framework on the use of fractional calculus to address the natural non-Newtonian properties of liquid steel in casting lines. Prior collaboration with Arcellor Mittal Gent in Belgium and availability of real data allows to validate the obtained fractional order models [193]. Consequently, a suitable control strategy is developed for fault reduction in the obtained product by controlling the non-Newtonian fluid flow in the caster. Industry 4.0 paradigms and fault reduction are tackled through the usage of fractional order event-based implementation of the obtained controller. The implementation is based on the fractional order event-based paradigms presented in Chapter 4.

Novelty elements of the chapter include the usage of fractional calculus to model and control non-Newtonian liquid steel flows, the applicability of these findings on a real CC plant, usage of real-life data to validate the obtained models, fractional order control of the CC process and its event-based implementation for fault reduction and optimization.

7.2 Continuous Casting Plant

7.2.1 Description

The ArcelorMittal Gent (AMGent) plant has been chosen as the continuous casting case study. ArcelorMittal is the second largest company in the world for steelmaking, with a reported tonnage of 78.46 Mt in 2020 [193]. The AMGent process is equipped with an electromagnetic stirrer that allows active control of the liquid steel flow. The operating principle of the caster in AMGent is shown in Fig. 7.1.

Firstly, the metal is melted into furnaces and introduced into a 300t

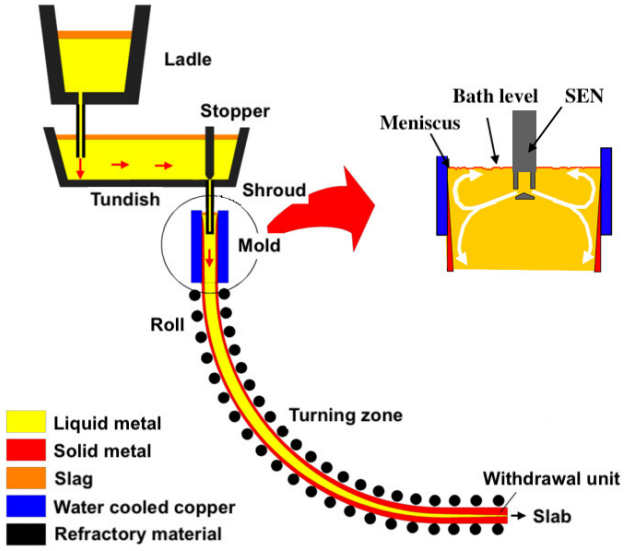

Figure 7.1: Diagram of a continuous casting line unit as part of a steel products manufacturing process.

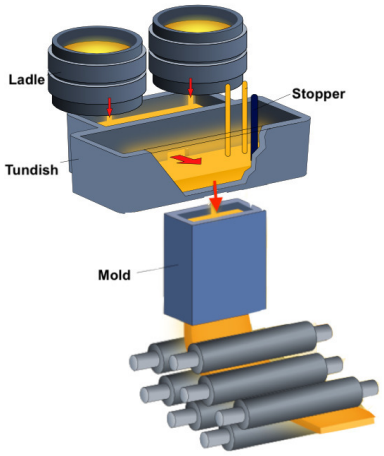

Figure 7.2: Diagram of tundish and mould details as part of a steel products manufacturing process [179]

ladle through a turning tower. Treatment such as alloying or degassing may be performed on the metal inside the ladle, as well as ensuring the proper casting temperature. In the AMGent plant, the ladle is placed on a two slot rotating turret at the top of the casting unit. One slot is in the

Figure 7.3: An illustrative example of a SEN ready for immersion (left) and a SEN in the mould (right). Observe the noisy environment and emerging deposits.

casting position, whereas the other is refilled and vice-versa.

The fluid is transferred from the ladle to a 60t holding reservoir, known as the tundish, via a refractory shroud. This element is a buffer which feeds the casting line and regulates the metal feed to the mould. In addition, the tundish ensures that liquid steel is continuously fed to the process, especially while the ladles are switched. Steel particles can stay up to ten minutes the AMGent tundish in order to allow enough time for ferrostatic particles to rise.

A submerged entry nozzle (SEN) controls the flow of the liquid steel from the tundish to an open-base copper mould. The size of the mould dictates the casting speed and size of steel section. A closer look of the tundish and mould is presented in Fig. 7.2. The primary cooling process takes place into the mould, where water cools the mould's walls causing hot metal to solidify in contact with it. The mould oscillates to prevent solidification on its walls. The metal in the mould is treated with various lubricants such as powders or liquids to prevent sticking to the walls and trap any slag particles. Clogging is prevent through introduction of argon or nitrogen. The metal is part-fluid, part-solid when it exists the mould, guided by grouped rolls. The metal is further cooled using water sprays or by cooling the segments itself. At the end of the solidification process of the slab, it is cut with a cross cutter with width ranging from 950 to 2000mm, thickness of 220mm, resulting the final product [194].

Even if the liquid steel is treated with various anti-clogging agents, the SEN is replaced every few hours due to solidified steel deposits. The tundish at AMGent is placed on a wagon that allows easy replacement of the SEN. Fig. 7.3 shows a fresh SEN and an immersed one.

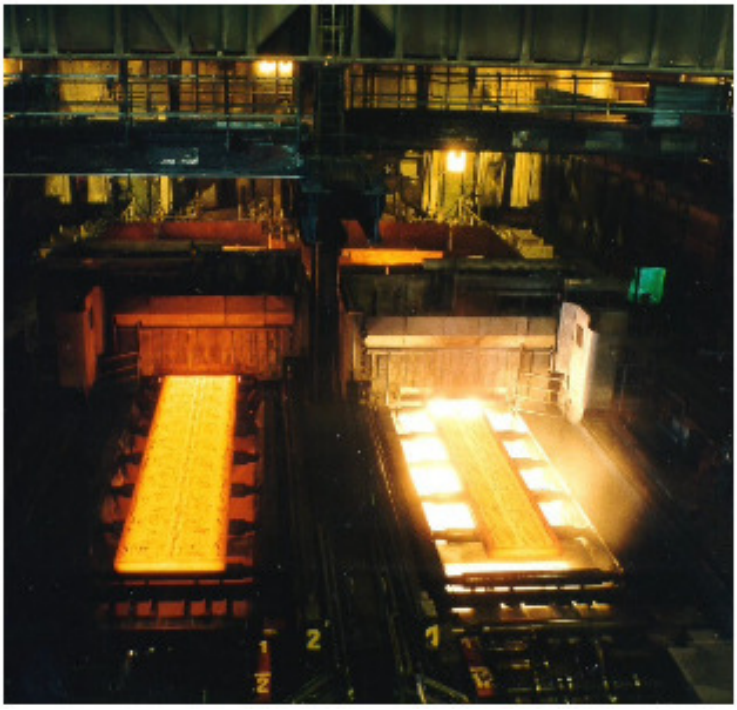

(a) View of the CC unit featuring cross cutters placed at the end of the casting line.

(b) Snapshot of depositing resulting slabs at AM Gent for a general idea regarding their size

Figure 7.4: ArcelorMittal Ghent plant.

The AMGent caster is a 'curved apron' machine: the strand exits vertically from the mould and is gradually curved by the rollers. Advantages of this design over fully horizontal or vertical machines consist in the quality of the resulting product, reducing final product's fault directly through the caster's construction [195].

Images of the the AMGent plant can be seen in Fig. 7.4 featuring cross cutters placed at the end of the casting line (Fig. 7.4a) and depositing of steel slabs (Fig. 7.4b).

7.2.2 Existing Control Loops

The AMGent continuous caster can be controlled through several variables.

The SEN immersion depth is set at 160mm, oscillating with amplitude 40mm and time period 20min. This increases the longevity of the nozzle, by spreading the corrosion over 80mm length instead of a single point.

Another control loop is built around the stopper rod height, in order to control the steel level in the mould. This prevents a possible calamitous event such as molten steel overflow and ensures that the molten metal stays enough time in the tundish to allow the rise of ferrostatic particles. The steel level is kept at around 1m in the tundish.

Argon gas is introduced in the mould to eliminate final products faults. The flow of the gas is a constant value, controlled by pressure of the argon introduced. This has an indirect effect on the size of gas bubbles, causing different liquid steel flow disturbances.

The casting speed slightly varies around a fixed value. Variations are caused by delayed arrival of ladles or various issues associated to the process. The operator can change the casting speed with respect to current events.

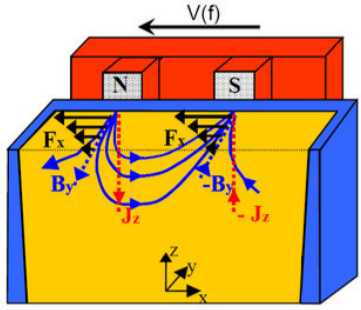

Figure 7.5: A schematic of the Lorenz force applied to liquid steel. In this figure, **J** is the current density vector, **H** is the magnetic field vector and **B** represents the magnetic flux, in the x, y, z axis coordinates.

A final loop is realized through electromagnetic stirring in order to control the liquid steel's flow with the main purpose of improving the product quality [196,197]. This is based on electromagnetism, a principle heavily applied in metallurgy [198]. The technology was firstly embedded in continuous casting in the 1970s by the French company ROTELEC. Eddy currents are induced in metal through a changing magnetic field. If an electromagnet applies a traveling field, the flow of the liquid steel will accelerate or brake to the traveling speed of the field, known as *Electromagnetic Stirring (EMS)*.

Fig.7.6 shows the visual representation of the fields and position of the coils. The arrows in the coils (grey) are the magnetic field vectors for the individual coils and the red arrows are the resulting magnetic field direction in the mould.

EMS uses the principle of a linear motor to control the flow where the liquid steel acts as the rotor, whereas the electromagnets act as the stator. The principle is shown in Fig. 7.5, for the flow speed and traveling direction of the field in the x-direction. J is the current density vector, H is the magnetic field vector and B represents the magnetic flux, on the x, y, z axes. The magnetic flux B travels with speed V(f). The B variation generates Eddy currents, J inside the liquid steel. B and J generate an electromagnetic volume force $F = \sigma v B^2$ [N/m3], which ultimately generates liquid steel flow. The speed of the field depends on the frequency of the applied current, the magnetic poles and the dimensions of the electromagnet [198].

The EMS installed at AMGent (Fig. 7.7) has three operating modes:

- **EMLS**- Electromagnetic Level Stabilizer: used to slow down steel when a double roll pattern has a too high flow rate, causing flux inclusions and high level fluctuations.

- **EMLA** - Electromagnetic Level Accelerator: used when the meniscus (the upper level of the steel) flow rate with a double roll is too low, or when a single roll pattern is present.

- **EMRS** - Electromagnetic Rotative Stirrer: used to homogenize steel temperature at the meniscus, which can prevent forming of oscillation marks and is not necessarily used for maintaining a double roll.

AMGent uses an automatic control computer that predicts the meniscus flow speed based on SEN, mould width, casting speed and Argon flow rate (F-value) and computes the current needed to produce the magnetic field in order to accelerate or brake the steel flow at the meniscus. The meniscus flow is estimated without EMS interactions, denoted as V-value. Each flow speed is correlated to a desired current through the electromagnets in the form of a look-up table. The ideal meniscus flow speed is found

at approx. 30cm/s. The electromagnets are fed with a 1 Hz sine wave with controlled amplitude.

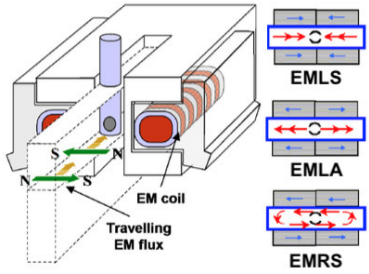

Figure 7.6: Placement of EMS at SEN exit hole height

Figure 7.7: Snapshot of the EMS unit installed in ArcelorMittal Gent

Currently, flow is controlled in an inferential manner, since there is no feedback used to check the actual meniscus flow speed. Previous works such as [199] proposes the closed loop control of the AMGent CC plant through a PID controller, but the study is limited to integer order differentiation.

7.2.3 Product Quality

The steel begins already to partly solidify at mould level, hence strongly affecting the steel "cleanliness". Impurities or inclusions are either re-

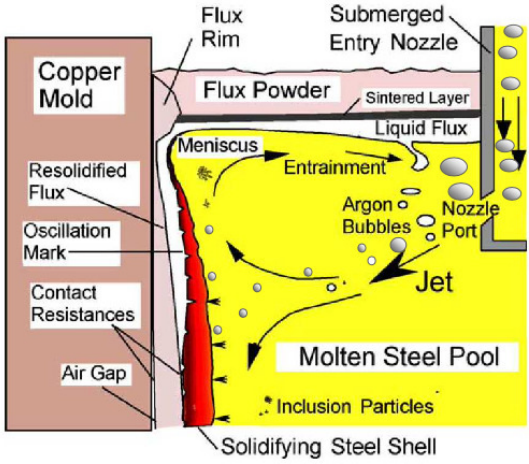

Figure 7.8: Flows in the CC mould [courtesy of AMGent]

moved by floatation/slag or become entrapped in the resulting slab product. The steel enters the mould through the SEN and spreads in an upwards rolls that reaches the meniscus or a downwards roll. The steel flow at the meniscus level is a measurable process parameter. Casting powder is used for lubrication and chemical/thermal insulations, but it can sometimes become included in the liquid metal. Some of the undesired defects in the end product are herein summarized. Flows in the CC mould are illustrated in Fig.7.8 - taken from [200].

Oscillation marks are caused by the molten steel pool not being uniform, causing problems during the mould oscillations and the steel skin near the meniscus being too close to floating casting powder. If a thin skin is pushed towards the wall by the pressure of the liquid steel as the skin moves downward causes a folding mark. If a thick skin is pushed, this will be overthrown instead of being bent, resulting in an oscillation mark. These can partially remelt in hot steel if the flow speed is high enough.

Surface cracks can be longitudinal, transverse or corner. The first type is formed at the mould level if the temperature is not well distributed. The brittleness of steel influence the ductibility point, forming corner and transverse cracks when steel bends through the curve of the caster. This type of defects can be improved by keeping the steel at high temperatures.

Slivers and blisters are caused by entrapments when steel solidifies. Slivers appear as a dark continue dot line in the rolling directions with a typical size of less than 1m for length and 1 to 5 mm for width. Blisters appear when inclusions float near the bend of the CC and are placed exclusively on the side corresponding to the slab intrados. Generally,

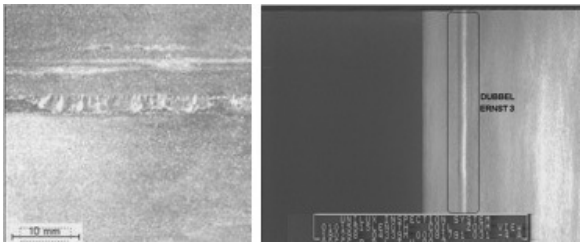

Figure 7.9: Example of Sliver (left) and Blister (right) defects in the end product slab.

blisters are formed by argon gas and alumina clusters, appearing as line protuberances in the rolling direction. The typical size is a length less than 1m and a width between 0.5 and 6mm.

The resulting slabs undergo Automatic Surface Inspection as well as Visual Inspection performed by operators to ensure the best quality of the resulting steel. Photos of sliver and blister faults identified by the Automatic Surface Inspection system are shown in Fig.7.9.

The purpose of the EMS flow control is to reduce surface defects, increasing product quality by controlling the meniscus flow of the liquid steel.

7.3 Lumped Model Identification for Control

7.3.1 Model Considerations

The flow of the liquid can be measured using SVC devices to measure the variations of meniscus velocity in the mould [201]. The SVC is an air-cooled torque sensor attached to a refractory probe that is able to acquire data under challenging operating conditions with minimal safety risks. The steel creates a drag force on the SVC probe, which is monitored in real-time by a torque sensor. The raw measurements are transformed into velocity signals using in-house calibration techniques.

In this context, prior ANSYS simulation studies indicate changes in the velocity gradient with both time and space. To employ our prior know-how on modelling time and volume variations in lungs by means of mechanical elements to characterize viscoelastic properties [7,75], we propose to consider the steel material as sheets of varying properties. Fig. 7.10 depicts the concept of changing mechanical properties as a function of flow properties at different time and space instances. Such distributed models have been already demonstrated to lead to the appearance of fractional order Laplace orders in lumped transfer function models [75,202,203]. As the cellular networks vary in time as a function of material properties

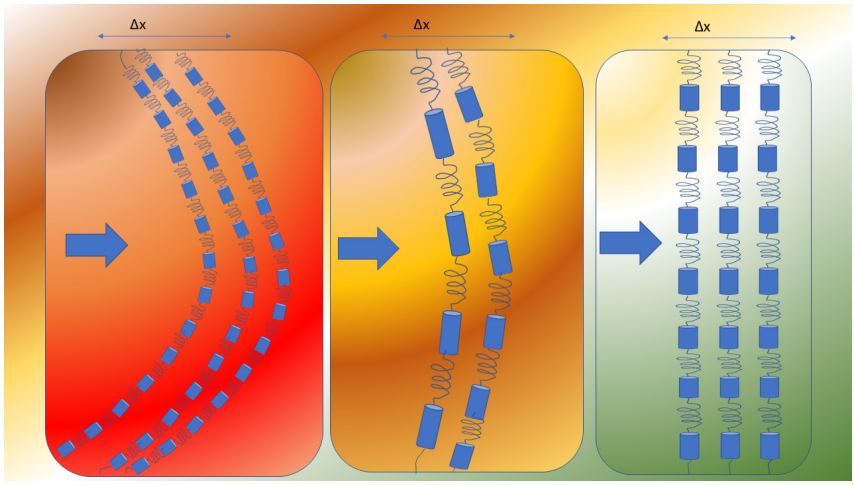

Figure 7.10: Concept illustration as to how distributed parameter Maxwell-Voigt elements models can be used to characterize time and space varying properties in varying flow conditions. Values range from high (red) to low (green).

(in our case non-Newtonian flow properties), so are the fractional orders, which in turn are related to time response dynamics (e.g. settling time, overshoot) and frequency response (e.g. phase margin, gain margin).

Apart from a mathematical derivation from distributed parameter systems, our preliminary works indicated that lower parameter models for identification are required if generalized order Laplace transfer function are used instead of classical integer-order models. Specific reports for non-Newtonian dynamics identified from experimental data with fractional order transfer function models are given in [142, 204, 205].

For the present study, the ultimate goal is to obtain a simple mathematical model that connects the current applied to the electromagnets with the speed of the liquid steel. The problem is separated in two steps: finding a model between the input and output currents of the EMA device, followed by a mathematical connection between the actual EMA current applied to the liquid metal and the meniscus steel flow.

A current through an electromagnet with voltage V_e, inductance L_e and an equivalent resistor R_e has the following transfer function:

$$P_{EMA}(s) = \frac{\frac{V_e}{R_e}}{s\frac{L_e}{R_e} + 1}. \tag{7.1}$$

However, real-life coil dynamics are better characterized with fractional derivatives capturing electromagnetic effects [206, 207, 208]. From these observations and our assumptions Fig. 7.10, we propose a simple general-

ized EMA transfer function model:

$$P_{FO-EMA}(s) = \frac{I^2(s)}{I^{2*}(s)} = \frac{a}{bs^{\alpha}+1}, \tag{7.2}$$

with a, b coefficients and α the fractional order. I and I^* are the input and output currents, respectively. This equation is a modification of the initial model in [196], which is also briefly introduced in Section 7.2.2.

7.3.2 Identification

The coil model is determined by applying step inputs to the electromagnets and measuring the generated currents. A fractional order coil model based on the structure from (7.3) is obtained for:

$$P_{FO-EMA}(s) = \frac{1}{2.0068s^{0.9628}+1}. \tag{7.3}$$

Fig. 7.11 and 7.12 show the validation of the obtained model on the available CC process data. Our prior study reported an integer order model [199] identified as: $P_{EMA}(s) = \frac{1}{2.2406s+1}$. This model is used in Fig. 7.11 and 7.12 for a comparison to the newly proposed fractional order model. It can be clearly seen that the fractional order transfer function outperforms at all times the integer order model.

The next step is to determine the speed model that connects the current generated by the EMA to the flow of the liquid steel in the meniscus. The SVC device is used to acquire data over large time periods for step signals applied to the EMA device. A limitation associated to this step is the application of fixed step amplitudes with 20A or 100A increments due to the process computer. Transient behaviors are difficult to capture because of current limitations of the data acquisition devices mounted on the plant. For this reason, the raw data is used without denoising to eliminate any possible delays introduced by filtering in order to find an accurate model. Experimental tests suggests that an increase in the current leads to a lower meniscus speed, indicating a negative gain of the transfer function model. Using a similar structure as (7.2), the identified speed model is given by:

$$P_{FO-speed}(s) = \frac{-4.813 \cdot 10^{-6}}{2.3102 \cdot 10^{-6}s^{0.8443}+1}. \tag{7.4}$$

The validation data is acquired by applying current steps to the EMA device and analyzing the connection between the EMA generated current (I^{2*}) and the fluids' velocity measured by the SVC device inside the meniscus. The model fitted over the experimental data is depicted in Fig. 7.13 for two different datasets acquired for approx. 20 minutes. Dataset 1 from Fig. 7.11 features mostly staircase inputs, whereas in Fig. 7.13 the validation is done mostly for ramp input signals.

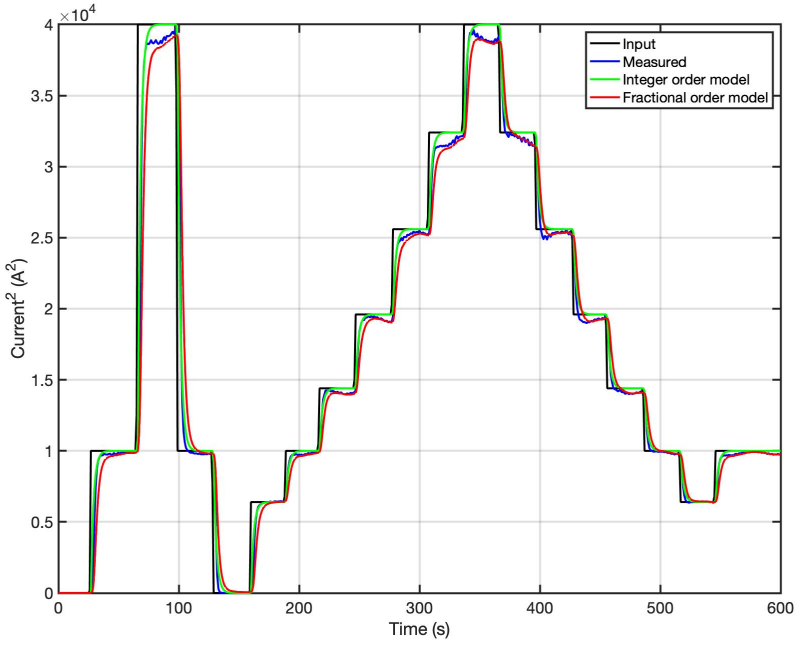

Figure 7.11: Electromagnet model (7.3) validation on real CC Dataset 1

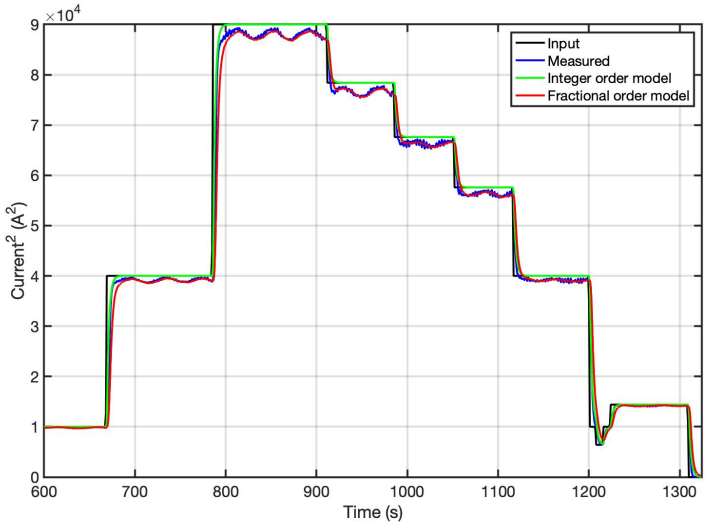

(a) Dataset 2

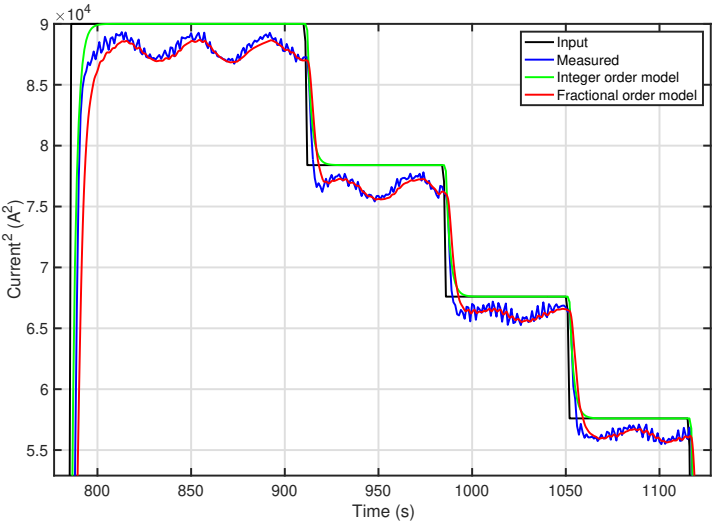

(b) Zoomed interval from dataset 2

Figure 7.12: Electromagnet model (7.3) validation on real CC Dataset 2

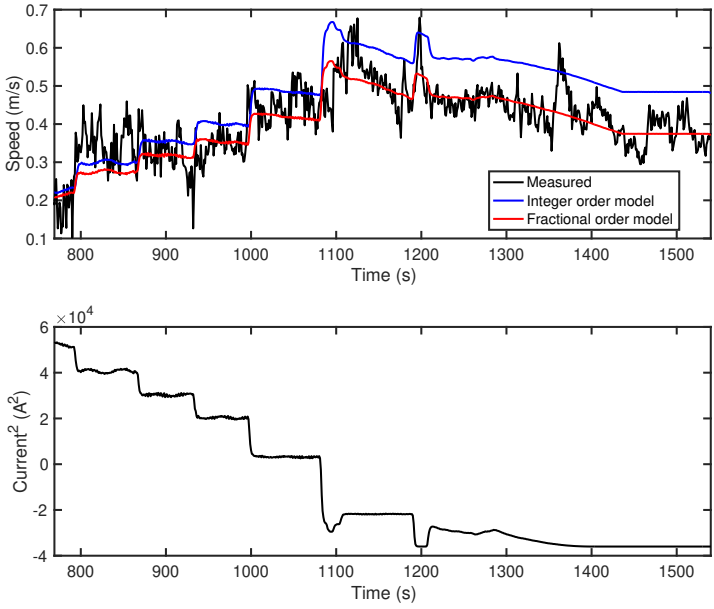

(a) Dataset 1

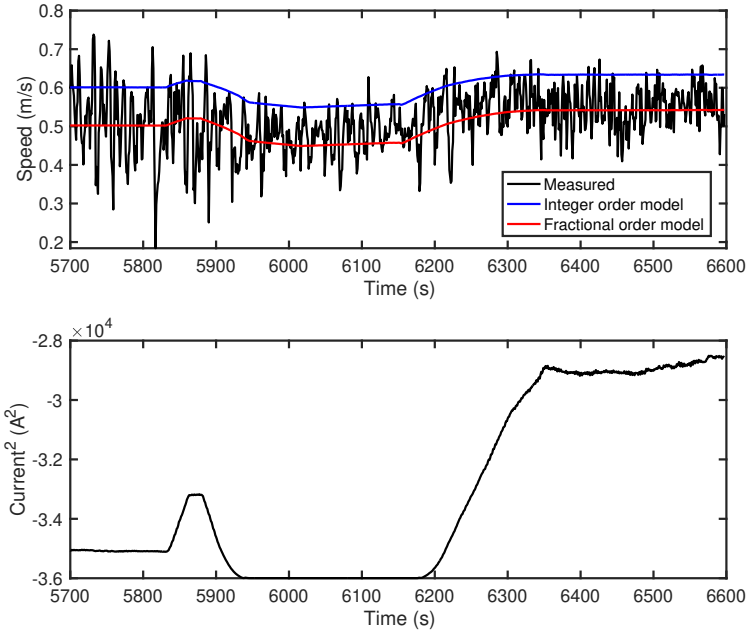

(b) Dataset 2

Figure 7.13: Speed model (7.4) validation on real CC data.

The integer order speed model identified in [199] as $P_{speed}(s) = \frac{-8.655 \cdot 10^{-6}}{s+1.462}$ is also included in the simulations, for comparison purposes and the results suggests that $P_{FO-speed}$ model outperforms P_{speed} model accuracy.

It follows that the complete transfer function model from the EMA to the liquid steel speed in the meniscus is given by:

$$\frac{0.24915}{0.24s^{1.8071} + 1.0389 \cdot 10^5 s^{0.9628} + 0.1195s^{0.8443} + 51766}. \tag{7.5}$$

The validation of the entire model from equation (7.5) connecting the applied EMA current I^2 to the speed is shown in Fig. 7.14. In this figure alone, the raw data is filtered for providing readable visual quality of results.

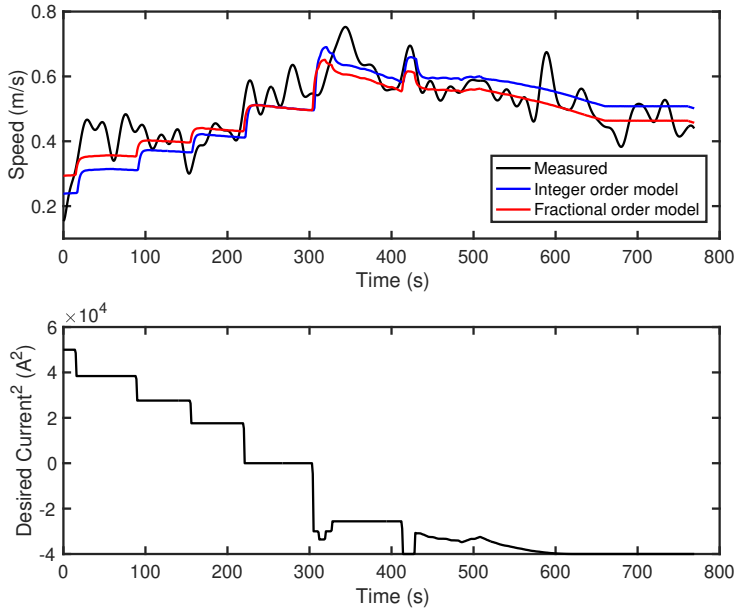

Figure 7.14: Validation of the complete fractional order model from EMA to meniscus speed on a filtered real plant data interval.

7.4 EMS Based Closed Loop Control

Standardly, open loop control is used in CC units based on estimations of the flow using a static model and a lookup table for the EMA input current. This inferential control was described in Section 7.2.2.

The development of a fractional order fluid flow model enables the possibility of closing the loop through the SVC sensor measurements in order to reduce possible faults caused by erroneous estimations of the velocity or human errors. This also considerably reduces the overall risks of plant calamities and offers a safer, cost efficient and quality focused production process.

The fractional order nature of the developed model from equation (7.5) justifies the usage of a fractional order controller, suitable for complex fractional order processes due to its multi degrees of freedom and ability to encapsulate complexity in a reduced number of parameters. Furthermore, robustness can be directly specified as a design parameter through the isodamping property [26, 209, 210, 141, 211]. A robust behavior of the closed loop system is paramount because of the various particles that are sometimes entrapped in the fluid such as Argon gas, casting powder and unknown parts of solidified metal. In turn, ensuring a constant fluid flow is a crucial factor in determining the quality of the end slab product.

A fractional order PI controller is chosen for the task because of its zero steady state error, ensuring the desired setpoint speed. When the process data is notably noisy, using a D component which is known to be very sensitive to noise is discouraged [212]. The most popular tuning procedure is used by imposing frequency domain specifications such as gain crossover frequency, phase margin and robustness of the open loop system $H_{ol}(s) = P(s)C(s)$, where $C(s)$ is the aforementioned controller described by:

$$C(s) = k_p \left(1 + \frac{k_i}{s^\lambda}\right). \tag{7.6}$$

The proportional and integral gains are given by k_p and k_i, while λ is the fractional order of integration, $\lambda \in (0, 1]$. For $\lambda = 1$ this corresponds to the classical PI controller.

Tuning the controller parameters can be easily achieved in frequency domain [209, 211]. The magnitude, phase and isodamping specifications at a chosen gain crossover frequency ω_{gc} are defined by:

$$\begin{cases} |H_{ol}(j\omega)|_{\omega=\omega_{gc}} = 1 \\ \angle H_{ol}(j\omega)|_{\omega=\omega_{gc}} = -\pi + \phi_m \\ \frac{dH_{ol}(j\omega)}{d\omega} = 0 \Big|_{\omega=\omega_{gc}} \end{cases}. \tag{7.7}$$

The Laplace operator s has been replaced by $s = j\omega$ to reference the frequency domain and ϕ_m denotes the desired phase margin.

The system of equations from equation (7.7) needs to be solved in order to determine the three parameters of the FOPI controller: k_p, k_i and λ. Various methods can be employed such as optimization tasks, neural networks, experimental strategies, etc. [59, 26]. However, for this example a simple graphical procedure is used.

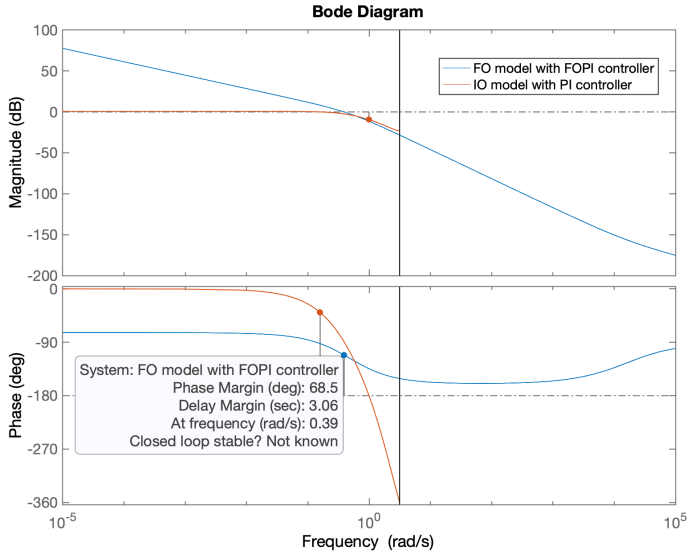

Figure 7.15: Bode diagram of the open loop system with the FOPI controller (7.8) and complete fractional order model of the process (7.5) compared to the integer order model with PI controller from [199]

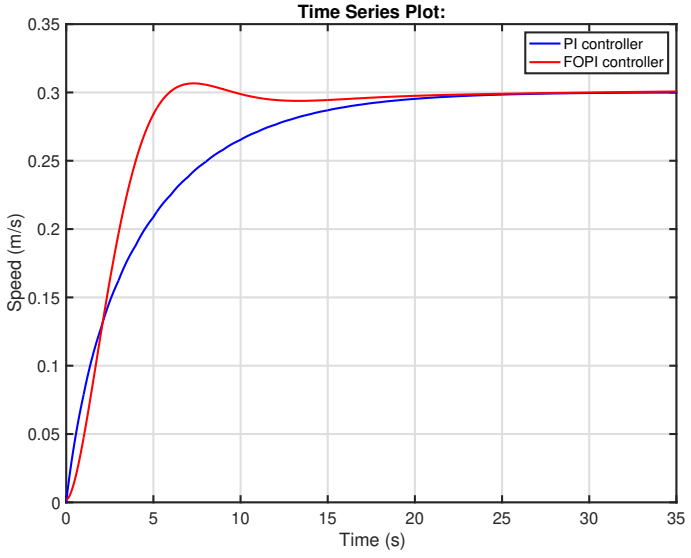

Figure 7.16: Step response of the closed loop system

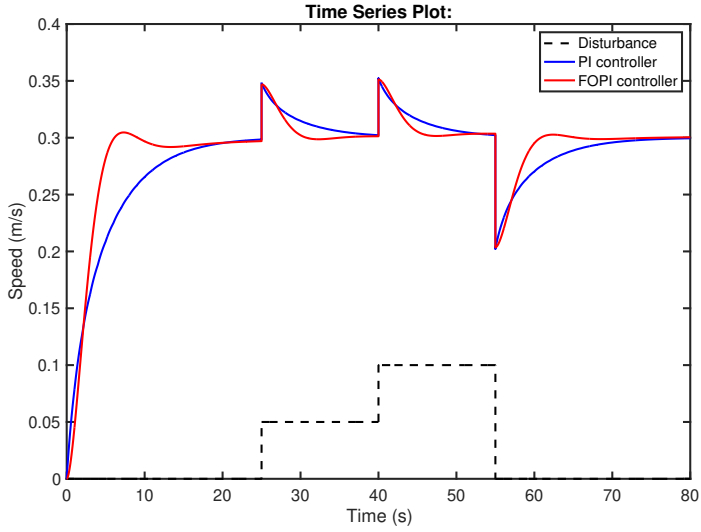

Figure 7.17: Step disturbance rejection tests for step load disturbance

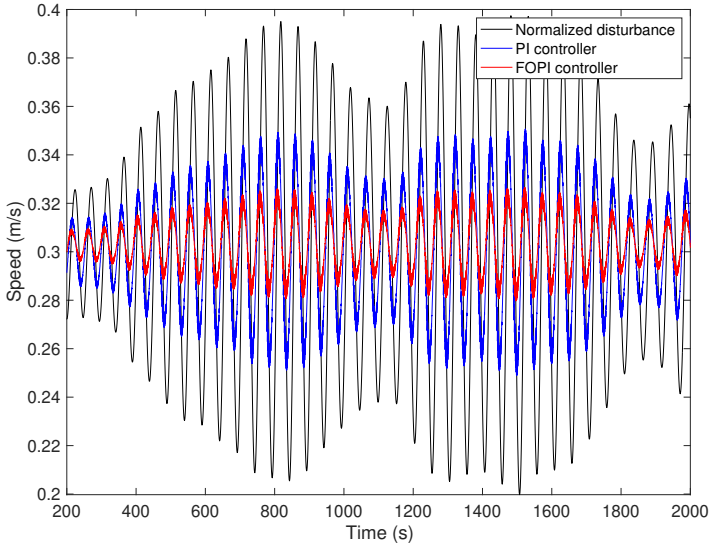

Figure 7.18: Step disturbance rejection tests for sinusoidal disturbance

The magnitude, phase and isodamping equations with imposed ω_{gc} and ϕ_m form a system of transcendental equations. The solution is found graphically such that k_p, k_i > 0 and $\lambda \in (0, 1]$. ω_{gc} and ϕ_m are chosen based on guidelines from [46], in order to obtain a physically relevant controller.

The following FOPI controller is determined for $\omega_{gc} = 0.4$ rad/s and $\phi_m = 65°$:

$$C(s) = 43.8708 \left(1 + \frac{290.03}{s^{0.8195}}\right) \tag{7.8}$$

and the loop Bode diagram depicted in Fig. 7.15 confirms that the desired set of specifications is met. The plot also includes the Bode of the open loop system composed by the integer order control and identified integer order model from [199].

Validation of the FOPI controller compared again to the integer order PI tuned in [199] is presented in Fig.7.16 for a step input of 0.3 m/s. The setpoint value is chosen to illustrate the current ideal operating velocity of the plant. The fractional order controller obtains a settling time of approximately 7 seconds, compared to the much larger 20 seconds obtained by the PI. Both controllers achieve zero steady state error.

Another test is performed for different step load disturbances applied to the plant, which in real situations can be caused by different fluctuations of the fluid level in the tundish, delays in replacing the ladles, operator interference, etc. The simulation results are shown in Fig. 7.17. The disturbance amplitude is 0 m/s for the time interval $t \in$ [0 25]seconds, changes to 0.05 m/s for the time interval $t \in$ [25 40]seconds, to 0.1 m/s for the time interval $t \in$ [40 55]seconds and remains 0 m/s for the remainder simulation time. We conclude the FOPI achieves better closed loop performance with about 30% reduction in settling times.

7.5 Event-Based Quality Control

The recent generalization of event-based control in the field of fractional calculus [213] allows the implementation of the previously tuned FOPI controller using this strategy. The challenges in event-based control strategies consist in control signals being randomly computed: instead of a new control value being computed every T_s seconds, where T_s denotes the periodic sampling time, the control value is computed at the triggering time instant of detected events [95, 105]. A manifold of benefits arise from this concept such as CPU optimization, reduced memory volume, bandwidth allocation, reduced energy demand, etc.

Intrinsic process events such as final product defects in the CC line can be used to trigger a new control signal computation with respect to the new state of the process in order to diminish the product's faults. In order to illustrate this strategy two types of product faults are considered:

- **Event A** - Blisters detected

- **Event B** - Slivers detected

The considered setpoint value of the fluid's speed is 0.3 m/s. However, in-house research associated the appearance of Events A and B to lower or higher velocities, as presented in Fig. 7.19. A speed much lower than 0.3m/s causes Argon gas inclusions to remain trapped, whereas a much larger velocity entraps casting powder, associated to Events A and B. Hence, at the appearance of a type A event, the velocity should be slightly increased, while for a type B event the velocity should be slightly decreased.

Events A and B are included in the proposed event-based approach, together with a safety condition consisting of the maximum allowed time between two consecutive control computations and the error condition, i.e. the difference between the setpoint and process values inside a predefined interval.

For the quality monitoring, the Automatic Surface Inspection System is included as part of the event-based control structure. A block diagram of the desired event-based strategy for the CC process is proposed and schematically depicted in Fig. 7.20. The results of implementing the FOPI controller using the Muir discretization, as exemplified in Chapter 4 is given in Fig. 7.21. The events are triggered by software detection techniques, causing the change in the setpoint value to improve the slab's quality. Furthermore, a realistic disturbance profile as that used in Fig. 7.18 is used for validation. We conclude the proposed strategy is applicable to this process with great valorization potential.

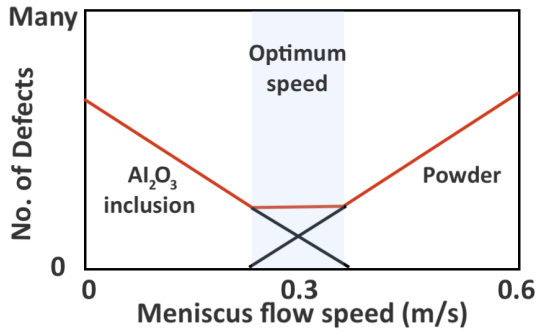

Figure 7.19: An example of how flow speed can be correlated to surface defects.

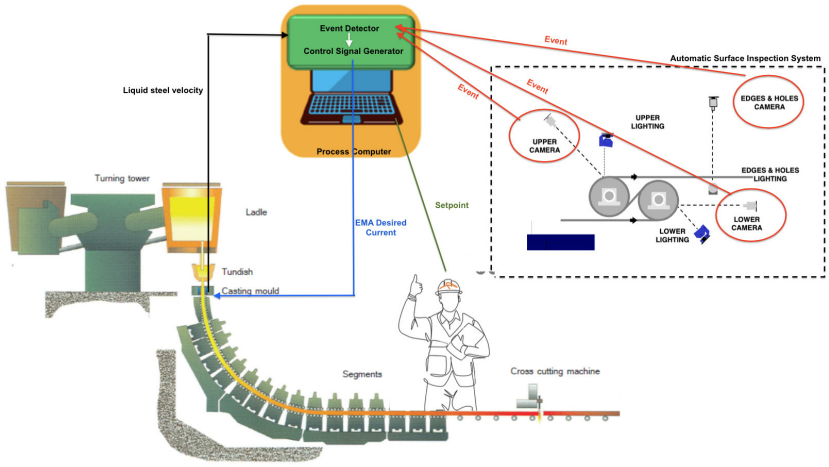

Figure 7.20: Event-based quality improving strategy for continuous casting

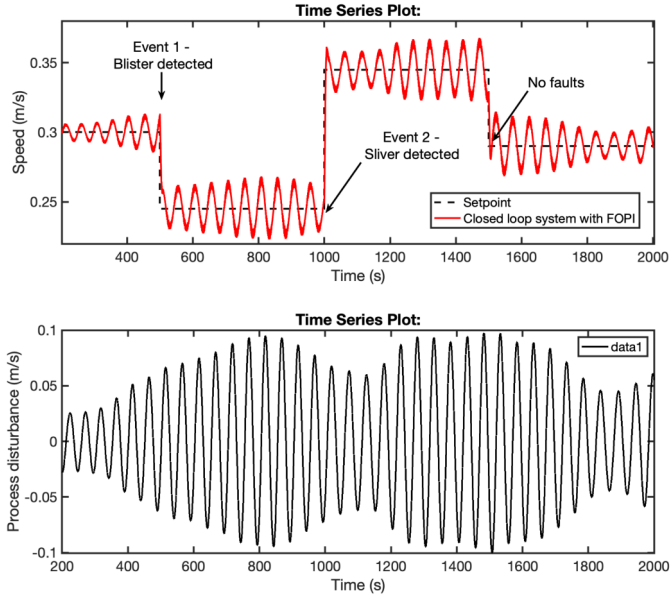

Figure 7.21: Event-based control validation with realistic disturbance rejection test.

Other type of disturbances are simulated, ranging from low frequency turbulence oscillations of the flow speed, to real, high frequency disturbances taken from plant measurements. The latter disturbance also features imperfect measurements (mechanical vibrations of probe, oscillating steel bath) and clogging in order to simulate realistic operating conditions. The results of this test are given in Fig. 7.18. The FOPI controller reduces by 50% the amplitude than the integer PI control.

7.6 Summary

The paper addresses the flow control problem in continuous casting unit lines by exploring properties of liquid steel as a non-Newtonian fluid. A naturally arising from physical effects and yet minimal in parameters model is obtained based on real data acquired from the ArcelorMittal plant in Gent, Belgium. The work proposes to use Navier-Stokes non-Newtonian equations adapted to distributed parameter compartments with generalized order differ-integration.

The resulting fractional order model is compared to a previous integer order model to asses the improvements offered by this generalization effort. Furthermore, a fractional order PI controller is tuned based on frequency domain specifications and tested under different operating conditions. A realistic disturbance that takes into account various factors i.e clogging and noise is implemented to prove the robustness and efficiency of the control approach.

Lastly, an original event-based structure that considers intrinsic events of the process triggered by automatic surface inspection system is proposed to improve the final product's quality.

The results presented in this chapter have been published in:

- **I. Birs**, C. Muresan, D. Copot, C. Ionescu. "Model Identification and Control of Electromagnetic Actuation in Continuous Casting Process with Improved Quality", in *Journal of Automatica Sinica* - **accepted**

Acknowledgment

This research is part of collaborating project with Arcellor Mittal Gent, Belgium during 2015-2018. We would like to thank Mr Michael De Docker from AMGent for access to data sets. As per copyright agreement, all data is normalized to arbitrary values.

8

Pharmaceutical Case Study - Impedance Spectroscopy Sensing Material Properties

8.1 Introduction

A core challenge of Industry 4.0 is the demand for versatile manufacturing that can cope with material availability and variability. Recent advances in technology and instrumentation have pushed forward the transition from batch to continuous process control in the pharmaceutical industry [214, 215]. One of the main advantages of continuous manufacturing is that it enables demand-driven scaling of production volume and product specifications. As a sensing technology, impedance spectroscopy is a powerful instrument with significant added value in optimizing control of manufacturing industries [216].

Tablet manufacturing industry has the highest production volume and thus changes in the manufacturing process have a significant impact on the overall production costs. The gold standard in pharmaceutical manufacturing of oral solid dosage forms is still batch-wise production [217]. In the fields of automotive, food, and petrochemical industries continuous manufacturing has been successfully implemented and has resulted in improved production and reduced costs in comparison to batch production [217]. However, the appearance of changes in raw material properties, equipment status with respect to physical wear and varying material properties along the production lines contribute to time-varying disturbances which in turn demand continuous corrective actions during production. Delayed corrective measures (i.e., end of the batch line) and sub-optimal

controller settings lead to sub-standard quality of end-product and consequently cost-related economic losses.

Some of the commonly encountered sub-unit processes in tablet manufacturing are: direct compaction, dry granulation, wet granulation, extrusion, granule lubrication, tablet pressing, coating, splitting, etc [218]. The material mixtures are essentially non-Newtonian in terms of fluid properties and classical characterization through modeling no longer captures the essential properties, as shown in Chapters 3 and 5 of this thesis.

Moreover, the models tend to be computationally demanding and not suitable for real-time parametric estimations. Fast and slow anomalous transport phenomena can be described by time-fractional diffusion equations of fractional order. These are commonly encountered in media with fractal, porous, or combined properties. The material used for making a tablet varies in its density and geometry as it transits a set of physical states: liquid, powder, granules, etc. When describing nonlinear transport phenomena such as anomalous diffusion of mixed materials, one must also account for memory effects, which are typically arising as a non-Brownian random walk motion equation [16, 219]. These are linked to density variations of non-Newtonian fluids, an initial state of material incipient properties in the pharmaceutical industry. Lumped parameter models of generalized (fractional) orders have been shown to be excellent tools in detecting and quantifying changes in material flow density from impedance spectroscopy data, both in Chapter 5 and specialized literature [220].

Furthermore, anomalous diffusion in porous media, e.g., granulated materials, is important as it enables to increase the effectiveness of various processes, such as absorption, catalysis, etc, by controlling the regime of mass flow transport. The diffusion coefficient representing the speed of molecule transitions has a strong dependence on porosity [150, 221]. Surface area and pore volume are key properties and a direct result of the controlled environment of pharmaceutical products.

A tablet comprises a mixture of active substances and excipients, usually in powder form, pressed or compacted from a powder, through mixed liquid into a solid dose. The excipients can include diluents, binders or granulating agents, flow aids and lubricants to ensure efficient tableting. A polymer coating is often applied to make the tablet smoother and easier to swallow, to control the release rate of the active ingredient, to make it more resistant to the environment (extending its shelf life), or to enhance its appearance. In short, the production thereof is a complex multivariable process and (intermediate) material properties variability can have important implications on the efficiency of the production process (e.g., changes in powder stickiness or mixture viscosity). Hence optimal control of production efficiency and product properties are essential to guarantee a manufacturing process that is adaptive while maintaining (semi-)finite product quality at all times [222].

In this chapter, a theoretical framework similar to the one introduced in Chapter 5 is used to characterize material properties in non-Newtonian fluids and anomalous diffusion in porous materials. This original and innovative approach allows using lumped fractional order parametric models for online estimations of material properties which in turn enable a self-tuning function for ratio control of material flows. While the concepts are generically applicable to other domains such as food and chemical industries, the particular application discussed in this work is the wet/dry granulation tableting process in the pharmaceutical industry.

8.2 Anomalous Diffusion

Diffusion kinetics in porous media is described by the second Fick's law:

$$\frac{\partial C}{\partial t} = D \cdot \frac{\partial^2 C}{\partial x^2} \tag{8.1}$$

where C is the linear concentration of diffusion species in mol/m; D is the diffusion coefficient in porous media in m^2/s, t is time in seconds and x is the spatial coordinate in metres. For time-fractional diffusion, a temporal derivative becomes a time-fractional derivative of order $0 < \alpha < 2$, accounting for sub-diffusion ($0 < \alpha < 1$) and for supra-diffusion ($1 < \alpha < 2$) dynamics:

$$\frac{\partial^\alpha C}{\partial t^\alpha} = K \cdot \frac{\partial^2 C}{\partial x^2} \tag{8.2}$$

where K denotes fractional diffusion coefficient in units m^2/s^α. A direct consequence of these time-fractional units in media is the intrinsic characterization of memory effects such as in non-Newtonian fluids (chapter 5) and viscoelastic materials, polymers and biological tissues [10]. The analytical solution can be obtained applying the Caputo definition of the time-fractional derivative:

$$D^\alpha C(x,t) = \frac{\partial^\alpha (x,t)}{\partial t^\alpha} = \frac{1}{\Gamma(m' - \alpha)} \cdot \int_0^t (t-\tau)^{m'-\alpha-1} \cdot \frac{\partial^{m'} C}{\partial \tau^{m'}} d\tau \tag{8.3}$$

with $m' = 1$ for sub-diffusion and $m' = 2$ for supra-diffusion, and $\Gamma(x)$ is the Euler Gamma function.

Applying spatial Fourier and temporal Laplace transform to equation (8.2) provides the space-time fractional diffusion equation [223]:

$$C(k,s) = \frac{s^{\alpha-1}}{s^\alpha - K \cdot (-i \cdot k)^2} \tag{8.4}$$

with $i = \sqrt{-1}$. Using the Mittag–Leffler function

$$E_\alpha(z) = \sum_{n=0}^{\infty} \frac{z^n}{\Gamma(\alpha \cdot n + 1)} \tag{8.5}$$

and inverse Laplace transform gives

$$C(k,t) = E_\alpha(-K \cdot k^2 \cdot t^\alpha), \tag{8.6}$$

which enables to characterize short and long time diffusion patterns separately through approximations:

$$\exp\left[-\frac{K \cdot k^2 \cdot t^2}{\Gamma(m'+\alpha)}\right]$$

and

$$\frac{1}{K \cdot k^2 \cdot t^2 \cdot \Gamma(m'-\alpha)},$$

respectively.

If mass transfer in the diffusion molecule is described using equation (8.1), we can impose initial condition $C(x,0) = C_0(x) = cte$ and boundary condition $\frac{\partial C}{\partial x}\|_{x=0} = 0$. The flow of diffusing species leaving the porous grain is defined as the difference between the concentration in the grain Cg in mole/m^3 and the linear concentration C at the longitudinal size of the grain l. Notice that extrapolation to granular flow mass becomes the concentration at the sensing site. The boundary condition at site is given by:

$$D \cdot \frac{\partial C}{\partial x}\|_{x=l} = \gamma \cdot (Cg(t) \cdot A - C(l,t)) \tag{8.7}$$

as a function of A the transversal area of the grain in m^2, and linear diffusion velocity coefficient γ in m/s. Mass balance relation is:

$$\frac{dCg}{dt} = \frac{\gamma\prime \cdot (Cg(t) \cdot A - C(l,t)) - v \cdot Cg(t)}{V}, \tag{8.8}$$

with V grain volume in m^3 and v is volumetric flow of species diffusion in m^3/s.

The asymptotic solution using Green function for normal diffusion is given by:

$$C(l,t) = \frac{C_0}{\sqrt{\pi}} \cdot \frac{l}{\sqrt{D \cdot t}} \tag{8.9}$$

and is linearized in logarithmic coordinates for short time as $(\ln \frac{C}{C_0})$-$\ln t$ and for long time as $\ln(\frac{C}{C_0})$-t. The relation between normal to time-fractional diffusion analytical solution is derived in [221]. The time-fractional diffusion equation for short times is

$$\ln \frac{C(l,t)}{C_0} = \ln \frac{l}{\sqrt{\frac{\pi K}{\Gamma(m'+\alpha)}}} - \frac{\alpha}{2} \cdot \ln t \tag{8.10}$$

and for long times is

$$\ln \frac{C(l,t)}{C_0} = \ln \frac{l^2}{K \cdot \Gamma(m'-\alpha)} - \alpha \cdot \ln t. \tag{8.11}$$

Diffusion transport phenomena can be thus fitted using these equations on experimental data as time varying property of the material.

Consider a material transiting as a granular flow. The diffusion of species will depend on material properties and follow the Stokes–Einstein relation [224]:

$$D = \frac{K_B \cdot T_K}{6\pi \cdot \eta \cdot r} \tag{8.12}$$

where K_B is the Boltzman constant in $\mathrm{kgm^2/Ks^2}$, η is viscosity in kg/ms, T_K is the absolute temperature in Kelvin and r the radius in m of the granular sphere or its approximation as a sphere. Diffusion depends on size and geometry (shape) of the grain as well as the viscosity of the material in flow conditions. For a sphere, its surface is given by $A = 4\pi r^2$ and its volume by $V = \frac{4}{3}\pi r^3$. Under the conditions of a variable r, the efficacy of diffusion is given by the ratio:

$$\frac{A}{V} = \frac{4\pi r^2}{\frac{4}{3}\pi r^3} = \frac{3}{r}. \tag{8.13}$$

This relation suggests that the diffusion efficacy decreases with the increase of sphere size.

8.3 Impedance Spectroscopy for Non-Newtonian Fluids

Electrochemical properties of materials have been successfully characterized with impedance spectroscopy and frequency response models [220].

Impedance spectroscopy was also used to capture time-varying non-Newtonian fluid properties by means of frequency-domain fractional order models in Chapter 5. A comprehensive summary of classes of non-Newtonian fluid properties is given in Chapter 3. From the time-dependent properties, the most important one when closed-loop control is envisaged is the fluid (mixture) density variability. This is of particular importance in mixtures based on feedforward and ratio control structures [225].

When non–Newtonian fluids are treated as electrochemical systems, they can be studied from impedance measurement data [220]. The measurement involves the application of a small perturbation, alternatively to classical identification methods based on linear sweep or potential step which perturbs the nonlinear dynamics far from a piecewise linear equilibrium. A small imposed perturbation can be applied potential, applied current or, hydrodynamic electrodes of convection rate. The fact that the perturbation is small brings advantages in terms of the solution of the

relevant mathematical equations, i.e., the systems behave piecewise linear time-invariant systems with the relative simplifying assumptions when applying frequency domain analysis.

The response to the applied perturbation, which is generally sinusoidal, can differ in phase and amplitude from the applied signal. Measurement of the phase difference and the amplitude, i.e., the impedance, permits analysis of the electrode process in relation to contributions from diffusion, kinetics, Debye effects, coupled homogeneous reactions etc [226].

The main flowchart of the procedure used in this work, called *Phase-sensitive detectors and transfer function analysers*, is showed in Figure 8.1. The detector compares the signal applied to the system and its response, giving the phase difference and the ratio of the amplitudes. In our case the reference signal is applied by means of a potentiostat (PSTAT) and then through the frequency response analyser (FRA) the actual measurement of the impedance can be carried out, processed and cleaned. When used in online estimation mode, the high frequency sampling raw data recordings are downloaded on a computer where a spectral analysis algorithm estimates time and frequency domain response for further use such as parametric modeling.

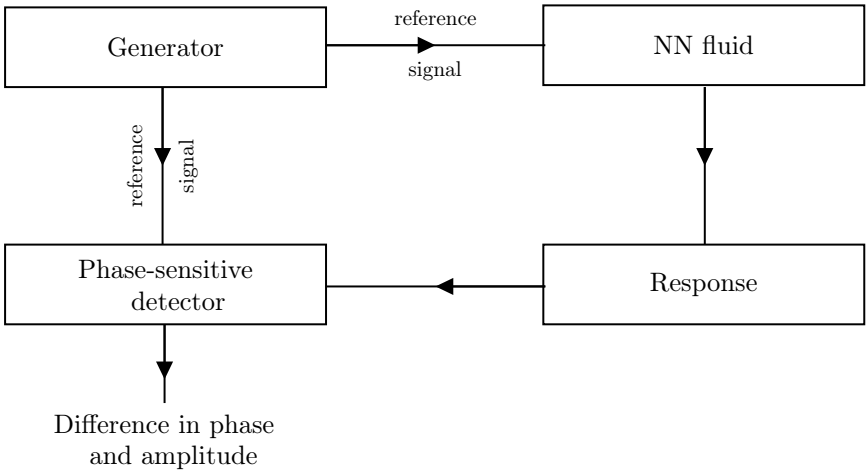

Figure 8.1: Generic principle of a phase-sensitive detector functionality.

8.3.1 Randle's Circuit

Any electrochemical cell can be represented in terms of an equivalent electrical circuit that comprises a combination of resistances and capacitances (inductances only for very high frequencies) [216]. This circuit should contain at the very least components to represent:

1. The double material layer: a pure capacitor of capacity C_d,
2. The impedance of the faradaic process Z_f,
3. The uncompensated resistance, R_Ω, which is usually the solution resistance between working and reference electrodes.

The textbook combination of these elements is shown in Fig. 8.2 and known as *Randle's circuit*, with Z_f and C_d in parallel arrangement. The impedance Z_f can be further subdivided in two equivalent ways:

1. Subdivision into a resistance, R_s, in series with a pseudo-capacitance C_s,
2. Subdivision into a resistance, accounting for the resistance to charge transfer, R_{ct}, and an impedance that measures the difficulty of mass transport of the electroactive species, called the *Warburg impedance*, Z_w.

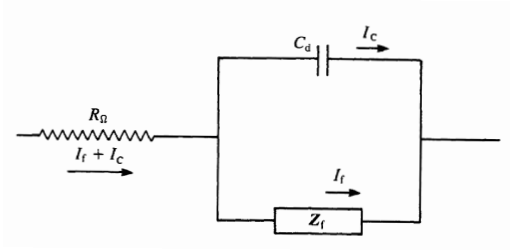

Figure 8.2: Randle's circuit: equivalent electrical circuit of an electrochemical cell for a simple electrode process. Z_f can be substituted with the series of R_{ct} and Z_w.

The last equivalence is often used because of its physical meaning: for kinetically-favoured reactions $R_{ct} \to 0$ and Z_w predominates, while for difficult reactions $R_{ct} \to \infty$ and predominates. More detail about mathematical formulations, based on electrochemical reaction, of the *Warburg impedance* and thus of the faradaic impedance can be found in [216].

The impedance for Randle's circuit will be a complex number which can be represented in its polar plot formalism for all tested frequencies. The explicit real and imaginary parts are given by:

$$\begin{aligned} Z' &= R_\omega + \frac{R_{ct}+\sigma\omega^{-0.5}}{(\sigma\omega^{0.5}C_d+1)^2+\omega^2C_d^2(R_{ct}+\sigma\omega^{-0.5})^2} \\ Z'' &= -\frac{\omega C_d(R_{ct}+\sigma\omega^{-0.5})^2+\sigma^2C_d+\sigma\omega^{-0.5}}{(\sigma\omega^{0.5}C_d+1)^2+\omega^2C_d^2(R_{ct}+\sigma\omega^{-0.5})^2} \end{aligned} \tag{8.14}$$

where σ is a coefficient depending on a combination of different material constants, and ω is the angular frequency in rad/s. Notice the presence

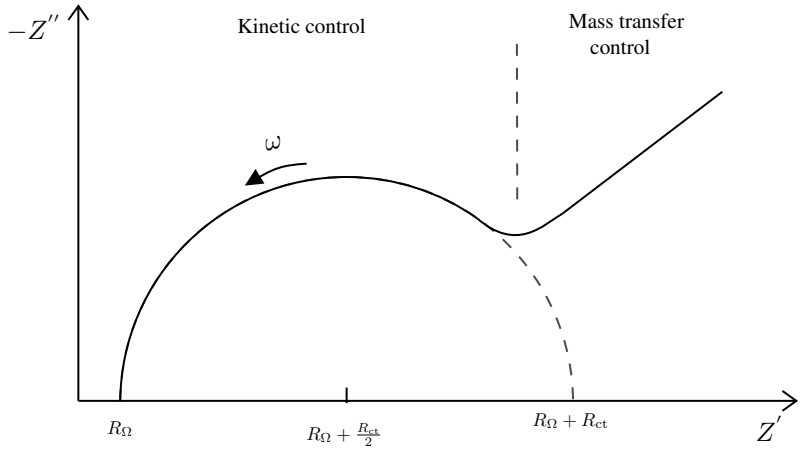

Figure 8.3: Illustration of a polar plot for the Randle's circuit impedance.

of a fractional-order exponent in the model which allows a frequency-dependent real part of impedance (as opposed to classical integer-order impedance whose linear components have a real part constant with frequency).

It is further useful to look at the polar plot of the functions in equation (8.14), also known in chemistry as Cole–Cole plot, as shown in Fig. 8.3. From this figure is possible to appreciate the division in two regions: one represents the behaviour of a kinetically favoured reaction, while the other one shows the predominance of the mass transfer effect.

It is also interesting to discuss the polar plot in Fig. 8.3, with respect to equation (8.14) and studying their limiting forms:

1. For $\omega \to 0$

$$\begin{aligned} Z^{'} &= R_\omega + R_{ct} + \sigma\omega^{-0.5} \\ Z^{"} &= -\sigma\omega^{-0.5} - \sigma^2 C_d \end{aligned} \tag{8.15}$$

   The low-frequency behavior is represented by the straight line of the unit slope and corresponds to a reaction controlled by sole diffusion, the impedance though assumes the form of the Warburg impedance, which dominates.

2. For $\omega \to \infty$

$$\begin{aligned} Z^{'} &= R_\omega + \frac{R_{ct}}{1+\omega^2 C_d^2 R_{ct}^2} \\ Z^{"} &= -\frac{\omega C_d R_{ct}^2}{1+\omega^2 C_d^2 R_{ct}^2} \end{aligned} \tag{8.16}$$

   For higher frequencies, the control of the reaction is purely kinetic and it traduces in the fact that $R_{ct} \gg Z_w$. Hence the electrical circuit in Fig. 8.2 can be simplified in a simple RC parallel. Moreover,

by rearranging equation (8.16) it is possible to obtain the equation of the circle as:

$$\left(Z^{'} - R_{\Omega} - \frac{R_{ct}}{2}\right)^{2} + (Z^{"})^{2} = \left(\frac{R_{ct}}{2}\right)^{2} \tag{8.17}$$

As observed in Fig. 8.3 this semi-circle has a radius of $R_{ct}/2$ and the ideal intercepts on the real axis are R_{ω} $(\omega \to \infty)$ and $R_{\omega} + R_{ct}$ $(\omega \to 0)$. Its success as a sensory instrument is that one can directly extract from a graphical inspection of the polar plot these values. It is also important to understand the physical meaning of the semi-circle, directly linked with the system's characteristic. For very high frequency the imaginary part in equation (8.16), which can be approximated as $Z^{"} \simeq -1/\omega C_{d}$, becomes very small, behaving like a short-circuit. The peak value of the semi-circle is instead reached for the maximum of $-Z^{"}$ in the frequency responsible for the time response (and this results in pole locations of the transfer function of the linear approximated system). For very low frequency it behaves like an open circuit and the current flows through R_{Ω} and R_{ct}.

8.3.2 Laboratory Setup

The setup used for this case study is similar to the one employed in Chapter 5. The same device as shown in Fig. 5.3 is used for measurements, Solatron Modulab Xm impedance analyzer (Solatron Analytical, UK) depicted in Fig. 8.4. Through the Solatron analyzer a 100 mV r.m.s. sinusoidal voltage has been applied to the outer couple of electrodes of the measurement probe which was immersed into the glass tube containing the analyzed sample. Impedance of the samples has been analyzed in the 1 Hz–1 MHz frequency range. The electrochemical cell consisted of a plastic cylindrical tank with an inner diameter of 20 mm and a length of 30 mm. The electrodes used to perform the experiments were screen-printed electrodes from Dropsens. These electrodes are chosen since they exhibit a high electrochemical activity and good repeatability [227]. The counter and working electrodes are platinum (4mm diameter) and the reference electrode is silver.

Figure 8.4: Available in lab device - Solatron ModulabXM impedance analyzer

The *Solatron Modulab Xm* is a highly versatile electrochemical test system that measures the characteristics of a wide range of electrochemical systems including organic/inorganic, specialized corrosion, electroplating and energy cells. Reference grade system components (potentiostat/ galvanostat, frequency response analyzer and optional high voltage amplifier) are combined in a single unit, avoiding the need for stacking and wiring separate units. The device communicates via an Ethernet link to an external PC, running XM-STUDIO ECS software for control and monitoring purposes. A very high sampling rate is available for recording the data samples and stored in real-time in in situ buffer memory slots. The system can export data in real-time (in stack data format) for raw data processing, or can deliver at end-experiment the estimated impedance. For a broader scope of utility of raw data samples, a time- and frequency domain analysis can be performed, hence providing both time-based signals (impedance) as well as image-based data formats (spectrograms).

8.4 Lumped Fractional Order Parametric Models

This subchapter is a revision of the proposed lumped fractional order models from Chapter 5, relevant for the pharmaceutical case study.

When describing time-varying properties of these static characteristics of stress–strain relationships [16], it is very practical to use generalized order models with electrical equivalent notations for material dynamic properties:

$$Z_e(s) = R_e + L_e(s)^{\alpha} + \frac{D_e}{s^{\beta}}, \tag{8.18}$$

where R_e is the electrical resistance related to material resistance, L_e the inductance related to inertance or molecular accelerations and $D_e = 1/C_e$ the compliance value as the inverse of the electrical capacitance. The units depend on the physical units used to derive the impedance from their time-domain measured signals. For electrical circuits, these time signals are in Volts, while for air/liquid measurements the time signals are in pressure (Pa) and flow in liters/s. The elements in this model have been in detail derived from mechanical and electrical equivalent properties analogy in [13]. When interpreting the model at a micro-scale level, the model refers to the diffusion process of glucose molecules in the simulated environment [220]:

$$Z(s) = \frac{D_e}{s^{\beta}}. \tag{8.19}$$

Thus, the complex representation in frequency domain of this generic fractional order model is:

$$Z_e(j\omega) = R_e + L_e(j\omega)^{\alpha} + \frac{D_e}{(j\omega)^{\beta}}, \qquad -2 < \alpha, \beta < 2 \tag{8.20}$$

When identifying real data samples, the real and imaginary parts can be evaluated in the cost function of a regressor estimator:

$$\begin{array}{ll} Z_e(j\omega) & = R_e + L_e\omega^{\alpha}\cos\left(\frac{\alpha\pi}{2}\right) + \frac{D_e}{\omega^{\beta}}\cos\left(\frac{\beta\pi}{2}\right) \\ Z_e(j\omega) & = -\left[L_e\omega^{\alpha}\sin\left(\frac{\alpha\pi}{2}\right) + \frac{D_e}{\omega^{\beta}}\sin\left(\frac{\beta\pi}{2}\right)\right] \end{array} . \tag{8.21}$$

When the material properties behave as an electrical circuit that has one resistor and two fractional order capacitors, also known as constant phase elements, the number of model parameters can be significantly reduced to

$$Z_e(s) = R_e + \frac{D_e}{s^{\alpha}}. \tag{8.22}$$

This was previously shown to be the case in non-Newtonian fluids with thixotropic properties. In this model, α can be fixed per tablet geometrical properties, while R_e and D_e are related to dynamic changes in viscosity and density of the material mixture. The drawback of this model structure is that its accuracy is limited over a rather small frequency interval (i.e., 1–2 decade interval).

An alternative solution for a much broader (i.e., several decades) frequency interval dependence of the polar plot representation is the model

$$Z(s) = \frac{Kp}{s^{\beta}\,(s+p)^{\alpha}} \tag{8.23}$$

which is a four parameters model. In this model, all parameters were sensitive to changes in material properties, and the results suggested that in order to increase the detectability of material properties, correlation matrices can be used to calibrate it for particular applications at hand. When parameters K, p, α, β are fixed to the material specifications, the parameter p has an excellent sensitivity to capture changes in viscosity.

8.5 Results and Discussion

The team from DySC Research Group at Ghent University developed a banchmark simulator describing tableting production using wet/dry granulation for simulation, analysis and control design and validation purposes. The continuous manufacturing process flowchart is depicted in Fig. 8.5. In the open-source simulation platform the wet and dry granulation routes are implemented, however, a model library is available for simulating the user-specified sub-processes production line.

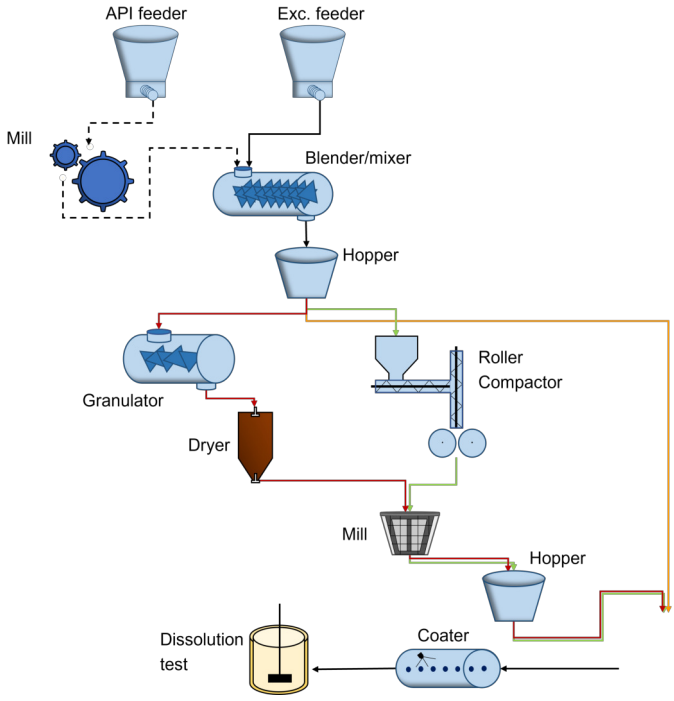

Figure 8.5: Continuous pharmaceutical tablet manufacturing processes: wet granulation (**red**), dry granulation (**green**) and direct compaction (**orange**) routes.

A schematic of the MATLAB/Simulink benchmark simulator is given in Fig. 8.6. Details related to the simulator's versatility and available implemented models can be found in [218].

In this thesis a study case on the blender unit, where the powder and excipient are mixed to produce a material that is granular in form has been investigated. A population balance modeling approach has been used to model the blending process [218]:

$$\frac{\partial m_{ij}}{\partial t} = F_f[m_{i-1,j} - m_{i,j}] + F_b[m_{i+1,j} - m_{i,j}] + F_r[m_{i,j+1} + m_{i,j-1} - m_{i,j}] \tag{8.24}$$

which represents the powder distribution of both the API and the excipient in each compartment. The corresponding flows (m^3/s) are obtained from:

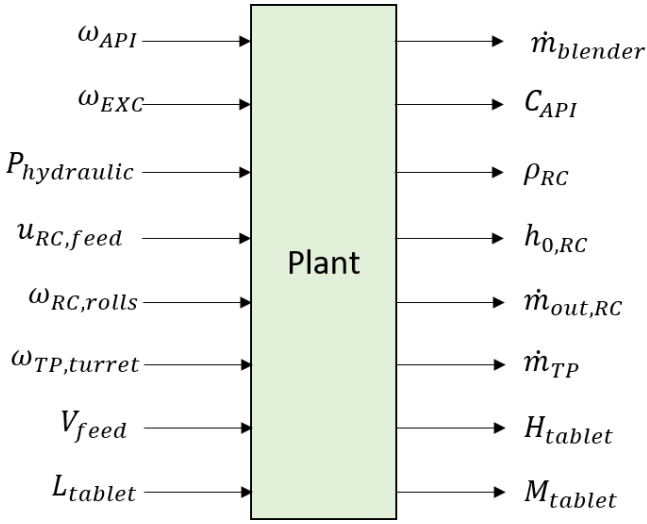

Figure 8.6: Schematic of the input-output pharmaceutical benchmark simulator

$$\begin{aligned} F_f &= av_b + b \\ F_b &= cv_b + d \\ F_r &= e \end{aligned} \quad , \tag{8.25}$$

where v_b represents the speed of the blender in rpm and the a, b, c, d, e coefficients are parameters estimated from experimental data to calibrate the model. The combined flow is given by

$$F_{blender} = \sum_{j=1}^{N_r} F_{f,API} m_{API,i=N_a,j} + \sum_{j=1}^{N_r} F_{f,Exc} m_{Exc,i=N_a,j}. \tag{8.26}$$

Consequently, the outlet concentration C_{API} in mol/m^3 is given by

$$C_{API} = \frac{\sum_{j=1}^{N_r} F_{f,API} m_{API,i=N_a,j}}{F_{blender}} \tag{8.27}$$

and the relative standard deviation (RSD_{API})

$$\frac{\sqrt{\frac{1}{N_r-1}\sum_{j=1}^{N_r}\left(\frac{F_{f,API} m_{API,i=N_a,j}}{F_{f,API} m_{API,i=N_a,j} + F_{f,Exc} m_{Exc,i=N_a,j}} - C_{API}\right)^2}}{C_{API}}. \tag{8.28}$$

Essentially, this process requires ratio control as a natural solution for mixing flows.

All transfer functions implemented in the benchmark pharma simulator are based on literature models. Every process units is characterized

by a specific transfer function representing the process dynamics. For the feeder unit, a simplified semi-empirical first order model (FOPDT) is utilized for modeling the feeder unit.. The relationship between the screw speed and the mass flow rate of the feeder is accurately predicted. It requires extra parameters, such as the vertical stress (σ_v Pa), the density constant (ρ kg/m^3), the mass and radius of the blade (M_{blade} kg and R_{blade} m), etc. For the blender unit, transfer function models have been derived from the population balance models given in equations (8.24)–(8.28).

All process parameters are detailed in Table 8.1.

Table 8.1: Parameters for the blending process unit.

Parameter	Symbol	Value	Unit
Number of axial compartments	N_a	10	-
Number of radial compartments	N_r	7	-
API forward flux parameter	a_{API}	5×10^3	kg/(s rpm)
API forward flux parameter	b_{API}	1×10^{-1}	kg/s
API backward flux parameter	c_{API}	6×10^{-4}	kg/(s rpm)
API backward flux parameter	d_{API}	0	kg/s
API radial flux parameter	e_{API}	1.1×10^{-2}	kg/(s rpm)
MCC forward flux parameter	a_{Exc}	2.5×10^3	kg/(s rpm)
MCC forward flux parameter	b_{Exc}	9.8×10^{-2}	kg/s
MCC backward flux parameter	c_{Exc}	1.3×10^{-3}	kg/(s rpm)
MCC backward flux parameter	d_{Exc}	0	kg/s
MCC radial flux parameter	e_{Exc}	6.4×10^{-3}	kg/(s rpm)

For two different species, the following impedance have been obtained, as illustrated in Fig. 8.7b. We compare the frequency response estimation against the parametric model estimation with one pole or two poles in the transfer function from equation (8.23). It turned out the result with one pole was sufficiently accurate.

The methods for identification have been detailed in 5. The identified optimal parameters are listed in Table 8.2.

If the grain particle size is decreasing, the number of particles per volume unit is increasing and viscosity is increasing to decrease flow. To

Table 8.2: Reduced order model parameters (8.23) for two species of different viscosity.

	K	p	α	ρ	$NMSE$
Species 1	$1.11 \cdot 10^8$	$1.46 \cdot 10^3$	0.70	0.015	$4.32 \cdot 10^{-5}$
Species 2	$1.33 \cdot 10^8$	$1.95 \cdot 10^3$	0.75	0.019	$9.61 \cdot 10^{-5}$

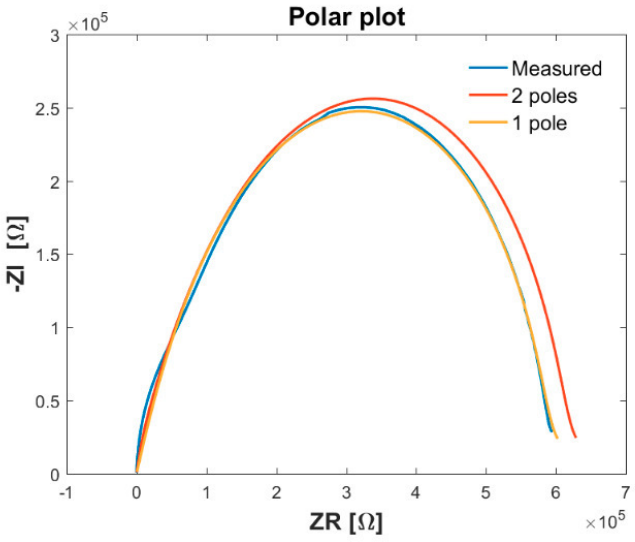

(a)

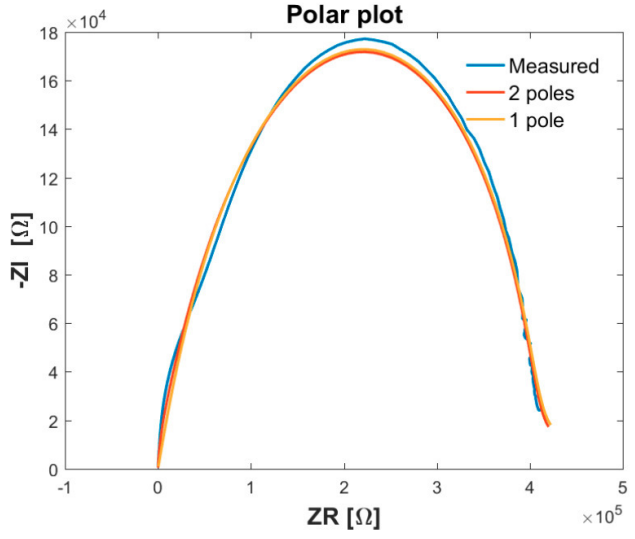

(b)

Figure 8.7: (**a**) Case 1 : performance of the empirical model (8.23) in polar plot. (**b**) Case 2: performance of the empirical model (8.23) in polar plots.

maintain a constant flow of species in the blender, the ratio controller gains should be adapted. An example of the relationship between the particle size and flow of species is given in Fig. 8.8.

Using mapping as that given in Fig. 8.8, adaptation to context variations in terms of material properties can be done. Context-aware control is a major trend in current engineering applications, and the pharmaceutical industry offers a great opportunity to pick up emerging solutions from more established fields of control applications, as the event based control illustrated in Chapter4.

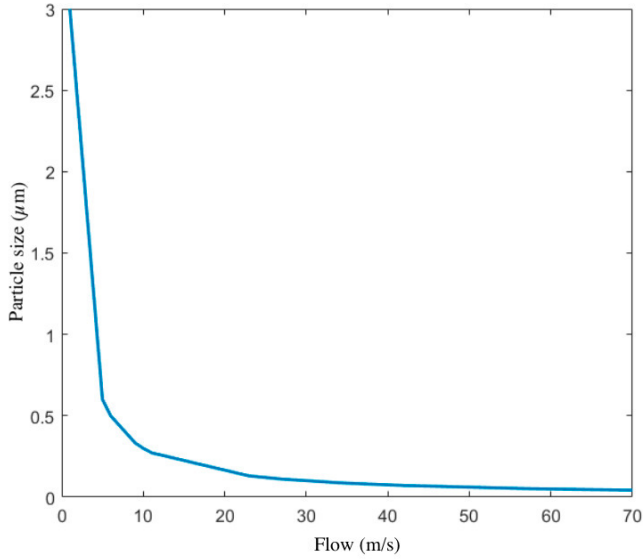

Figure 8.8: An example of how the particle size of species influences the flow as part of the ratio control algorithm.

This very complex process of tablet manufacturing is described by several sub-processes (e.g., dispensing, blending, granulation, drying, tableting) as depicted in Fig. 8.5. To ensure optimal production each unit needs to operate such that to assure the critical quality attributes. The development of advanced inline monitoring techniques (e.g., the sensing spectroscopy) tracks the product at each individual stage of manufacturing and eventually saves additional analysis time, thereby enabling the direct release of the continuously manufactured batch into the market without delay.

The production thereof is a complex multivariable process and modifications to any of the mentioned components can have important implications on the efficiency of the production process (e.g., changes in powder stickiness or mixture viscosity). Therefore, optimal control of production

efficiency and product properties is essential to guarantee a manufacturing process that is adaptive while maintaining quality at all times. This implies that every unit in the production line has to be controlled such that the manufactured tablets are within the very strict performance criteria. However, the focus of this study case is not on the control of the continuous manufacturing line, but to show the potential of sensing spectroscopy for the self-tuning ratio control.

8.6 Summary

The study case investigates material properties analysis in the pharmaceutical industry using impedance spectroscopy sensing. It aims to enable the use of material properties in varying conditions to self-tune control algorithms. The solution proposed here exploits the capability of generalized order lumped parametric models to capture material properties and their suitability for online estimations. The results indicate the potential of the proposed methodology for self-tuning ratio control, where the model parameters obtained using impedance spectroscopy will be then used for the self-tuning control gain. This constitutes a step forward in the paradigm shift from batch to continuous manufacturing in the pharma industry as the end-to-end process consists of different control loops. Moreover, the algorithm is a versatile theoretical framework and can be extended to other industries, e.g., food, oil, petrochemical. The particular application presented in this chapter is to show the feasibility of the proposed theoretical framework to a real-life industrial process, enhancing the advantage of modeling and control techniques in the field of pharmaceutical applications to facilitate the transition from batch-wise production to continuous manufacturing.

The results presented in this chapter have been published in:

- M. Ghita, **I. Birs**, D. Copot, I. Nascu, C. Ionescu. "Impedance Spectroscopy Sensing Material Properties for Self-Tuning Ratio Control in Pharmaceutical Industry", in *Applied Sciences*, vol. 12, no. 1, pp. 509, DOI: 10.3390/app12010509, 2022.

9

Conclusions and Perspectives

This section summarizes the main conclusions of this thesis and outlines the directions of future research related to non-Newtonian fluids.

9.1 Conclusions

The thesis focuses on fractional calculus, a powerful mathematical tool that has gained popularity in the last two decades. The addition of fractional orders of differentiation and integration enable a generalization of mathematical models and control strategies, which are proven to be more powerful than classical, integer order, elements. Fractional order models capture physical phenomena in an intrinsic manner, with differ-integral operations of any arbitrary, non-integer order. Previous works focusing on the modeling of viscoelastic phenomena in biological tissue using fractional order differentiation already proved the superiority of the approach. However, fractional calculus was not yet explored in conjunction with non-Newtonian fluids: a class of fluids known to exhibit viscoelastic behavior.

Navier-Stokes equations from classical fluid flow theory combined with fractional constitutive equations for velocity profiles and flow give a general framework for modeling velocity profiles and suspended (infinitesimal) objects in non-Newtonian fluid environments. The theoretical analysis under steady and pulsatile flow conditions of incrompressible fluids from Chapter 3 claims that fractional calculus is a natural solution to model velocity and friction drag effect upon a suspended object in non-Newtonian fluids.

Fractional impedance models can also be used to capture fluid mechanics properties in frequency domain experimental data sets. This is a conclusion that has been drawn experimentally based on the study from Chapter 5. The properties of four classes of fluids featuring different

NN properties: oils, sugar, detergent and liquid soap were measured using impedance spectroscopy. Nonlinear identification models such as least squares, genetic algorithms and particle swarm optimization obtain a good characterization of non-Newtonian viscoelastic properties. The minimal parameter versatile fractional order impedance model successfully characterize viscosity-related properties in non-Newtonian fluids. The experimental test samples and identified model parameters suggest the model is adequate to determine variations in fluid properties from several applications.

One of the main difficulties identified when analyzing non-Newtonian fluid interactions was the lack of (affordable) lab scale setups mimicking main properties of this type of fluids and lack of systematic analysis tools. This motivated the design and construction of a laboratory benchmark setup for non-Newtonian fluid analysis. Apart from a non-Newtonian circulatory system, the benchmark also features a miniature submersible able to transit the environment. The result of this activity is a research and education appropriate experimental setup that can be easily recreated using low-cost, widely available components.

Non-Newtonian fluid interactions with a transiting vehicle can be modeled using experimental data acquired from the benchmark and fractional order models developed starting from basic navigation in Newtonian fluids. For the obtained non-Newtonian fractional order process model, a fractional order PD control approach is employed to regulate the submerged object's position inside the environment. The presented modeling and control methodologies are endorsed by real-life experimental data used to validate the veracity of the presented concepts. The control strategy is robust to environmental changes, experimentally validated for both Newtonian and non-Newtonian environments. This study claims that integer order controllers are unsuitable for thrusting in non-Newtonian fluids and that fractional order control components are desired due to their improved performance, stability and robustness.

A novel concept related to event-based fractional order control is used throughout the thesis. This represents an original contribution to the generalization of event-based control to the field of fractional calculus, combining the benefits brought by the two approaches into an industrial-suitable control strategy. Although in recent years, control applications based on fractional order differ-integral operators have gained popularity due to their proven superior performance when compared to classical, integer order, control strategies, the current industrial setting is not yet prepared to fully adapt to these newcomer solutions. Benefits of event-based control such as resource optimization and bandwidth allocation can be successfully combined with the superior performance of fractional order control. Theoretical and implementation aspects are developed in order to provide a generalization of event-based control into the fractional calculus field. Different numerical examples validate the proposed methodology,

providing a useful tool, especially for industrial applications where the event-based control is most needed. Several event-based fractional order implementation possibilities are explored, the final result being an event-based fractional order control methodology.

Case studies involving the experimental benchmark validate the event-based fractional order approach using environmental assessment based on context aware information. Context aware control can be successfully used for energy efficiency and decision-making based on changing operating conditions, without hindering the performance, stability and robustness obtained by fractional order control.

The proposed non-Newtonian framework based on fractional calculus can be employed in industrial manufacturing processes that involve both Newtonian and non-Newtonian characteristics such as steel manufacturing and pharmaceuticals (material properties of granulation processes).

Fractional calculus can also be used to develop non-Newtonian fluid flow models of liquid steel in a continuous casting process. Real plant data from ArcellorMittal Gent is used to calibrate the model obtained for non-Newtonian interactions. Furthermore, a suitable fractional order PI controller is tuned and validated through simulations while taking into account real life operating conditions and disturbances. The obtained results using the proposed approach are compared to previous results achieved with an integer order PI controller. The comparison clearly proves the superiority of both fractional order modeling and control for liquid steel manufacturing.

In addition, the proposed event-based structure that considers intrinsic events of the process triggered by automatic surface inspection system is an elegant solution to improve the final product's quality.

The last case study claims that material properties in the pharmaceutical industry can be analyzed using impedance spectroscopy sensing. It enables the use of material properties in varying conditions to self-tune control algorithms. The proposed solution highlights the capability of generalized order lumped parametric models to capture material properties and their suitability for online estimations. The results indicate the potential of the proposed methodology for self-tuning ratio control, where the model parameters obtained using impedance spectroscopy will be then used for the self-tuning control gain.

The tablet manufacturing case study shows the feasibility of the proposed theoretical framework to a second real-life industrial process, enhancing the advantage of modeling and control techniques in the field of pharmaceutical applications to facilitate the transition from batch-wise production to continuous manufacturing.

The problems stated in to the Problem Formulation section from the Introduction related to non-Newtonian modeling and control have been solved:

- Powerful emerging tools from fractional calculus not yet acknowledged by the scientific community, with limited and scarce studies has been directly approached by Chapters 2 and 4. However, the entire thesis raises awareness of the endless possibilities offered by fractional order operators, with an emphasis on non-Newtonian fluid modeling and control.
- The lack of established know-how on motion of suspended objects in non-Newtonian fluids has been tackled in Chapters 3 from a theoretical perspective, followed by a practical approach in Chapter 6.
- The lack of know-how on closed loop control of velocity, position or other functionality of suspended objects in non-Newtonian environments is the topic of Chapter 6.
- Optimal natural solutions replacing linear approximations of high order and high numerical complexity are explored in Chapter 5 for various classes of non-Newtonian fluids.
- The lack of affordable lab scale setups mimicking the main properties of non-Newtonian fluids has been resolved by the experimental benchmark proposed in Chapter 6.
- Missing industrial and practical use of non-Newtonian related studies has been approached in Chapters 7 and 8 for two different industries: steel manufacturing and pharmaceutical tablet manufacturing.
- The lack of systematic analysis tools has been successfully explored in Chapters 5, 6, 7 and 8.

9.2 Perspectives

The non-Newtonian framework and environmental assessment based on context aware information can be useful in a wide variety of multidisciplinary processes such as below ice cap exploration (the mixture of water and ice being a non-Newtonian fluid), muddy water monitoring (in waste water treatment plants/basins), transportation (pipelines), biomedical applications such as targeted drug delivery, lung inflammatory response monitoring (fluid in lungs), anesthesia (in vivo or by-pass blood concentration monitoring), etc. or in manufacturing processes that involve both Newtonian and non-Newtonian characteristics such as steel manufacturing, pharmaceuticals (material properties of granulation processes), etc.

One of the main advantages of the impedance models from Chapters 5 and 7 is that they are lumped. The fractional order models that efficiently capture non-Newtonian fluid properties and can be identified in real-time

for further use in prediction or control applications. This has a manifold of applicability in various industries (e.g., food, oil, petrochemical, etc.) where Newtonian/non-Newtonian changes occur throughout due to various operating conditions. This constitutes a step forward in the manufacturing paradigm shift as the end-to-end process consists of different control loops.

Future developments include the physical implementation of the fractional order controller developed for liquid steel manufacturing on the real plant at ArcellorMittal Gent together with the context aware paradigms for final product fault reduction. The event-based strategy can be extended to include more types of defects (i.e. oscillation marks, surface cracks). The RAMI 4.0 architecture can be used to update existing control loops to a more context-aware focused solution that isolates intrinsic events and automatically performs decision-making at the lowest layer of the architectural chain.

Another perspective consists of clear allocation of context-aware tasks in the hierarchy levels of the RAMI 4.0 industrial architecture. This enable the implementation of event-based control strategies with isolated decisions performed between the field and control devices.

The current pharmaceutical industry trend is to move from batch to continuous manufacturing process. Material property based control is an ideal solution to pursue, since the product changes various states (i.e. solid, liquid) during wet/dry granulation routes. Providing accurate models for different stages enables suitable control options, a paramount issue in the pharmaceutical industry where error tolerances are unyielding.

Targeting drug delivery is an emerging field with enormous biomedical potential impact. Non-Newtonian frameworks are highly relevant since blood is a non-Newtonian fluid. Current medicine trends involve treatment application with nanorobots that are able to diagnose and perform localized drug delivery in living environments. Localized treatments reduce the quantity of substance necessary for treatment, leading to decreased intoxication of the cells, with major benefits such as reduced side effects, faster drug absorption and a more efficient and safer treatment for the patient. Context awareness is a necessity since robots used for localized delivery should sense the environment: measure intoxication levels, detect blood clogs, etc, in order to provide the feedback needed to close the control loop for automated substance administration. Hence, a possible extension of the modeling and control concepts connected to non-Newtonian fluids introduced throughout the thesis is in the field of targeted drug delivery. Accurate interactions between blood and transiting carrier particles can be modeled starting from the previously introduced concepts.

Bibliography

[1] Frank M. White. *Fluid Mechanics 7^{th} edition (In SI Units)*. McGraw Hill, 2011.

[2] Iwona Chlebicka, Piotr Gwiazda, Agnieszka Swierczewska-Gwiazda, and Aneta Wróblewska-Kamińska. *Non-Newtonian Fluids*, pages 261–332. Springer, Cham, 2021.

[3] Ingrid de Almeida Ribeiro and Maurice de Koning. Non-Newtonian flow effects in supercooled water. *Physical Review Research*, 2:022004, Apr 2020.

[4] Esmaeel Fatahian, Naser Kordani, and Hossein Fatahian. A review on rheology of non-Newtonian properties of blood. *IIUM Engineering Journal*, 19(1):237–250, Mar. 2018.

[5] Christian D. Langevin. Modeling axisymmetric flow and transport. *Ground Water*, 46:579–590, 2008.

[6] Richard Magin, Blas Vinagre, and Igor Podlubny. Can Cybernetics and Fractional Calculus Be Partners?: Searching for New Ways to Solve Complex Problems. *IEEE Systems, Man, and Cybernetics Magazine*, 4(3):23–28, 2018.

[7] Clara Ionescu, Antonio Lopes, Dana Copot, Jose Antonio Tenreiro Machado, and Jason H.T. Bates. The role of fractional calculus in modeling biological phenomena: A review. *Communications in Nonlinear Science and Numerical Simulation*, 51:141–151, 2017.

[8] Hyun-Taek Choi and Junku Yuh. *Underwater Robots*. Springer, Cham, 2016.

[9] Roderic Lakes. *Viscoelastic Materials*. Cambridge University Press, 2009.

[10] Clara Ionescu and James F. Kelly. Fractional calculus for respiratory mechanics: Power law impedance, viscoelasticity, and tissue heterogeneity. *Chaos, Solitons and Fractals*, 102:433–440, 2017.

[11] Yan Li, Yang Quan Chen, and Igor Podlubny. Mittag-Leffler stability of fractional order nonlinear dynamic systems. *Automatica*, 45:1965–1969, 2009.

[12] Yan Li, Yang Quan Chen, and Igor Podlubny. Stability of fractional-order nonlinear dynamic systems: Lyapunov direct method and generalized Mittag-Leffler stability. *Computers and Mathematics with Applications*, 59:1810–1821, 2010.

[13] Clara M. Ionescu. A memory-based model for blood viscosity. *Communications in Nonlinear Science and Numerical Simulation*, 45:29–34, 2017.

[14] Jose Tenreiro Machado and Virginia Kiryakova. The Chronicles of Fractional Calculus. *Fractional Calculus and Applied Analysis*, 20(2):307–336, 2017.

[15] Deshun Yin, Wei Zhang, Chen Cheng, and Yanqing Li. Fractional time-dependent Bingham model for muddy clay. *Journal of Non-Newtonian Fluid Mechanics*, 187-188:32–35, 2012.

[16] James F. Kelly and Robert J. McGough. Fractal ladder models and power law wave equations. *The Journal of the Acoustical Society of America*, 126:2072–2081, 2009.

[17] Guido Ala, Mario Di Paola, Elisa Francomano, Yan Li, and Francesco P. Pinnola. Electrical analogous in viscoelasticity. *Communications in Nonlinear Science and Numerical Simulation*, 19:2513–2527, 2014.

[18] Dana Copot, Richard L. Magin, Robin De Keyser, and Clara Ionescu. Data-driven modelling of drug tissue trapping using anomalous kinetics. *Chaos, Solitons and Fractals*, 102:441–446, 2017.

[19] Yamaan Saadeh and Dinesh Vyas. Nanorobotic Applications in Medicine: Current Proposals and Designs. *American Journal of Robotic Surgery*, 1:4–11, 2015.

[20] Concepción Monje, YangQuan Chen, Blas Vinagre, Dingyu Xue, and Vicente Feliu. *Fractional Order Systems and Control - Fundamentals and Applications*. Springer, 01 2010.

[21] Igor Podlubny. Fractional-order systems and PI˘D-controllers. *IEEE Transactions on Automatic Control*, 44:208–214, 1999.

[22] Rafail K. Gazizov and Stanislav Yu. Lukashchuk. Higher-Order Symmetries of a Time-Fractional Anomalous Diffusion Equation. *Mathematics*, 9(3):1–11, 2021.

[23] Yuli Chen, Fawang Liu, Qiang Yu, and Tianzeng Li. Review of fractional epidemic models. *Applied Mathematical Modelling*, 97:281–307, 2021.

[24] Clara M. Ionescu, Eva H. Dulf, Maria Ghita, and Cristina I. Muresan. Robust controller design: Recent emerging concepts for control of mechatronic systems. *Journal of the Franklin Institute*, 357(12):7818–7844, 2020.

[25] Robin De Keyser, Cristina I. Muresan, and Clara M. Ionescu. A novel auto-tuning method for fractional order PI/PD controllers. *ISA Transactions*, 62:268–275, 2016. SI: Control of Renewable Energy Systems.

[26] Isabela Birs, Cristina Muresan, Ioan Nascu, and Clara Ionescu. A Survey of Recent Advances in Fractional Order Control for Time Delay Systems. *IEEE Access*, 7:30951–30965, 2019.

[27] Ali Ahmadi Dastjerdi, Blas M Vinagre, YangQuan Chen, and S. Hassan HosseinNia. Linear fractional order controllers; A survey in the frequency domain. *Annual Reviews in Control*, 47:51–70, 2019.

[28] Pritesh Shah and Sudhir Agashe. Review of fractional PID controller. *Mechatronics*, 38:29–41, 2016.

[29] D. Valério, J. Trujillo, M. Rivero, J. Machado, and D. Baleanu. Fractional calculus: A survey of useful formulas. *The European Physical Journal Special Topics*, 222:1827–1846, 2013.

[30] Manuel Ortigueira and Jose Antonio Tenreiro Machado. What is a fractional derivative? *Journal of Computational Physics*, 293:4–13, 2015.

[31] Michele Caputo. Linear Models of Dissipation whose Q is almost Frequency Independent-II. *Geophysical Journal International*, 13(5):529–539, 11 1967.

[32] Ludomir Dorcak. Numerical Models for the Simulation of the Fractional-Order Control Systems. *arXiv: Optimization and Control*, pages 1–12, 05 2002.

[33] Antonio M Lopes and Jose Tenreiro Machado. Fractional order models of leaves. *Journal of Vibration and Control*, 20(7):998–1008, 2014.

[34] Abdon Atangana. Chapter 5 - Fractional Operators and Their Applications. In Abdon Atangana, editor, *Fractional Operators with Constant and Variable Order with Application to Geo-Hydrology*, pages 79–112. Academic Press, 2018.

[35] Lakshman Mahto, Syed Abbas, and Angelo Favini. Analysis of Caputo impulsive fractional order differential equations with applications. *International Journal of Differential Equations*, 2013:704547, 2013.

[36] Dumitru Baleanu and Ravi P. Agarwal. Fractional calculus in the sky. pages 1–9, 2021.

[37] Mahmood Ghanbari and Mohammad Haeri. Order and pole locator estimation in fractional order systems using bode diagram. *Signal Processing*, 91(2):191–202, 2011.

[38] Hongguang Sun, Wen Chen, and YangQuan Chen. Variable-order fractional differential operators in anomalous diffusion modeling. *Physica A: Statistical Mechanics and its Applications*, 388:4586–4592, 11 2009.

[39] Guy Jumarie. Modified Riemann-Liouville derivative and fractional Taylor series of nondifferentiable functions further results. *Computers and Mathematics with Applications*, 51:1367–1376, 2006.

[40] Ronald L. Bagley and Peter J. Torvik. A Theoretical Basis for the Application of Fractional Calculus to Viscoelasticity. *Journal of Rheology*, 27:201–210, 1983.

[41] F. C. Meral, T. J. Royston, and R. Magin. Fractional calculus in viscoelasticity: An experimental study. *Communications in Nonlinear Science and Numerical Simulation*, pages 939–945, 2010.

[42] R. C. Koeller. Applications of Fractional Calculus to the Theory of Viscoelasticity. *Journal of Applied Mechanics*, pages 229–307, 2009.

[43] Richard L. Magin. Fractional Calculus in Bioengineering, Part3. *Critical Reviews in Biomedical Engineering*, pages 195–377, 2005.

[44] Gianluca Alaimo and Massimiliano Zingales. Laminar flow through fractal porous materials: The fractional-order transport equation. *Communications in Nonlinear Science and Numerical Simulation*, pages 889–902, 2015.

[45] J. Kim and P. Moin. Application of a fractional-step method to incompressible Navier-Stokes equations. *Journal of Computational Physics*, pages 308–323, 1985.

[46] Cristina Muresan, Isabela Birs, Clara Ionescu, and Robin De Keyser. Tuning of fractional order proportional integral/proportional derivative controllers based on existence conditions. *Proceedings of the Institution of Mechanical Engineers. Part I: Journal of Systems and Control Engineering*, 233:384–391, 2019.

[47] Swati Sondhi and Yogesh Hote. Fractional Order Controller and its Applications: A Review. 04 2012.

[48] Ammar Soukkou, M C Belhour, and Salah Leulmi. Review, Design, Optimization and Stability Analysis of Fractional-Order PID Controller. *International Journal of Intelligent Systems and Applications*, 8(7):73, 2016.

[49] Bo Yang Leng, Zhi Dong Qi, Liang Shan, and Hui Juan Bian. Review of Fractional Order Control. In *Modern Technologies in Materials, Mechanics and Intelligent Systems*, volume 1049 of *Advanced Materials Research*, pages 983–986. Trans Tech Publications, 2014.

[50] Pritesh Shah and Sudhir Agashe. Review of fractional PID controller. *Mechatronics*, 38:29–41, 2016.

[51] Ali Yüce, Nusret Tan, and Derek P Atherton. Fractional Order PI Controller Design for Time Delay Systems. *IFAC-PapersOnLine*, 49(10):94–99, 2016.

[52] Talar Sadalla, Dariusz Horla, Wojciech Giernacki, and Piotr Kozierski. Influence of time delay on fractional-order PI-controlled system for a second-order oscillatory plant model with time delay. In *Polish Academy of Sciences*, 2017.

[53] T. Sadalla, D. Horla, W. Giernacki, and P. Kozierski. Stability analysis and tracking performance of fractional-order PI controller for a second-order oscillatory system with time-delay. In *2016 21st International Conference on Methods and Models in Automation and Robotics (MMAR)*, pages 322–326, Aug 2016.

[54] Amin Jajarmi and Dumitru Baleanu. Suboptimal control of fractional-order dynamic systems with delay argument. *Journal of Vibration and Control*, 24(12):2430–2446, 2018.

[55] Fabrizio Padula and Antonio Visioli. Tuning rules for optimal PID and fractional-order PID controllers. *Journal of Process Control*, 21(1):69–81, 2011.

[56] Seied Jalil Sadati, Abolfazl Ranjbar Noei, and Reza Ghaderi. Fractional-order control of a nonlinear time-delay system: case study in oxygen regulation in the heart-lung machine. *Journal of Control Science and Engineering*, 2012:1–8, 2012.

[57] Mohamed Azab and Alexandre Serrano-Fontova. Optimal Tuning of Fractional Order Controllers for Dual Active Bridge-Based DC Microgrid Including Voltage Stability Assessment. *Electronics*, 10:1109, 2021.

[58] Aleksei Tepljakov, Baris Baykant Alagoz, Celaleddin Yeroglu, Emmanuel A. Gonzalez, S. Hassan Hosseinnia, Eduard Petlenkov, Abdullah Ates, and Martin Cech. Towards Industrialization of FOPID Controllers: A Survey on Milestones of Fractional-Order Control and Pathways for Future Developments. *IEEE Access*, 9:21016–21042, 2021.

[59] Ali Ahmadi Dastjerdi, Blas M. Vinagre, Yang Quan Chen, and S. Hassan HosseinNia. Linear fractional order controllers; A survey in the frequency domain. *Annual Reviews in Control*, 47:51–70, 2019.

[60] Y Li, D Xue, and Y Chen. Sensitivity function of LTI fractional order dynamic systems with respect to the orders. In *Proceedings of the 2010 American Control Conference*, pages 6692–6697, jun 2010.

[61] Masoomeh Shahiri, Abolfazl Ranjbar Noei, Mohammad Reza Karami, and Reza Ghaderi. Tuning Method for Fractional Complex Order Controller Using Standardized k-Chart: Application to PEMFC Control. *Asian Journal of Control*, 18(3):1102–1118, 2017.

[62] Isabela Roxana Birs, Cristina I. Muresan, Ioan Nascu, Silviu Corneliu Folea, and Clara Mihaela Ionescu. Experimental results of fractional order PI controller designed for second order plus dead time (SOPDT) processes, 2018.

[63] Aida Baltag, Gheorghe Livint, and Alina Georgiana Baciu. Design of Fractional Order Controllers for Wind Turbines. *2020 International Conference and Exposition on Electrical And Power Engineering (EPE)*, pages 727–732, 2020.

[64] J J Gude and E Kahoraho. Simple tuning rules for fractional PI controllers. In *2009 IEEE Conference on Emerging Technologies Factory Automation*, pages 1–8, sep 2009.

[65] S Das, S Das, and A Gupta. Fractional Order Modeling of a PHWR Under Step-Back Condition and Control of Its Global Power With a Robust $PI^{\lambda}D^{\mu}$ Controller. *IEEE Transactions on Nuclear Science*, 58(5):2431–2441, oct 2011.

[66] T Vinopraba, N Sivakumaran, N Selvaganesan, and S Narayanan. Stabilization Using Fractional-Order $PID\alpha$ Controllers for First Order Time Delay System. In *Advances in Computing, Control, and Telecommunication Technologies, International Conference on(ACT)*, volume 00, pages 725–728, 2010.

[67] Ying Luo and YangQuan Chen. Stabilizing and robust fractional order PI controller synthesis for first order plus time delay systems. *Automatica*, 48(9):2159–2167, 2012.

[68] A Narang, S L Shah, and T Chen. Tuning of fractional PI controllers for fractional order system models with and without time delays. In *Proceedings of the 2010 American Control Conference*, pages 6674–6679, jun 2010.

[69] Farshad Merrikh-Bayat. General rules for optimal tuning the $PI^{\lambda}D^{\mu}$ controllers with application to first-order plus time delay processes. *The Canadian Journal of Chemical Engineering*, 90(6):1400–1410, 2018.

[70] Rabindra Kumar Sahu, Sidhartha Panda, and Umesh Kumar Rout. DE optimized parallel 2-DOF PID controller for load frequency control of power system with governor dead-band nonlinearity. *International Journal of Electrical Power & Energy Systems*, 49:19–33, 2013.

[71] Xu Yang, Yingjie Liang, and Wen Chen. A spatial fractional seepage model for the flow of non-Newtonian fluid in fractal porous medium. *Communications in Nonlinear Science and Numerical Simulation*, 65:70–78, 2018.

[72] Hong Guang Sun, Yong Zhang, Song Wei, Jianting Zhu, and Wen Chen. A space fractional constitutive equation model for non-Newtonian fluid flow. *Communications in Nonlinear Science and Numerical Simulation*, 62:409–417, 2018.

[73] Yury Carrera, Gabriela Avila-de la Rosa, Jaime Vernon-Carter, and Jose Alvarez-Ramirez. A fractional-order Maxwell model for non-Newtonian fluids. *Physica A: Statistical Mechanics and its Applications*, 482:276–285, 2017.

[74] Bastian E. Rapp. *Microfluidics: Modeling, mechanics and mathematics*. Elsevier, 2016.

[75] Clara M. Ionescu. *The Human respiratory System: An Analysis of the Interplay between Anatomy, Structure, Breathing and Fractal Dynamics*. Springer, 2013.

[76] Arild Saasen and Jan David Ytrehus. Viscosity models for drilling fluids - Herschel-bulkley parameters and their use. *Energies*, 13:5271, 2020.

[77] Takshak Shende, Vahid J. Niasar, and Masoud Babaei. An empirical equation for shear viscosity of shear thickening fluids. *Journal of Molecular Liquids*, 325:115220, 2021.

[78] Minghai Wei, Li Sun, Peipei Qi, Chunguang Chang, and Chunyang Zhu. Continuous phenomenological modeling for the viscosity of

shear thickening fluids. *Nanomaterials and Nanotechnology*, 8:1–7, 2018.

[79] Karl Perktold and Gerhard Rappitsch. Computer simulation of local blood flow and vessel mechanics in a compliant carotid artery bifurcation model. *Journal of Biomechanics*, 28:845–856, 1995.

[80] Marcel J. Crochet, A. R. Davies, and Kenneth Walters. *Numerical simulation of non-Newtonian fluid flow*. Elsevier, 1984.

[81] Roland Glowinski. *Numerical methods for nonlinear variational problems*. Springer, 1984.

[82] R. Glowinski, T. W. Pan, T. I. Hesla, D. D. Joseph, and J. PÃ©riaux. A Fictitious Domain Approach to the Direct Numerical Simulation of Incompressible Viscous Flow past Moving Rigid Bodies: Application to Particulate Flow. *Journal of Computational Physics*, 169:363–426, 2001.

[83] Songdong Shao and Edmond Y.M. Lo. Incompressible SPH method for simulating Newtonian and non-Newtonian flows with a free surface. *Advances in Water Resources*, 26:787–800, 2003.

[84] L. G. Leal. The motion of small particles in non-Newtonian fluids. *Journal of Non-Newtonian Fluid Mechanics*, 5:33–78, 1979.

[85] Aristides Dokoumetzidis, Richard Magin, and Panos MacHeras. Fractional kinetics in multi-compartmental systems. *Journal of Pharmacokinetics and Pharmacodynamics*, 37:507–524, 2010.

[86] H. Schiessel and A. Blumen. Mesoscopic Pictures of the Sol-Gel Transition: Ladder Models and Fractal Networks. *Macromolecules*, 28:4013–4019, 1995.

[87] Tariq Samad, Margret Bauer, Scott Bortoff, Stefano Di Cairano, Lorenzo Fagiano, Peter Fogh Odgaard, R. Russell Rhinehart, Ricardo Sanchez-Pena, Atanas Serbezov, Finn Ankersen, Philippe Goupil, Benyamin Grosman, Marcel Heertjes, Iven Mareels, and Raye Sosseh. Industry engagement with control research: Perspective and messages. *Annual Reviews in Control*, 49:1–14, 2020.

[88] Yang Quan Chen, Ivo Petráš, and Dingyü Xue. Fractional order control - A tutorial. In *Proceedings of the American Control Conference*, pages 1397–1411, 2009.

[89] Cristina I. Muresan, Abhishek Dutta, Eva H. Dulf, Zehra Pinar, Anca Maxim, and Clara M. Ionescu. Tuning algorithms for fractional order internal model controllers for time delay processes. *International Journal of Control*, pages 579–593, 2016.

[90] Karima Amoura, Rachid Mansouri, Maâmar Bettayeb, and Ubaid M. Al-Saggaf. Closed-loop step response for tuning PID-fractional-order-filter controllers. *ISA Transactions*, pages 247–257, 2016.

[91] Bettayeb Maâmar and Mansouri Rachid. IMC-PID-fractional-order-filter controllers design for integer order systems. In *ISA Transactions*, pages 1620–1628, 2014.

[92] L. Grüne, S. Hirche, O. Junge, P. Koltai, D. Lehmann, J. Lunze, A. Molin, R. Sailer, M. Sigurani, C. Stöcker, and F. Wirth. *Event-Based Control*, pages 169–261. InternSpringerational Publishing, Heidelberg, 2014.

[93] Jan Lunze and Daniel Lehmann. A state-feedback approach to event-based control. *Automatica*, pages 211–215, 2010.

[94] Antonio Visioli. Research trends for PID controllers. *Acta Polytechnica*, pages 144–150, 2012.

[95] Jose Sanchez, Maria Guinaldo, Antonio Visioli, and Sebastian Dormido. Identification of process transfer function parameters in event-based PI control loops. *ISA Transactions*, 75:157–171, 2018.

[96] Ercan Oztemel and Samet Gursev. Literature review of Industry 4.0 and related technologies. *Journal of Intelligent Manufacturing*, 31:127–182, 2020.

[97] Xun Xu, Yuqian Lu, Birgit Vogel-Heuser, and Lihui Wang. Industry 4.0 and Industry 5.0-Inception, conception and perception. *Journal of Manufacturing Systems*, 61:530–535, 2021.

[98] Saurabh Vaidya, Prashant M. Ambad, and S. M. Bhosle. Industry 4.0 - A Glimpse. *Procedia Manufacturing*, 20:233–238, 2018.

[99] Alaa Abdelaal, Tamir Hegazy, and Mohamed Hefeeda. Event-based control as a cloud service. pages 1017–1023, 05 2017.

[100] Abdelrahim Mohamed, Muhammad Ali Imran, Pei Xiao, and Rahim Tafazolli. Memory-Full Context-Aware Predictive Mobility Management in Dual Connectivity 5G Networks. *IEEE Access*, 6:9655–9666, 2018.

[101] Hong Linh Truong and Schahram Dustdar. A survey on context-aware web service systems. *International Journal of Web Information Systems*, pages 5–31, 2009.

[102] Jiankun Sun, Jun Yang, and Shihua Li. Reduced-order GPIO based dynamic event-Triggered tracking control of a networked one-DOF link manipulator without velocity measurement. *IEEE/CAA Journal of Automatica Sinica*, pages 725–734, 2020.

[103] Roland Heidel, Michael Hoffmeister, Martin Hankel, and Udo Döbrich. The Reference Architecture Model RAMI 4.0 and the Industrie 4.0 component. 2019.

[104] Karl Johan Åström and Bo Bernhardsson. *Systems with Lebesgue Sampling*, pages 1–13. Springer, 2007.

[105] Luca Merigo, Manuel Beschi, Fabrizio Padula, and Antonio Visioli. A noise-filtering event generator for PIDPlus controllers. *Journal of the Franklin Institute*, pages 774–802, 2018.

[106] William Dunham. *The calculus gallery: Masterpieces from Newton to Lebesgue*. Princeton University Press, 2015.

[107] K. J. Åström and B. M. Bernhardsson. Comparison of Riemann and Lebesgue sampling for first order stochastic systems. In *Proceedings of the IEEE Conference on Decision and Control*, pages 2011–2016, 2002.

[108] Rafael Socas, Raquel Dormido, and SebastiÃ¡n Dormido. New control paradigms for resources saving: An approach for mobile robots navigation. *Sensors (Switzerland)*, 18:281, 2018.

[109] Ernesto Aranda-Escolastico, Maria Guinaldo, Ruben Heradio, Jesus Chacon, Hector Vargas, Jose Sanchez, and Sebastian Dormido. Event-based control: A bibliometric analysis of twenty years of research. *IEEE Access*, 8:47188–47208, 2020.

[110] Peter J. Gawthrop and Liuping Wang. Event-driven intermittent control. *International Journal of Control*, pages 2235–2248, 2009.

[111] Qinglei Hu and Yongxia Shi. Event-based coordinated control of spacecraft formation flying under limited communication. *Nonlinear Dynamics*, 99:2139–2159, 12 2019.

[112] Jose Sanchez, Miguel Guarnes, and S. Dormido. On the Application of Different Event-Based Sampling Strategies to the Control of a Simple Industrial Process. *Sensors (Basel, Switzerland)*, 9:6795–818, 09 2009.

[113] A. Pawlowski, J. L. Guzmán, M. Berenguel, F. G. Acién, and S. Dormido. *Event-Based Control Systems for Microalgae Culture in Industrial Reactors*, pages 1–48. Springer Singapore, Singapore, 2017.

[114] Enrique Rodriguez-Miranda, Manuel Beschi, Jose Guzman, M. Berenguel, and Antonio Visioli. Daytime/Nighttime Event-Based PI Control for the pH of a Microalgae Raceway Reactor. *Processes*, 7:247, 04 2019.

[115] Xiaojing Han and Yuechao Ma. Passivity analysis for singular systems with randomly occurring uncertainties via the event-based sliding mode control. *Computational and Applied Mathematics*, 39(2):99, 2020.

[116] A. E. Abdelaal, T. Hegazy, and M. Hefeeda. Event-based control as a cloud service. In *2017 American Control Conference (ACC)*, pages 1017–1023, 2017.

[117] W. P.M.H. Heemels, K. H. Johansson, and P. Tabuada. An introduction to event-triggered and self-triggered control. In *Proceedings of the IEEE Conference on Decision and Control*, pages 3270–3285, 2012.

[118] Maria del Mar Castilla, Carlos Bordons, and Antonio Visioli. Event-based state-space model predictive control of a renewable hydrogen-based microgrid for office power demand profiles. *Journal of Power Sources*, 450:227670, 2020.

[119] Qinyuan Liu, Zidong Wang, Xiao He, and D. H. Zhou. A survey of event-based strategies on control and estimation. pages 90–97, 2014.

[120] Aleksei Tepljakov, Eduard Petlenkov, and Juri Belikov. Efficient analog implementations of fractional-order controllers. *Proceedings of the 2013 14th International Carpathian Control Conference, ICCC 2013*, pages 377–382, 05 2013.

[121] Emmanuel A. Gonzalez, Vassilis Alimisis, Costas Psychalinos, and Aleksei Tepljakov. Design of a Generalized Fractional-Order PID Controller Using Operational Amplifiers. In *2018 25th IEEE International Conference on Electronics, Circuits and Systems (ICECS)*, pages 253–256, 2018.

[122] Ilias Dimeas, Ivo Petras, and Costas Psychalinos. New analog implementation technique for fractional-order controller: A DC motor control. *AEU - International Journal of Electronics and Communications*, pages 192–200, 2017.

[123] Shayok Mukhopadhyay, Calvin Coopmans, and Yang Quan Chen. Purely analog fractional order PI control using discrete fractional capacitors (fractors): Synthesis and experiments. In *Proceedings of the ASME Design Engineering Technical Conference*, pages 1307–1314, 2009.

[124] YangQuan Chen, Dingyu Xue, and Huifang Dou. Fractional Calculus and Biomimetic Control. In *2004 IEEE International Conference on Robotics and Biomimetics*, pages 901–906, 2004.

[125] BM Vinagre, I Podlubny, A Hernandez, and V Feliu. Some approximations of fractional order operators used in control theory and applications. *Fractional calculus and applied analysis*, pages 1–18, 2000.

[126] Jose Tenreiro Machado. Discrete-time fractional-order controllers. *Fractional Calculus and Applied Analysis*, 4:47–66, 01 2001.

[127] Ramiro Barbosa and Jose Tenreiro Machado. Implementation of Discrete-Time Fractional-Order Controllers based on LS Approximations. *Acta Polytechnica Hungarica*, 3:5–22, 2006.

[128] Changpin Li, Deliang Qian, and Yangquan Chen. On Riemann-Liouville and Caputo derivatives. *Discrete Dynamics in Nature and Society*, pages 1–15, 2011.

[129] Zhengang Zhao and Changpin Li. Fractional difference/finite element approximations for the time-space fractional telegraph equation. *Applied Mathematics and Computation*, pages 2975–2988, 2012.

[130] A. Oustaloup, B. Mathieu, and P. Lanusse. The CRONE Control of Resonant Plants: Application to a Flexible Transmission. *European Journal of Control*, 1:113–121, 1995.

[131] L. Dorcak, I. Petras, Ján Terpák, and Martin Zborovjan. Comparison of the methods for discrete approximation of the fractional-order operator. In *Proc. of the ICCC'2003 conference*, pages 851–856, High Tatras, Slovak Republic, 2003.

[132] Robin De Keyser, Cristina I. Muresan, and Clara M. Ionescu. An efficient algorithm for low-order direct discrete-time implementation of fractional order transfer functions. *ISA Transactions*, pages 229–238, 2018.

[133] Shakoor Pooseh, Ricardo Almeida, and Delfim F.M. Torres. Discrete direct methods in the fractional calculus of variations. *Computers and Mathematics with Applications*, pages 668–676, 2013.

[134] Jaydeep Swarnakar, Prasanta Sarkar, and Lairenlakpam Joyprakash Singh. Direct Discretization Method for Realizing a Class of Fractional Order System in Delta Domain - a Unified Approach. *Automatic Control and Computer Sciences*, pages 127–139, 2019.

[135] Blas M. Vinagre, Yang Quan Chen, and Ivo Petráš. Two direct Tustin discretization methods for fractional-order differentiator/integrator. *Journal of the Franklin Institute*, pages 349–362, 2003.

[136] Yang Quan Chen and Kevin L. Moore. Discretization schemes for fractional-order differentiators and integrators. *IEEE Transactions on Circuits and Systems I: Fundamental Theory and Applications*, 49:363–367, 2002.

[137] Mohsen Hadian, Alireza Aarabi, Amin Biglari Makvand, and Milad Mehrshadian. A New Event-Based PI Controller Using Evolutionary Algorithms. *Journal of Control, Automation and Electrical Systems*, 30:30–47, 09 2019.

[138] Rongjun Liu, Junfeng Wu, and Dan Wang. Event-based reference tracking control of discrete-time nonlinear systems via delta operator method. *Journal of the Franklin Institute*, 356(17):10514 – 10531, 2019. Special Issue on Distributed Event-Triggered Control, Estimation, and Optimization.

[139] Angel Ruiz, Manuel Beschi, Antonio Visioli, S. Dormido, and Jorge Jimenez. A Unified Event-based Control Approach for FOPTD and IPTD Processes Based on the Filtered Smith Predictor. *Journal of the Franklin Institute*, 354:1239–1264, 11 2016.

[140] Isabela Birs, Silviu Folea, Ovidiu Prodan, Eva Dulf, and Cristina Muresan. An Experimental Tuning Approach of Fractional Order Controllers in the Frequency Domain. volume 10, page 2379, 2020.

[141] Ramon Vilanova and Antonio Visioli. *PID control in the third millennium*. Springer, 2012.

[142] Isabela Birs, Cristina Muresan, Dana Copot, Ioan Nascu, and Clara Ionescu. Identification for control of suspended objects in non-newtonian fluids. *Fractional Calculus and Applied Analysis*, 22:1378–1394, 2020.

[143] Giuseppe Failla and Massimiliano Zingales. Advanced materials modelling via fractional calculus: Challenges and perspectives. *Philosophical Transactions of the Royal Society A: Mathematical, Physical and Engineering Sciences*, 378:2172, 2020.

[144] Manuel D. Ortigueira, Clara M. Ionescu, Jose Tenreiro Machado, and Juan J. Trujillo. Fractional signal processing and applications. *Signal Processing*, 107:197, 2015.

[145] Dumitru Baleanu, Tamas Kalmar-Nagy, Themistoklis Sapsis, and Hiroshi Yabuno. Special Issue: Nonlinear Dynamics: Models, Behavior, and Techniques. *Journal of Computational and Nonlinear Dynamics*, 12:48001, 04 2017.

[146] Dana Copot and Clara Ionescu. Models for Nociception Stimulation and Memory Effects in Awake and Aware Healthy Individuals. *IEEE Transactions on Biomedical Engineering*, 66:718–726, 2019.

[147] Maria Ghita, Dana Copot, Mihaela Ghita, Eric Derom, and Clara Ionescu. Low Frequency Forced Oscillation Lung Function Test Can Distinguish Dynamic Tissue Non-linearity in COPD Patients. *Frontiers in Physiology*, 10:1390, 2019.

[148] Emanuel Bologna, Francesca Graziano, Luca Deseri, and Massimiliano Zingales. Power-Laws hereditariness of biomimetic ceramics for cranioplasty neurosurgery. *International Journal of Non-Linear Mechanics*, 115:61–67, 2019.

[149] Majid Abbasian, Mehrzad Shams, Ziba Valizadeh, Abouzar Moshfegh, Ashkan Javadzadegan, and Shaokoon Cheng. Effects of different non-Newtonian models on unsteady blood flow hemodynamics in patient-specific arterial models with in-vivo validation. *Computer Methods and Programs in Biomedicine*, 186:105185, 2020.

[150] Sercan Gul, Oney Erge, and Eric van Oort. Frictional pressure losses of Non-Newtonian fluids in helical pipes: Applications for automated rheology measurements. *Journal of Natural Gas Science and Engineering*, 73:103042, 2020.

[151] Libo Feng, Fawang Liu, Ian Turner, and Pinghui Zhuang. Numerical methods and analysis for simulating the flow of a generalized Oldroyd-B fluid between two infinite parallel rigid plates. *International Journal of Heat and Mass Transfer*, 115:1309–1320, 2017.

[152] Clara Ionescu. A memory-based model for blood viscosity. *Communications in Nonlinear Science and Numerical Simulation*, 45:29–34, 04 2017.

[153] Bin Zhu, Lian Fang Tian, Qi Liang Du, Qiu Xia Wu, Farisi Zeyad Sahl, and Yao Yeboah. Adaptive dual fractional-order variational optical flow model for motion estimation. *IET Computer Vision*, 13:277–284, 2019.

[154] Clara M. Ionescu. Phase constancy in a ladder model of neural dynamics. *IEEE Transactions on Systems, Man, and Cybernetics Part A:Systems and Humans*, 42:1543–1551, 2012.

[155] Karabi Biswas, Gary Bohannan, Riccardo Caponetto, Antonio Mendes Lopes, and Jose Antonio Tenreiro Machado. *Introduction to fractional-order elements and devices*. 2017.

[156] Sourabh Katoch, Sumit Singh Chauhan, and Vijay Kumar. A review on genetic algorithm: past, present, and future. *Multimedia Tools and Applications*, 80:1–36, 2021.

[157] Dongshu Wang, Dapei Tan, and Lei Liu. Particle swarm optimization algorithm: an overview. *Soft Computing*, 22:387–408, 2018.

[158] Wenping Fan, Xiaoyun Jiang, and Haitao Qi. Parameter estimation for the generalized fractional element network Zener model based on the Bayesian method. *Physica A: Statistical Mechanics and its Applications*, 427:40–49, 2015.

[159] Mario Di Paola, Giuseppe Failla, Antonina Pirrotta, Alba Sofi, and Massimiliano Zingales. The mechanically based non-local elasticity: An overview of main results and future challenges. *Philosophical Transactions of the Royal Society A: Mathematical, Physical and Engineering Sciences*, 371:20120433, 2013.

[160] J.M. Pérez Zerpa, A. Canelas, B. Sensale, D. Bia Santana, and R.L. Armentano. Modeling the arterial wall mechanics using a novel high-order viscoelastic fractional element. *Applied Mathematical Modelling*, 39(16):4767–4780, 2015.

[161] Damian Craiem and Ricardo Armentano. A fractional derivative model to describe arterial viscoelasticity. *Biorheology*, 44:251–63, 2007.

[162] George P. Sutton and Howard S. Seifert. *Rocket Propulsion Elements,* 9^{th} *edition*. Wiley, 2009.

[163] Stephen J. Ebbens and Jonathan R. Howse. In pursuit of propulsion at the nanoscale. *Soft Matter*, pages 726–738, 2010.

[164] MAN Diesel & Turbo. *Basic Principles of Ship Propulsion*. MAN, 2013.

[165] Nicolas Mano and Adam Heller. Bioelectrochemical propulsion. *Journal of the American Chemical Society*, pages 11574–11575, 2005.

[166] E. M. Purcell. The efficiency of propulsion by a rotating flagellum. *Proceedings of the National Academy of Sciences of the United States of America*, pages 11307–11311, 1997.

[167] Poul Andersen, Jens J Kappel, and Eugen Spangenberg. Aspects of Propeller Developments for a Submarine. In *Proceedings of the First International Symposium on Marine Propulsors - smp'09*, pages 551–561, 2009.

[168] P. N. Joubert. *Some Aspects of Submarine Design Part 1. Hydrodynamics*. 2004.

[169] Sascha Merz, Nicole Kessissoglou, and Roger Kinns. Extraction of a Submarine Hull by Propeller forces. In *14th International Congress on Sound & Vibration*, 2007.

[170] Isabela Birs, Cristina Muresan, Silviu Folea, and Ovidiu Prodan. An experimental nanomedical platform for controller validation on targeted drug delivery. In *2017 Australian and New Zealand Control Conference (ANZCC)*, pages 161–165, Dec 2017.

[171] M E Sahin, F ; Blaabjerg, and A Sangwongwanich. A Review on Supercapacitor Materials and Developments. *Turkish Journal of Materials*, 5, 2020.

[172] Kieu The Loan Trinh, Wenming Wu, and Nae Yoon Lee. Fabrication of a 3D Teflon microdevice for energy free homogeneous liquid flow inside a long microchannel and its application to continuous-flow PCR. *RSC Advances*, 7:10624–10630, 2017.

[173] Martin Tajmar, Matthias Kößling, Marcel Weikert, and Maxime Monette. The SpaceDrive Project - First Results on EMDrive and Mach-Effect Thrusters. 05 2018.

[174] Heidi Fearn, Adam Zachar, Keith Wanser, and James Woodward. Theory of a Mach Effect Thruster I. *Journal of Modern Physics*, 06:1510–1525, 2015.

[175] Borja Pozo, Jose Ignacio Garate, Jose Angel Araujo, and Susana Ferreiro. Energy harvesting technologies and equivalent electronic structural models - review. *Electronics (Switzerland)*, 8:486, 2019.

[176] M. Sakar, H. R. Chandan, and R. Shwetharani. Graphene paper-based electrochemical sensors for biomolecules. *Graphene-Based Electrochemical Sensors for Biomolecules: A Volume in Micro and Nano Technologies*, pages 297–320, 2018.

[177] S. Thone. Mayfair 750 GPH Bilge Pump Thruster Testing. `http://www.homebuiltrovs.com/mayfair750test.html`. Accessed: 2021-01-25.

[178] Karl J. Aström. *Event based control*, pages 1–13. Springer, Cham, 2021.

[179] Brian G. Thomas. Review on Modeling and Simulation of Continuous Casting. *Steel Research International*, 89:1700312, 2018.

[180] T. Kvackaj. The review of steel and steel products flat-rolled production. *Metalurgija*, 39:1–15, 2000.

[181] Manickaraj Jeyakumar, Mohamed Hamed, and Sumanth Shankar. Rheology of liquid metals and alloys. *Journal of Non-Newtonian Fluid Mechanics*, 166(14):831–838, 2011.

[182] Brian G. Thomas. Modeling of continuous-casting defects related to mold fluid flow. pages 2–17, 2005.

[183] B G Thomas, Q Yuan, B Zhao, and S P Vanka. Transient Fluid-Flow Phenomena in the Continuous Steel-Slab Casting Mold and Defect Formation. *Journal of Metals - electronic edition*, pages 1–8, 2006.

[184] Ravi Golani, Vikas Singh, S. K. Ajmani, and Ravi Ranjan. Investigation of surface flow velocity and vortex formation flow patterns in continuous slab casting mold through physical modelling. *Proceedings of the 6th International Congress on the Science and Technology of Steelmaking, ICS 2015*, pages 30–36, 2015.

[185] Hong Xiao, Shao xiang Li, Pu Wang, Hai yan Tang, and Jia quan Zhang. Study on the In-mold Flow Behavior Driven by a Subsurface Electromagnetic Stirring for IF Steel Slab Casting. *Minerals, Metals and Materials Series*, 5:590 – 601, 2021.

[186] X. Deng, C. Ji, Y. Cui, L. Li, X. Yin, Y. Yang, and A. McLean. Flow pattern control in continuous slab casting moulds: physical modelling and plant trials. *Ironmaking and Steelmaking*, 44:461–471, 2017.

[187] A. K. Tieu and I. S. Kim. Simulation of the continuous casting process by a mathematical model. *International Journal of Mechanical Sciences*, 39:185–192, 1997.

[188] Bum Ja Jin and Kyungkeun Kang. Caccioppoli type inequality for non-Newtonian stokes system and a local energy inequality of non-Newtonian navier-stokes equations without pressure. *Discrete and Continuous Dynamical Systems- Series A*, 37:4815–4834, 2017.

[189] Boling Guo and Chunxiao Guo. The convergence of non-Newtonian fluids to Navier-Stokes equations. *Journal of Mathematical Analysis and Applications*, 357:468–478, 2009.

[190] Zhiqian Wang, Baoquan Mao, Rui Zhu, Xianghua Bai, and Xiaoping Han. Fractional Maxwell Model for Oscillating Flow of a Viscoelastic Elastomer Shock Absorber. *Binggong Xuebao/Acta Armamentarii*, 41:984–995, 2020.

[191] Virginia Kiryakova. A guide to special functions in fractional calculus. *Mathematics*, 9:106, 2021.

[192] Mohammad Amirian Matlob and Yousef Jamali. The concepts and applications of fractional order differential calculus in modeling of viscoelastic systems: A primer. *Critical Reviews in Biomedical Engineering*, 47:249–276, 2019.

[193] Olivier Lefevre. ArcelorMittal - Annual Report 2020, 2020. Accessed: 2-1-2021.

[194] Seppo Louhenkilpi. Chapter 1.8 - Continuous Casting of Steel. In Seshadri Seetharaman, editor, *Treatise on Process Metallurgy*, pages 373–434. Elsevier, Boston, 2014.

[195] V. Sinelnikov, V. Genkin, and A. Leites. Types of Continuous Casters and the Quality of Continuous-Cast Slabs for Obtaining Rolled Products for Crucial Applications. *Metallurgist*, 49:383–389, 09 2005.

[196] Jean-Francois Domgin, Marine Anderhuber, Michael De Doncker, and A. De Paepe. Optimization of an Electromagnetic Technology in ArcelorMittal Gent for Improving Products Quality in Steel Industry. *Journal for Manufacturing Science and Production*, 15(1):105–117, 2015.

[197] Michaël De Doncker and Jean Francois Domgin. Reduction of slivers by the use of an electromagnetic actuator. *Metallurgical Research and Technology*, 112:402, 2015.

[198] Seong-Mook Cho and Brian G. Thomas. Electromagnetic Forces in Continuous Casting of Steel Slabs. *Metals*, 9(4):471, 2019.

[199] Kevin Dekemele, Clara-Mihaela Ionescu, Michael De Doncker, and Robin De Keyser. Closed loop control of an electromagnetic stirrer in the continuous casting process. In *2016 European Control Conference (ECC)*, pages 61–66, 2016.

[200] Bin Zhao, Suria Pratap Vanka, and Brian G. Thomas. Numerical study of flow and heat transfer in a molten flux layer. *International Journal of Heat and Fluid Flow*, 26:105–118, 2005.

[201] Rui Liu, Joydeep Sengupta, D. Crosbie, S. Chung, M. Trinh, and Brian Thomas. *Measurement of Molten Steel Surface Velocity with SVC and Nail Dipping during Continuous Casting Process*, pages 51 – 58. 04 2011.

[202] Alain Oustaloup. *Diversity and Non-integer Differentiation for System Dynamics*. Wiley, 2014.

[203] Ke cai Cao, YangQuan Chen, and Dan Stuart. A Fractional Micro-Macro Model for Crowds of Pedestrians Based on Fractional Mean Field Games. *IEEE/CAA Journal of Automatica Sinica*, 3:261–270, 2016.

[204] Clara Ionescu, Isabela Birs, Dana Copot, Cristina Muresan, and Ricardo Caponetto. Mathematical modelling with experimental validation of viscoelastic properties in non-Newtonian fluids. *Philosophical Transactions of the Royal Society A: Mathematical, Physical and Engineering Sciences*, 378:20190284, 2020.

[205] Isabela Birs, Cristina Muresan, Ovidiu Prodan, Silviu Folea, and Clara Ionescu. An experimental approach towards motion modeling and control of a vehicle transiting a non-newtonian environment. *Fractal and Fractional*, 5:104, 2021.

[206] Ingo Schafer and Klaus Kruger. Modelling of coils using fractional derivatives. *Journal of Magnetism and Magnetic Materials*, 307:91–98, 2006.

[207] Ingo Schafer and Klaus Kruger. Modelling of lossy coils using fractional derivatives. *Journal of Physics D: Applied Physics*, 41:45001 – 45021, 2008.

[208] Marcin Sowa and Lukasz Majka. Ferromagnetic core coil hysteresis modeling using fractional derivatives. *Nonlinear Dynamics*, 101:775–793, 2020.

[209] Fabrizio Padula and Antonio Visioli. *Advances in Robust Fractional Control*. Springer, 2015.

[210] Antonio Visioli. *Practical PID control*. Springer, 2006.

[211] Jocelyn Sabatier, Patrick Lanusse, Pierre Melchior, and Alain Oustaloup. *Fractional order differentiation and robust control design*. Springer, 2015.

[212] Paolo Lino, Guido Maione, Fabrizio Padula, Silvio Stasi, and Antonio Visioli. Synthesis of fractional-order PI controllers and fractional-order filters for industrial electrical drives. *IEEE/CAA Journal of Automatica Sinica*, 4:58–69, 2017.

[213] Isabela Birs, Ioan Nascu, Clara Ionescu, and Cristina Muresan. Event-based fractional order control. *Journal of Advanced Research*, pages 191–203, 2020.

[214] Jan Reschke and Sergio Gallego-Garcia. A novel methodology for assessing and modeling manufacturing processes. *Applied Sciences (Switzerland)*, 11:10117, 2021.

[215] Duarte Alemao, Andre Dionisio Rocha, and Jose Barata. Smart manufacturing scheduling approaches-systematic review and future directions. *Applied Sciences (Switzerland)*, 11:2186, 2021.

[216] Bhavik Patel. *Electrochemistry for Bioanalysis*. Elsevier, 2020.

[217] Valerie Vanhoorne and Chris Vervaet. Recent progress in continuous manufacturing of oral solid dosage forms. *International Journal of Pharmaceutics*, 579:119194, 2020.

[218] Diego Malevez and Dana Copot. From batch to continuous tablet manufacturing: a control perspective. *IFAC-PapersOnLine*, 54:562–567, 2021.

[219] Christoph Clemens, Mario Radschun, Annette Jobst, Jörg Himmel, and Olfa Kanoun. Detection of density changes in soils with impedance spectroscopy. *Applied Sciences (Switzerland)*, 11:1568, 2021.

[220] Dana Copot, Robin De Keyser, Jasper Juchem, and Clara M. Ionescu. Fractional order impedance model to estimate glucose concentration: In vitro analysis. *Acta Polytechnica Hungarica*, 14:207–220, 2017.

[221] Kamal Shah, Fahd Jarad, and Thabet Abdeljawad. Stable numerical results to a class of time-space fractional partial differential equations via spectral method. *Journal of Advanced Research*, 25:39–48, 2020.

[222] Sigur Skogestad and Chriss Grimholt. *PID Control in the Third Millenium - Lessons Learned and New Approaches*. Springer, 2012.

[223] Fenghui Huang and Fawang Liu. The space-time fractional diffusion equation with Caputo derivatives. *Journal of Applied Mathematics and Computing*, 19:179–190, 2005.

[224] Edward Cussler. Diffusion. Mass Transfer in Fluid Systems. *Journal of Electroanalytical Chemistry and Interfacial Electrochemistry*, 194, 1985.

[225] Tore Hägglund and Jose Luis Guzman. Development of Basic Process Control Structures. volume 51, pages 775–780, 2018.

[226] Ahmed Y. Kallel, Dhouha Bouchaala, and Olfa Kanoun. Critical implementation issues of excitation signals for embedded wearable bioimpedance spectroscopy systems with limited resources. *Measurement Science and Technology*, 32:84011, 2021.

[227] Rashid O. Kadara, Norman Jenkinson, and Craig E. Banks. Characterisation of commercially available electrochemical sensing platforms. *Sensors and Actuators, B: Chemical*, 138:556–562, 2009.

An abstract representation of non-Newtonian fluids, a class of fluids which falls beyond the classical linear Newtonian properties as is the case for liquid steel.